Linear and Nonlinear Structure-Soil-Structure Interaction During Earthquakes

By

Felipe Adolfo Vicencio Navarrete

Department of Civil Engineering

University of Bristol

A dissertation submitted to the University of Bristol in accordance with the requirements for award of the degree of Doctor of Philosophy in the Faculty of Engineering

June 2020

Word Count: sixty-four thousand

To my parents and my family

ABSTRACT

This thesis aims to evaluate the effects of Structure-Soil-Structure Interaction (SSSI), by performing time-history seismic simulations, given different parameters of structures, inter-building spacings, and soil types. Different linear and nonlinear reduced-order models are generated and subjected to varied acceleration ground motions.

An extended 2D linear model that enables higher mode interaction between structures is proposed (Chapter 3). Results suggest that the coupled effects are possible between more than just the primary modes. Therefore, there is a significant interaction between a small building closely flanked by a much taller one.

Chapter 4 introduces a 2D model that examines the SSSI between unsymmetrical-plan and symmetrical-plan buildings. Results suggest that a taller torsionally-irregular building adjacent to smaller buildings could be adversely affected by SSSI. This contradicts previous studies, where the taller buildings benefit from adjacent smaller buildings.

Nonlinear soil behaviour is incorporated in the two-dimension model (Chapter 5) by employing Bouc-Wen's model, for the soil underneath the foundations. The ground motion is spectrally matched with Eurocode-8 elastic spectra. Results show that the SSSI effects could be more pronounced when the nonlinear behaviour is considered.

Chapter 6 presents a 3D model of SSSI between multiple buildings which shortens computational run-times for large clusters. The auto-rotational and inter-rotational spring stiffnesses of foundations are determined by a surficial displacement field (based on Boussinesq approximation and calibrated against FEA) and inverse system identification (using least-squares or Kronecker products). Different building arrangements are presented to compare with previous research and highlight the method's versatility.

Chapter 7 investigates the effects of the rotational ground motions upon buildings. Rotational ground components are extracted by using a multi-station procedure, and data from the SMART-1 array are employed. Results show that the rotational ground motion can amplify the responses of certain structures, depending on the ratio of rotational to horizontal ground motions.

.

This page intentionally left blank

ACKNOWLEDGEMENT

I am deeply thankful to my Supervisor, Dr Nicholas A. Alexander, for his vision and for guiding me to accomplish this work. During these four years of hard work, Nick gave me countless opportunities to grow as a person, a researcher, and an engineer. He consistently challenged me to give the best of me and I had the privilege of discussing each of the topics of my research, without any limitation of time or resources. I have learned so much from him in both technical and personal aspects. I am very grateful to count him among my friends.

I would like to thank Professor George Mylonakis for his insightful comments on my research during the whole process. I am very grateful too for the support of the Faculty of Engineering at the University of Bristol and in particular the team of the Advanced Computing Research Centre (ACRC), as most of the computations necessary for this work were carried out on BlueCrystal, the High-Performance Computing (HPC) machines of the University of Bristol. Also, I would like to thank my office mates for sharing ideas, coffee, and all the support when it was most needed.

This research would not have been possible without the financial support from the Ministry of Education, Chile and the Commission for Scientific and Technological Research (CONICYT) through grant BCH 72170305. I appreciate this opportunity to study in one of the best universities in the U.K.

I am more than happy that I have lived in a city like Bristol with my family. This gave me the opportunity to meet amazing people, discover new places and enjoy the beautiful scenery. I really enjoyed being here all this period.

All my gratitude and love to my whole family. Without their support, all this work would not have been possible. My parents, Emilia and Adolfo, always taught me discipline, focus and to enjoy the road more than the end. Thanks to my lovely son Rafael, for being an infinite source of happiness and motivation. Looking at you, growing up every day is the most amazing gift that I have received in my life. Finally, I would like to express my eternal gratitude to my gorgeous wife Luna. She is the most important part of this accomplishment, with her tireless encouragement, company, and love.

This page intentionally left blank

AUTHOR'S DECLARATION

I declare that the work in this dissertation was carried out in accordance with the requirements of the University's Regulations and Code of Practice for Research Degree Programmes and that it has not been submitted for any other academic award. Except where indicated by specific reference in the text, the work is the candidate's own work. Work done in collaboration with, or with the assistance of, others, is indicated as such. Any views expressed in the dissertation are those of the author.

SIGNED: FELIPE VICENCIO NAVARRETE DATE: 25 JUNE 2020

This page intentionally left blank

LIST OF PUBLICATIONS

This thesis is based on the work published in the following papers, on all of which F. Vicencio is the first author.

Peer reviewed journal papers:

[1] Vicencio, F., and Alexander, N.A. (2018a). Dynamic interaction between adjacent buildings through nonlinear soil during earthquakes. *Soil Dynamics and Earthquake Engineering*, 108, 130-141.

[2] Vicencio, F., and Alexander, N.A. (2018b). Higher mode seismic SSSI between adjacent buildings during earthquakes. *Engineering Structures*, 174, 322-337.

[3] Vicencio, F., and Alexander, N.A. (2019a). A parametric study on the effect of rotational ground motions on building structural responses. *Soil Dynamics and Earthquake Engineering*, 118, 191-206.

[4] Vicencio, F., and Alexander, N.A. (2019b). Dynamic Structure-Soil-Structure interaction in unsymmetrical plan buildings due to seismic excitation. *Soil Dynamics and Earthquake Engineering*, 127, 105817.

[5] Vicencio, F., and Alexander, N.A. (2021). Method to evaluate the dynamic Structure-Soil-Structure Interaction of 3-D buildings arrangement due to seismic excitation. *Soil Dynamics and Earthquake Engineering*, 141, 106494.

Peer reviewed conference papers:

[6] Vicencio, F., and Alexander, N.A. (2017). Discrete model for dynamic SSSI through nonlinear soil. *In: Presented at the SEISMICON 2017. First international conference on seismic design of structures and foundations*. London, (UK).

[7] Vicencio, F., and Alexander, N.A. (2018c). Discrete model for dynamic SSSI between critical structures under strong ground motion. *In: Presented at the 16th European Conference on Earthquake Engineering*. Thessaloniki, Greece.

[8] Vicencio, F., and Alexander, N.A. (2019c). Numerical analysis of Structure-Soil-Structure Interaction for two different buildings during earthquakes. *In: Presented at the COMPDYN 2019. 7th International Conference on Computational Methods in Structural Dynamics and Earthquake Engineering.* Crete, Greece.

This page intentionally left blank

TABLE OF CONTENTS

LIST OF TABLES

This page intentionally left blank

LIST OF FIGURES

Chapter 1

Introduction

1.1 Motivation of the study

Urbanisation and modern lifestyles have caused a gradual shift in the human population from rural to urban areas (United Nations - DESA, 2018). This migration means that in 2018, 55% of the world's population lives in metropolitan regions, and this percentage is increasing every day. In 2018, the number of cities with at least 1 million inhabitants was 548. By 2030, a projected 706 cities will have at least 1 million residents, according to the United Nations (2018). To accommodate the increase of residents and commerce in large cities, new constructions in the limited available urban space are needed. These new buildings are often built closely beside other structures, resulting in the possibility of significant seismic interaction of adjacent buildings through the underlying soil. Therefore, this growth in urbanisation in the last decades has caused a growing need to study this phenomenon deeply.

The population concentration in mega-cities has produced an increase in the seismic hazard in urban areas of countries such as United States (California), Chile, China, Greece, Indonesia, Italy, Japan, Mexico, and New Zealand. On 27 February 2010, a high-magnitude earthquake (Moment magnitude $M_w = 8.8$) affected a large portion of the territory of Chile, including its capital Santiago. Santiago is one of the largest cities in America and the most densely populated conurbation in Chile with 7 million inhabitants (Figure 1.1). The ground shaking lasted for more than two minutes, and the peak horizontal and vertical ground acceleration was larger than 0.6 g. Even though the seismic design and construction standards are high, more than 300,000 buildings were damaged at different levels (Elnashai et al., 2010), including some cases of collapse (see Figure 1.2). The causes of these damages are many, including poor quality construction, inadequate structural design and very poor detailing solutions, site conditions, among others (Elnashai et al., 2010).

As seen in Figure 1.1, the structures are built closely spaced on top of the soil deposit. This suggests that the dynamic interaction between the buildings must occur due to (i) static and dynamic stiffening of the closely spaced soil/structure systems and (ii) the radiation/transfer of vibration energy from a vibrating structure, through the soil, to the other surrounding structures. Then, it is reasonable to say that the seismic response of a building founded in mutual soil cannot be independent but interacts with the adjacent structures. This phenomenon is better known as Structure-Soil-Structure Interaction (SSSI), and it produces substantial technical challenges to the scientific community because of the high system complexity and the considerable uncertainty of future seismic ground motion time series.

Figure 1.1 Picture of the dense metropolitan area in Santiago, Chile

The significance of SSSI was highlighted in the early analytical studies by Warburton et al. (1971) and Luco and Contesse (1973), where the dynamic interaction between two parallel infinite shear walls exited by a vertically incident SH wave was considered. The interaction was found to be prominent in the low-frequency range associated with a resonance frequency of the SSSI system. The SSSI effect is also referred to as Dynamic Cross Interaction (DCI) by Kobori et al. (1973), where a multi-mass system on a Voight type viscoelastic stratum over the rigid block is considered. The results show that the DCI effects depend on the type of excitation, the number of structures and the dynamical characteristics of the structures. In addition, the DCI becomes complicated as the number of buildings increase.

One of the most relevant industries that have helped the early development of SSSI research is nuclear power facilities, where a reactor building is adjacent to a turbine building and a control building. Due to

the spatial configurations of these facilities, the SSSI can induce additional seismic effects which are typically neglected in traditional seismic design. This could increase the probability of failure in these critical structures and the consequence of failure, can be catastrophic to people, the environment, and the facility. In the pioneering work of Lee and Wesley (1973), an analytical approach to evaluate the SSSI effects between several nuclear reactors in a 3D arrangement was used. The seismic action was considered as vertically propagating S-waves through an elastic half-space. The results show that an improper plant layout can increase the magnitude of the dynamical loads, when comparing them with the dynamical loads predicted for the individual structures as independent systems. The coupling effects become more pronounced as the stiffness of the soil decreases.

Figure 1.2 Damaged reinforced concrete building, Santiago, Chile (Elnashai et al., 2010)

Various experimental and numerical studies on SSSI have been conducted in the last decades (which will be described in detail in the next chapter), considering different soil properties, building geometries, and the spacing between the buildings. In general, these works have demonstrated that the coupled effects can be either beneficial or detrimental for the structures. However, despite all these studies, a significant gap remains in the course of current knowledge of SSSI between multiple structures considering linear or nonlinear soil behaviour and various ground motions.

Therefore, this study focuses on the evaluation of the SSSI effects for a broad set of system parameters using linear and nonlinear reduced-order models and considering different types of ground motion time series. For this purpose, this research considers various kinds of reduced-order models that vary according to the kind of behaviour that is sought. The reduced-order modelling has some advantages over the Finite Element Analysis in the framework of a large parametric exploration of the problem. Several rational assumptions are made in these low-order approaches that allow us to cluster the number of system

parameters and reduce the number of degrees of freedom used. Therefore, it is computationally simple/efficient enough for an extensive range of critical system parameters to be explored. The ground motion time series are obtained from the Pacific Earthquake Engineering Research Centre Database (PEER, 2014). Most of the computations necessary for this work were carried out on BlueCrystal, the High-Performance Computing (HPC) machine of the Advanced Computing Research Centre at the University of Bristol.

1.2 Research objectives and contribution to the state of the art

Through the implementation of different reduced-order models, this research makes contributions to address the following key issues:

(i) To evaluate the interaction between a low-rise building adjacent to a neighbouring much taller building. To this end, an additional degree of freedom for each structure that enables higher mode interaction between structures (an extra mode) is considered.

(ii) Is there evidence to suggest that different types of ground motion (Far-Field, Near-Field Without Pulse and Near-Field Pulse-Like) can affect the SSSI behaviour?

(iii) To examine the influence of the SSSI problem on the seismic response of unsymmetrical-plan buildings subject to seismically induced coupled torsion/sway motions.

(iv) To investigate the effect of the soil nonlinearity on the Structure-Soil-Structure Interaction (SSSI) system between two buildings during earthquakes. For that, the size of the adverse/beneficial coupled effects is evaluated. Also, the differences between nonlinear SSSI and linear SSSI are compared.

(v) To propose an efficient mathematical formulation to define the auto-rotational spring coefficients (soil foundation system) and inter-rotational spring coefficients (coupling springs between the buildings) of foundations for any number of buildings.

(vi) To explore the influence of SSSI between multiple buildings in a three-dimensional arrangement under seismic excitation. The formulation has been developed to include the presence of any number of buildings with different heights, widths, and inter-building distances.

(vii) To investigate the effects of the rotational ground motions upon buildings, which includes the influence of Soil-Structure Interaction (SSI). This subject has no direct connection with the coupled effects between buildings, but it is helpful to evaluate the effects of rotational ground motion on structural responses. For this purpose, an indirect method of extracting rotational

ground components using a multi-station procedure is employed. Ground accelerogram data recorded from the SMART-1 array in Taiwan for three different events are used.

1.3 Structure of the thesis

The research in this thesis is presented in eight chapters. Each of the following chapters are summarised below.

- **Chapter 2** presents a literature review of the past and the latest contributions of Structure-Soil-Structure Interaction research, focusing on the state of the art of the interaction problem for multiple buildings. The chapter is divided into the different analytical, numerical, and experimental methods of analysis as implemented by various researchers. Moreover, the pros and cons of discrete models used in the current research are discussed. Finally, some recent studies on Site-City effects and their significant findings are given.

- **Chapter 3** presents an extended version of the reduced-order linear model of SSSI between two buildings under seismic excitation, by including higher mode interaction between structures. This feature enables the exploration of the interaction between buildings with a very large difference in height. A database of strong ground motion records with Far-Field, Near-Field Without Pulse and Near-Field Pulse-Like characteristics is employed (FEMA P695, 2009, Appendix A). The parametric exploration undertaken in this chapter explores the system response behaviour for an extensive range of buildings, inter-building spacings, soil types, as well as ground motion excitations. Over 3 million system/ground motion cases are analysed in this parametric study.

- **Chapter 4** investigates the influence of Structure-Soil-Structure Interaction (SSSI) between a pair of buildings, one of which is unsymmetrical in plan and hence subject to seismically induced coupled torsion/sway motions. A reduced-order parametric model of this system is proposed and validated using finite element analysis. A database of 15 strong ground motion records selected from the PEER-NGA database is employed. The parametric exploration undertaken in this chapter explores the system response behaviour for a large range of building parameters. These dynamic simulations involve over 3 million time-history analyses.

- **Chapter 5** evaluates the effects of SSSI between two buildings given different parameters of the buildings, inter-building spacings and soil type. A two-dimensional reduced-order nonlinear model is proposed. A nonlinear phenomenological Bouc-Wen model for the soil directly underneath the foundations is assumed. Linear rotational interaction springs between buildings and linear behaviour of buildings are considered. The seismic ground motion employed here is spectrally matched with the Eurocode 8 elastic spectra.

- **Chapter 6** explores the influence of SSSI between multiple buildings in a three-dimensional arrangement under seismic excitation. A numerically simplified reduced-order model is proposed to significantly shorten computational run-times for the case of very large clusters of buildings. This formulation has been developed to include the presence of any number of buildings with different height, width, and inter-building distances. The auto-rotational spring stiffnesses and inter-rotational spring stiffnesses of foundations used in this model are determined by the application of an empirical surficial displacement field (loosely based on a form derived from a Boussinesq elastic half-space approximation that is calibrated against FEA) and inverse system identification using either least-squares or an application of Kronecker products. Different spatial building arrangements are presented, in order to compare with previous research and highlight the versatility of the method.

- **Chapter 7** introduces a reduced-order model to investigate the effects of the rotational ground motions upon buildings, which includes the influence of Soil-Structure Interaction (SSI). This chapter has no direct relationship with the SSSI effects. Still, it should be viewed as an initial exploration of the impact of rotational ground motion in the structures, and its future extension to the SSSI problem. An indirect method of extracting rotational ground components using a multi-station procedure is employed. Ground accelerogram data recorded from the SMART-1 array in Taiwan for three different events are used (SMART-1, 1991). The analyses have been undertaken for different parameters of the buildings, soil type, and seismic events. There are of the order of 1.6 million different full time-history analyses in this chapter, with a set of more than 5000 different horizontal-rotational ground motion time-histories employed.

- **Chapter 8** summarises the main conclusions and findings of this research. Recommendations for future research are also proposed.

Chapter 2

Literature Review

2.1 Soil-Structure Interaction background

During an earthquake, structures interact with the surrounding soil beneath their foundations. These structures are typically analysed dynamically as stand-alone structures, i.e. without any consideration of their neighbouring structures. This phenomenon is widely known as Soil-Structure Interaction (SSI), and the importance of including its beneficial or adverse structural effects has been the focus of attention for more than 50 years. An extensive early literature review was presented by Kausel (2010). A State-of-the-Art review was presented by Anand and Kumar (2018). The SSI effects are typically divided into inertial interaction effects and kinematic interaction effects. Inertial interaction refers to the vibrational energy of the superstructure that is transferred into the surrounding soil, causing further deformation in the soil. Inertial interaction results in (i) the period lengthening of the structure due to the soil flexibility (in comparison to its fixed-base period (Veletsos and Meek, 1974)) and (ii) the increase of the system damping due to scattering part of the vibration energy into the soil medium and by hysteretic action in the soil itself (Veletsos and Nair, 1975). Kinematic interaction refers to the difference between the ground motion recorded at the foundation level of a structure and the free-field away from the influence of any structure (Stewart et al., 1999). These differences are due to the ground motion incoherence, wave inclination and foundation embedment.

The methods to resolve the SSI can be divided into (i) the direct analysis (Figure 2.1), where the soil and structure are included within the same finite-element or boundary-element model and analysed as a complete system, and (ii) the substructure approach (Figure 2.1), where the problem is divided into three stages (NEHRP-NIST, 2012). The first stage is to evaluate the foundation input motion (FIM), to take into account the stiffness and geometry of the foundation. Since inertial effects are neglected in this stage

(structure having no mass), the transfer function represents the effects of kinematic interaction. After that, the frequency-dependent impedance functions at the base of the buildings are calculated. The real part of these functions represents the stiffness component of the supporting soil, and the imaginary part reflects the radiation and material damping components of the supporting soil. Finally, the dynamic response of the structure that is supported on the impedance functions, and excited by the seismic input calculated in the first stage is calculated. In general, the linear SSI solution of the substructure approach is performed in the frequency domain using the Fourier transform techniques, driven by the dependency on excitation frequency of the impedance functions. Its dependence on frequency is attributed to the influence that frequency has on inertia rather than soil properties (Gazetas, 1983).

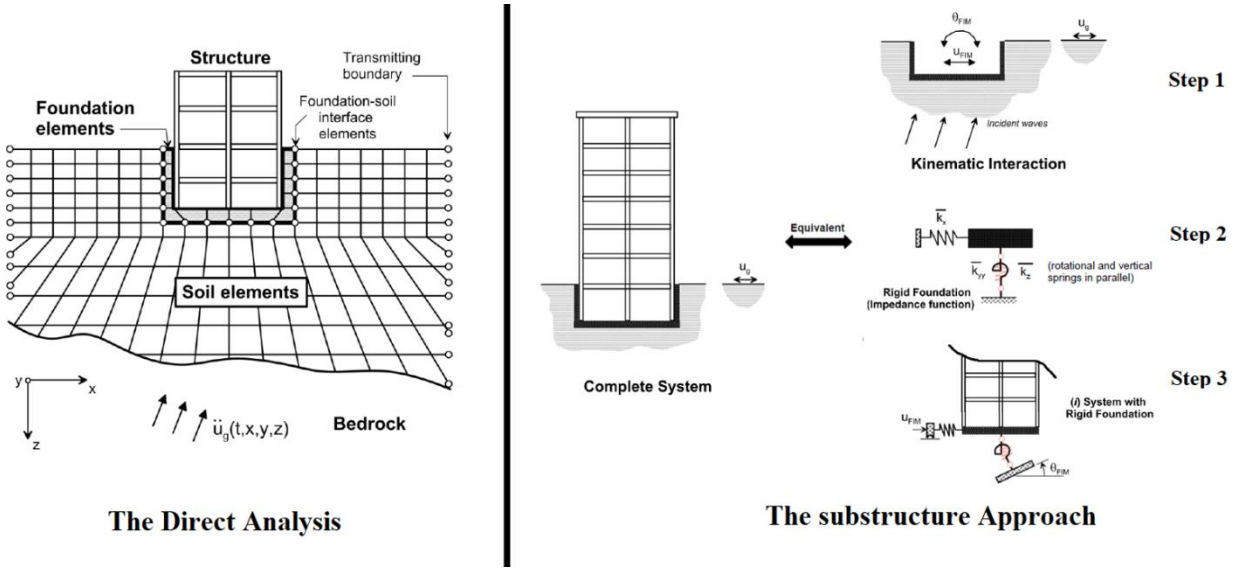

Figure 2.1 Schematic illustration of the direct analysis (left) and the substructure approach (right) to analysis of SSI, after the report NEHRP-NIST (2012)

The advantages of the direct analysis are the possibility to perform nonlinear analysis and consider complex geometries. Instead, the disadvantage is the complexity of the problem from a computational standpoint when the system is becoming geometrically complicated. The downside of the substructure approach is that it requires an assumption of linear soil and structure behaviour.

In the past, neglecting SSI has been considered conservative (Mylonakis and Gazetas, 2000). Nowadays, there is evidence that SSI cannot always be considered conservative, being detrimental for some structures (Priestley and Park, 1987; Miranda and Bertero, 1994; and Mylonakis and Gazetas, 2000). For example, a stiff building may change its period and produces an increase in the design spectra or move the structure into a resonant condition with the soil medium.

SSI is one of the significant subjects in soil dynamics and earthquake engineering and in general, the engineering community has focused its energy in researching the different aspects of SSI. Nevertheless, the existence of a high density of buildings in large cities inevitably results in the possibility of seismic interaction of adjacent structures through the underlying soil. SSSI is a relatively new area of seismic

analysis and has not yet reached the same level of attention as SSI. Notwithstanding, due to the rapid progress of computer processing power and simulation tools such as Finite Elements, SSSI has become an important research topic in the last 20 years.

This chapter aims to provide an exhaustive literature review, considering the past and most recent published research about SSSI and Site-City effects. Menglin et al. (2011) provided a systematic summary of the history and status of the SSSI research before 2010.

2.2 Structure-Soil-Structure Interaction research

The study of the dynamic interaction between several structures is a complex topic, where different approaches are required to have a proper understanding of the phenomenon. There are too many parameters involved, e.g. spatial distribution of buildings, dynamic characteristics of structures, soil properties, seismic excitation, etc. that it is very challenging to develop a unique method that considers all the parameters in one single model. Therefore, researchers have performed different techniques, where a small number of configurations and load cases for the SSSI problem are considered. Most of the studies can be categorised into (i) analytical methods or reduced-order methods, (ii) numerical methods (Finite Element method, boundary element method or hybrid method), (iii) experimental methods and (iv) instrumented measurements of real structures.

2.2.1 Analytical Methods

Analytical methods are one of the first attempts to analyse the SSSI and their effects on structures. The revolutionary work of Warburton et al. (1971) presented a theoretical expression for the displacement responses of two rigid foundations with a circular base attached to the surface of the elastic half-space. The results show that the second mass produces small rocking and horizontal translation displacement on the first mass. Later, Wong and Trifunac (1975) extended the analytical solution of Luco and Contesse (1973), where several two-dimensional shear walls constructed on an elastic homogeneous half-space were analysed, according to Figure 2.2. The rigid foundations with semi-circular cross-section were subjected to harmonic plane SH waves. The results showed that the presence of multiple buildings could lead to a significant amplification on the input motion due to the scattering, diffraction, and interference of waves from and around the foundation.

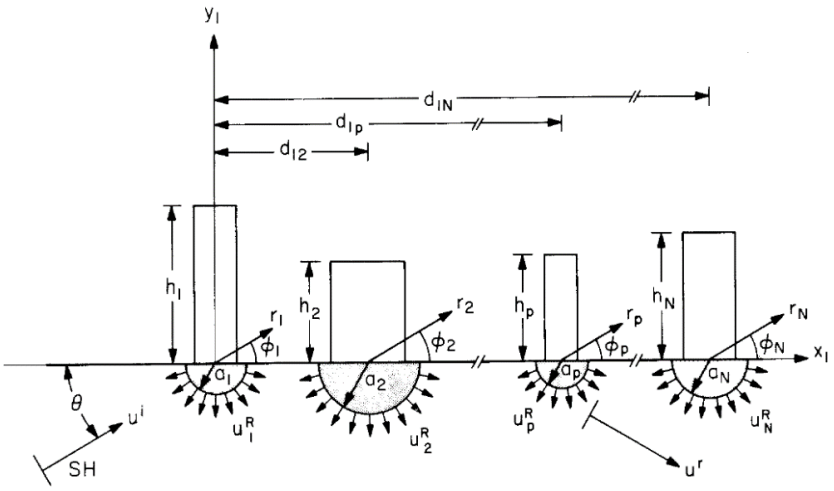

Figure 2.2 The arrangement of structures, after Wong and Trifunac (1975)

Kobori and Kusakabe (1980) investigated the vibrational characteristics and the seismic responses of SSSI between two buildings with an embedded foundation in a visco-elastic soil. In general, the maximum increase of the response for the coupled cases corresponds when the two buildings are different. Triantafyllidis and Prange (1987, 1989) presented a rigorous mathematical formulation to solve the dynamic subsoil-coupling between rigid rectangular or circular foundations subjected to harmonic excitations. The soil was considered as a linear elastic homogeneous half-space, where the foundations were perfectly bounded to the surface. The problem has been formulated by a set of Fredholm integral equations which are solved by the Bubnov-Galerkin method. Triantafyllidis and Neidhart (1989) extend the previous analytical work, including far-field incident Rayleigh waves acting on two rigid circular foundations and wave propagation through the underlying soil. The study highlights that additional loads perpendicular to the incident waves act on the foundations due to scattered waves.

2.2.1.1 Reduced-order methods

Discrete soil/foundation-spring models with a limited number of DOFs have been well recognised and successfully applied in the evaluation of static and dynamic SSSI problems. In this lumped parametric model, the soil and the structures can be modelled as a combination of springs, masses, and dashpots. Mulliken and Karabalis (1998) calculated the interaction between adjacent two and three identical rigid surface foundations and structures supported by a homogeneous half-space soil, and subjected to impulsive, moment, sinusoidal and random loads. The model utilises frequency-independent springs and dashpots for the foundations and inter-foundation interaction. The analysis includes time lagging effects of the input, and time-domain solution by using a modification of the Wilson-θ method. The results indicated that significant differences in response could be produced due to the presence of adjacent structures.

To perform a complete seismic analysis for structures with large foundations (e.g. dams), structures with multiple supports (e.g. long bridges) and long buried structures (e.g. tunnels), it is necessary to consider the spatial variation of ground motion. This variation involves deterministic and stochastic components. The deterministic part, or wave passage effects, is calculated using the wave equation in the soil medium. The assumption that all points of the ground surface beneath the structures are excited equally is valid only for vertically propagating coherent wave fields. The stochastic part refers to the spatial incoherence of the seismic ground motion, i.e. the displacement of two different points of the ground does not vary in the same way together. Therefore, Behnamfar and Sugimura (1999) address these issues, where they analysed the SSSI effects of two structures under spatially variable seismic waves (P, SV and Rayleigh waves). The ground motion is defined by the deterministic approach and stochastic approach, considering the degree of coherency between motions at every two points of the ground surface. The buildings consist of a rigid roof held by massless columns, that are connected to the rigid foundation bonded to the half-space soil. It is shown that resonance frequency and seismic response on low to medium-rise buildings increases if the buildings are close together.

More recently, Naserkhaki and Pourmohammad (2012) developed a discrete analysis for the study of SSSI effects on the response of twin buildings during earthquake excitations, as is depicted in Figure 2.3. It was found that the SSSI is influenced by the soil type, where the SSSI is important for soft soil. The interaction between twin buildings slightly mitigates the soil effects on building period compared to one building.

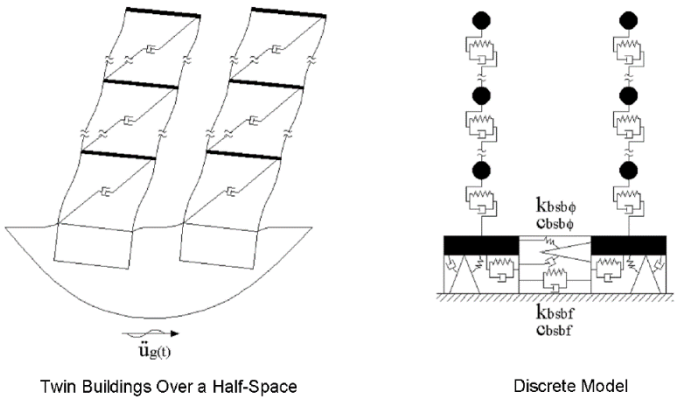

Figure 2.3 Discrete coupled model for twin buildings, after Naserkhaki and Pourmohammad (2012)

Alexander et al. (2013) proposed a set of frequency-independent rotational coupling spring coefficients that are used to model the interaction between two adjacent closely spaced buildings in two-dimensions. These coupling springs are obtained by the Euler Lagrange equations from the low order discrete model, Finite Element model, and validated with shake table tests performed by Aldaikh et al. (2016) and centrifuge test presented by Knappett et al. (2015). The linear computational analysis shows that there are detrimental and beneficial configurations of the dynamic characteristics of the buildings. The effects of interaction are unfavourable for building 1 (shorter building) when building 2 is taller, i.e. the power of the earthquake passes from the taller structure to the smaller structure. Later, Aldaikh et al. (2018) proposed

an alternative closed-form analytical expression for these interaction springs based on a Boussinesq approximation of the surficial displacement fields. The foundation rotational and coupling spring stiffness coefficients showed excellent agreement with the Finite Element model and physical experimental model. The limitation of these studies is that it is a linear analysis, limited to just symmetric buildings and considering only two or three buildings in a two-dimensional spatial arrangement.

Mykoniou et al. (2016) developed a substructure technique to evaluate the seismic interaction between adjacent tank-liquid containers in the frequency domain. The liquid-storage tanks are represented as mechanical models and the soil/foundation system as discrete springs and dashpots. The influence of the number, spatial arrangement, and the distance of the cylindrical tanks are evaluated. The results show that the impulsive component of the response is affected by the coupled effects, and the group effects should not be ignored a priori. Later, Lu et al. (2020) propose a simple linear model that allows the SSSI between structures with rigid, circular foundations. Frequency-dependant soil/foundation springs and interaction springs, to take into account the SSSI, are considered. The dynamic stiffness matrix is formulated based on modification factors of the static stiffness matrix, which is calculated employing compliance matrices. The equation of motion can be solved in time and frequency domain. This model can produce accurate qualitative results when is compared with Finite Element analysis. Nevertheless, it has some limitations as it just considers (i) similar structural properties between the buildings, (ii) linear elastic analysis, and symmetric structures.

All these previous studies provide a theoretical and mathematical foundation for the study of SSSI. Among the benefits of these reduced-order models are that they (i) capture the most significant dynamic behaviour, (ii) have a relatively small number of system parameters, and (iii) are computationally simple enough to explore a considerable number of generic cases. Nevertheless, these parametric studies should be viewed as an initial and complementary exploration of the problem. When the geometries of a structure, the foundations and the soil domain become complex, for ‘real world’ architectural reasons, this leads to a large complexity in mathematical solution as there are just too many system parameters to explore. So, the reduced-order models employed are not meant to replace advanced computational models (FEM) and/or experimental models of a specific example of a particular building scenario required for design analysis.

2.2.2 Numerical Methods

The numerical methods are one of the most effective and versatile tools for the study of complex problems. The rapid increase of computational power has allowed the development of increasingly sophisticated analysis, where it is possible to consider nonlinearities, radiating damping of a half-space soil medium and complicated geometric configuration. Therefore, the Finite Element Method (FEM), the Boundary Element Method (BEM), and the hybrid Finite/Boundary Element Method have been successfully applied in the evaluation of SSSI problems in recent decades. Also, these numerical methods have served as an essential

validation point for simplified and reduced-order models. However, it is difficult to characterise both structure and soil in a broad and universal sense for a whole class of system configurations. In addition, those models have a large number of degrees of freedom involved and a considerable number of system parameters. So, this precludes their use in a vast parametric study due to excessive computational cost and complexity.

2.2.2.1 Finite Element Method (FEM)

Aydinoglu and Cakiroglu (1977) evaluated the SSSI for a ten-story building frame by using FEM. The soil is modelled as a 2D linear elastic single layer and discretised by means of the nodal point on the surface. The building response due to rocking motion decreased and the response due to swaying motion increased. Solari et al. (1980) evaluated the accuracy with respect to the primary parameters (influencing the computation cost) of the 3D FEM. The structures correspond to two buildings with surficial squared rigid foundations. Later, Matthees and Magiera (1982) performed a sensitivity study for the seismic interaction between adjacent structures belonging to a nuclear power plant. Three different numerical methods (site-dependent method, site-independent method, and excitation-independent method), for linear and nonlinear structural and soil parameters, are used. It has been shown that the SSSI can increase the seismic response to such a large extent that it cannot be disregarded.

Lin et al. (1987) developed a hybrid method for the study of dynamic interaction between adjacent foundations. The near-field domain, where all geometric irregularities and material inhomogeneities are incorporated, is partitioned into a finite region. The far-field domain is assumed to be horizontally layered. It was found that the interaction depends on the distance between the foundations, direction of alignment and embedment of the foundations.

Yahyai et al. (2008) evaluated the seismic behaviour of two adjacent 32-storey buildings using the ANSYS program, and ETABS to check the uncoupled response. Three soil classes (soft clay, sandy gravel, and compacted sandy gravel) and different inter-building distances are considered. The results showed an increase of the seismic base shear and lateral displacement on the buildings. Later, Wang et al. (2013) and Wang et al. (2017) explored the SSSI between underground structures and pile-supported structures under vertically incident S waves, using the software for Finite Element analysis ANSYS. Different configurations for the arrangement of structures, inter-building distances, shaking direction of seismic waves, storey numbers, and pile lengths are considered. The low buildings surrounded by underground structures are largely affected by the coupled effect. The arrangement of the structures and the seismic direction are the most important factors that affect the SSSI in these works.

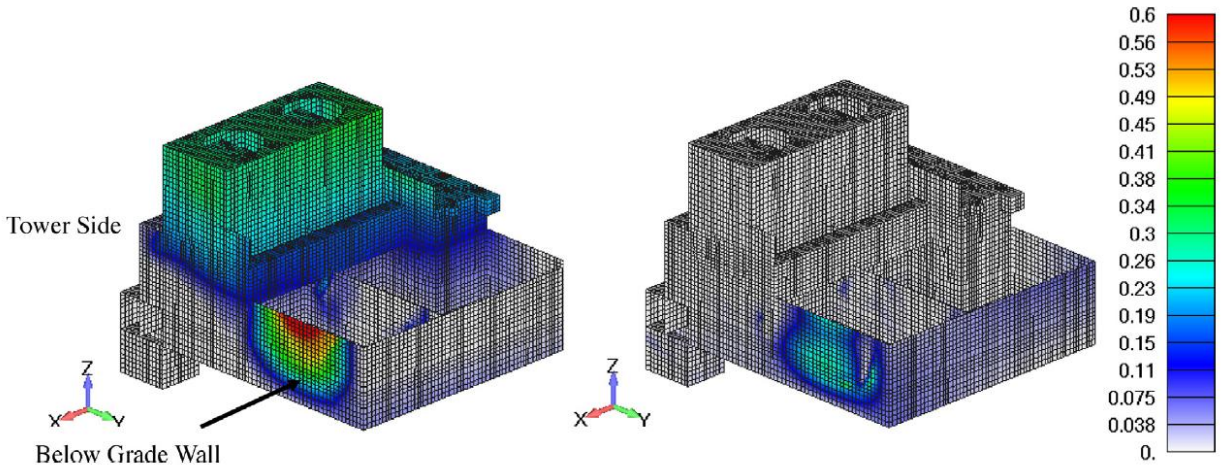

Figure 2.4 Increase of the structure acceleration response (unit in g) for an inter-building spacing of 3 meters (left) and 18.3 meters (right), after Roy et al. (2015)

Roy et al. (2015) examined the dynamic interaction between two adjacent heavy structures for different soil conditions and inter-building distances, Figure 2.4. The linear elastic analysis was performed in the software SASSI2000, with the impedance function solved in the frequency domain. The analysis demonstrated that the SSSI is important for a light or a heavy structure when it is close to a nearby heavy structure. Ghandil et al. (2016) performed a nonlinear analysis to evaluate the SSSI between two buildings, considering elasto-plastic frame hinges in the structure, under seismic loads using OpenSees. Three buildings with 10, 15 and 30 stories, two soil profiles (sand and clay) with a reduction of the soil shear modulus in areas close to the foundations, and different inter-building distances are considered. The results showed an increase in the displacement and reduction of the story shears when the coupled effect is considered.

Despite the versatility of FEM, this method has the problem of accurate modelling of the infinite or semi-infinite soil domain, due to wave reflections at the mesh boundaries. Therefore, large mesh sizes, infinite elements and complicated non-reflecting boundaries solutions are required, which may lead to substantial increase in computational costs. Yet, tied node boundaries solution can be more efficient to model a semi-infinite soil domain and a good option to resolve this problem, Zienkiewicz et al. (1988), Tsinidis et al. (2014) and Li et al. (2018). To address these problems, researchers have been developing more advanced computational technologies for modelling the soil and their boundaries, like BEM.

2.2.2.2 Boundary Element Method (BEM)

The boundary element method is a numerical computational method of solving linear partial differential equations through integral equations, which was developed after FEM. The BEM only discretizes the boundary of the defined domain (minimizing the spatial dimensions of the problem), instead of discretizing the whole space domain. The radiation at the infinite soil domain is automatically considered. In the

pioneering work of Wong and Luco (1986), an efficient boundary integral equation to calculate the seismic interaction between foundations bounded to a viscoelastic half-space is derived. It was found that the choice of discretization is important when the foundations are close.

Qian and Beskos (1995) employed the boundary element method in the frequency domain to evaluate the SSSI of a system of 3D rigid, massless, and shallow foundations subjected to harmonic forces. The technique uses the dynamic Green's function for the surface and isoparametric quadratic quadrilateral boundary elements. It was found that the statement included in ATC-3 (1984) regarding 'neglecting the coupled effect is always conservative', is not correct for all systems. Later, Qian and Beskos (1996) extended the previous research, including obliquely incident harmonic P, SV, SH and Rayleigh waves. The results have shown that the interaction generates displacement components that would not exist for a single foundation.

Betti (1997) developed an efficient methodology (substructure deletion method) for the study of cross-interaction between multiple embedded foundations. The soil is modelled as a homogeneous viscoelastic half-space, and the foundations are subjected to incoming SH and SV waves. The translation, rocking and torsional component of the impedance matrix changed up to 30% due to the interaction in the low-frequency range.

The two-dimensional formulation for linear in-plane dynamic SSSI for twin buildings in layered half-space was investigated by Liang et al. (2017, 2018). They presented an Indirect Boundary Element Method (IBEM) for the modelling of the soil and the structure is represented analytically, where incident SH-wave and SV-waves are considered. Results show that the vertical motions are coupled with the rocking motions. At close distances, the structure response is amplified by 50% for vertically incident SV-wave, 25% for obliquely incident SV-wave and 50% for SH-wave. Later, Han et al. (2020) used the two-dimensional IBEM to evaluate the SSSI on the Millikan Library building for any incident direction of the seismic waves. The numerical analysis shows that the coupled effect may amplify the response by 40%, and this amplification is sensitive to the adjacent building's parameters. Also, the SSSI was noted inclusively for large inter-building distances.

The disadvantages of the BEM are that it is not possible to use in nonlinear problems, and it is difficult to apply in the case of a heterogeneous soil.

2.2.2.3 Hybrid element method

In order to address the disadvantages of FEM and BEM, the hybrid method of FEM/BEM was developed to evaluate the SSSI. As a general trend, the soil medium is modelled using BEM, and the superstructures and their foundations are modelled using FEM. Imamura et al. (1992) presented one of the first attempts to use a hybrid method to evaluate the seismic response characteristic of an embedded nuclear reactor

building considering SSSI. Using three different analysis methods, it has been shown that the dynamic response of the reactor building may be affected by the adjacent heavy buildings, where the maximum response acceleration and shear forces become larger.

Wang and Schmid (1992) analysed the SSSI between two water towers (3D lumped mass model) and two chimneys (distributed mass model) using a coupling finite and boundary elements. A harmonic force on two structures is applied. The conclusions of this study confirm the previous findings, where the inter-building distances and the direction of alignment between foundations have a significant influence on the interaction. Also, the natural frequencies of the excited structure play a decisive role in the interaction.

Qian et al. (1996) and Tham et al. (1998) extended the frequency domain BEM, the half-space Green's function, and 8 node quadratic element discretisation to study the interaction between flexible foundations. The results show that the foundation stiffness has a significant effect on the vertical response, but a minor impact on the horizontal response. The Rayleigh wave produces torsional motion on the foundation due to a horizontal response in the perpendicular direction of the wave.

Lehmann and Antes (2001) applied the symmetric Galerkin boundary element method, to the analysis of the coupled dynamic behaviour of high-rise buildings. The viscoelastic soil medium is modelled using the boundary element method and the structure using Finite Element Method. The numerical example (two stairway cores coupled through the soil) evaluated in this research demonstrated that this hybrid method can be used to evaluate the structure-soil-structure interaction problem.

Padron et al. (2009) analysed the dynamic interaction between pile-supported structures in a viscoelastic half-space soil by using a 3D BEM-FEM formulation in the frequency domain. Incident S and Rayleigh waves are considered. The results highlight the importance of SSSI when the structures have similar dynamic characteristics. The seismic response can be amplified or attenuated. Later, Alamo et al. (2015) extended the previous work by using obliquely incident waves and the dynamic response in the time domain. It was found that for non-slender structures, the SSSI can influence the maximum dynamic response significantly.

Clouteau et al. (2012) developed a BEM-FEM method to analyse the experimental tests performed by the Nuclear Power Engineering Corporation (NUPEC) in Japan. Single and coupled buildings, shallow and embedded foundation subjected to forced and seismic loads, have been studied. The numerical results are in good agreement with the results shown in the NUPEC experimental program. In addition, SSSI has an important effect on embedded foundations, with a decrease of the acceleration response of 30% at the top of the structure.

2.2.3 Experimental Methods

Another approach is physical modelling, which has been implemented in recent years for the SSSI phenomenon. These studies represent an important validation point for numerical models and provide preliminary estimates of the effects of complex interaction problems. One of the first efforts to evaluate the coupled response of two foundations by experimental test are the works of Maccalden and Matthiesen (1974) and Kobori et al. (1977). In these works, analytical results have been compared to the experimental evidence. They highlight the importance of the phenomenon over the wide frequency range as the distance between foundations becomes small. Later, Mizuno (1980) evaluated the SSSI using a full-scale building and a model structure of the full-scale building, considering different excitations (forced vibration tests, microtremor measurements and seismic observations). These experiments confirmed that the structural response is increased by the radiation waves of the other structure.

The Nuclear Power Engineering Corporation (NUPEC) has performed an extensive research study on the dynamic cross interaction (DCI) between different structures (reactor building, turbine building and control building) belonging to a nuclear power plant (NPP). The project started in 1994 and it was completed in 2002, with the following papers published, Kitada et al. (1999), Yano et al. (2000), Kitada et al. (2001), Naito et al. (2001), Hirotani et al. (2001), Kuzama et al. (2003), and Yano et al. (2003). The program consists of both field tests (see Figure 2.5) and laboratory tests. The test site for the field tests was in Aomori Prefecture in the north of Japan and consisted of large-scale models of NPP structures using forced vibration tests and earthquake observations in the field. The structures also consider both excavated and embedded foundations. The laboratory tests were performed using shaking table tests on 1/230-scale prototypes of NPP structures made of aluminium, subjected to strong earthquake motions. This extensive study provides the first large-scale experimental data on SSSI.

Figure 2.5 Two identical embedded buildings model, after Kusama et al. (2003)

Currently, centrifuge tests have been used extensively in the study of SSSI because they are particularly useful in testing materials like soil which exhibit significant nonlinear behaviour. The National Centre for Earthquake Engineering Research (NCEER) at the University at Buffalo has developed the project "Seismic Performance Assessment of Buildings in Urban Regions (City Block project)", which involved a team of six universities (University of California, Berkeley, University of California, Davis, University of California, San Diego, University at Buffalo and the California Polytechnic State University). For this aim, numerical simulations and six centrifuge experiments (Figure 2.6 shows the first two tests) were performed at the University of California Davis geotechnical centrifuge facility, with the following papers published, Trombetta et al. (2012), Trombetta et al. (2013), Mason et al. (2013), and Trombetta et al. (2014, 2015). The inelastic structural response of two adjacent steel moment-resisting frames, where two tests are founded on dry sand and four experiments on liquefiable soil, have been investigated. In addition, Botisetti and Whittaker (2015) presented the linear and nonlinear numerical simulations developed in the time-domain code LS-DYNA and frequency-domain code SASSI for the tests performed in the centrifuge experiment. Specific cases can be modelled using this method. The results showed that SSSI could be beneficial or detrimental, depending on the seismic excitation and the dynamic structural parameters. The SSSI produces an increase in the peak foundation moment, foundation base shear demands, and creates a rise on the moment, shear and curvature ductility demands on the structural elements.

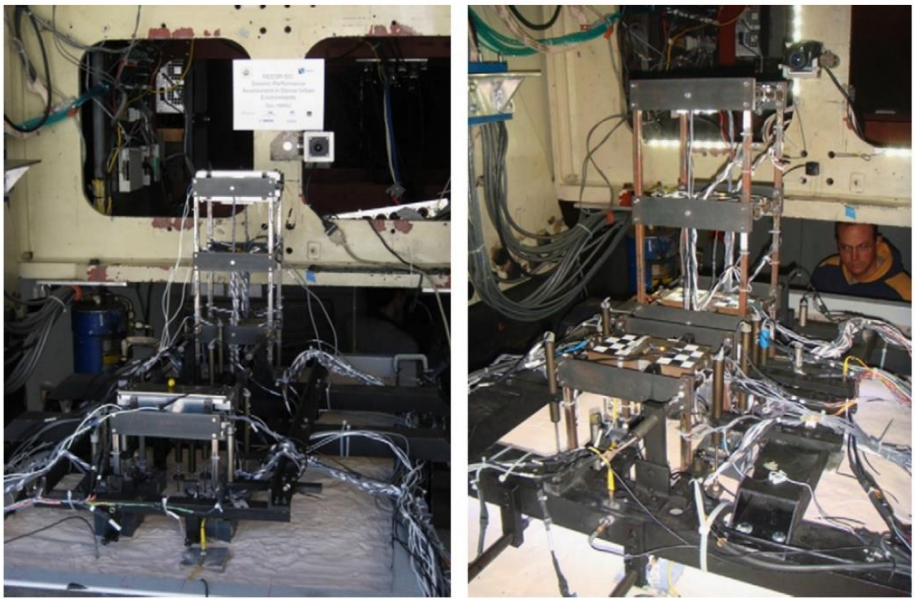

Figure 2.6 Centrifuge Test-1 (left) and Test-2 (right) fully instrumented, after Mason et al. (2013)

Knappett et al. (2015) analysed similar and highly dissimilar buildings on shallow foundations using centrifuge modelling. Buildings responses were shown to either increase or decrease depending on the relative dynamic properties of a pair of adjacent structures. Jabary and Madabhushi (2017) investigated the dynamic SSSI between two closely spaced buildings. The structures are considered with and without tuned mass damper (TMD). The results showed an increase in the adjacent structures' peak roof acceleration and inter-story drift when the damper was de-tuned. In addition, TMD effects are more

noticeable under minor earthquakes and could produce damage to the adjacent building. Later, Ngo et al. (2019) highlighted the importance of height ratio and mass ratio on SSSI phenomenon of two structures, by using a centrifugal experiment. On the other hand, Kirkwood and Dashti (2018) conducted centrifuge tests on closely spaced structures to evaluate how to maximise the benefits of SSSI and minimise the adverse consequences on buildings. The structures are founded on a layered liquefiable soil profile. Results show that for certain spatial configurations, the SSSI produces reduction on foundations' transverse accelerations, soil stiffness, deflection in the superstructure and an increase in soil damping. Recently, Qi and Knappett (2020) evaluated the dynamic behaviour of structures with different types of shallow foundations (strips and rafts) adjacent to a heavier neighbouring structure with the same kind of foundations. Centrifuge tests to investigate the effects of liquefaction on seismic performance are performed. The results show that the seismic accelerations are less important when the soil liquefies, the SSSI effects produce changes in the system's natural period and damping, and an increase in post-earthquake permanent deformation.

Shaking table tests have also been used to evaluate the SSSI, providing valuable insight into understanding the dynamic behaviour of multiple adjacent structures. Li et al. (2012) conducted a 1:15 scale model shaking table tests on the interaction of two identical adjacent 12 storey cast-in-place reinforced concrete frames buildings supported by a group of 3 by 3 pile foundations. The El Centro wave and Shanghai bedrock wave earthquakes were considered. The SSSI was found to have some influence on the soil frequency and damping ratio, but little impact on the frequency and characteristics of the vibration modes. Also, the peak accelerations of the soil between the piles, the peak contact pressure along the pile and damage of the structures was greater when considering the SSSI effects. Li et al. (2017) presented the 3D Finite Element numerical simulation for the previous shaking table test using ANSYS software. By comparing the numerical and experimental results, the simulation can adequately predict the dynamic response of the shaking table tests. Results show that the contact pressure, strain amplitude and pile slip increase when the SSSI is considered.

Aldaikh et al. (2015) explored the SSSI on a group of three buildings under seismic excitation. A physical experimental shake table test program is used to validate the discrete theoretical model presented originally in Alexander et al. (2013). It was found that the coupled effect is detrimental for the central building when the adjacent buildings are 10-20% taller, with amplification in the response total power of 170%. The interaction is more significant when the buildings are close together, and the effect is negligible when the inter-building distance is around 2.5 times the width of the buildings. Later, Aldaikh et al. (2016) conducted a series of shaking table tests at the Earthquake and Large Structures Laboratory (EQUALS) at the University of Bristol. To provide repeatability of the tests (soil properties invariant during the tests), the scaled models are placed upon a flexible soil model made of cellular polyurethane foam. It was found that the SSSI is highly dependent on the buildings' height, and the coupled effects can be amplified by the peak acceleration responses up to 25%.

Ge et al. (2019a) investigated the cluster effects, or soil and structure cluster interaction (SSCI), using shaking table tests subjected to El Centro earthquake and Shanghai artificial wave and nonlinear numerical simulation using the software ANSYS. Several configurations of 5, 7 and 11 buildings with different inter-building spacing are considered. It was found that the SSCI effect reduces the displacement of the central building but increases on the surrounding structures. The number of buildings is the most significant factor that affects the cluster effects, where the maximum influences of the SSCI can be seen in the displacement response. Ge et al. (2019b) extended the previous research through shaking table tests and parametric numerical simulation, where the superstructure is simplified as a concrete column at a 1:20 scale. It is found that the number of structures, spacing, height and spatial distribution play a significant role in the SSCI effects.

Experimental and numerical methods have been used to create new applications to reduce the vibration of buildings using the interaction effects between structures. For example, the numerical and experimental (shake table tests) by Cacciola et al. (2015) and Tombari et al. (2018) developed a novel vibration control device called Vibrating Barrier (ViBa), based on the favourable effect of SSSI phenomenon to reduce the structural vibrations of structures due to seismic action. This device is held in the soil and separated from the buildings. A significant reduction of 46% on the structural response is achieved.

The disadvantages of the experimental methods are that they are technically challenging to undertake and produce several difficulties with the accurate scaling of the soil strains prototype and inertial forces. Additionally, they represent a small statistical sample, and they provide an only limited parametric exploration of the generalised problem.

2.2.4 Instrumented structures and case studies

Research of recorded seismic responses of instrumented buildings constitute an integral part of seismic reductions studies conducted to improve the design and analysis procedures. Strong motion instrumentation programs are carried out in seismically active regions such as Los Angeles, where the two major faults produce large earthquakes with magnitudes 7.0 – 8.0. In a two-part paper, Celebi (1993a, 1993b) studied the Whittier Narrows earthquake response of two adjacent seven-storey buildings in Norwalk, California. The data analysed includes motion from the two buildings, from a downhole below the foundation of building B and three free-field sites (see Figure 2.7). The results show evidence of SSSI, where the site frequency appears in cross spectra of all locations, and the roof motions of both buildings are highly coherent and in phase at the fundamental frequencies of building B. This indicated that the building A is the receiving structure while building B is the influencing structure.

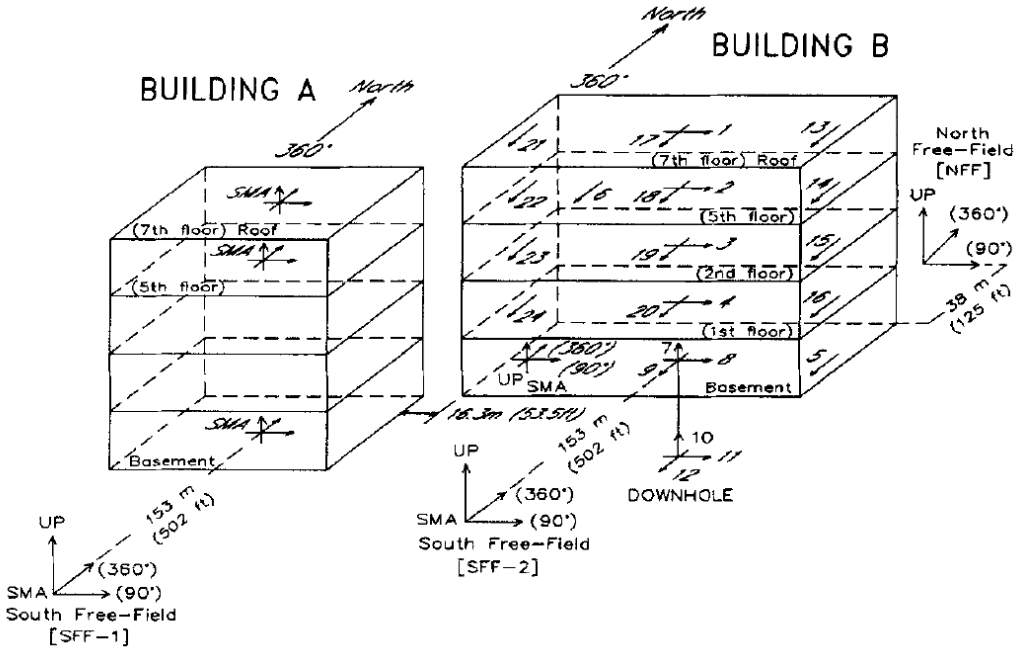

Figure 2.7 General layout of two instrumented buildings, after Celebi (1993a)

Hans et al. (2005) evaluated the dynamic response of five buildings considering ambient vibrations, harmonic excitation, and shock loading. In particular, the SSSI was investigated in a group of three similar buildings (namely D, E and F), where the building D remains intact, and buildings E and F are demolished independently. The results show that the change in the natural frequencies are not important and can reach 10% in the most significant case, and the rocking impedance is smaller for the isolated building. The vulnerability assessment is presented and discussed in the companion paper Boutin et al. (2005).

Laurenzano et al. (2010) performed 2D simulations to analyse the effect of SSSI for the real case of 2 buildings located in Bonefro, Italy. The study was conducted using the Chebyshev spectral element method and included the bedrock (limestone) with the overlying clay 30 meters layer. This study confirms the interaction of neighbouring buildings through the extended coupled system frequency response functions. Gueguen and Colombi (2016) analysed three identical stand-alone buildings located in Grenoble, France after an $M_L = 4.1$ earthquake. A local survey based on the protocol used for macroseismic intensity analysis was conducted among the inhabitants of the three towers. The survey reveals the SSSI between the buildings, resulting in different levels of perception of seismic loading by inhabitants (Gueguen and Colombi, 2016). This interaction was confirmed using numerical simulations.

2.3 Site-City effects research

A related problem that has been addressed recently is site-city interaction (SCI) or city effects, where the seismic free-field ground motion is affected by building clusters in dense urban areas. Several studies have been undertaken in the last decades, such as those of Gueguen et al. (2000), Clouteau and Aubry (2001),

Chavez-Garcia and Cardenas-Soto (2002), Gueguen et al. (2002), Semblat et al. (2002), Tsogka and Wirgin (2003), Boutin and Roussillon (2004), Semblat et al. (2004), and Kham et al. (2006), among others. These works have shown that (i) the SCI effect is influenced by the separation/size of the structures, the angle of incidence of the incoming waves, and the relative stiffness to the soil, (ii) a part of the seismic energy transmitted to the buildings is redistributed in their neighbourhood through multiple interaction between the soil foundation and the buildings, and (ii) the ground motion is affected by the presence of a large group of structures, producing a spatial variation of the ground acceleration.

Semblat et al. (2008) evaluated the site-city effects on alluvial basins using a 2D numerical model. The closeness between the fundamental frequencies of the urbanized area and the soil layers can lead to a significant seismic wave-field modification when compared to the free-field case. The site-city effects can be detrimental and beneficial for different parts of the city and depend heavily on the urban configuration. Later, Ghergu and Ionescu (2009) calculated the site-city effects for buildings, following the idea of Wirgin and Bard (1996), that are modelled as elastic springs with two concentrated masses and rigid foundations. The soil is modelled as anti-plane shearing elastic half-space, which contains rigid segment boundary conditions. The results show that the city has a principal frequency that does not depend on the number of buildings but depends on the soil properties and specific buildings' properties.

The Southern California Earthquake Centre's Community Modelling Environmental group (SCEC/CME) and the Quake group at Carnegie Mellon University have developed the octree-based Finite Element earthquake simulator, Hercules. This computational module allows the incorporation of large Finite Element unstructured meshes of idealised buildings models, with the purpose of solving the wave propagation problem of earthquake simulations at a regional scale. Taborda and Bielak (2011a, 2011b) tested the Hercules implementation on the problem of site-city interaction effects into a large-scale simulation in 3 dimensions. The region simulated corresponded to a domain of 16 km x 29 km x 41 km, located in the Mygdonian basin between the Lagada and Volvi lakes near Thessaloniki in Northern Greece. The hypothetical earthquake has a magnitude of Mw = 5.2, with the presence of an array of 74 buildings on a subregion of 3 km x 3km (see Figure 2.8). The results show that the presence of the built environment considerably changes the ground response of the city and an increase in the ground motion spatial variability. Later, Isbiliroglu et al. (2015) extended the simulation to the case of multiple simplified building models located in the San Fernando Valley and subjected to the Northridge earthquake. The simulation highlights the importance of considering the SCI, and that the effects depend mainly on the number and dynamic properties of the buildings, their separations, and their impedance with respect to the soil.

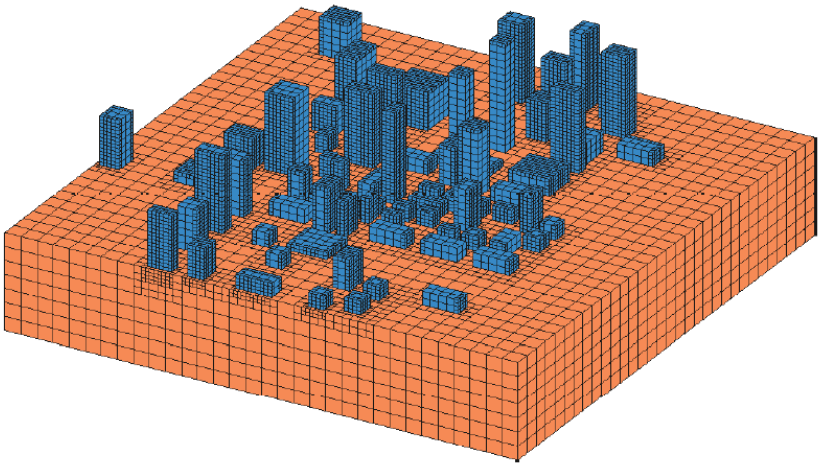

Figure 2.8 Coarse mesh representation of the 74 buildings array, after Taborda and Bielak (2011a)

Schwan et al. (2016) performed a theoretical, numerical, and experimental crossed analysis to the study of SSSI. The experimental shaking table test consists of an idealised site-city system with up to 37 anisotropic resonant structures supported on an elastic layer. The theoretical formulation is based on the idealised ∑-periodic city with slender resonant structures on a rigid foundation founded to an elastic half-space (effective surface impedance). The numerical model corresponds to the direct BEM developed by Padron et al. (2009). The parametric study shows that multiple SSSI can have significant effects on the seismic response of the buildings and the ground motion.

Lu et al. (2018) proposed a nonlinear coupled model for the study of SCI on a regional scale. An open-source program SPEED (spectral elements in electrodynamics with discontinuous Galerkin) to model the structures and soil is used. The proposed numerical formulation is validated using a shaking table test. The case study corresponds to the Tsinghua University campus, where the results show that the SCI effects reduce the seismic response in almost all the buildings. However, some buildings have an increase in their seismic responses and suffer much more severe damage when the SCI is considered.

2.4 Nonlinear soil behaviour

The mechanical behaviour of soils can be complex under seismic loads, inducing irregular cyclic loadings that results in a large range of stress and strains. This behaviour results in nonlinearities with gradual softening of the soil, i.e. decrease on shear modulus with strain, Hardin and Drnevich (1972). The geotechnical community has been performed an extensive theoretical and experimental work to characterise the cyclic shear behaviour of soils and tree-dimensional behaviour of soils. The complexity of the problem makes the development of numerical models quite challenging. Different numerical models of varying complexity have been developed in geotechnical earthquake engineering and can be categorised according to: i) equivalent linear models, ii) cyclic nonlinear models, and iii) advanced constitutive models,

Kramer (1996). Equivalent linear models and cyclic nonlinear models are based on shear behaviour only, where several field and laboratory testing research are demonstrated that for shear strain larger than 10^{-4}, the nonlinear soil behaviour in the soil starts, Kramer (1996). Advances constitutive models incorporate the three-dimensional nonlinear behaviour of the soil and are used in advance complex three-dimensional model of site-response and SSI analysis.

2.4.1 Equivalent linear models

The hysteretic loops observed in soils subjected to symmetrical shear cycles can be defined according to Figure 2.9. The stiffness of the soil can be described at any point during the cycling as the tangent shear modulus G_{tan}, which varies throughout the whole process. In addition, these values decrease with the increase in strain, indicating softening in the soil.

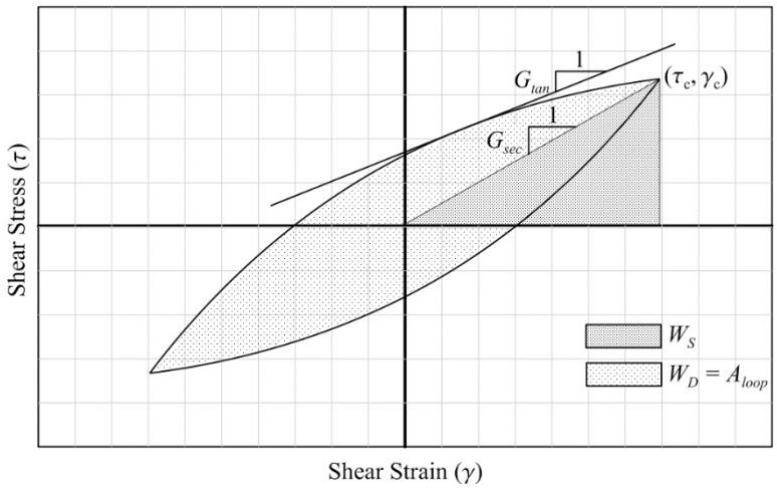

Figure 2.9 Hysteretic loops, after Hardin and Drnevich (1972)

The average, in every loop, of the shear modulus can be approximated as $G_{sec} = \tau_c/\gamma_c$, where τ_c is the shear stress and γ_c is the shear strain. The equivalent damping ratio ξ_{eq} is related to the energy dissipated W_D, the maximum strain energy W_S, and can be described as follows,

$$\xi_{eq} = \frac{W_D}{4\pi W_s} = \frac{1}{2\pi}\frac{W_D}{G_{sec}\gamma_c^2} \quad \textbf{(2-1)}$$

The parameters G_{sec} and ξ_{eq} are often referred to as equivalent linear material parameters. As the maximum strain of the loading cycling γ_c is increased, the secant modulus G_{sec} reduces and the equivalent damping ratio ξ_{eq} raises. Usually, these parameters are graphically depicted as the modulus reduction curve and the damping curve, see Figure 2.10. The largest value of shear modulus corresponds to the initial shear modulus (zero strain) $G_s = G_0 = \rho_s V_s^2$, where ρ_s is the soil density and V_s is the shear velocity of the soil.

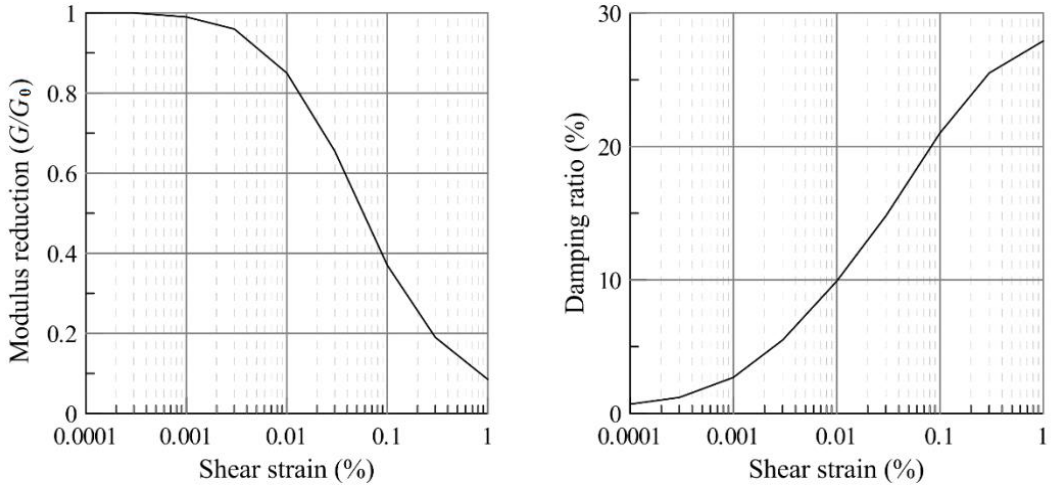

Figure 2.10 Shear modulus reduction and damping curves, after Hardin and Drnevich (1972)

2.4.2 Cyclic nonlinear models

The nonlinear stress-strain behaviour of the soils can be represented by nonlinear hysteretic models, which can follow the actual stress-strain path during the cycling loading. A variety of nonlinear models can be found in the literature, like backbone curve (Ramberg and Osgood (1943) and Takeda et al. (1970)), "rule-base" hysteretic models (Masing (1926), Kramer (1996)), and theoretical numerical models (Gerolymos and Gazetas (2005) and Drosos et al. (2012)). The most well-know set of hysteretic rules are based on the extended Masing rules, Kramer (1996).

Among the theoretical numerical models, the phenomenological constitutive Bouc-Wen model is capable to reproduces the nonlinear hysteretic behaviour of a variety of soils, and possesses considerable flexibility to represent complex patters of cyclic behaviour such as stiffness decay and damping curves by the calibration of only three parameters, Figure 2.11.

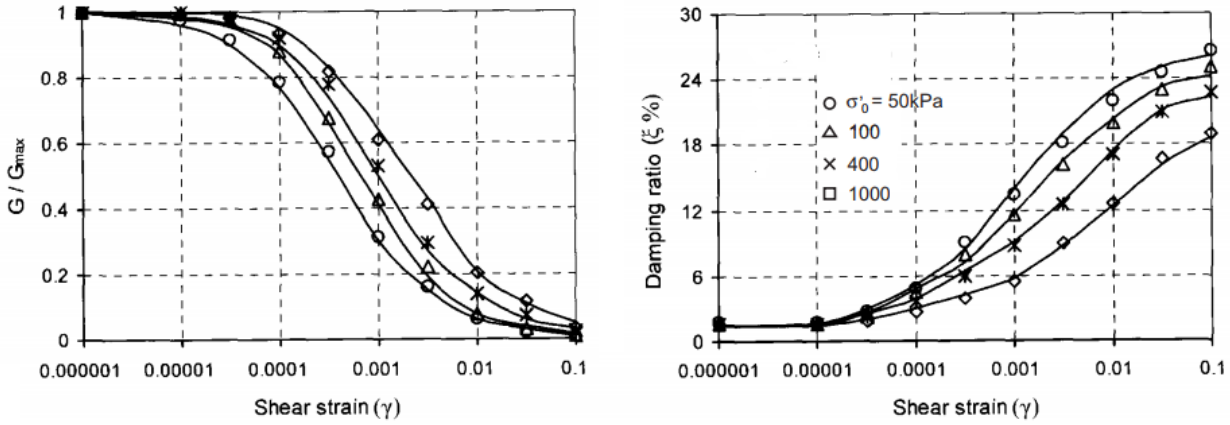

Figure 2.11 Prediction of shear modulus reduction and damping curves for experimental curves, after Gerolymos and Gazetas (2005)

In the same way, the effectiveness of the Bouc-Wen model was checked against sophisticated elastoplastic model based on multi-surface plasticity framework and implemented in a Finite Element code named Cyclic1D, see Figure 2.12.

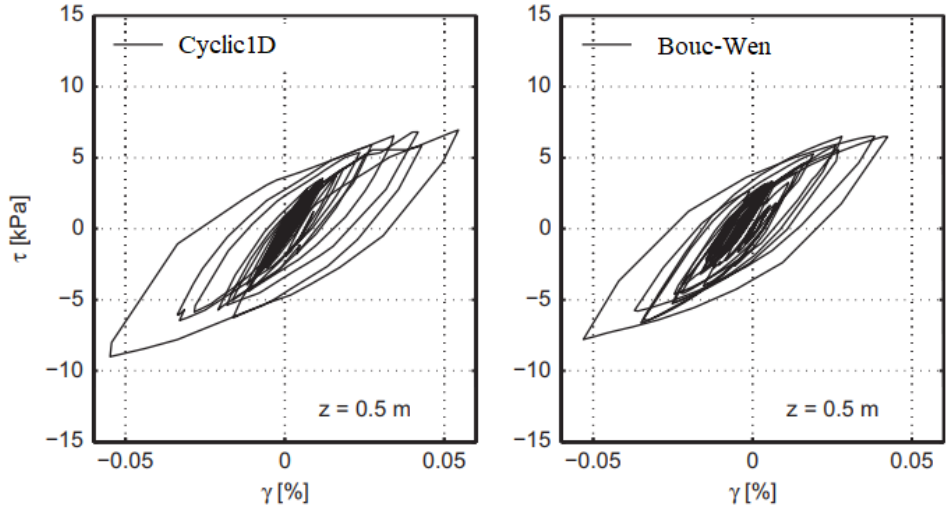

Figure 2.12 Comparison of stress-strain loops computed with Cyclic1D and Bouc-Wen model. Dense sand, shaking Kobe JMA 090 record, after Drosos et al. (2005)

2.5 Summary

A comprehensive review of the existing theoretical, mathematical, and experimental studies for modelling the dynamic Structure-Soil-Structure Interaction problem was provided. The conclusions and results of previous research on the influence of SSSI effects have also been discussed. The outcome of the literature review and the gaps in the existing models that have been addressed in this thesis can be summarised as below:

- The papers presented in this chapter highlight that the SSSI can be relevant for multiple configurations, and it is an issue that should not be neglected in a proper dynamic analysis. Due to the complexity of the problem, most of the studies are based on numerical techniques like FEM, BEM, or a combination of both. These models have considered particular cases for the buildings' spatial configuration, soil properties and a limited number of excitation cases and do not provide a complete parametric exploration of the problem.
- Physical models like centrifuge experimental tests and shaking table tests have provided interesting results in complex configurations of SSSI problems. The results show that SSSI can be beneficial or detrimental, depending on the properties of the structural system and the ground motion. Also, they have been used to validate numerical models and theoretical formulations and provide valuable insight into the physical nature of the SSSI. The disadvantages of these studies are that they are difficult to perform and usually represent a small sample of the whole possible configuration cases.

- Lumped parameter models (reduced-order model) with a limited number of DOF have been used and effectively applied in the evaluation of the SSSI effects on the dynamic response of buildings. In these mechanical models, it was considered that all masses, springs, and dash pots are lumped into a single mass, spring, and damping constant for each mode of vibration. The linear analysis of Mulliken and Karabalis (1998) and Alexander et al. (2013) highlight the versatility of these simple theoretical models for two and three buildings. Therefore, simple but rigorously mathematically formulated reduced-order models have been chosen to perform a large parametric investigation of the SSSI problems. In this novel research, both linear and nonlinear behaviour of the soil is considered as well as unsymmetrical plan buildings. An extensive database of strong ground motions records (with far-field, near-field without pulse and near-field pulse-like characteristics) and multiple buildings in a three-dimensional arrangement are employed.

This page intentionally left blank

Chapter 3

Higher mode seismic Structure-Soil-Structure Interaction between adjacent buildings during earthquakes

---

The contents of this chapter have been adapted from that published in:

Vicencio, F., and Alexander, N.A. (2018b). Higher mode seismic Structure-Soil-Structure Interaction between adjacent buildings during earthquakes. *Engineering Structures*, 174, 322-337.

Part of the introduction has been removed and included in Chapter 2 - Literature Review.

3.1 Introduction to an extended model of SSSI between two buildings

In this chapter, the previous work of Alexander et al. (2013) on the SSSI of two buildings is extended, by including an additional degree of freedom (DOF) for each of the buildings. This extra building DOF enables an extra mode for each structure. Hence, the parametric scope of the previous study is extended to include the case of a low-rise building adjacent to a neighbouring much taller building. Additionally, real ground motions are now employed rather than a Kanai-Tajimi artificial ground motion. These strong ground motions are classified into three groups: Far-Field (FF), Near-Field Without Pulse (NFWP) and Near-Field Pulse-Like (NFPL). This allows performing different seismic analysis considering a broader range of ground motion characteristics, with differences in amplitude, duration, envelope shape, and power spectral content. The ground motion database chosen in this research is obtained from the report Quantification of Building Seismic Performance Factors, Appendix A: Ground motion records sets (FEMA P695, 2009).

Over 3.1 million different time-history cases are explored. This computationally challenging study required the High-Performance Computing (HPC) machine, BlueCrystal, belonging to the Advance Computing Research Centre (ACRC) at the University of Bristol. The ACRC operates a number of different HPC system, being BlueCrystal Phase 3 (BC3) used in this research. BC3 has the following specification: 223 standard compute nodes, each with 2x2.6GHz 8-core Intel E5-2670 chips, 4GB of RAM per code, and 1TB SATA disk. There are an additional 100 identical nodes that can host dual GPGUs. BlueCrystal Phase 3 featured in the top 500 supercomputers in the world in 2013.

Note that the interaction springs defined by Alexander et al. (2013) were validated with Finite Element Analyses (Aldaikh et al., 2015), shake table tests (Aldaikh et al., 2016), and matched closed-form analytical expressions (Aldaikh et al., 2018). The research performed by Alexander et al. (2013) highlighted the possibility that the power of the earthquake passed from the taller structure to the smaller structure when the height ratio is close to 1.1 (i.e. the second building is 10% taller than the first building), and the buildings are closely spaced. Nevertheless, these results were bounded to the use of a single artificial ground motion and limited values for the height ratio of the buildings.

3.1.1 Aims

The aim of this chapter is to answer the following questions.

(i) Does the introduction of additional degrees of freedom (and hence modes) in the buildings influence the size of adverse/beneficial SSSI behaviour?

(ii) Is there evidence to suggest that different types of ground motion (FF, NFWP and NFPL) can affect the SSSI behaviour?

(iii) Do displacement responses follow a similar trend to total acceleration responses?

3.2 A theoretical reduced-order model for SSSI

3.2.1 Non-dimensional equations of motion

A two buildings system is shown in Figure 3.1 and is described in terms of six degrees of freedom (DOFs). Buildings are coupled with a rotational interaction spring κ. The soil/foundation system of each building has one rotational DOF at the foundation level θ_j. The building super-structures have two translational DOFs (x_{2j-1} and x_{2j}) relative to the ground, with $j \in [1,2]$. Thus, the three DOFs of each building can be viewed as a projection, onto a three modes vector basis, of a generalised multi-storey building of height h_j. In the same way, this extended simplified reduced model enables SSSI between the 'second sway mode' of a tall building and the 'first sway mode' of a shorter building. This effect was neglected in previous studies (Alexander et al., 2013; Aldaikh et al., 2015). A known ground displacement field x_g is applied at both foundations, i.e. wave passage effects and spatially heterogeneous ground displacement are neglected in the present work. Building pounding is not permitted as inter-building distance is assumed large enough to avoid pounding.

The kinetic energy T_E and potential energy U_E for this system are given by the equations (3-1) and (3-2) respectively. The total kinetic energy can be specified as the sum of (i) translational kinetic energy (due to sway and foundation rotation) of each building's mass and (ii) the rotational energies of each soil/foundation masses. The potential energy is the sum of (i) the internal work due to buildings' deformations, (ii) the rotation of the foundation springs underneath the buildings, and (iii) the differential rotation between buildings.

$$T_E = \frac{1}{2}\sum_{j=1}^{2}\left(\frac{1}{2}m_{bj}\left(\dot{x}_{2j-1} + \dot{x}_g - \frac{1}{2}h_j\dot{\theta}_j\right)^2 + \frac{1}{2}m_{bj}\left(\dot{x}_{2j} + \dot{x}_g - h_j\dot{\theta}_j\right)^2 + m_{sj}r_j^2\theta_j^2\right) \quad \textbf{(3-1)}$$

$$U_E = \frac{1}{2}\sum_{j=1}^{2}\left(k_{bj}x_{2j-1}^2 + k_{bj}\left(x_{2j} - x_{2j-1}\right)^2 + k_{sj}\theta_j^2\right) + \frac{1}{2}\kappa(\theta_2 - \theta_1)^2 \quad \textbf{(3-2)}$$

where h_j are the total heights of the buildings and m_{bj} are the total masses of the buildings. m_{sj} are the soil/foundation masses underneath building 1 and 2, r_j are the soil/foundation masses radius of gyration,

and $m_{sj}r_j^2$ are the soil/foundation mass polar second moments of area (moments of inertia). k_{bj} are the building lateral stiffnesses, κ is the stiffness of the inter-building soil rotational spring and b_j are the width of the buildings' foundation. k_{s1} and k_{s2} are the rotational stiffnesses of the soil/foundation of the buildings 1 and 2, respectively.

The Euler-Lagrange equation of motion describing the dynamics of the discretised system can be derived in the standard way by calculus and is formulated in the equation (3-3).

$$\widehat{\mathbf{M}}\ddot{\mathbf{x}} + \hat{\mathbf{C}}\dot{\mathbf{x}} + \widehat{\mathbf{K}}\mathbf{x} = \hat{\mathbf{p}}\ddot{x}_g \tag{3-3}$$

where the system matrices $\widehat{\mathbf{M}}$, $\widehat{\mathbf{K}}$, and the vectors $\hat{\mathbf{p}}$, and $\mathbf{x}$ are defined as follows,

$$\widehat{\mathbf{M}} = \begin{bmatrix} \frac{1}{2}m_{b1} & 0 & -\frac{1}{4}m_{b1}h_1 & 0 & 0 & 0 \\ 0 & \frac{1}{2}m_{b1} & -\frac{1}{2}m_{b1}h_1 & 0 & 0 & 0 \\ -\frac{1}{4}m_{b1}h_1 & -\frac{1}{2}m_{b1}h_1 & \frac{5}{8}m_{b1}h_1^2+m_{s1}r_1^2 & 0 & 0 & 0 \\ 0 & 0 & 0 & \frac{1}{2}m_{b2} & 0 & -\frac{1}{4}m_{b2}h_2 \\ 0 & 0 & 0 & 0 & \frac{1}{2}m_{b2} & -\frac{1}{2}m_{b2}h_2 \\ 0 & 0 & 0 & -\frac{1}{4}m_{b2}h_2 & -\frac{1}{2}m_{b2}h_2 & \frac{5}{8}m_{b2}h_2^2+m_{s2}r_2^2 \end{bmatrix} \tag{3-4}$$

$$\widehat{\mathbf{K}} = \begin{bmatrix} 2k_{b1} & -k_{b1} & 0 & 0 & 0 & 0 \\ -k_{b1} & k_{b1} & 0 & 0 & 0 & 0 \\ 0 & 0 & k_{s1}+\kappa & 0 & 0 & -\kappa \\ 0 & 0 & 0 & 2k_{b2} & -k_{b2} & 0 \\ 0 & 0 & 0 & -k_{b2} & k_{b2} & 0 \\ 0 & 0 & -\kappa & 0 & 0 & k_{s2}+\kappa \end{bmatrix}, \hat{\mathbf{p}} = \begin{bmatrix} -\frac{1}{2}m_{b1} \\ -\frac{1}{2}m_{b1} \\ \frac{3}{4}m_{b1}h_1 \\ -\frac{1}{2}m_{b2} \\ -\frac{1}{2}m_{b2} \\ \frac{3}{4}m_{b2}h_2 \end{bmatrix}, \mathbf{x} = \begin{bmatrix} x_1 \\ x_2 \\ \theta_1 \\ x_3 \\ x_4 \\ \theta_2 \end{bmatrix} \tag{3-5}$$

The dimensional form of the system (3-3) contains too many system parameters. This is a rather large number for a parametric study even in a linear system. Hence, a reduction in the number of parameters is seeker through a process of removing all system dimensions. Thereby, the following non-dimensional parameter groups are introduced,

$$\eta_1 = \frac{h_1}{r_1}, \quad \eta_2 = \frac{h_2}{r_2}, \quad \alpha_1 = \frac{m_{s1}}{m_{b1}}, \quad \alpha_2 = \frac{m_{s2}}{m_{b2}}, \quad \beta = \frac{r_1}{r_2}, \quad \lambda = \frac{m_{b2}r_2^2}{m_{b1}r_1^2} \tag{3-6}$$

and the frequency parameters of the system are,

$$\omega_{b1}^2 = \frac{k_{b1}}{m_{b1}}, \quad \omega_{s1}^2 = \frac{k_{s1}}{m_{s1}r_1^2}, \quad \omega_{b2}^2 = \frac{k_{b2}}{m_{b2}}, \quad \omega_{s2}^2 = \frac{k_{s2}}{m_{s2}r_2^2}, \quad \varpi^2 = \frac{\kappa}{m_{b1}r_1^2} \tag{3-7}$$

and the non-dimensional frequency ratios normalised by ω_{b1},

$$\Omega_b = \frac{\omega_{b2}}{\omega_{b1}},\ \ \Omega_{s1} = \frac{\omega_{s1}}{\omega_{b1}},\ \ \Omega_{s2} = \frac{\omega_{s2}}{\omega_{b1}},\ \ \Omega_0 = \frac{\varpi}{\omega_{b1}} \tag{3-8}$$

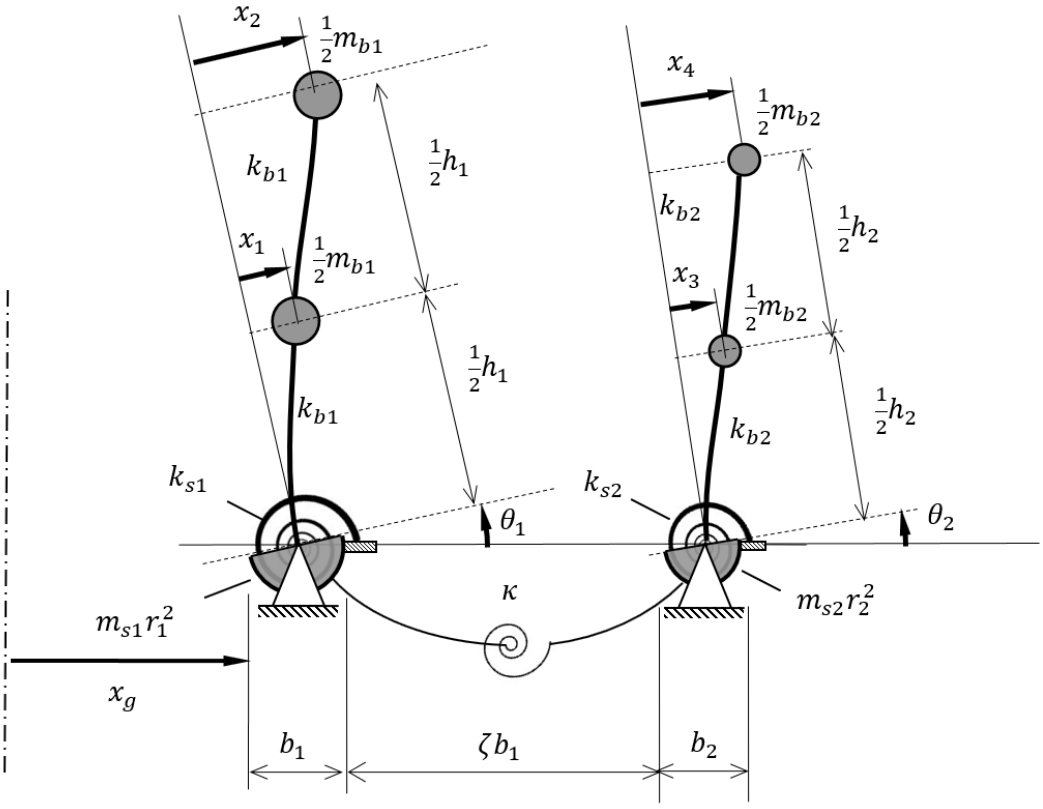

Figure 3.1 Structural model of a two-building system subjected to horizontal ground motion

To define the properties of the system is seeker to estimate the frequency parameter ω_{b1}, which can be related to the first modal circular frequency (on a fixed base) ω_{rb1} for the building 1. If the equation of motion (3-3) is derived for a rigid base case, then the static condensation of the equation of motion (3-3) results in a two DOF system (without any interaction between the buildings). Figure 3.2 shows the model of a two degrees of freedom system x_1 and x_2, where a rigid base foundation for the building is considered. m_b is the total mass of the building, k_b is the building's lateral stiffness, and h is the total height of the building.

Hence, the equation of motion (stiffness and mass matrix) of the two DOF system can be defined according to,

$$\tfrac{1}{2}m_b \begin{bmatrix} 1 & 0 \\ 0 & 1 \end{bmatrix} \begin{bmatrix} \ddot{x}_1 \\ \ddot{x}_2 \end{bmatrix} + k_b \begin{bmatrix} 2 & -1 \\ -1 & 1 \end{bmatrix} \begin{bmatrix} x_1 \\ x_2 \end{bmatrix} = 0 \Longrightarrow \mathbf{M\ddot{x} + Kx = 0} \tag{3-9}$$

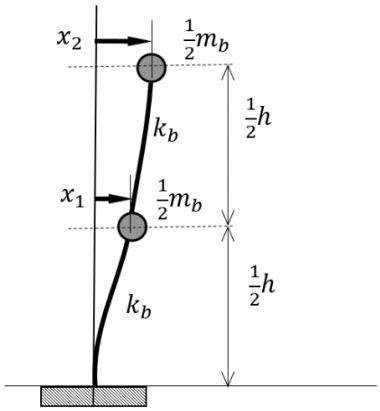

Figure 3.2 Idealised two degrees of freedom model

Through solving the resultant homogeneous eigenvalue problem $|\mathbf{K} - \omega\mathbf{M}| = 0$, the first ω_{rb1} and second ω_{rb2} modal circular frequencies are obtained. The natural circular frequency of an equivalent single degree of freedom system, with a total mass of m_b and stiffness k_b, is equal to $\sqrt{k_b/m_b}$. Therefore, the natural circular frequencies of the system in Figure 3.2 and the ratio of the frequencies are defined as follows,

$$\omega_{rb1} = 0.874\sqrt{\frac{k_b}{m_b}} = 0.874\omega_{b1},\ \ \omega_{rb2} = 2.288\sqrt{\frac{k_b}{m_b}},\ \ \frac{\omega_{rb2}}{\omega_{rb1}} = 2.618 \qquad \textbf{(3-10)}$$

where the coefficient 0.874 indicated in equation (3-10) is obtained through solving the eigenvalue problem's quadratic characteristic polynomial for the first root. The first building frequency ω_{rb1} are approximated by using the SEAOC Bluebook (1976) estimate of the natural period of a structure on a rigid foundation, that is $T_x = n_S/10$ (where T_x is the fundamental natural period of a structure in seconds, and n_S is the number of storeys). If an average storey height of 3.2m is assumed, the total height of the building is $h_1 = 3.2n_s$ and hence the period is $T_x = h_1/32$. The period has a relationship with the circular frequency of $\omega_{rb1} = 2\pi/T_x$. Therefore, the fundamental natural frequencies, on a rigid base, are $\omega_{\mathrm{rb1}} \approx 200/h_1$ and $\omega_{\mathrm{rb2}} \approx 200/h_2$ for the building 1 and 2 respectively. Thus, the frequency parameters described in the equation (3-7) are re-expressed for buildings 1 and 2 in terms of the buildings' heights.

$$\omega_{b1} \approx \frac{228.83}{h_1}, \qquad \omega_{b2} \approx \frac{228.83}{h_2} \qquad \textbf{(3-11)}$$

Finally, the following change of variables $x_{2j-1} = u_{2j-1}r_j,\ x_{2j} = u_{2j}r_j,\ x_g = u_g r_1$ and the time scale $\tau = \omega_{b1}t$ are introduced. This completes the full non-dimensionalisation of the problem, where u_{2j-1} and u_{2j} are the non-dimensional relative displacements of buildings to ground and u_g is the non-dimensional horizontal ground displacement (absolute). Therefore, after some calculus, the Euler-Lagrange equations of motion can be stated thus,

$$\mathbf{M\ddot{u}} + \mathbf{C\dot{u}} + \mathbf{Ku} = \mathbf{p}\ddot{u}_g \tag{3-12}$$

where Newtonian dots above now indicate derivatives with respect to scaled time τ, i.e. $(\dot{\bullet}) = \partial\bullet/\partial\tau$ and $(\ddot{\bullet}) = \partial^2\bullet/\partial\tau^2$. The matrices and vectors for the above equation are stated as follows,

$$\mathbf{M} = \frac{1}{2}\begin{bmatrix} 1 & 0 & -\frac{1}{2}\eta_1 & 0 & 0 & 0 \\ 0 & 1 & -\eta_1 & 0 & 0 & 0 \\ -\frac{1}{2}\eta_1 & -\eta_1 & \frac{5}{4}\eta_1^2+2\alpha_1 & 0 & 0 & 0 \\ 0 & 0 & 0 & \lambda & 0 & -\frac{1}{2}\eta_2\lambda \\ 0 & 0 & 0 & 0 & \lambda & -\eta_2\lambda \\ 0 & 0 & 0 & -\frac{1}{2}\eta_2\lambda & -\eta_2\lambda & \left(\frac{5}{4}\eta_2^2+2\alpha_2\right)\lambda \end{bmatrix} \tag{3-13}$$

$$\mathbf{K} = \begin{bmatrix} 2 & -1 & 0 & 0 & 0 & 0 \\ -1 & 1 & 0 & 0 & 0 & 0 \\ 0 & 0 & \alpha_1\Omega_{s1}^2+\Omega_0^2 & 0 & 0 & -\Omega_0^2 \\ 0 & 0 & 0 & 2\lambda\Omega_b^2 & -\lambda\Omega_b^2 & 0 \\ 0 & 0 & 0 & -\lambda\Omega_b^2 & \lambda\Omega_b^2 & 0 \\ 0 & 0 & -\Omega_0^2 & 0 & 0 & \alpha_2\lambda\Omega_{s2}^2+\Omega_0^2 \end{bmatrix}, \quad \mathbf{p} = \frac{1}{2}\begin{bmatrix} -1 \\ -1 \\ \frac{3}{2}\eta_1 \\ -\lambda\beta \\ -\lambda\beta \\ \frac{3}{2}\eta_1\lambda\beta \end{bmatrix}, \quad \mathbf{u} = \begin{bmatrix} u_1 \\ u_2 \\ \theta_1 \\ u_3 \\ u_4 \\ \theta_2 \end{bmatrix} \tag{3-14}$$

The system's linear viscous damping matrix $\mathbf{C}$ defined in equation (3-12) assumes that each natural mode $n \in [1,6]$ is damped at $\xi_n = 0.05$ of critical damping. $\boldsymbol{\phi}_n$ is the eigenvector for mode *n*, and ω_n are the natural frequencies of the system. Thus, the Caughey orthogonal damping matrix $\mathbf{C}$ can be calculated as equation (3-15), by Chopra (2000).

$$\mathbf{C} = \mathbf{M}\left(\sum_{n=1}^{6} \frac{2\xi_n\omega_n}{\boldsymbol{\phi}_n^T\mathbf{M}\boldsymbol{\phi}_n}\boldsymbol{\phi}_n\boldsymbol{\phi}_n^T\right)\mathbf{M} \tag{3-15}$$

3.2.2 Reducing the number of system parameters

Equation (3-12) is expressed in terms of ten linear system parameters η_1, η_2, α_1, α_2, λ, Ω_0, Ω_b, Ω_{s1}, Ω_{s2} and ω_{b1}. Additionally, the ground excitation has its own statistical descriptors, which can be viewed as further system parameters. Therefore, it still has a large system parameter space to explore for a comprehensive parametric study. To reduce this number, the procedure described by Alexander et al. (2013) is followed, where the scope of the analysis is limited by assuming that:

(i) The same soil profile exists under both buildings, this means $k_{s1} = k_{s2}$.

(ii) Both buildings have a similar square plan area and raft foundations of b^2, this means $m_{s1} = m_{s2}$ and $r_1 = r_2 = 0.33b$.

(iii) Both buildings have the same average density, ρ_b.

(iv) The buildings can be of different heights, h_j.

(i) The buildings are spaced at some arbitrary distance from each other, ζb, where ζ is the non-dimensional inter-building distance.

Newmark and Rosenblueth (1971) proposed that the dynamic mass of soil beneath buildings is equal to $m_s = 0.35b^3\rho_s$. The mass of the buildings can be calculated as $m_{bj} = \rho_b h_j b^2$, where ρ_s and ρ_b are the densities of soil and building respectively. Based on typical spans and floor loading, the average building density is $\rho_b = 400 - 800[kg/m^3]$, while typical soil density ranges between $\rho_s = 1200 - 2100[kg/m^3]$. Hence, the soil density and the proportionality constant c_1 (equation (3-16)) used in this chapter are defined in Table 3-1. The radius of gyration of the soil-cylinder (directly under the rigid foundation) is calculated according to the Newmark's empirical expression $r \approx 0.33b$. Parameters η_1, η_2, α_1, α_2, and λ are contracted into two geometric parameters Height ratio $\varepsilon = h_2/h_1$ and Aspect ratio $s = h_1/b$.

$$\varepsilon = \frac{h_2}{h_1},\ \ s = \frac{h_1}{b},\ \ \eta_1 = 3s,\ \ \eta_2 = 3\varepsilon s,\ \ \alpha_1 = \frac{c_1}{s},\ \ \alpha_2 = \frac{c_1}{\varepsilon s},\ \ \lambda = \varepsilon,\ \ c_1 = 0.35\frac{\rho_s}{\rho_b} \qquad \textbf{(3-16)}$$

Empirical forms for the rotational and inter-building interaction spring defined by Alexander et al. (2013) are used. As was noted before, these values were validated using Finite Element Models (Alexander et al., 2013), physical experimental models (Aldaikh et al., 2015; Aldaikh et al., 2016) and closed-form analytical models (Aldaikh et al., 2018). Therefore, the values of foundation rotational springs $k_{s1} = k_{s2}$, and the interaction spring stiffness κ is modelled as an inverse cube function of non-dimensional inter-building separation distance ζ. The term $q_\kappa(\zeta)$ and $q_2(\zeta)$ are graphed in Figure 5.2, section 5.2.3. It is worth noting that a revised and extended 3D version of the coupled springs κ and their respective functions q_k and q_2 has been calculated in Chapter 6.

$$k_{s1} = k_{s2} = k_s q_2,\ \ \kappa = k_{s1} q_k,\ \ q_k = -\frac{0.25}{(1+\zeta)^3},\ \ q_2 = 1 + \frac{0.5}{(1+\zeta)^3},\ \ k_s = \frac{1}{2}\frac{G_s b^3}{1-\mu_s} \qquad \textbf{(3-17)}$$

The rotational stiffness spring coefficient k_s is obtained by using the empirical formula (deduced by Pais and Kausel, 1988) in the absence of building interaction. G_s is the elastic shear modulus of the soil (typically called $G_0 = \rho_s V_s^2$ in the literature, Kramer (1996)) and μ_s is the Poisson's ratio of the soil. Hence, the soil frequency can be expressed in the form,

$$\omega_{s1}^2 = \omega_{s2}^2 = \frac{k_{s1}}{m_{s1} r_1^2} = \frac{\frac{1}{2}\frac{G_s b^3}{1-\mu_s} q_2}{(0.35 b^3 \rho_s)(0.33b)^2} = 13.1 \times 10^6 \frac{1}{1-\mu_s}\frac{1}{b^2} q_2 \bar{V}_s^2 \quad \textbf{(3-18)}$$

And the soil frequency ratios as,

$$\Omega_{s1}^2 = \Omega_{s2}^2 = \frac{\omega_{s1}^2}{\omega_{b1}^2} = \frac{13.1 \times 10^6 \frac{1}{1-\mu_s}\frac{1}{b^2} q_2 \bar{V}_s^2}{\frac{228.23^2}{h_1^2}} = c_2 q_2 \bar{V}_s^2 s^2, \qquad c_2 = \frac{250.52}{1-\mu_s} \quad \textbf{(3-19)}$$

where $V_s = \sqrt{G_s/\rho_s}$ is the shear wave velocity of the soil in [m/s], $\bar{V}_s = V_s/1000$ is the normalised non-dimensional shear wave velocity (to a reference of 1000 m/s), and c_2 is the soil constant. The shear wave velocity and the soil constant are defined in Table 3-1. The frequency ratio parameters Ω_0 and Ω_b are contracted and re-expressed in terms of,

$$\Omega_0^2 = \frac{\varpi^2}{\omega_{b1}^2} = \frac{\kappa}{\omega_{b1}^2 m_{b1} r_1^2} = \frac{\frac{1}{2}\frac{G_s b^3}{1-\mu_s} q_2 q_k}{\frac{228.23^2}{h_1^2}(\rho_b h_1 b^2)(0.33b)^2} = c_1 c_2 q_2 q_k s \bar{V}_s^2, \;\; \Omega_b = \frac{1}{\varepsilon}, \;\; \lambda = \beta \quad \textbf{(3-20)}$$

Table 3-1 Linear elastic stiffness parameters for soil classes

Soil Class (sand)	$\boldsymbol{\rho_s [kg/m^3]}$	$\boldsymbol{\mu_s}$ []	$\boldsymbol{c_1}$ []	$\boldsymbol{c_2}$ []	$\boldsymbol{V_s}$ $\boldsymbol{[m/s]}$
Dense	2000	0.35	1.17	385.4	325
Medium	1600	0.30	0.93	357.9	250
Loose	1300	0.30	0.76	357.9	156

Thus, the matrices of equations (3-13) and (3-14) can be re-expressed as follows,

$$\mathbf{M} = \frac{1}{2}\begin{bmatrix} 1 & 0 & -\frac{3}{2}s & 0 & 0 & 0 \\ 0 & 1 & -3s & 0 & 0 & 0 \\ -\frac{3}{2}s & -3s & \frac{45}{4}s^2 + 2c_1 s^{-1} & 0 & 0 & 0 \\ 0 & 0 & 0 & \varepsilon & 0 & -\frac{3}{2}\varepsilon^2 s \\ 0 & 0 & 0 & 0 & \varepsilon & -3\varepsilon^2 s \\ 0 & 0 & 0 & -\frac{3}{2}\varepsilon^2 s & -3\varepsilon^2 s & \frac{45}{4}\varepsilon^3 s^2 + 2c_1 s^{-1} \end{bmatrix} \quad \textbf{(3-21)}$$

$$\mathbf{K}=\begin{bmatrix} 2 & -1 & 0 & 0 & 0 & 0 \\ -1 & 1 & 0 & 0 & 0 & 0 \\ 0 & 0 & c_1c_2q_2s\bar{V}_s^2(1+q_k) & 0 & 0 & -c_1c_2q_2q_ks\bar{V}_s^2 \\ 0 & 0 & 0 & 2\varepsilon^{-1} & -\varepsilon^{-1} & 0 \\ 0 & 0 & 0 & -\varepsilon^{-1} & \varepsilon^{-1} & 0 \\ 0 & 0 & -c_1c_2q_2q_ks\bar{V}_s^2 & 0 & 0 & c_1c_2q_2s\bar{V}_s^2(1+q_k) \end{bmatrix}, \mathbf{p}=\frac{1}{2}\begin{bmatrix} -1 \\ -1 \\ \frac{9}{2}s \\ -\varepsilon \\ -\varepsilon \\ \frac{9}{2}\varepsilon^2 s \end{bmatrix} \quad \textbf{(3-22)}$$

Therefore, in this analysis, only 3 geometric non-dimensional parameters and one site classification are needed. This allows us to perform an intensive study that explores a huge number of generic cases. Hence, the complete problem, in equation (3-12), is reduced to a four parameter problem, in equations (3-21) and (3-22). These four parameters are listed as follows:

(i) The aspect ratio $s = h_1/b$ (for building 1)

(ii) The height ratio $\varepsilon = h_2/h_1$ between the buildings 2 to 1

(iii) The normalised inter-building distance ratio ζ (ratio of the distance between buildings to buildings' width).

(iv) The soil class, that is defined using c_1, c_2, $\bar{V}_s$, ρ_s and μ_s (see Table 3-1).

3.2.3 Defining system performance measures

As a measure of change in the response between the coupled (SSSI) and uncoupled (SSI) systems, the following performance measures are used in this study,

$$U_j = u_{2j} - 3\frac{h_j}{b}\theta_j, \qquad A_j = \ddot{u}_{2j} + \ddot{u}_g - 3\frac{h_j}{b}\ddot{\theta}_j \quad \textbf{(3-23)}$$

where U_j and A_j are respectively the relative (sway + rotational) displacements and total (sway + ground + rotational) accelerations for the top of building "j" in non-dimensional form. So, U_1 and U_2 are the displacements at the top of buildings one and two. The error in the response total power when using uncoupled SSI analyses rather than coupled SSSI analyses, is defined as follows,

$$\chi_j = 100\left\{\frac{\left[E_s(U_j)\right]_{SSSI}}{\left[E_s(U_j)\right]_{SSI}} - 1\right\} \quad \textbf{(3-24)}$$

where $E_s(U_j)$ is the total power spectral density (which is based on all data points of response time series U_i), which is defined using Parseval's theorem, according to equation (3-25).

$$E_s(U_j) = \int_{-\infty}^{\infty} \left|U_j(\tau)\right|^2 d\tau = \frac{1}{2\pi} \int_{-\infty}^{\infty} \left|U_j(\omega)\right|^2 d\omega \qquad \textbf{(3-25)}$$

where $U_j(\omega)$ is the continuous Fourier transform of $U_j(\tau)$. This error/difference term χ_j would be zero if there is no difference between SSSI and SSI analyses; thus, indicating no inter-building coupling effects. Therefore, χ_j could be viewed as the error in not employing SSSI analyses for a coupled building configuration. χ_1 is the error in the top displacement of building 1, and χ_2 is the error for the top displacement of building 2.

Using the total power as a comparative metric delivers a statistical estimate of magnitude that provides more information about the response than employing a single peak of the function. The uncoupled system response (SSI) case could be obtained by either (i) increasing inter-building distance ζ to a very large value or (ii) setting $q_\kappa = 0$ and $q_2 = 1$. In this research to evaluate the SSI response (without coupled interaction), the rotational interaction spring κ equal to zero (i.e. $q_\kappa = 0$ and $q_2 = 1$) was employed. Similarly, the error/difference in acceleration responses are defined as,

$$\ddot{\chi}_j = 100\left\{\frac{\left[E_s(A_j)\right]_{SSSI}}{\left[E_s(A_j)\right]_{SSI}} - 1\right\} \qquad \textbf{(3-26)}$$

Additionally, for a more forensic exploration of system responses used later, the norms of the system transfer functions are defined. In frequency domain system analysis (Clough and Penzien, 1993), it can determine the system response through the displacement transfer function $\mathbf{v}(\omega)$ between the degrees of freedom u_j and the earthquake $\ddot{u}_g$. By taking a Fourier transform of equation (3-12) the set of differential equations with a set of algebraic equations is re-expressed, thus,

$$\mathbf{U}(\omega) = \mathbf{v}(\omega)\ddot{U}_g(\omega), \;\; \mathbf{v}(\omega) = -(\mathbf{K} + i\omega\mathbf{C} - \omega^2\mathbf{M})^{-1}\mathbf{p} = [v_1(\omega), \cdots, v_6(\omega)]^T \qquad \textbf{(3-27)}$$

where the vector $\boldsymbol{U}(\omega)$ is the Fourier transform of vector $\mathbf{u}(\tau)$, $\ddot{U}_g(\omega)$ is the Fourier transform of the ground acceleration $\ddot{u}_g(\tau)$, and ω is the Fourier frequency. This can be expressed as the norm of the transfer function for the building 1 and 2.

$$\|\mathbf{v}_{b1}(\omega)\|_2 = \sqrt{v_1^2 + v_2^2 + v_3^2}, \qquad \|\ddot{\mathbf{v}}_{b1}(\omega)\|_2 = \|(i\omega)^2\mathbf{v}_{b1}(\omega)\|_2 \qquad \textbf{(3-28)}$$

$$\|\mathbf{v}_{b2}(\omega)\|_2 = \sqrt{v_4^2 + v_5^2 + v_6^2}, \qquad \|\ddot{\mathbf{v}}_{b2}(\omega)\|_2 = \|(i\omega)^2\mathbf{v}_{b2}(\omega)\|_2 \qquad \textbf{(3-29)}$$

where $\|\mathbf{v}_{b1}(\omega)\|_{\mathbf{2}}$ and $\|\mathbf{v}_{b2}(\omega)\|_{\mathbf{2}}$ are the Euclidian norms of displacement response transfer functions for the buildings 1 and 2 respectively. The acceleration transfer function is equal to $\ddot{\mathbf{v}}(\omega) = (i\omega)^2\mathbf{v}(\omega)$. Similarly, $\|\ddot{\mathbf{v}}_{b1}(\omega)\|_{\mathbf{2}}$ and $\|\ddot{\mathbf{v}}_{b2}(\omega)\|_{\mathbf{2}}$ are the Euclidian norms of acceleration response transfer functions for the buildings 1 and 2 respectively. Thus, it will be employed,

(i) Difference/error in total power responses, (Eqn. (3-24) and (3-26)) as an overall system comparative metric.

(ii) The Euclidian norms of response transfer functions (Eqn. (3-28) and (3-29)) for a more forensic system examination metric.

3.3 Analyses

3.3.1 Ground motion selection

To determine the effect of SSSI on the system three types of ground motions are considered. These include the Far-Field (FF), Near-Field Without Pulse (NFWP) and Near-Field Pulse-Like (NFPL) record sets obtained from the Pacific Earthquake Engineering Research Center database (PEER, 2014). The earthquakes that occur in fields close to a ruptured fault can have different characteristics than those further away from the seismic source. The Near-Field zone is a set of ground motions recorded at sites located less than 10km from the fault rupture, and the Far-Field zone is to be at sites greater than 10km from the fault rupture (FEMA P695, 2009). A pulse-like ground motion is considered to be a record with a short-duration pulse that occurs early in the velocity time history and has large amplitude (Baker, 2015). One cause of these velocity pulses are forward-directivity effects in the near-fault region.

The ground motions dataset (events and stations) is obtained from FEMA P695, which includes records with different characteristics, i.e. FF, NFPL and NFWP. The recorded acceleration time series of these ground motions are downloaded from the Pacific Earthquake Engineering Research, PEER-NGA West database, PEER (2014). FEMA P695 recommends a set of 22 FF records that are taken from 14 events that occurred between 1971 and 1999 (listed in Table 3-2). Eight of them occurred in California, and six of them are taken from different places around the world. The other set for Near Field included 28 pairs of ground motions, fourteen records have pulses and fourteen records do not have pulses (listed in Table 3-3). Each record has two horizontal components. Event magnitudes range from $M_w = 6.5$ to $M_w = 7.6$ with an average magnitude of $M_w = 7.0$. Values of their peak ground accelerations (PGAs) vary from 0.21g to 0.82g with a mean value of 0.43g. Figure 3.3 shows the elastic response spectra for all the records and the mean of the elastic response spectra for the FF, NFPL and NFWP records set.

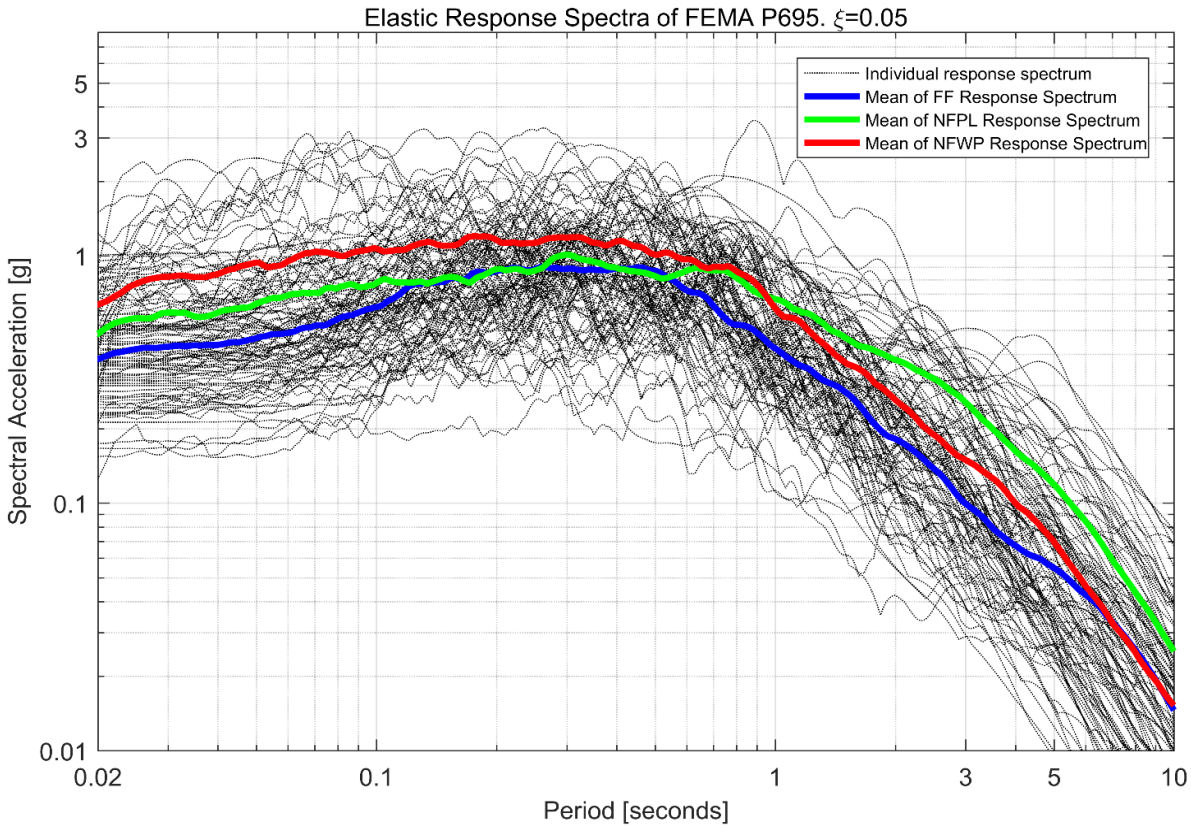

Figure 3.3 Elastic response spectra of FEMA P695 ground motions

Table 3-2 Summary of Earthquake records for the Far-Field Record Set

Record Name – Station	PGA [g]	M_w	Record Name – Station	PGA [g]	M_w
Northridge, USA – Beverly Hills	0.52	6.7	Landers, USA – Coolwater	0.42	7.3
Northridge, USA – Canyon Country	0.48	6.7	Loma Prieta, USA – Capitola	0.53	6.9
Duzce, Turkey – Bolu	0.82	7.1	Loma Prieta, USA – Gilroy Array #3	0.56	6.9
Hector Mine, USA – Hector	0.34	7.1	Manjil, Iran – Abbar	0.51	7.4
Imperial Valley, USA – Delta	0.35	6.5	Superstition Hills, USA – El Centro	0.36	6.5
Imperial Valley, USA – EC #11	0.38	6.5	Superstition Hills, USA – Poe Road	0.45	6.5
Kobe, Japan – Nishi-Akashi	0.51	6.9	Cape Mendocino, USA – Rio Overpass	0.55	7.0
Kobe, Japan – Shin-Osaka	0.24	6.9	Chi-Chi, Taiwan – CHY101	0.44	7.6
Kocaeli, Turkey – Duzce	0.36	7.5	Chi-Chi, Taiwan – TCU045	0.51	7.6
Kocaeli, Turkey – Arcelik	0.22	7.5	San Fernando, USA – LA Hollywood	0.21	6.6
Landers, USA – Yermo Fire Station	0.24	7.3	Friuli, Italia - Tolmezzo	0.35	6.5

Table 3-3 Summary of Earthquake records for the Near-Field Record Set

Record Name NFPL – Station	PGA [g]	M_w	Record Name NFWP – Station	PGA [g]	M_w
Imperial Valley, USA – El Centro #6	0.45	6.5	Gazli, USA – Karakyr	0.86	6.8
Imperial Valley, USA – El Centro #7	0.47	6.5	Imperial Valley, USA – Bonds Corner	0.78	6.5
Irpinia, Italy – Sturno	0.32	6.9	Imperial Valley, USA – Chihuahua	0.27	6.5
Superstition Hills, USA – Parachute	0.43	6.5	Nahanni, Canada – Site 1	1.20	6.8
Loma Prieta, USA – Saratoga	0.51	6.9	Nahanni, Canada – Site 2	0.52	6.8
Erzican, Turkey – Erzican	0.50	6.7	Loma Prieta, USA – Bran	0.50	6.9
Cape Mendocino, USA – Petrolia	0.66	7.0	Loma Prieta, USA – Corralitos	0.64	6.9
Landers, USA – Lucerne	0.79	7.3	Cape Mendocino, USA – C. Mendocino	1.49	7.0
Northridge, USA – Rinaldi Receiving	0.87	6.7	Northridge, USA – LA Sepulveda	0.93	6.7
Northridge, USA – Sylmar Olive View	0.84	6.7	Northridge, USA – Saticoy	0.46	6.7
Kocaeli, Turkey – Izmit	0.23	7.5	Kocaeli, Turkey – Yarimca	0.32	7.5
Chi-Chi, Taiwan – TCU065	0.79	7.6	Chi-Chi, Taiwan – TCU067	0.50	7.6
Chi-Chi, Taiwan – TCU102	0.30	7.6	Chi-Chi, Taiwan – TCU084	1.01	7.6
Duzce, Turkey – Duzce	0.51	7.1	Denali, Alaska – TAPS Pump Sta.	0.33	7.9

Due to the complexity of the problem and the number of parameters considered, the results are divided into four sections, as follows,

(i) Section 3.3.2 demonstrates different cases of beneficial and adverse SSSI effect in building 1 and 2 for the Near-Field Pulse-Like Loma Prieta earthquake. The interaction between the second sway mode of the taller building with the first sway mode of the smaller building is also discussed.

(ii) Section 3.3.3 explores the influence of the height ratio ε and aspect ratio s in the SSSI response of buildings, considering a hundred acceleration ground motion time series (This includes Far-Field (FF), Near-Field Without Pulse (NFWP) and Near-Field Pulse-Like (NFPL) record sets (PEER, 2014).

(iii) Section 3.3.4 explores the influence of the soil class, aspect ratio s, and height ratio ε in the SSSI responses of buildings, considering all of the acceleration ground motion time series.

(iv) Section 3.3.5 explores the influence of the height ratio ε and the inter-building distance ζ in the SSSI responses of buildings, considering all of the acceleration ground motion time series.

3.3.2 Response of the system for a set of parameters

The analysis is carried out first for the Near-field Pulse-Like Loma Prieta earthquake (18/10/1989, Loma Prieta Saragota – Aloha Ave-90 Station) for a selected combination of parameters as a starting example. Figure 3.4 shows the acceleration ground motion time series and the power spectral density of the record. The case when the two buildings are placed in very close proximity to each other are examined, i.e. at a spacing distance of $0.1b$ and hence $\zeta = 0.1$. This building spacing has been demonstrated to be large enough to avoid pounding but close enough to maximise the SSSI effects (Alexander et al., 2013; Aldaikh et al., 2016, 2018). The rigid base frequency of building 1 is $\omega_{rb1}/2\pi = 3.3$Hz.

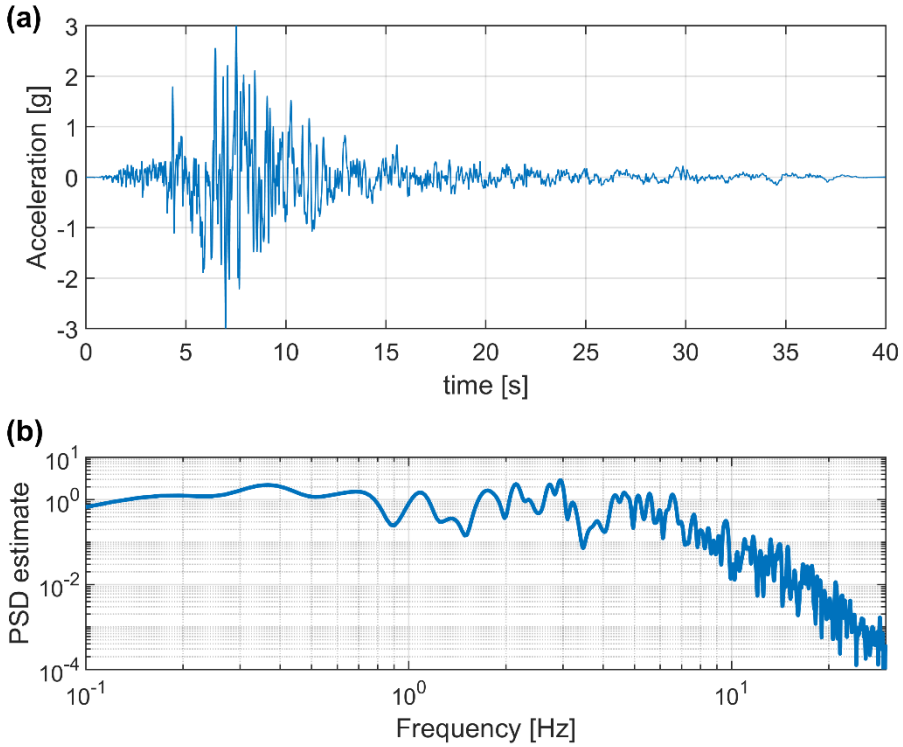

Figure 3.4 (a) Acceleration ground motion and (b) Power spectral density (Loma Prieta 18/10/1989)

An important feature of the SSSI systems is that the fundamental frequencies of the coupled system do not change very much compared to the uncoupled system, i.e. there is a maximum of 9% variation in the natural frequencies between the SSI and SSSI systems. For example, Figure 3.5(a) shows the first three natural periods of vibration ($T_1 = 0.57s$, $T_2 = 0.47s$, and $T_3 = 0.129s$) and the modal shapes for the coupled case (SSSI configuration), considering the parameter set of height ratio $\varepsilon = h_2/h_1 = 1.1$ and

aspect ratio $s = h_1/b = 2.6$. Figure 3.5(b) shows the natural periods of vibration and the modal shapes for the uncoupled case (SSI configuration), where the mode 1 represents the first mode of building 2 ($T_1 = 0.564s$), the mode 2 corresponds to the first mode of building 1 ($T_2 = 0.497s$), and the mode 3 corresponds to the second mode of building 2 ($T_3 = 0.129s$). As is observed, the values of the fundamental periods are quite similar between the SSSI and SSI analyses. Besides, this characteristic can be seen in the changes of peaks for the transfer functions, between the uncoupled and coupled system, in the following figures.

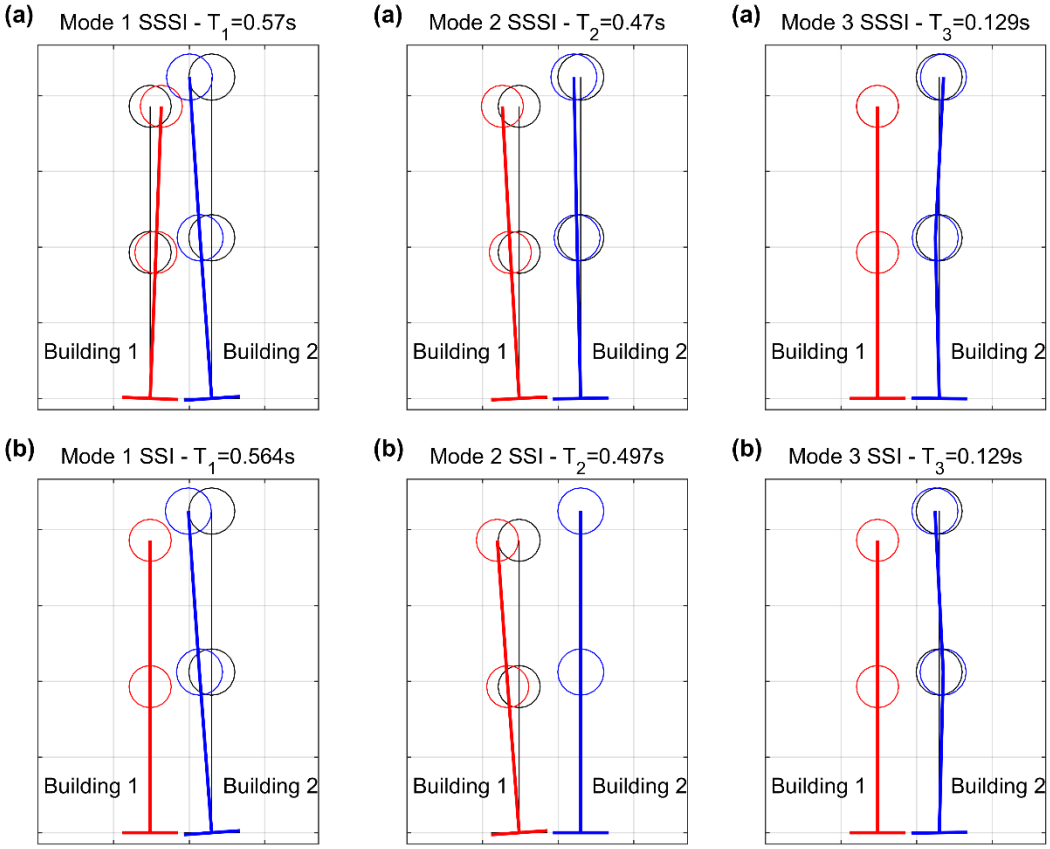

Figure 3.5 (a) Modal shapes for the SSSI case and (b) Modal shapes for the SSI case – Dynamic properties on loose soil for the parameter set (ε = 1.1, s = 2.6, ζ = 0.1)

Figure 3.6(a) shows the uncoupled SSI (blue line) and coupled SSSI (red line) response for the top of the building 1 (namely the displacement U_1 and the total acceleration A_1, defined in equation (3-23)). This is for the case where the second building is 10% taller than building 1, and building 1 has a height to width ratio equal to 2.6 (height ratio $\varepsilon = h_2/h_1 = 1.1$ and aspect ratio $s = h_1/b = 2.6$). Comparing the SSI and SSSI responses, it is observed that the maximum displacement of buildings increases, when the coupling is considered, as well as total acceleration in almost all the time-history. Figure 3.6(b) shows the corresponding power spectral density for the displacements and total acceleration for the building 1 considering the uncoupled and coupled case. Comparing the SSSI and SSI responses, it is observed that building 1 is significantly affected by the taller building 2. There are big amplifications in the displacement and acceleration power spectral density for a Fourier frequency equal to 2.2Hz (which mainly represents building 1's first natural frequency). Building 1's displacement response power increases by $\chi_1 = 78\%$

(change in power defined in equation (3-24)), and the system has a larger amplification in acceleration response power of $\ddot{\chi}_1 = 120\%$ (change in power defined in equation (3-26)). In general, greater amplifications are observed for accelerations than for displacements, for height ratios close to 1.1.

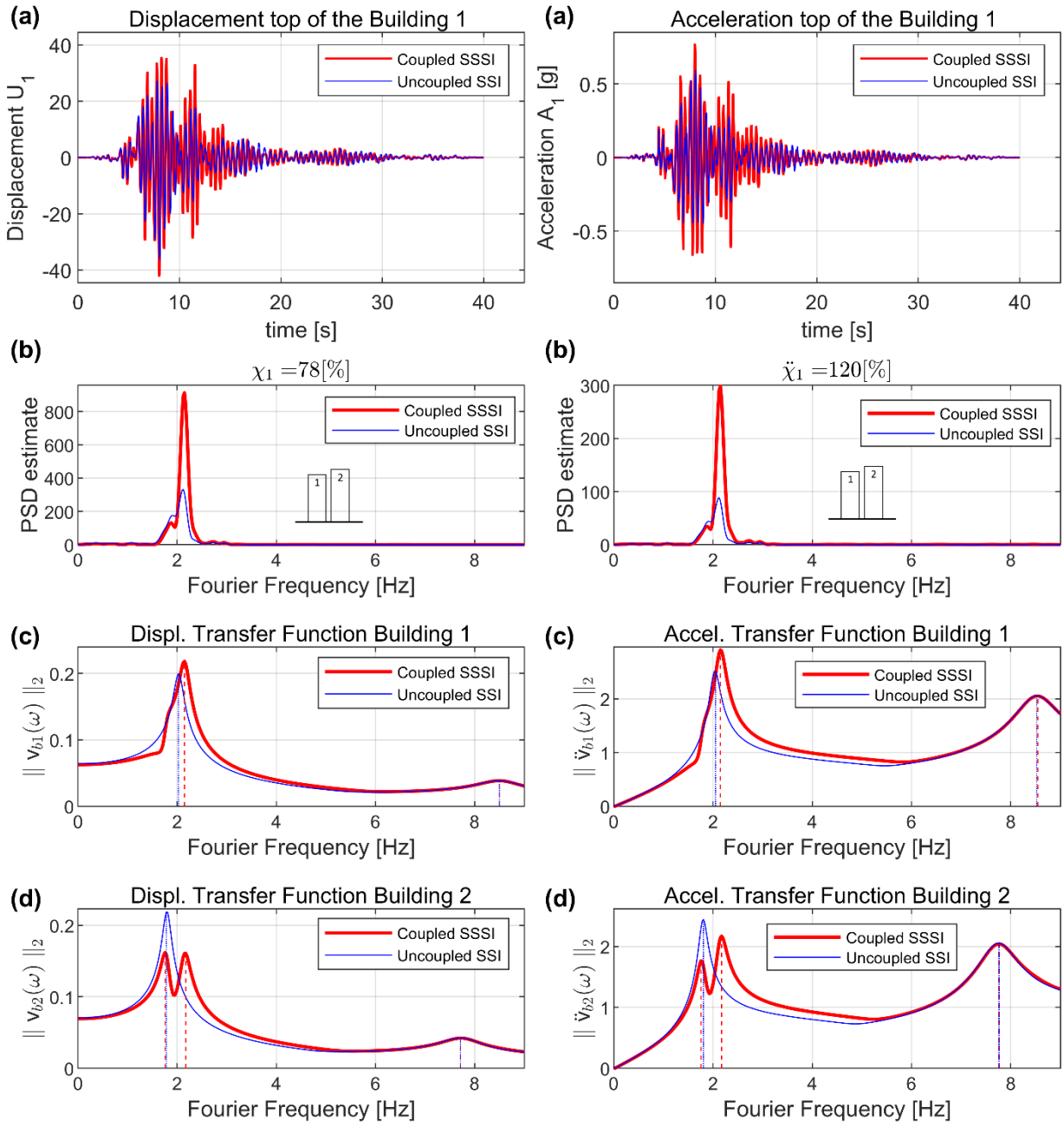

Figure 3.6 (a) Displacement and total acceleration responses for the building 1, (b) Power spectral density of displacement and acceleration, (c) Transfer function for the building 1 and (d) Transfer function for the building 2 – Responses on loose soil for the parameter set (ε = 1.1, s = 2.6, ζ = 0.1)

Figure 3.6(c) displays the norm transfer function for the displacements $\|\mathbf{v}_{b1}(\omega)\|_2$ and accelerations $\|\ddot{\mathbf{v}}_{b1}(\omega)\|_2$ for building 1. Comparing the uncoupled (blue line) and coupled case (red line) responses, there is a transfer of earthquake energy between building 2 (represented as the first peak in Figure 3.6(d) with a Fourier frequency of 1.8Hz) to building 1 (represented as the first peak in Figure 3.6(c) with a

Fourier frequency of approximately 2.2Hz). The higher modes of the system do not produce a significant change in the response of the system, for height ratios close to 1.1 (buildings of similar height). Figure 3.6(d) displays the norm transfer function for the displacement $\|\mathbf{v}_{b2}(\omega)\|_2$ and acceleration $\|\ddot{\mathbf{v}}_{b2}(\omega)\|_2$ for building 2. The response of building 2 is discussed in Figure 3.7.

Figure 3.7 shows the uncoupled SSI (blue line) and coupled SSSI (red line) responses of the top of the building 2 (namely the displacement U_2 and the total acceleration A_2). There is a decrease of energy in building 2 which produces a reduction in the response of $\chi_2 = -45.2\%$ and $\ddot{\chi}_2 = -16.7\%$ in the displacement and acceleration respectively. These effects are mainly due to the decrease in the first peak in the coupled SSSI case. These reductions can be seen clearly in Figure 3.6(d) (norm transfer function for the displacement $\|\mathbf{v}_{b2}(\omega)\|_2$ and acceleration $\|\ddot{\mathbf{v}}_{b2}(\omega)\|_2$) and Figure 3.7(b) (power spectral density for the displacements and total acceleration). This behaviour corresponds to the classical tuned mass damper (TMD) characteristic, where building 1 can be viewed as a TMD for building 2.

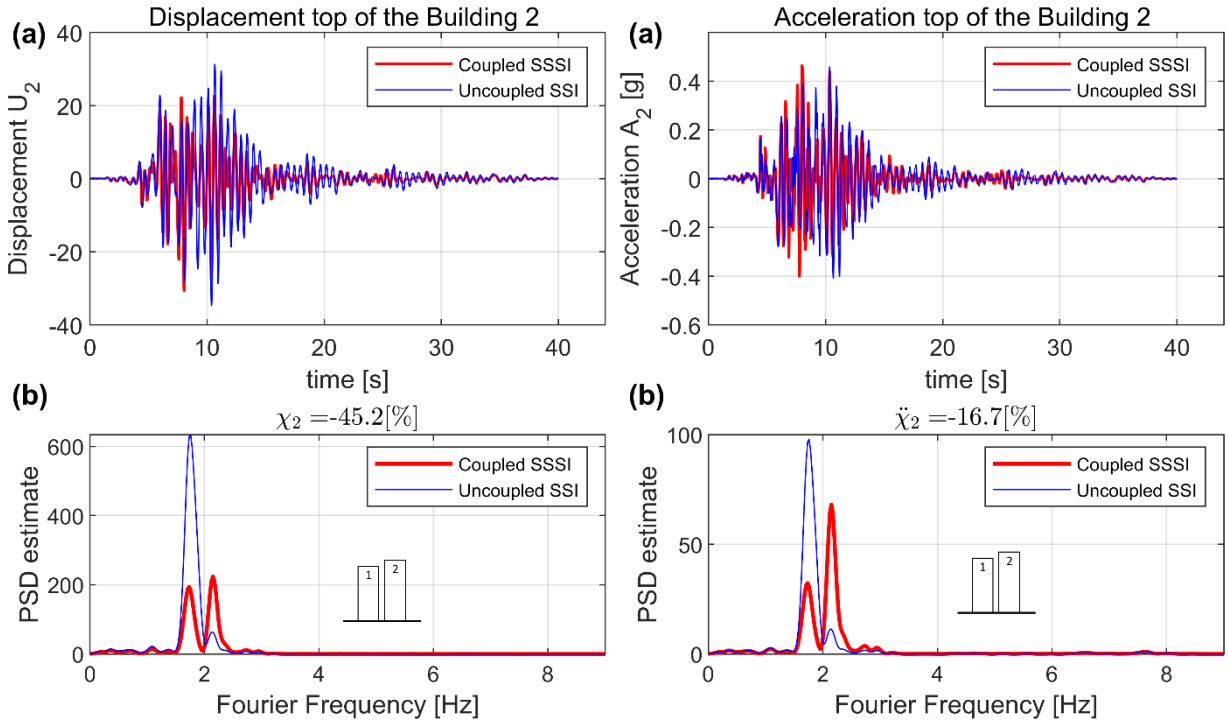

Figure 3.7 (a) Displacement and acceleration responses for the building 2, (b) Power spectral density of displacement and acceleration for the building 2 – Responses on loose soil for the parameter set (ε = 1.1, s = 2.6, ζ = 0.1)

Figure 3.8 displays the response for a system of which the second building has a height 2.5 times the first building, and building 1 has a height to width ratio equal to 2.6 (aspect ratio $s = h_1/b = 2.6$ and height ratio $\varepsilon = h_2/h_1 = 2.5$). Figure 3.8(a) shows the uncoupled and coupled responses for the top of building 1, that is the displacement U_1 and the total acceleration A_1. Comparing the uncoupled and coupled responses, it is observed that the maximum displacement and acceleration of buildings increases for the SSSI case, just like in the initial example, Figure 3.6.

Figure 3.8(b) shows the power spectral density for the displacements and total accelerations. It is observed that building 1's total response power increases about $\chi_1 = 63.7\%$ and $\ddot{\chi}_1 = 51.3\%$ in the displacement and the acceleration, respectively. In general, for height ratios greater than 2.0, higher amplifications are observed for displacement than for acceleration. The main difference observed with the previous case is that there are three closely spaced resonances/modes (see Figure 3.8(b)) as opposed to two closely spaced resonances/modes in the previous case of Figure 3.6(b).

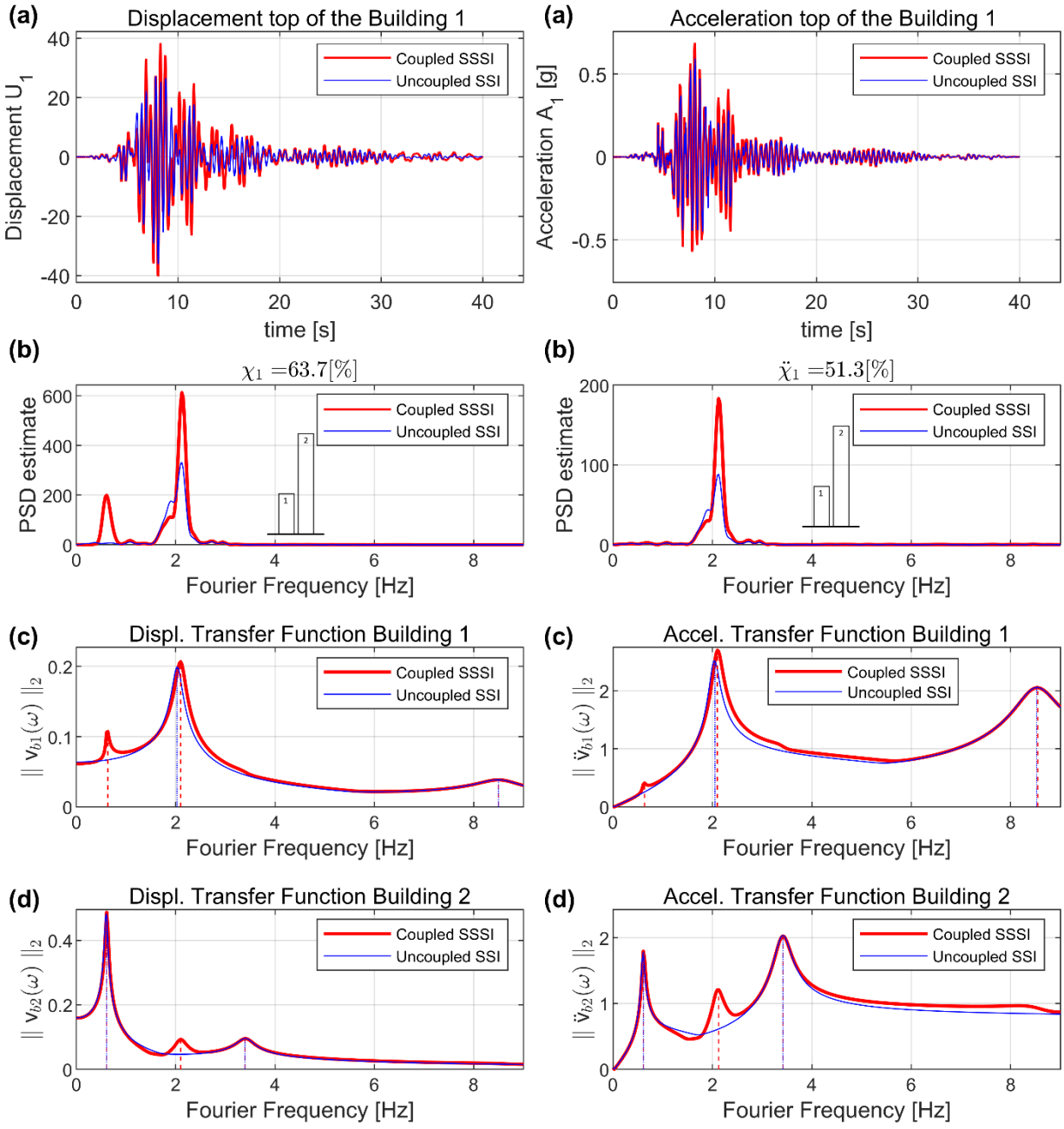

Figure 3.8 (a) Displacement and acceleration responses for the building 1, (b) Power spectral density of displacement and acceleration, (c) Transfer function for the building 1 and (d) Transfer function for the building 2 - Responses on loose soil for the parameter set (ε = 2.5, s = 2.6, ζ = 0.1)

There is a significant amplification in the displacement power spectral density for a Fourier frequency equal to 0.61Hz. This is mainly due to building 2's first uncoupled natural frequency. As stated previously, the eigenfrequencies for the coupled and uncoupled system are very similar. However, the eigenmodes are different for the coupled system as they span the two buildings rather than a single building in the uncoupled system. The resonance at 0.61Hz is not significant for acceleration, mainly because the acceleration response is not as susceptible to low-frequency content by definition. This is a direct result of the Eulerian relationship $\ddot{\mathbf{v}}(\omega) = (i\omega)^2\mathbf{v}(\omega)$. The second resonance peak in the displacement and acceleration occurs at a Fourier frequency equal to 2.1Hz (which corresponds to building 1's first uncoupled natural frequency). While the third resonance peak is due to building 2's second uncoupled natural frequency.

Therefore, for this parameter setting, the 'first modal frequency' of building 1 (represented by the second peak with a Fourier frequency of 2.1Hz) is close to the natural frequency of the second mode in building 2 (represented by the third peak in Figure 3.8(d) with a Fourier frequency of 3.4Hz). This produces an additional amplification in the response of building 1. Figure 3.8(c) and Figure 3.8(d) display the norm of the transfer function for the displacement and acceleration for building 1 and 2 respectively.

As in the previous case (Figure 3.6), there is a transfer of earthquake energy from building 2 to building 1, producing a reduction in building 2's responses of $\chi_2 = -12.3\%$ and $\ddot{\chi}_2 = -4.1\%$ in the displacement and acceleration respectively, see Figure 3.9.

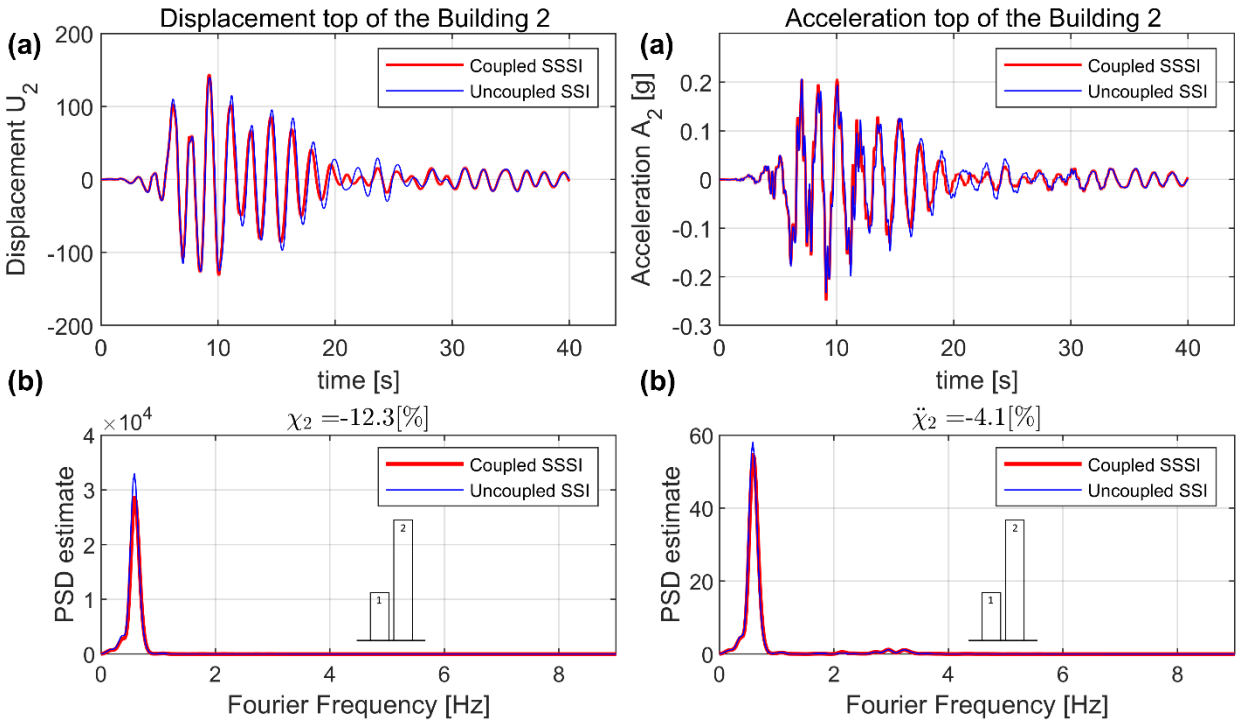

Figure 3.9 (a) Displacement and acceleration responses for the building 2, (b) Power spectral density of displacement and acceleration for the building 2 – Responses on loose soil for the parameter set (ε = 2.5, s = 2.6, ζ = 0.1)

To quantify the effect of secondary modes of building 2 on building 1, the response for the equivalent system described by Alexander et al. (2013) will be calculated. This model represents a pair of buildings with 2 DOFs each, whose response is shown in Figure 3.10. The main feature that differentiates the two models is that the reduced-order model presented in this chapter allows the interaction between the second sway mode of the taller building with the first sway mode of the smaller building. This additional interaction was not explored in the works of Alexander et al. (2013) and Aldaikh et al. (2015).

Figure 3.10 shows the uncoupled and coupled response (system with original 4 DOFs model by Alexander et al. (2013)) where the second building is 2.5 times as high as the first building, and the first building has a height to width ratio equal to 2.6. In this case, building 1's total response power increases about $\chi_1 = 20\%$ and $\ddot{\chi}_1 = 24.6\%$ for the displacement and acceleration respectively, versus the values of $\chi_1 = 63.7\%$ and $\ddot{\chi}_1 = 51.3\%$ for the change of power shown in Figure 3.8(b). This difference is mainly due to the additional degree of freedom in each building, and it generally occurs when the first natural frequency of building 1 is close to the second natural frequency of building 2. This is likely to happen if the height ratio between the two buildings is greater than 2.

In addition, in Figure 3.10(c) is observed that the third and fourth peaks shown in Figure 3.8(c) disappeared. Hence, the amplification or reduction in the response is only influenced by the first two modes. Thus, adding an extra degree of freedom to building 1 and 2 may increase the interaction between the buildings. Nevertheless, incorporating further additional degrees of freedom into the buildings (i.e. greater than 3 DOFs per building) does not significantly affect the SSSI system response. This is because the modal participation factors of additional higher system modes are very small.

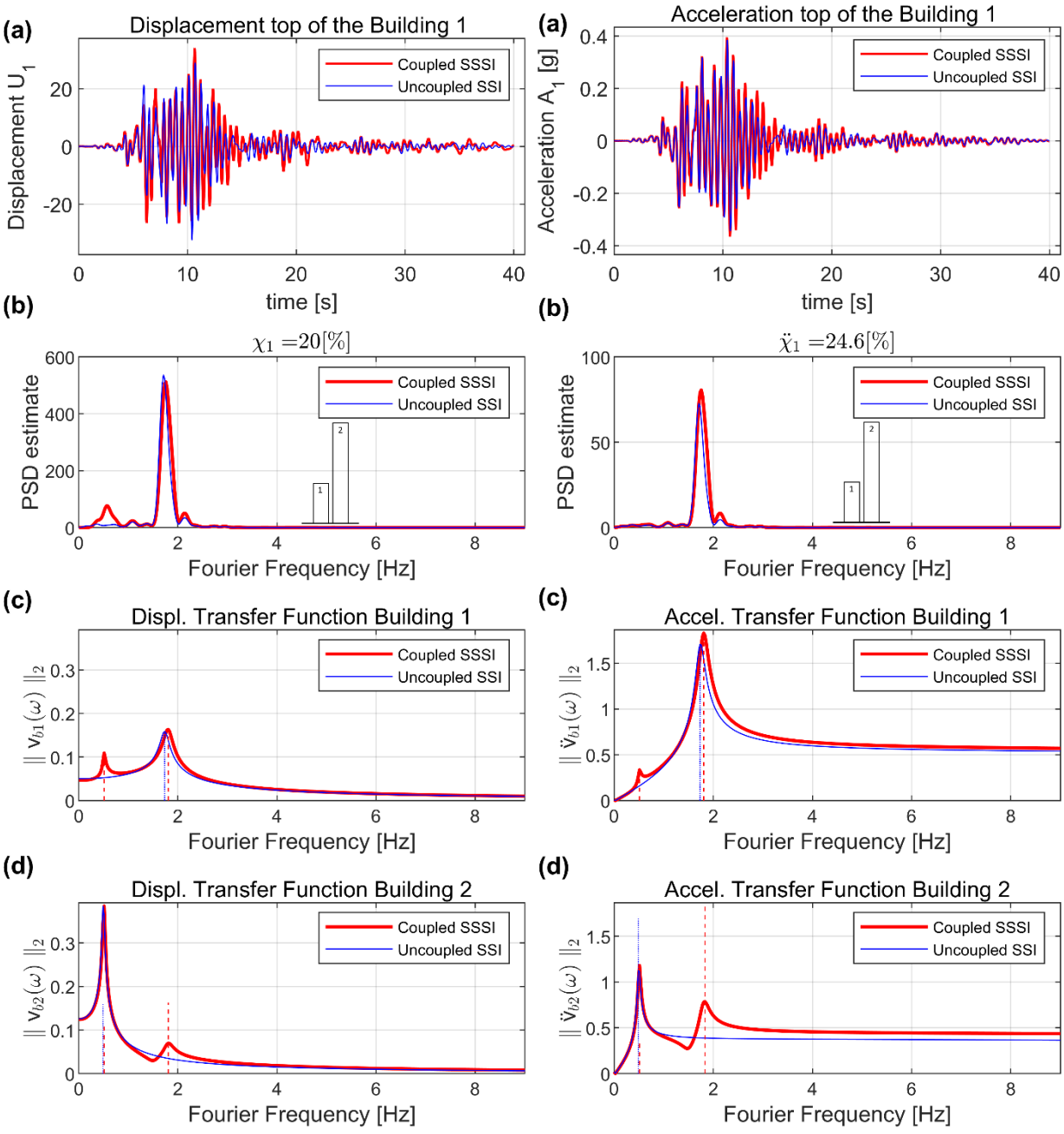

Figure 3.10 (a) Displacement and acceleration response for a system with 4 DOFs, (b) Power spectral density for the building 1, (c) Transfer function for the building 1 and (d) Transfer function for the building 2 - Responses on loose soil for the parameter set (ε = 2.5, s = 2.6, ζ = 0.1)

For some specific ground motion, e.g. the Near-field Pulse-Like Erzican ground motion, there is a significant amplification in displacement when the height ratios are greater than 2.0. Figure 3.11 shows the acceleration ground motion time series and the power spectral density of this record. It is possible to appreciate the large amplitude short-duration pulse at the beginning of the time series.

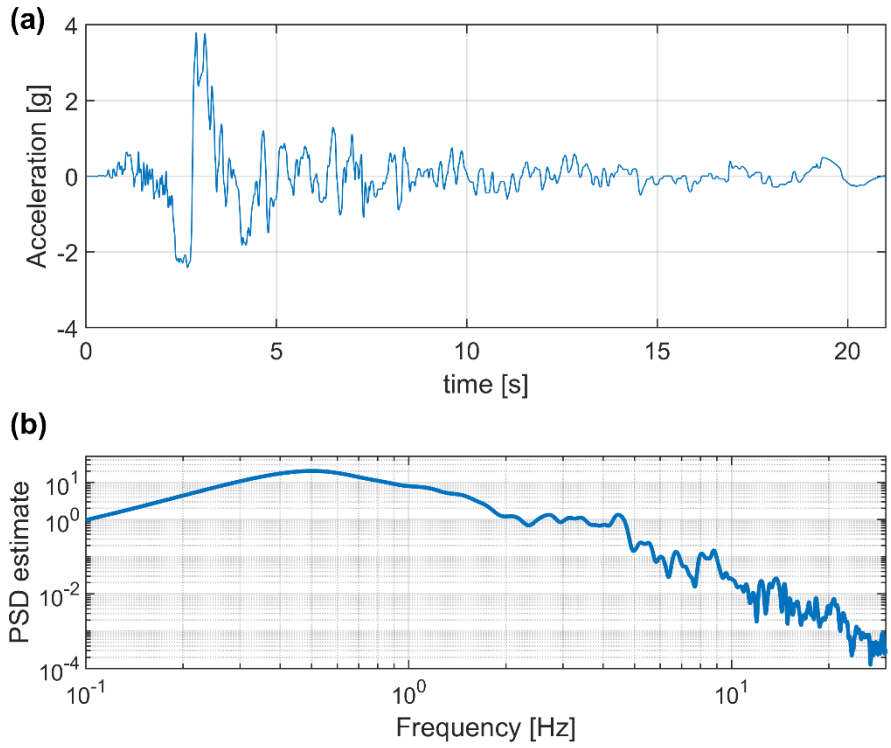

Figure 3.11 (a) Acceleration ground motion and (b) Power spectral density (Erzican Turkey 13/03/1992)

Figure 3.12(a) shows the response for the Near-field Pulse-Like Erzican ground motion (13/03/1992, Erzican Turkey NS Station) for a system on which the second building has a height 2.5 times the first building, and the first building has a height to width ratio equal to 2.6. Comparing the SSI and SSSI responses, there is a significant amplification in the displacements (change in power of $\chi_1 = 258\%$) but not in accelerations (change in power of $\ddot{\chi}_1 = 18.6\%$). Figure 3.12(b) displays the relative displacement u_1 and acceleration $\ddot{u}_1$ to the base. Figure 3.12(c) displays the rotation (multiplied by $3s$, so it is possible to compare with the other degrees of freedoms) displacement $3s\theta_1$ and acceleration $3s\ddot{\theta}_1$, and Figure 3.12(d) displays the norm of the transfer function for each degree of freedom corresponding to building 1. It is seen that the amplification in displacement comes through the amplification of the rotation/rocking of building 1 (see Figure 3.12(c), where the differences between SSI and SSSI is larger), due to the presence of the taller building 2 (degree of freedom corresponding to θ_1). The taller building has a fundamental modal frequency at 0.8Hz when it is uncoupled. In the coupled system, this 0.8Hz mode, remains at approximately 0.8Hz, but has an eigenvector (spanning the entire coupled system) with a large rotational component in building 1. Thus, it is observed very large differences in displacement responses from SSI and SSSI analyses for this case. The taller building seems to induce a large 'rigid body rocking mode' in the smaller building, which is represented by the peak (at 0.8Hz) in the transfer function for the rotation of building 1 (red line).

This behaviour is not observed for the acceleration responses because low-frequency acceleration responses are not subjected to low-frequency amplification. This is a result of the Eulerian relationship $\ddot{\mathbf{v}}(\omega) = (i\omega)^2\mathbf{v}(\omega)$.

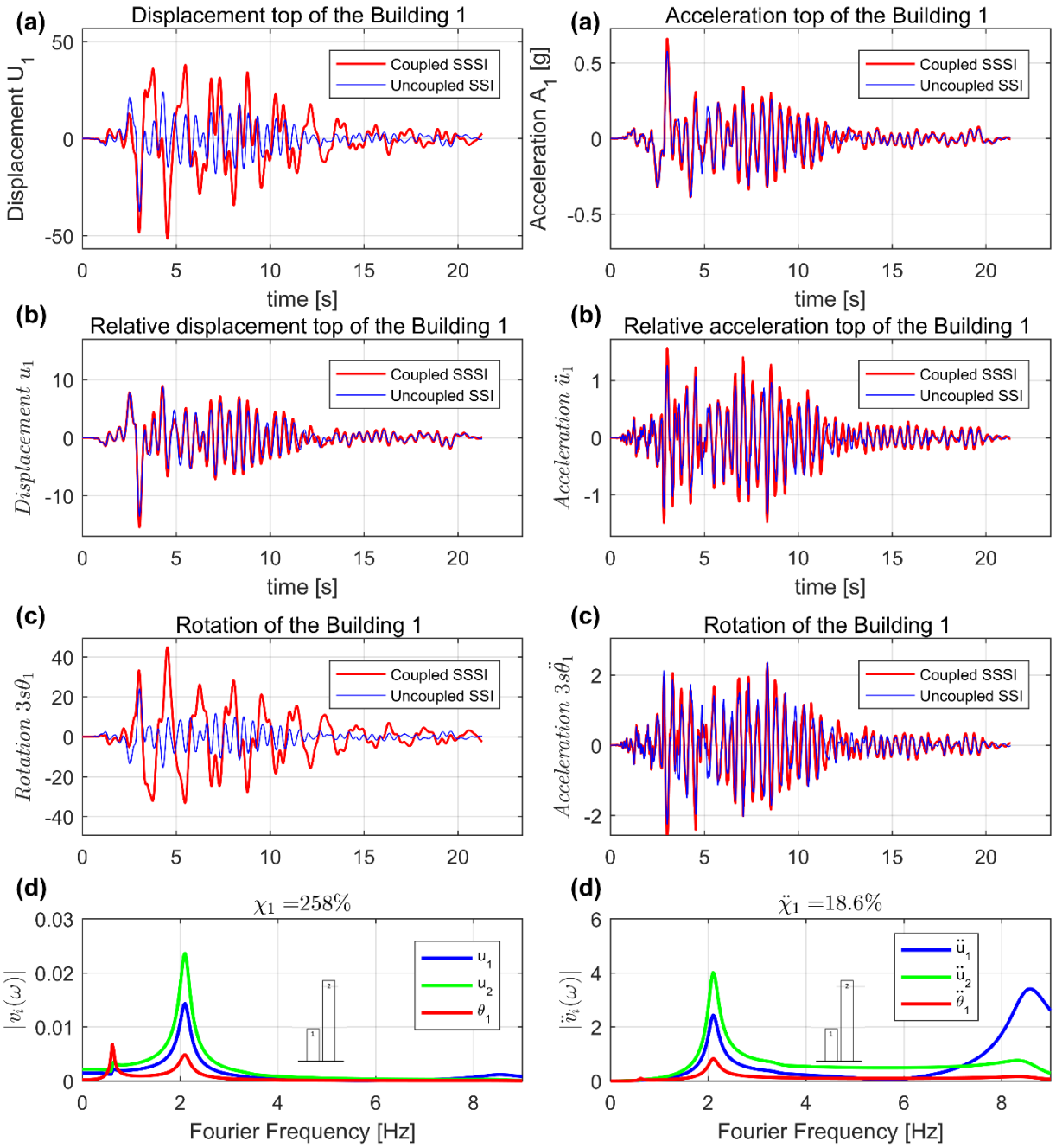

Figure 3.12 (a) Displacement and acceleration responses for the building 1, (b) Displacement and acceleration responses relative to the base, (c) Rotation and rotation acceleration (d) Transfer function for individual DOFs in SSSI case – Responses on loose soil for the parameter set (ε = 2.5, s = 2.6, ζ = 0.1)

3.3.3 Change in power for loose soil due to the variation in aspect ratio s and height ratio ε

Now the error in the total power of building 1 for the displacement $\chi_1(s,\varepsilon)$ is analysed (defined in equation (3-24)) and for the acceleration $\ddot{\chi}_1(s,\varepsilon)$ (defined in equation (3-26)). This error, i.e. difference term between the responses, would be zero if there was no difference between the coupled (SSSI) and uncoupled (SSI) analyses.

The variation of error in power, with the height ratio $\varepsilon = h_2/h_1$ varying between 0.5 and 3, and the aspect ratio $s = h_1/b$ varying between 0.5 and 3, is plotted. The system presented in this section corresponds to the case when the two buildings are close together (inter-building distance of $\zeta = 0.1$) and for loose soil. The system is subjected to all earthquake events, classified by Far-Field (FF), Near-Field Without Pulse (NFWP) and Near-Field Pulse-Like (NFPL) record sets. For each of these record sets, the maximum value of maxima error (for these record sets), the mean error (for these record sets) and the standard deviation of the error (for these record sets) are presented.

Figure 3.13(a) displays the contour plots of variation of error $\chi_1(s,\varepsilon)$ for the displacement U_1 on top of building 1, for the Far-Field records set. Figure 3.13 contains the results of 460,000 different time-histories analyses. It is employed University of Bristol's supercomputer, BlueCrystal, for these simulations and required approximately 2 hours run-time. The critical zones in the figure are in red, i.e. where the total response power of building 1 is amplified by the presence of building 2. Blue indicates when the response power is reduced. With the aim of making the figure more readable, the change in the colour contour is shown up to a value of 90%, and for larger values only the contour line is marked. For height ratios greater than 1, i.e. when adjacent buildings are taller, the response of building 1 is amplified. The maximum increase in total displacement power response occurred when the structure configuration lies around $\chi_1(2.6,1.1) = 110\%$ (the second building is 10% taller than building 1), and when the height ratio is greater than 2, with a maximum amplification of 150%. On average, the amplification reaches a value of 20% and a standard deviation of 15%. Thus, a very similar trend is observed on the change in power for all FF earthquakes for the whole range of parameters.

Figure 3.13(b) displays the contour plots of variation of error in power $\ddot{\chi}_1(s,\varepsilon)$ (i.e. the error in using SSI analysis for a coupled building scenario) for the acceleration A_1, considering the top of building 1 and FF records set. As with the displacement, for height ratios greater than 1 the response of building 1 is amplified. The maximum increase in total acceleration power response occurred when the building parametric configuration lies around $\ddot{\chi}_1(2.5,1.1) = 110\%$ and its average is approximately $\ddot{\chi}_1(\mathrm{s},1.1) = 40\%$. The dispersion of the values is small, with a maximum of 40%, for the whole range of analysed parameters.

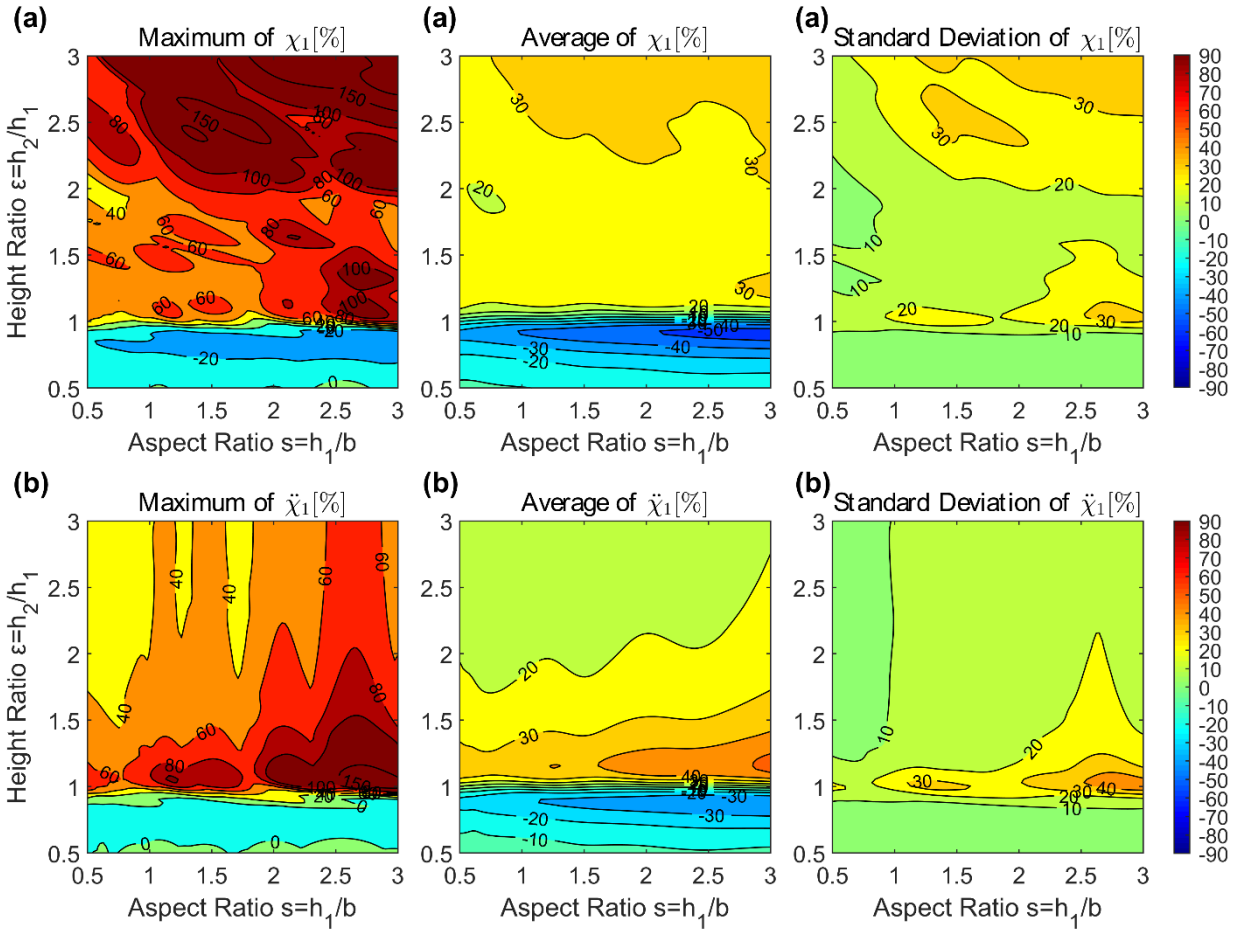

Figure 3.13 Maximum value, average and standard deviation for change in (a) Displacement power $\chi_1(s,\varepsilon)$ and (b) Acceleration power $\ddot{x}_1(s,\varepsilon)$ for the building 1 with the variation in aspect ratio s and height ratio ε - Response on loose soil and inter-building distance ζ = 0.1 for Far-Field records set

Figure 3.14(a) displays the contour plots of variation of error in power $\chi_1(s,\varepsilon)$ for the displacement U_1 considering the Near-Field Pulse-Like records set. Again in Figure 3.14 and Figure 3.15 contain the result of 560,000 different time-histories analyses. For that, it required approximately 2.5 hours run-time on BlueCrystal. Unlike Figure 3.13(a), there is a significant amplification in the displacement when the height ratio is greater than 2.0, reaching values above $\chi_1 = 400\%$ of amplification.

Figure 3.14(b) displays the contour plots of variation of change in power $\ddot{\chi}_1(s,\varepsilon)$ for the acceleration A_1, for NFPL records set. As with the FF records set, the maximum increase in total acceleration power response occurred when the structure configuration lies around $\chi_1(2.6,1.1) = 110\%$. The dispersion of the values is small, with a maximum of 30%, for the whole range of analysed parameters. However, unlike the results shown in Figure 3.13(a) and Figure 3.14(a), the variation of power for the acceleration decreases as the height ratio increases. This is because the response accelerations are not susceptible to low-frequency content, as shown in Figure 3.6(b). On the other hand, the displacement responses are susceptible to low-frequency content, as exemplified by the peak produced in the power spectral density in Figure 3.8(b),

especially when the height ratio is greater than 2 (the taller building 2 has an important influence on building 1).

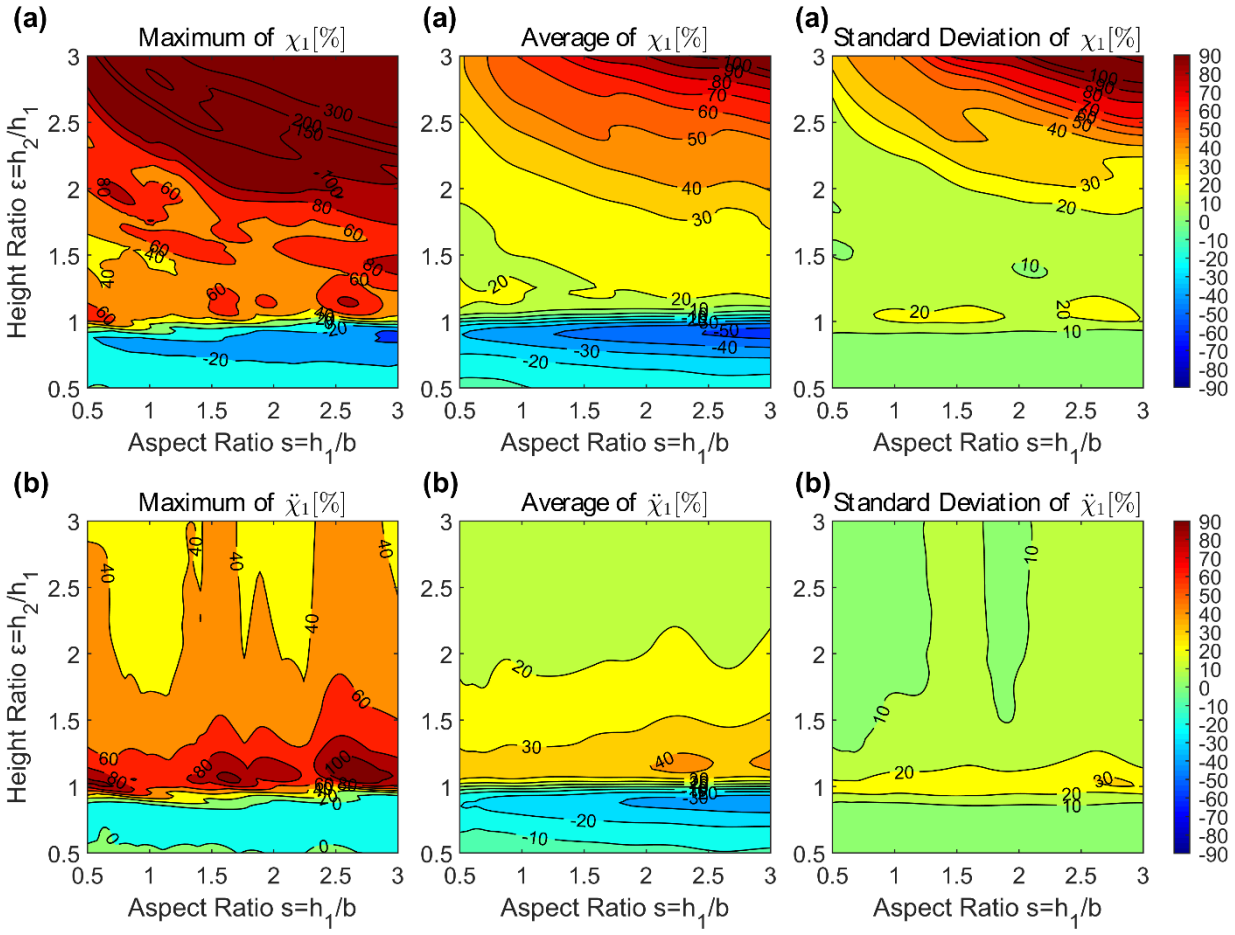

Figure 3.14 Maximum value, average and standard deviation for change in (a) Displacement power $\chi_1(s,\varepsilon)$ and (b) Acceleration power $\ddot{x}_1(s,\varepsilon)$ for the building 1 with the variation in aspect ratio s and height ratio ε - Response on loose soil and inter-building distance ζ = 0.1 for Near-Field Pulse-Like records set

Figure 3.15 shows the variation of error in power for the displacement U_1 and acceleration A_1 considering Near-Field Without Pulse records. In general, the behaviour of NFPL and NFWP earthquakes follows a similar pattern for maximum values, averages, and standard deviation. Comparing the Far-Field and Near-Field earthquakes, the contour plots suggest that the low-frequency content of the earthquake (especially for Near-Field records) can affect the size of adverse SSSI effects, especially for displacement responses when the height ratio is greater than 2.0.

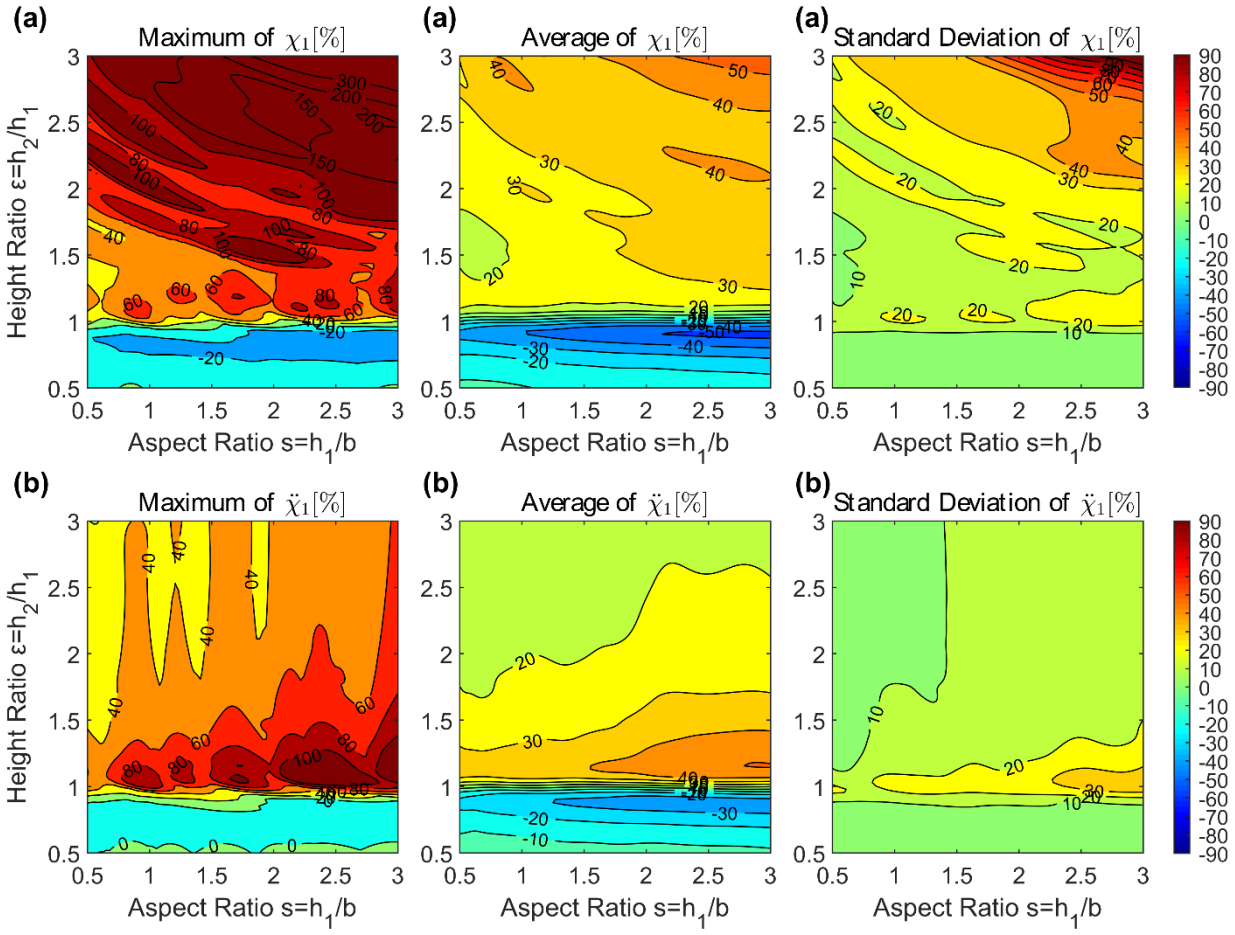

Figure 3.15 Maximum value, average and standard deviation for change in (a) Displacement power $\chi_1(s,\varepsilon)$ and (b) Acceleration power $\ddot{x}_1(s,\varepsilon)$ for the building 1 with the variation in aspect ratio s and height ratio ε - Response on loose soil and inter-building distance ζ = 0.1 for Near-Field Without-Pulse records set

Figure 3.16 depicts the power spectral density estimate of all earthquakes and the average for FF, NFPL and NFWP records sets. It is observed that on average, the Near-Field records set has a larger average low-frequency content (Fourier frequency between 0.01Hz and 1Hz). This larger low-frequency content results in more significant responses in displacements (through a 'rigid body rocking mode' in the smaller building) when a small building is adjacent to a tall building.

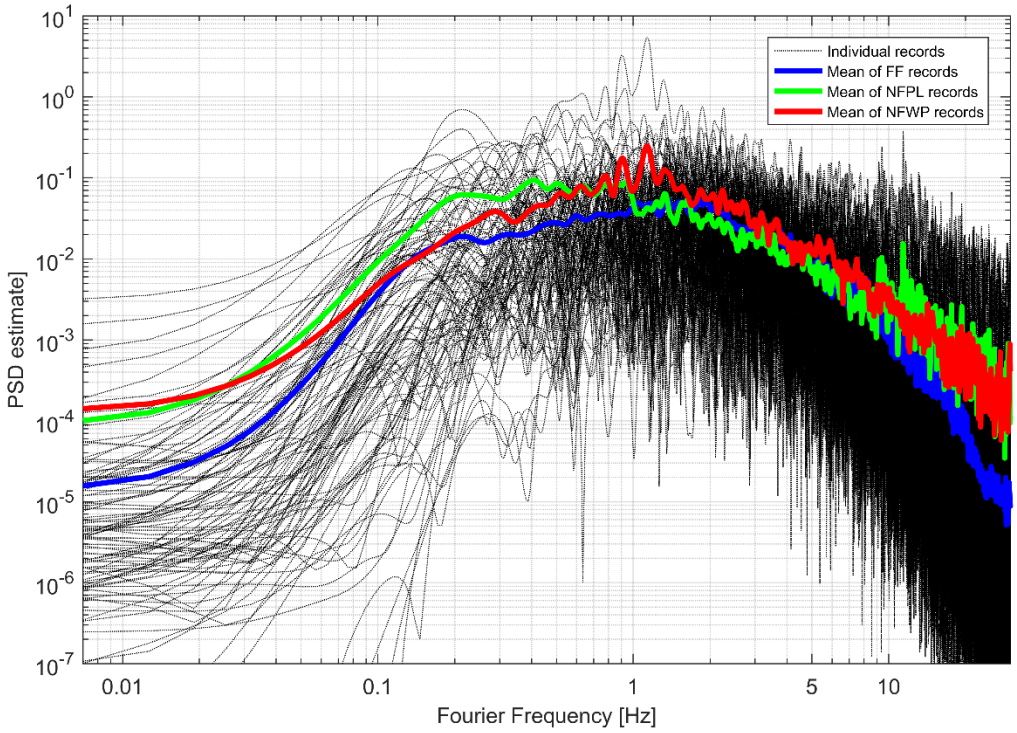

Figure 3.16 Power spectral density estimate for the ground acceleration records

3.3.4 Change in power for dense soil due to variation in aspect ratio s and height ratio ε

Figure 3.17 displays the previous analysis for the case of dense sand and the three types of ground motions plotted together. Figure 3.17 and Figure 3.18, contain more than 2 million different time-histories analyses. In this case, the amplifications or reductions in the change of power are more limited, $\chi_1(2.6,2.5) = 110\%$ and $\ddot{\chi}_1(2.8,1.1) = 60\%$ in the displacement and acceleration respectively. Therefore, the worst seismic interaction condition occurs on loose soil, as reported previously by Alexander et al. (2013), Aldaikh et al. (2015), and Aldaikh et al. (2016).

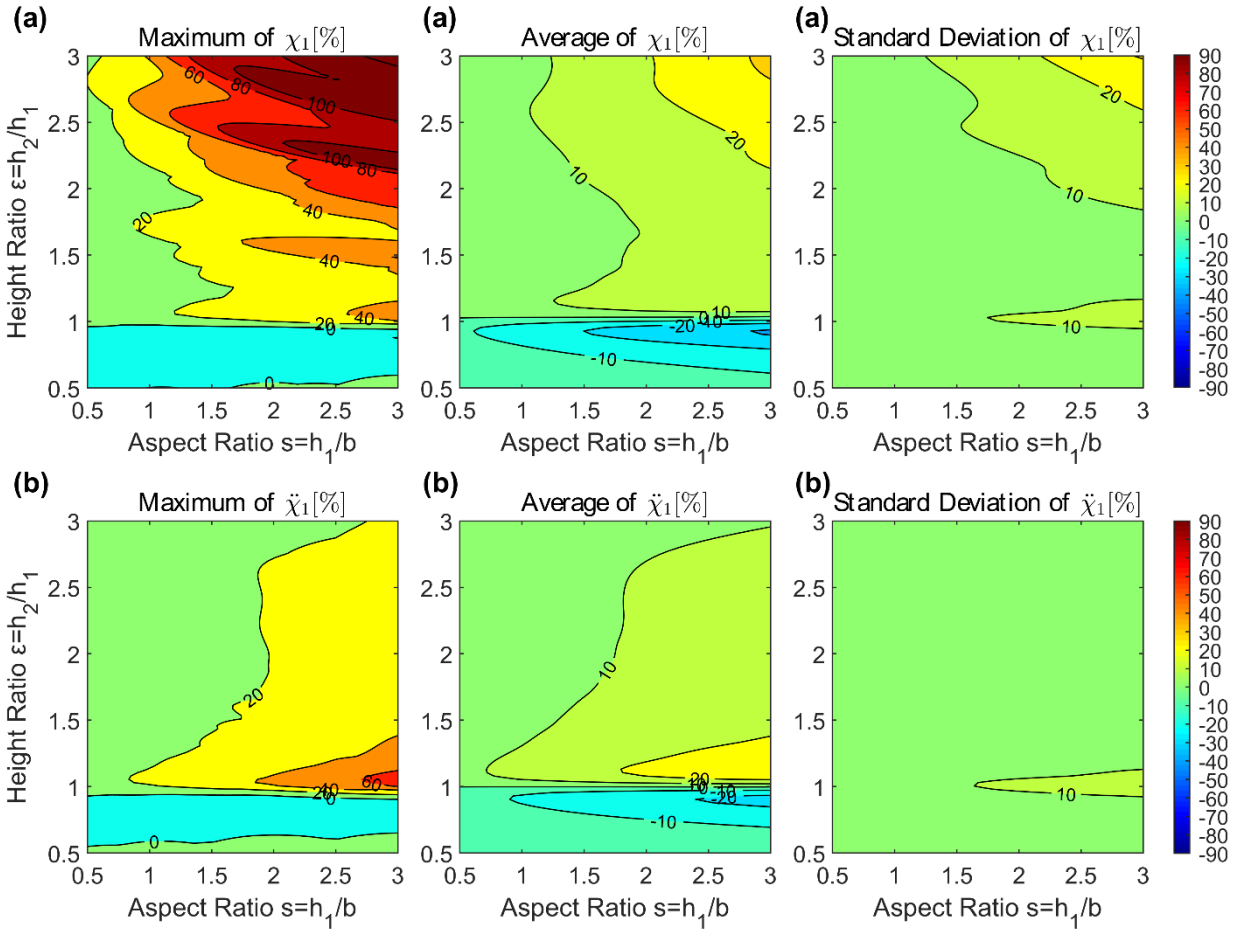

Figure 3.17 Maximum value, average and standard deviation for change in (a) Displacement power $\chi_1(s,\varepsilon)$ and (b) Acceleration power $\ddot{x}_1(s,\varepsilon)$ for the building 1 with the variation in aspect ratio s and height ratio ε - Response on dense soil and inter-building distance ζ = 0.1 under all ground motion records set

3.3.5 Change in power for loose soil due to variation in height ratio ε and inter-building distance ζ

Figure 3.18(a) shows the variation of power $\chi_1(s,\varepsilon,\zeta)$ for the displacement with height ratio $\varepsilon = h_2/h_1$ varying between 0.5 and 3, and inter-building distance ζ varying between 0.1 and 3. It is considered that the three types of ground motions plotted together. The aspect ratio was set equal to $s = h_1/b = 2.0$. As expected, the effects of SSSI decrease when increasing the inter-building distance, being practically negligible, i.e $\chi_1(2.0,\varepsilon,2.0) = 3.5\%$, for a distance between foundations greater or equal to $2b$. Figure 3.18(b) repeats the previous analysis for the change in power $\ddot{\chi}_1(s,\varepsilon,z)$ in the acceleration and similarly, the interaction effect drops to a value of $\ddot{\chi}_1(2.0,\varepsilon,2.0) = 2.8\%$ when increasing the inter-building distance.

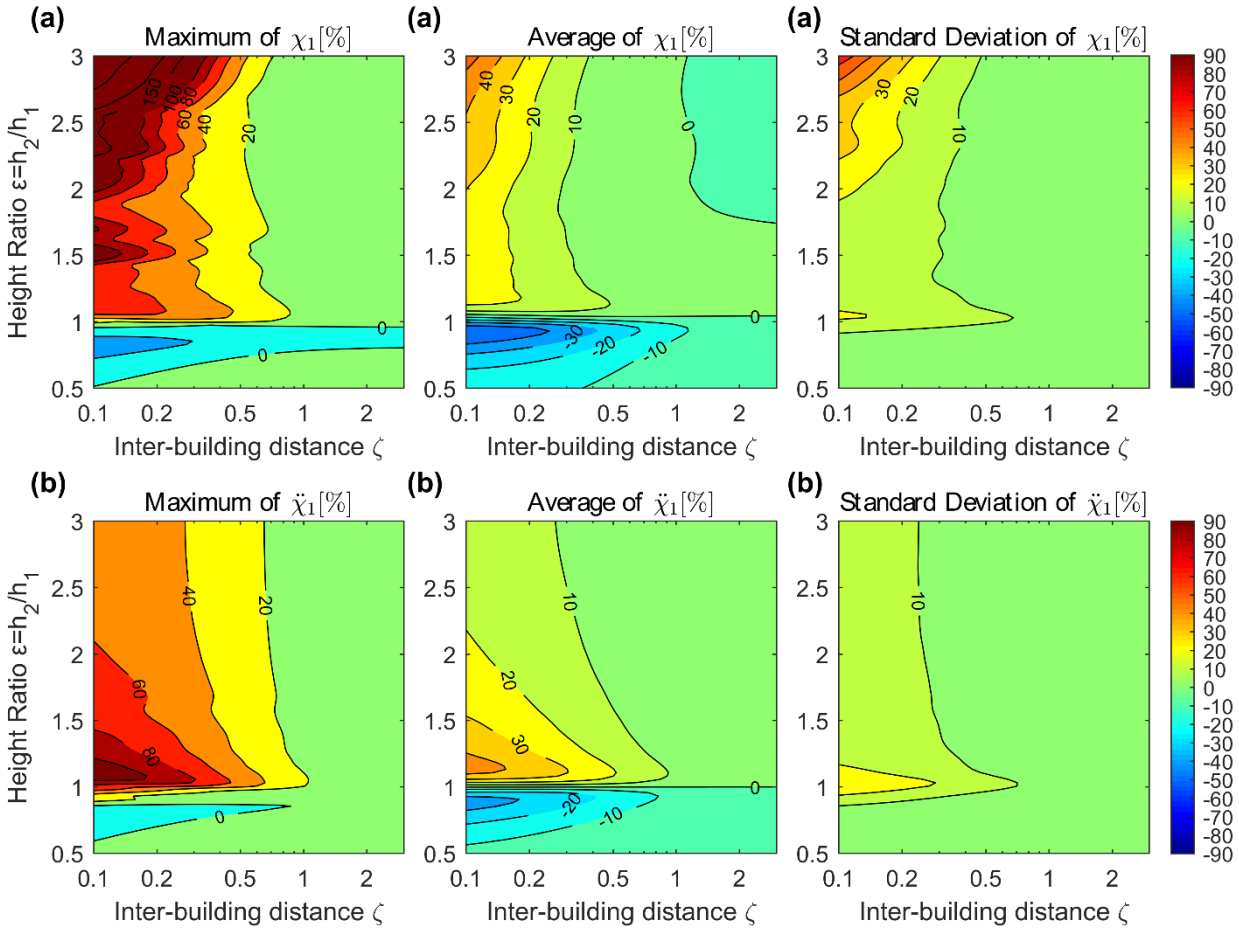

Figure 3.18 Maximum value, average and standard deviation for change in (a) Displacement power $\chi_1(\varepsilon,\zeta)$ and (b) Acceleration power $\ddot{x}_1(\varepsilon,\zeta)$ for the building 1 with the variation in height ratio ε and inter-building distance ζ - Response on loose soil and aspect ratio s = 2.0 under all ground motion records set

3.4 Summary

In this chapter, a theoretical formulation, which is a reduced-order model, for the 2D Structure-Soil-Structure interaction between two buildings that are coupled through the soil is presented. Three types of ground motion sets were considered (Far-Field, Near-Field Without Pulse and Near-Field Pulse-Like records sets), selected from FEMA P695. It is shown that the complexity of the analysis is high due to a large number of system parameters, even for this reduced-order model. Hence, a series of reasonable assumptions have been made to further reduce the amount of system parameters. The parametric exploration undertaken in this chapter explores the system response behaviour for an extensive range of buildings, inter-building distance, soil type, as well as ground motion excitations. These dynamic simulations involve over 3.1 million unique time-history analyses. It should be noted that the reduced order SSSI model was previously calibrated and validated with (i) Finite Element Analyses (Alexander et al., 2013), (ii) physical experimental test using the University of Bristol's shaking table (Aldaikh et al., 2015;

Aldaikh et al., 2016), the University of Dundee's centrifuge (Knappett et al., 2015), and (iii) an analytical formulation derived from a Boussinesq deformation field of an elastic half-space (Aldaikh et al., 2018).

The research presented in this chapter has led to the following principal findings:

- The linear SSSI parametric study showed that there are detrimental and beneficial configurations for the dynamic characteristics of buildings. Regardless of the earthquake event (FF, NFWP or NFPL), it is found that the effect of interaction is unfavourable for building 1 when building 2 is taller: i.e. the power of the earthquake passed from the taller structure to the smaller structure.

- For the displacement responses, there is an increase in the response of up to $\chi_1 = 400\%$, when there is a large difference in height (height ratio $\varepsilon = h_2/h_1 > 2.0$) between the buildings. This result was not observed in previous studies (Alexander et al., 2013; Aldaikh et al., 2015; Aldaikh et al., 2016). This significant amplification in the displacement is due to the taller building imposing a low frequency 'rigid body rocking mode' on the smaller building. If this behaviour is combined with ground motions that have a more substantial low-frequency content (i.e. the near field records), then there is a significant error in using SSI analyses rather than SSSI analyses for these cases.

- In the case of the acceleration responses, the greatest amplifications, of up to $\ddot{\chi}_1 = 120\%$, are observed for height ratio approximately of $\varepsilon = h_2/h_1 = 1.1$ (i.e. buildings of 10% difference in height). This finding confirms the results of previous studies (Alexander et al., 2013; Aldaikh et al., 2015) with a 4 DOFs model and artificial ground motion records.

- Results also indicated that there is a beneficial geometric configuration ($\varepsilon = h_2/h_1 < 1.0$) where the seismic risk is reduced in building 1 by the presence of a smaller building 2. A maximum reduction of $\chi_1 = -55\%$ and $\ddot{\chi}_1 = -35\%$ for the displacements and accelerations respectively are observed. Both adverse and beneficial effects diminish as (i) building spacing increases and as (ii) the soil stiffness increases.

- Results obtained from this 6 DOFs model suggest that the introduction of two additional DOFs (i.e. extending the 4 DOFs model presented by Alexander et al. (2013) to the 6 DOFs model developed here) can affect the size of interaction between the buildings. In this case, the 6 DOFs model permits the interaction of the second sway mode of a much taller building with the first sway mode of a shorter building of less than half its height. This indicates that modal coupling is possible between more than just the primary modes of each building and therefore suggests a significant interaction between a taller building 1 and much shorter building 2. This result cannot be observed in the 4dof model where the most significant interactions occur when the heights of the buildings are within 10% of each other (Alexander et al., 2013; Aldaikh et al., 2015). This

raises the question as to whether there is a possible interaction between first and third building sway modes, second and third building sway modes, etc. Mathematically, these interactions are permissible with a reduced-order model that has a sufficiently large number of DOFs, and an appropriate set of system parameters. However, it should be noted that these interactions are likely to be less significant because the modal participation factor for higher modes is much smaller than for the primary modes.

- Finally, there is evidence to suggest that the ground motion type can affect linear SSSI behaviour. The SSSI displacement responses do not follow the same trend as acceleration responses, and the introduction of the higher mode model does help to capture the SSSI behaviour in the case of a small building adjacent to a tall building.

3.5 Nomenclature

The units correspond to those defined by the International System of Units, where the abbreviations represent [M] mass, [T] time, [L] length and [rad] radians.

α_1, α_2	Ratios of soil/foundation to building masses of the buildings 1 and 2 respectively []
β	Ratio of soil/foundation radii of gyration (building 1 to 2) []
ε	Height ratio between the buildings 2 to 1 []
η_1, η_2	Height to the radius of gyration ratios for the buildings 1 and 2 respectively []
θ_1, θ_2	Rotational degrees of freedom at the base of the buildings 1 and 2 respectively []
κ	Inter-building soil rotational spring between the buildings 1 and 2 [ML^2T^{-2}]
λ	Ratio of building 2 to building 1 mass (square of the radii of gyration) []
μ_s	Poison's ratio of the soil []
ξ_n	Ratio of critical damping of the system []
ρ_b, ρ_s	Average densities of the buildings and the soil respectively [ML^{-3}]
τ	Scaled time []
$\boldsymbol{\phi}_n$	Modal eigenvector of the linear system for the mode "n" []
χ_j	Change in displacement power when moving from uncoupled to coupled state for the building *j* [%]
$\ddot{\chi}_j$	Change in acceleration power when moving from uncoupled to coupled state for the building *j* [%]
$\omega_{rb1}, \omega_{rb2}$	First and second modal circular frequencies on a rigid base for the building 1 respectively [$radT^{-1}$]
ω_{b1}, ω_{b2}	Modal circular frequency parameters for the buildings 1 and 2 respectively [$radT^{-1}$]
ω_{s1}, ω_{s2}	Circular frequencies of soil/foundation for the buildings 1 and 2 respectively [$radT^{-1}$]
ω	Fourier frequency [$radT^{-1}$]
ω_n	Natural frequencies of the linear system [$radT^{-1}$]
ϖ	Interaction circular frequency ratio parameter [$radT^{-1}$]
Ω_0	Ratio of interaction frequency parameter to building 1 (ω_{b1}) circular frequency []
Ω_b	Ratio of building 2 (ω_{b2}) to building 1 (ω_{b1}) circular frequencies []
Ω_{s1}	Ratio of building 1 soil/foundation to building 1 (ω_{b1}) circular frequencies []
Ω_{s2}	Ratio of building 2 soil/foundation to building 1 (ω_{b1}) circular frequencies []
A_1, A_2	Total acceleration on top of the buildings 1 and 2 respectively []
b_1, b_2	Foundation widths for the buildings 1 and 2 respectively [L]
$\mathbf{C}$	Non-dimensional damping matrix of the system []
$\hat{\mathbf{C}}$	Dimensional damping matrix of the system [MT^{-1}]
c_1	Density ratio (soil/buildings) parametric constant []
c_2	Soil parametric constant []

E_s	Total power spectral density []
G_s	Shear modulus of the soil [$ML^{-1}T^{-2}$]
h_1, h_2	Total heights of the buildings 1 and 2 respectively [L]
$\mathbf{K}$	Non-dimensional stiffness matrix of the system []
$\widehat{\mathbf{K}}$	Dimensional stiffness matrix of the system [MT^{-2}]
k_s	Soil/foundation rotational stiffness in absence of buildings interaction [ML^2T^{-2}]
k_{b1}, k_{b2}	Lateral modal stiffnesses of buildings 1 and 2 respectively [MT^{-2}]
k_{s1}, k_{s2}	Rotational soil stiffnesses of the soil beneath the buildings 1 and 2 respectively [ML^2T^{-2}]
$\mathbf{M}$	Non-dimensional mass matrix of the system []
$\widehat{\mathbf{M}}$	Dimensional mass matrix of the system [M]
M_w	Moment magnitude scale of the earthquake
m_{b1}, m_{b2}	Total modal masses of the buildings 1 and 2 respectively [M]
m_{s1}, m_{s2}	Soil/foundation masses of the buildings 1 and 2 respectively [M]
n_s	Number of storeys of the buildings []
$\mathbf{p}$	Non-dimensional force vector of the system []
$\widehat{\mathbf{p}}$	Dimensional force vector of the system [M]
PGA	Peak ground acceleration [LT^{-2}]
q_2, q_κ	Interaction functions that depend on the inter-building distance ζ []
r_1, r_2	Soil/foundation mass radius of gyration for the buildings 1 and 2 respectively [L]
s	Aspect ratio. Height to width ratio of the building 1 []
T_E	System kinematic energy [ML^2T^{-2}]
T_x	Fundamental period of the structure on a rigid foundation [T]
t	Time [T]
U_1, U_2	Total displacements on top of buildings 1 and 2 respectively []
U_E	System potential energy [ML^2T^{-2}]
$U_j(\omega)$	Fourier transform of $U_j(\tau)$
u_1, u_2	Non-dimensional relative displacement to ground of the building 1 []
u_3, u_4	Non-dimensional relative displacement to ground of the building 2 []
u_g	Non-dimensional horizontal ground displacement time series []
$\ddot{u}_g$	Non-dimensional acceleration ground motion []
$\mathbf{u}$	Non-dimensional degrees of freedom (vector) of the system []
V_s	Shear wave velocity of the soil [LT^{-1}]
$\bar{V}_s$	Normalised shear wave velocity of the soil []
$\mathbf{v}_{b1}(\omega)$	Displacement transfer function for the building 1 []
$\mathbf{v}_{b2}(\omega)$	Displacement transfer function for the building 2 []

$\ddot{\mathbf{v}}_{b1}(\omega)$	Acceleration transfer function for the building 1 []
$\ddot{\mathbf{v}}_{b2}(\omega)$	Acceleration transfer function for the building 2 []
x_1, x_2	Horizontal displacement (degrees of freedom) of the building 1 [L]
x_3, x_4	Horizontal displacement (degrees of freedom) of the building 2 [L]
x_g	Horizontal ground displacement time series [L]
$\ddot{x}_g$	Horizontal acceleration ground motion [LT^{-2}]
$\mathbf{x}$	Degrees of freedom (vector) of the system [L]
ζ	Inter-building distance coefficient []

Chapter 4

Dynamic Structure-Soil-Structure Interaction in unsymmetrical plan buildings due to seismic excitation

---

The contents of this chapter have been adapted from that published in:

Vicencio, F., and Alexander, N.A. (2019b). Dynamic Structure-Soil-Structure Interaction in unsymmetrical plan buildings due to seismic excitation. *Soil Dynamics and Earthquake Engineering*, 127, 105817.

Part of the introduction has been removed and included in Chapter 2 - Literature Review.

4.1 Introduction to unsymmetrical plan buildings

During an earthquake, torsional deformation about the vertical axis in buildings can result from a variety of sources, such as asymmetric building geometry or accidental eccentricity due to discrepancies between the mass, stiffness and strength distribution used in the analysis. Many building codes, such as ASCE/SEI 7 (2005), the Eurocode 8 EN-1998 (2004), and the Chilean Code NCh 433 (2009), require that the effects on torsion be considered by applying the equivalent lateral forces at a distance e from the centre of stiffness (CS). This results in storey torques and non-uniform displacements that are additional to the shear forces and overturning moments usually considered. Many studies have focused on understanding the change in buildings' responses that arise from building asymmetry, by (i) linear models (for example the studies of Hejal and Chopra (1989) and De la Llera and Chopra (1995b)), (ii) simplified single-story models (e.g. the research of Syamal (1985)), and (iii) lumped plasticity nonlinear frame models (e.g. De la Llera and Chopra (1995a) and Stathopoulos and Anagnostopoulos (2010)). For a more detailed literature review, please see the paper of De Stefano and Pintucchi (2002). Although these works are an essential step in trying to understand the behaviour of asymmetric systems, they do not take into consideration the SSSI effects between buildings. So, more research on the topic of SSSI in unsymmetrical buildings is needed.

4.1.1 Aims

This chapter aims to introduce a reduced-order mathematical formulation of the problem of an unsymmetrical-plan building that is coupled with an adjacent building via the underlying soil. This two-dimensional reduced-order modelling has some advantages over the Finite Element Analysis in the context of a large parametric exploration of the problem. The rotational interaction-springs used in this chapter were calibrated and validated with Finite Element Analysis (Alexander et al., 2013), shake table tests (Aldaikh et al., 2015; Aldaikh et al., 2016), centrifuge tests (Knappett et al., 2015), and matched closed-form analytical expressions (Aldaikh et al., 2018). The code used in this study was developed in MATLAB (2016). There are of the order of 3.2 million different full time-histories analyses in this chapter. For this, it was used BlueCrystal, the High-Performance Computing (HPC) machine (the Advance computing research centre at the University of Bristol). 50 different real ground motions, recorded from 15 events that occurred between 1971 and 2007 in different parts of the world (FEMA P695, 2009) are employed. These records have differences in amplitude, duration, envelope shape, and power spectral content. Due to the two-dimensional nature of the model used, only one of the horizontal components of seismic excitation is considered.

The objectives of this chapter are to answer the following questions.

(i) How significant is the SSSI problem on the seismic response of unsymmetrical-plan buildings?

(ii) In the previously published literature on symmetric-plan buildings (Alexander et al., 2013; Aldaikh et al., 2015) the taller adjacent building is subjected to beneficial SSSI while the shorter adjacent building is subjected to detrimental SSSI effects. Is this still true for unsymmetrical-plan adjacent buildings?

(iii) Do torsionally-stiff and torsionally-flexible structures behave differently in their SSSI responses?

(iv) Do buildings with small and large statical eccentricities behave differently in their SSSI responses?

4.2 Discrete reduced-order model for asymmetric-plan buildings including SSSI

4.2.1 Equations of motion of the coupled system

Consider the following system shown in Figure 4.1 and Figure 4.2. It is a pair of buildings coupled by a rotational (about the y-axis) ground spring k_{y12} and separated by an inter-building distance of ζb, where b is the foundations' width. The system is idealised as single-storey buildings consisting of a rigid roof diaphragm, where all the system mass is lumped at the top. The lateral resistance is provided by vertically rigid structural elements located along resisting planes in the *x* and *y* directions (as shown in the building plan Figure 4.3). These resisting planes may have different stiffnesses in the *y*-direction and may be unsymmetrically located about the *x*-axis, creating an eccentricity *e* between the centre of mass (CM) and the centre of stiffness (CS) of the building 1 (depicted on Figure 4.1 and Figure 4.3). On the other hand, the second building considered in this study is symmetric about the *x*-axis and *y*-axis (namely symmetric Building 2).

The dynamic response of the system to earthquake ground acceleration in the *x*-direction is described by five degrees of freedom (DOFs). The soil/foundation system of each building has one rotational DOF at the foundation level, called θ_{y1} and θ_{y2} for the building 1 and 2, respectively. The first building's super-structure is described by two DOFs: the translational displacement x_1 of the CM along the *x*-direction, and the rotation of the rigid diaphragm θ_{z1}. The second building's super-structure is described by one translational DOF x_2. A known ground displacement x_g is applied at both foundations, i.e. wave passage effects and spatially heterogeneous ground displacement are neglected in the present work. The vertical soil spring support is not included in this study since it is not significant in the seismic response of the structure when the SSSI is considered (Alexander et al., 2013; Aldaikh et al., 2015). Building pounding is not permitted as inter-building spacing is assumed large enough to avoid pounding. The torsional coupling spring between the two structures is not considered mainly because its influence in the seismic response is

not relevant in the SSSI problem, Mulliken and Karabalis (1998). In the same way, the torsional springs for the foundations are neglected since its stiffness are larger, compared with the rocking springs, and so produces smaller torsional rotation during the seismic movement i.e. the SSSI effects diminishes rapidly as the interbuilding distances increases.

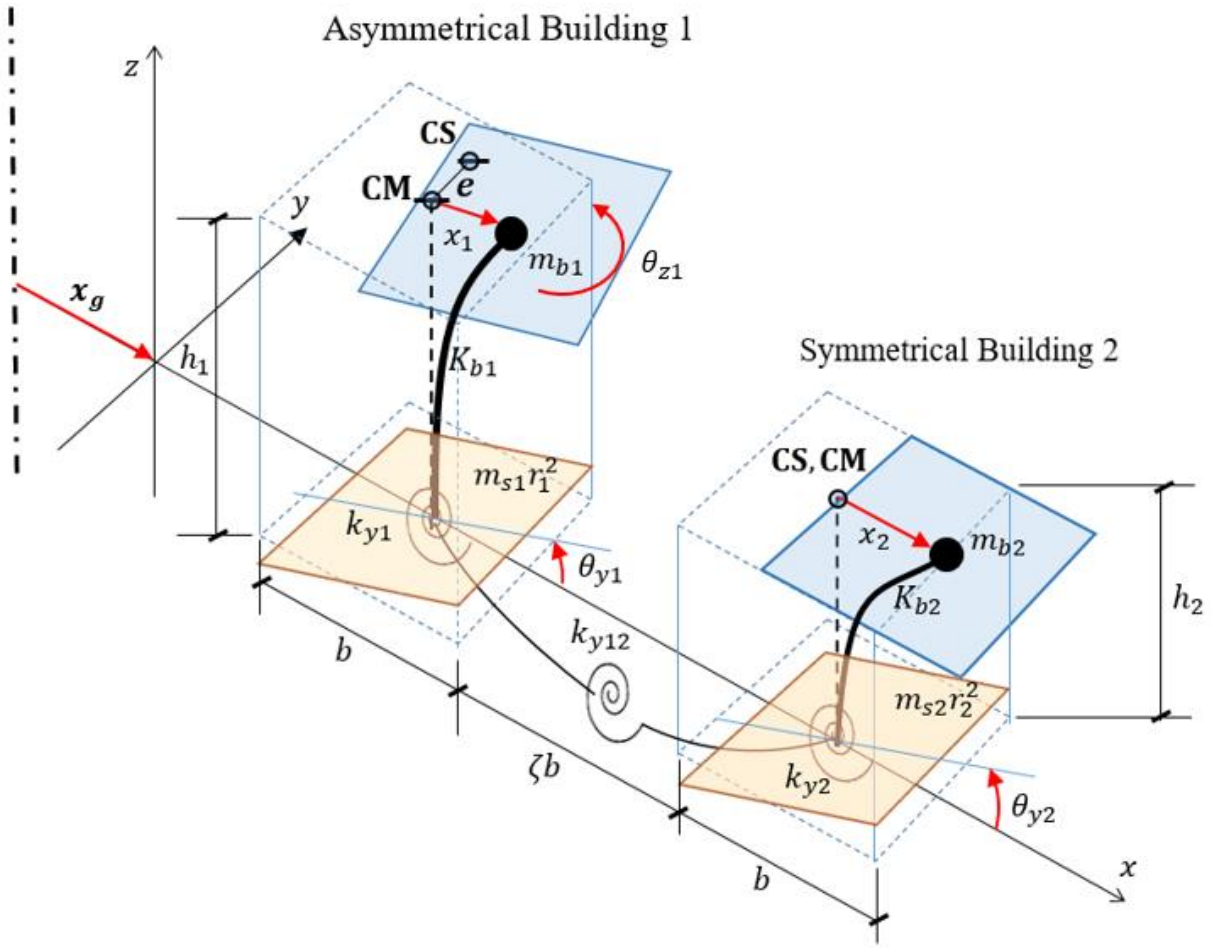

Figure 4.1 Two building SSSI model for asymmetrical-symmetrical case

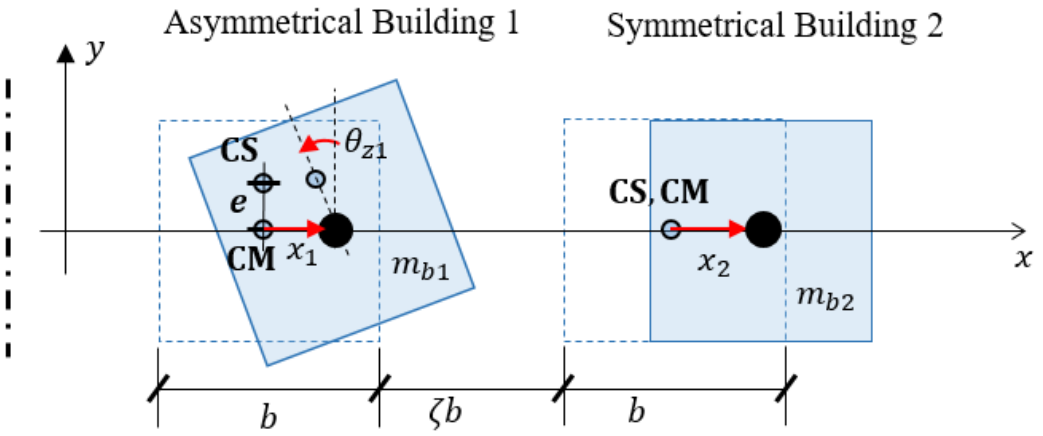

Figure 4.2 Lateral-torsional displacement of asymmetrical-symmetrical case – Plan view from above

Employing Lagrangian energy mechanics, the equation of motion describing the dynamics of the discretised system is formulated. The kinetic energy T_E and potential energy U_E for this system are written in equations (4-1) and (4-2) respectively. The total kinetic energy can be specified as the sum of (i) translational kinetic energy (due to sway and foundation rotation) of each building's mass, (ii) the rotational torsion energy of building 1 and (iii) the rotational energies of each soil/foundation mass. The potential energy is the sum of (i) internal work due to buildings' deformation, (ii) rotation of the foundation springs underneath the buildings, and (iii) the differential rotation between buildings.

$$T_E = \frac{1}{2}\left(m_{b1}\left(\dot{x}_1 + \dot{x}_g - h_1\dot{\theta}_{y1}\right)^2 + m_{b1}r_{z1}^2\dot{\theta}_{z1}^2 + m_{s1}r_1^2\dot{\theta}_{y1}^2\right) + \cdots + \frac{1}{2}\left(m_{b2}\left(\dot{x}_2 + \dot{x}_g - h_2\dot{\theta}_{y2}\right)^2 + m_{s2}r_2^2\dot{\theta}_{y2}^2\right) \quad \textbf{(4-1)}$$

$$U_E = \frac{1}{2}\left(K_{b1}(x_1 - e\theta_{z1})^2 + K_{\theta R}\theta_{z1}^2 + k_{y1}\theta_{y1}^2\right) + \frac{1}{2}\left(K_{b2}x_2^2 + k_{y2}\theta_{y2}^2\right) + \frac{1}{2}k_{y12}\left(\theta_{y2} - \theta_{y1}\right)^2 \quad \textbf{(4-2)}$$

where h_1 and h_2 are the heights and m_{b1} and m_{b2} are the total lumped masses of the buildings 1 and 2, respectively. m_{s1} and m_{s2} are the soil/foundation masses, and $m_{s1}r_1^2$ and $m_{s2}r_2^2$ are the soil/foundation mass polar second moments of area (moments of inertia) underneath the buildings 1 and 2 respectively. r_1 and r_2 are the soil/foundation masses radius of gyration of the buildings 1 and 2, r_{z1} is the radius of gyration of the system plan about a vertical axis passing through the CM of the building 1, and b is the foundation's width. The terms k_{y1} and k_{y2} are the rotational stiffnesses of the soil/foundation of the buildings 1 and 2, respectively.

The total lateral stiffness K_{b1} of building 1, the torsional stiffness K_θ of building 1 with respect to the CM, and the torsional stiffness $K_{\theta R}$ of building 1 with respect to the CS are defined in equation (4-3). The static eccentricity e of building 1 is defined in equation (4-4). As shown in the building 1 floor-plan (Figure 4.3), the *i*th resisting element in the *x*-direction has stiffness $\bar{k}_{xi}$ and is located at distance $\bar{y}_i$ from the CM of the building 1. In the same way, in the *y*-direction the *i*th resisting element has stiffness $\bar{k}_{yi}$ and is located at distance $\bar{x}_i$ from the CM of the building 1. The number of resisting elements in the *x* and *y* directions are N_x and N_y, respectively.

$$K_{b1} = \sum_{i=1}^{N_x}\bar{k}_{xi}, \quad K_\theta = \sum_{i=1}^{N_x}\bar{k}_{xi}\,\bar{y}_i^2 + \sum_{i=1}^{N_y}\bar{k}_{yi}\,\bar{x}_i^2, \quad K_{\theta R} = K_\theta - K_{b1}e^2 \quad \textbf{(4-3)}$$

$$e = \frac{\sum_{i=1}^{N_x}\bar{k}_{xi}\,\bar{y}_i}{\sum_{i=1}^{N_x}\bar{k}_{xi}} \quad \textbf{(4-4)}$$

The Euler-Lagrange equation of motion describing the dynamics of the discretised system can be derived in the standard way by calculus and is written, in matrix form, as follows:

$$\widehat{\mathbf{M}}\ddot{\mathbf{x}} + \widehat{\mathbf{C}}\dot{\mathbf{x}} + \widehat{\mathbf{K}}\mathbf{x} = \widehat{\mathbf{p}}\ddot{x}_g \tag{4-5}$$

where the system matrices are defined as follows,

$$\widehat{\mathbf{M}} = \begin{bmatrix} m_{b1} & 0 & -h_1 m_{b1} & 0 & 0 \\ 0 & m_{b1} r_{z1}^2 & 0 & 0 & 0 \\ -h_1 m_{b1} & 0 & m_{b1} h_1^2 + m_{s1} r_1^2 & 0 & 0 \\ 0 & 0 & 0 & m_{b2} & -h_2 m_{b2} \\ 0 & 0 & 0 & -h_2 m_{b2} & m_{b2} h_2^2 + m_{s2} r_2^2 \end{bmatrix} \tag{4-6}$$

$$\widehat{\mathbf{K}} = \begin{bmatrix} K_{b1} & -eK_{b1} & 0 & 0 & 0 \\ -eK_{b1} & K_{\theta R} + K_{b1} e^2 & 0 & 0 & 0 \\ 0 & 0 & k_{y1} + k_{y12} & 0 & -k_{y12} \\ 0 & 0 & 0 & K_{b2} & 0 \\ 0 & 0 & -k_{y12} & 0 & k_{y2} + k_{y12} \end{bmatrix}, \quad \widehat{\mathbf{p}} = \begin{bmatrix} -m_{b1} \\ 0 \\ h_{b1} m_{b1} \\ -m_{b2} \\ h_{b2} m_{b2} \end{bmatrix}, \quad \mathbf{x} = \begin{bmatrix} x_1 \\ \theta_{z1} \\ \theta_{y1} \\ x_2 \\ \theta_{y2} \end{bmatrix} \tag{4-7}$$

The equation of motion (4-5) contains too many system parameters to explore a comprehensive parametric study. Hence, to reduce this number, the following assumptions are made, where the scope of the analysis is limited by assuming that:

(i) The same soil profile exists under both buildings; this means the rotational stiffnesses of the soil/foundation of buildings 1 and 2 are $k_{y1} = k_{y2} = k_y$.

(ii) Both buildings have a similar square plan area and raft foundations of b^2; this means the soil/foundation masses are $m_{s1} = m_{s2} = m_s$, and the soil/foundation masses radius of gyration are $r_1 = r_2 = r_s = 0.33b$.

(iii) Both buildings have the same average density of ρ_b.

(iv) The buildings are spaced at some arbitrary distance from each other ζb, where ζ is the non-dimensional inter-building separation distance.

Also, the following mass parameters α_1, α_2 and the aspect ratio s of the building 1 are introduced,

$$\alpha_1 = \frac{m_s}{m_{b1}}, \quad \alpha_2 = \frac{m_{b2}}{m_{b1}}, \quad s = \frac{h_1}{b} \tag{4-8}$$

where α_1 is the soil/foundation of buildings 1 and 2 to building mass ratios of building 1, and α_2 is the ratio between the building mass 2 to building mass 1. The frequency parameters are given as,

$$\omega_{b1}^2 = \frac{K_{b1}}{m_{b1}},\ \ \omega_{\theta}^2 = \frac{K_{\theta R}}{m_{b1} r_{z1}^2},\ \ \omega_s^2 = \frac{k_y}{m_s r_s^2},\ \ \omega_{b2}^2 = \frac{K_{b2}}{m_{b2}},\ \ \omega_{y12}^2 = \frac{k_{y12}}{m_{b1} r_s^2} \quad \textbf{(4-9)}$$

where ω_{b1} and ω_{b2} are the uncoupled lateral frequencies of the buildings 1 and 2 respectively (on a fixed base), ω_θ is the uncoupled torsional frequency of the building 1, and ω_{s} is the soil/foundation frequency parameter. The term ω_{y12} represents the interaction circular frequency ratio parameter. In the same way, the frequency ratio between the buildings Ω_b, and the non-dimensional frequency ratios Ω_θ, Ω_s, and Ω_{y12} normalised by ω_{b1} are introduced,

$$\Omega_b = \frac{\omega_{b1}}{\omega_{b2}},\quad \Omega_\theta = \frac{\omega_\theta}{\omega_{b1}},\quad \Omega_s = \frac{\omega_s}{\omega_{b1}},\quad \Omega_{y12} = \frac{\omega_{y12}}{\omega_{b1}} \quad \textbf{(4-10)}$$

The fundamental natural period of a structure T_x, on a rigid foundation (i.e. with no soil/foundation rotation, equivalent to $\theta_{y1} = \theta_{y2} = 0$), has been investigated by many researchers and it is summarised in the work of Crowley and Pinho (2010). For simplicity here, is adopt the approximate empirical relationship suggested in the Eurocode 8 EN-1998 (2004) for reinforced concrete moment resisting frames, where the fundamental natural period is defined as $T_x = \mathrm{C}_t \mathrm{h}_1^{3/4}$. The height of the building is taken in meters, and the dimensional factor C_t is equal to $C_t = 0.075[s\, m^{-0.75}]$. Note that the approach to estimating T_x variates compared to the simpler definition in Chapter 3, Chapter 5, and Chapter 7 ($T_x = h_1/32$) because here is not possible to produce a complete non-dimensionalisation of the system, and so the exponent of the height of the buildings $\mathrm{h}_1^{3/4}$ is not a limitation when defining the system parameters. The period has a relationship with the uncoupled lateral frequency of the building as $\omega_{b1} = 2\pi/T_x$. Therefore, the fundamental natural frequencies, on a rigid base, and the height ratio between the buildings results as,

$$\omega_{b1} \approx \frac{83.77}{h_1^{3/4}},\qquad \omega_{b2} \approx \frac{83.77}{h_2^{3/4}},\qquad \frac{h_2}{h_1} = \left(\frac{\omega_{b1}}{\omega_{b2}}\right)^{\frac{4}{3}} = \Omega_b^{4/3} \quad \textbf{(4-11)}$$

The torsional frequency of a structure ω_θ depends on the number and distribution of the resisting planes in the x and y directions. It is considered that each element of the system has the same stiffness $\bar{k}_x = \bar{k}_y = \bar{k}$, the separation between the elements is x_s, and $N_x = N_y$ is the number of elements in each direction (see Figure 4.3). The term $n = N_x/2$ (where $n \in \mathbb{N}$) is the number of grids each centred at CS. Hence, the total lateral stiffnesses K_x, K_y, and the lateral frequencies ω_{b1} can be defined as,

$$K_x = K_y = (2n)^2 \bar{k},\qquad \omega_x^2 = \omega_y^2 = \omega_{b1}^2 = (2n)^2 \frac{\bar{k}}{m} \quad \textbf{(4-12)}$$

The radius of gyration r_{z1} of the system plan about a vertical axis passing through the CM of the building 1 is defined in equation (4-13), where I_p is the polar moment of inertia of the building 1 and A is the plan area of the building 1.

$$r_{z1}^2 = \frac{I_p}{A} = \frac{(2n-1)^2}{6} x_s^2, \quad I_p = \frac{b^4}{6}, \quad A = b^2, \quad b = (2n-1)x_s \tag{4-13}$$

Therefore, the torsional stiffness K_θ is stated as follows,

$$K_\theta = k\sum\left(y_i^2 + x_i^2\right) = 2\bar{k}\left[\left(2(2n)\left(\frac{x_s}{2}\right)^2 + 2(2n)\left(\frac{3x_s}{2}\right)^2 + \cdots\right)\right] = 2\bar{k}x_s^2\left(\frac{4}{3}n^4 - \frac{1}{3}n^2\right) \tag{4-14}$$

Using the equations (4-9) and (4-10), the uncoupled torsional frequency ω_θ can be calculated as follows,

$$\omega_\theta^2 = \frac{K_{\theta R}}{m_{b1}r_{z1}^2} = \frac{K_\theta - K_{b1}e^2}{m_{b1}r_{z1}^2} = \frac{2\bar{k}x_s^2\left(\frac{4}{3}n^4 - \frac{1}{3}n^2\right)}{\frac{1}{6}(2n-1)^2x_s^2m_{b1}} - \frac{K_{b1}e^2}{m_{b1}r_{z1}^2}$$

$$\omega_\theta^2 = \frac{4(2n+1)n^2}{(2n-1)}\frac{\bar{k}}{m} - \frac{K_{b1}}{m_{b1}}\left(\frac{e}{r_{z1}}\right)^2 \tag{4-15}$$

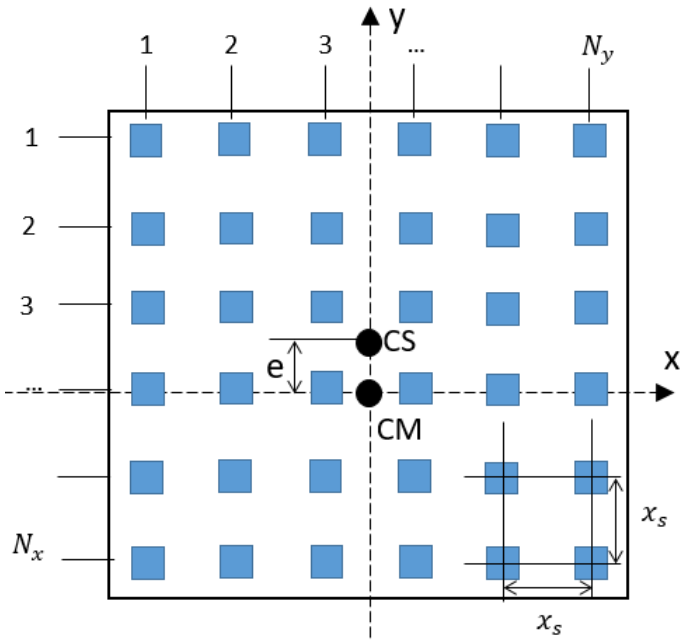

Figure 4.3 Plan of single-storey unsymmetrical building 1

Therefore, the ratio between the uncoupled torsional and lateral frequencies Ω_θ can be written as follows,

$$\Omega_\theta^2 = \frac{\omega_\theta^2}{\omega_{b1}^2} = \frac{(2n+1)}{(2n-1)} - \epsilon_r^2, \quad \epsilon_r = \frac{e}{r_{z1}} = \frac{e}{b}\sqrt{6} \tag{4-16}$$

where $2n$ ($n \in \mathbb{N}$) is the number of elements in each direction and ϵ_r is the ratio of eccentricity to the radius of gyration ratio for building 1. Therefore, by using equation (4-16), the torsional to lateral frequency Ω_θ can vary between 0.8 and 1.7, when the eccentricity ratio in building 1 is $e/b \in [0,0.2]$. The term b corresponds to the foundation's width. Structures with $\Omega_\theta > 1$ are defined as torsionally-stiff and structures with $\Omega_\theta \leq 1$ as a torsionally-flexible system, according to De la Llera and Chopra (1995b).

Newmark and Rosenblueth (1971) proposed that the volume of soil mass beneath buildings is approximately equal to $m_s = 0.35\rho_s b^3$, for a square base building. The mass of the buildings can be calculated as $m_{bj} = \rho_b b^2 h_j$, where ρ_s and ρ_b are the densities of soil and building respectively. Based on typical spans and floor loading, the average building density is $\rho_b = 400 - 800[kg/m^3]$, while typical soil density ranges between 1200 to 2100 $[kg/m^3]$. The soil density used in this chapter corresponds to loose sand, with a value of $\rho_s = 1300[kg/m^3]$. The proportionality constant can be defined as $c_1 = 0.35\,\rho_s/\rho_b = 0.76$, where the average building density can be considered as $\rho_b = 600[kg/m^3]$. The radius of gyration of the soil-cylinder (directly under the rigid foundation) is calculated according to the Newmark's empirical expression $r_s \approx 0.33b$. Parameters α_1, and α_2 are contracted into aspect ratio *s* and frequency ratio Ω_b.

$$\alpha_1 = 0.35\frac{\rho_s}{\rho_b}\frac{b}{h_1} = \frac{c_1}{s}, \quad \alpha_2 = \Omega_b^{4/3} \tag{4-17}$$

Empirical forms for the rotational and inter-building interaction springs defined in Alexander et al. (2013) are used. These values were validated using Finite Element models, physical experimental models and closed-form analytical models (Aldaikh et al., 2015; Aldaikh et al., 2016, 2018). Therefore, the values of the foundation rotational spring k_y, and the interaction spring stiffness k_{y12} is modelled as an inverse cube function of non-dimensional inter-building separation distance ζ. A revised and extended 3D version of the interaction spring stiffness k_{y12} and their respective functions q_k and q_2 has been calculated in Chapter 6. The rotational stiffness spring coefficient k_s is obtained by using the empirical formulae (deduced by Pais and Kausel (1988)) in the absence of building interaction. The kinematic interaction between the foundation and the ground motion is neglected in the present work. It has been demonstrated that SSSI structures supported on loose soil may exhibit significant interaction (Alexander et al., 2013). Hence, the soil properties used in this chapter correspond to loose sand, where the soil density is $\rho_s = 1300[kg/m^3]$, the elastic shear modulus of the soil is $G_s = 31[MPa]$ (note that $G_s = G_0 = \rho_s V_s^2$) and the Poisson's ratio of the soil is $\mu_s = 0.30$.

$$k_y = k_s q_2, \quad k_{y12} = k_s q_2 q_k, \quad q_k = -\frac{0.25}{(1+\zeta)^3}, \quad q_2 = 1 + \frac{0.5}{(1+\zeta)^3}, \quad k_s = \frac{1}{2}\frac{G_s b^3}{1-\mu_s} \tag{4-18}$$

Dividing by m_{b1} the equation (4-5) and rewriting the mass and stiffness matrix in term of the frequency parameters and frequency ratios, the equation of motion (4-5) can be stated as follows,

$$\mathbf{M}\ddot{\mathbf{x}} + \mathbf{C}\dot{\mathbf{x}} + \mathbf{K}\mathbf{x} = \mathbf{p}\ddot{x}_g \tag{4-19}$$

where the matrices **M**, **K** and the vectors **p** and **x** can be conveniently written as follows:

$$\mathbf{M} = \begin{bmatrix} 1 & 0 & -3s & 0 & 0 \\ 0 & 1 & 0 & 0 & 0 \\ -3s & 0 & 9s^2 + c_1 s^{-1} & 0 & 0 \\ 0 & 0 & 0 & \Omega_b^{4/3} & -3s\Omega_b^{8/3} \\ 0 & 0 & 0 & -3s\Omega_b^{8/3} & 9s^2\Omega_b^4 + c_1 s^{-1} \end{bmatrix}, \quad \mathbf{x} = \begin{bmatrix} x_1 \\ r_{z1}\theta_{z1} \\ r_s\theta_{y1} \\ x_2 \\ r_s\theta_{y2} \end{bmatrix} \tag{4-20}$$

$$\mathbf{K} = \omega_{b1}^2 \begin{bmatrix} 1 & -\epsilon_r & 0 & 0 & 0 \\ -\epsilon_r & \epsilon_r^2 + \Omega_\theta^2 & 0 & 0 & 0 \\ 0 & 0 & \alpha_1\Omega_s^2 + \Omega_{y12}^2 & 0 & -\Omega_{y12}^2 \\ 0 & 0 & 0 & \Omega_b^{-2/3} & 0 \\ 0 & 0 & -\Omega_{y12}^2 & 0 & \alpha_1\Omega_s^2 + \Omega_{y12}^2 \end{bmatrix}, \quad \mathbf{p} = \begin{bmatrix} -1 \\ 0 \\ 3s \\ -\Omega_b^{4/3} \\ 3s\Omega_b^{8/3} \end{bmatrix} \tag{4-21}$$

where $s = h_1/b$ is the width ratio for the building 1. The soil to building frequency ratio Ω_s and the coupled to building frequency ratio Ω_{y12} can be expressed as,

$$\Omega_{s1}^2 = \Omega_{s2}^2 = \Omega_s^2 = \frac{k_y}{\omega_{b1}^2 m_s r_s^2} = \frac{\frac{1}{2}\frac{G_s b^3}{1-\mu} q_2}{\omega_{b1}^2 (0.35\rho_s b^3)(0.33b)^2} = \frac{\frac{1}{2}\frac{1}{(1-\mu)}}{0.35 \cdot 0.33^2}\frac{G_s}{\rho_s}\frac{1}{b^2}\frac{1}{\omega_{b1}^2} q_2 \tag{4-22}$$

$$\Omega_{y12}^2 = \frac{k_{y12}}{\omega_{b1}^2 m_b r_s^2} = \frac{\frac{1}{2}\frac{G_s b^3}{1-\mu} q_2 q_\kappa}{\omega_{b1}^2 \alpha_1^{-1} (0.35\rho_s b^3)(0.33b)^2} = \frac{\frac{1}{2}\frac{1}{(1-\mu)}}{0.35 \cdot 0.33^2}\frac{G_s}{\rho_s}\frac{c_1}{s}\frac{1}{b^2\omega_{b1}^2} q_2 q_\kappa \tag{4-23}$$

These rotational frequency parameters are proportional to the square of the shear wave velocity in the soil $V_s = \sqrt{G_s/\rho_s}$. The normalised non-dimensional shear wave velocity $\bar{V}_s = V_s/1000$ (to a reference of 1000 [m/s]) and the width of the building can be written as $b = h_1/s = 83.33^{4/3}/\omega_{b1}^{4/3} s$ are introduced. Hence,

$$\Omega_s^2 = \frac{\frac{1}{2}1000^2}{0.35(1-\mu)0.33^2(83.77)^{8/3}} \bar{V}_s^2 \frac{\omega_{b1}^{8/3}}{\omega_{b1}^2} s^2 q_2 = c_2 q_2 \bar{V}_s^2 s^2 \omega_{b1}^{2/3} \tag{4-24}$$

$$\Omega_{y12}^2 = \frac{\frac{1}{2}1000^2}{0.35(1-\mu)0.33^2(83.77)^{8/3}} \bar{V}_s^2 \frac{\omega_{b1}^{8/3}}{\omega_{b1}^2} s^2 q_2 q_\kappa = c_1 c_2 q_2 q_\kappa s \bar{V}_s^2 \omega_{b1}^{2/3} \quad \textbf{(4-25)}$$

where $c_2 = 97.6/(1-\mu)[(s/rad)^{2/3}]$ is defined as the soil constant. For loose soil, it is considered that the velocity is equal to $V_s = 156[m/s]$ and the Poisson's ratio is $\mu_s = 0.3$. So, after some calculation, the stiffness matrix **K** can be conveniently written as follows:

$$\mathbf{K} = \omega_{b1}^2 \begin{bmatrix} 1 & -\epsilon_r & 0 & 0 & 0 \\ -\epsilon_r & \epsilon_r^2 + \Omega_\theta^2 & 0 & 0 & 0 \\ 0 & 0 & c_1 c_2 q_2 s \bar{V}_s^2 \omega_{b1}^{2/3}(1+q_\kappa) & 0 & -c_1 c_2 q_2 q_\kappa s \bar{V}_s^2 \omega_{b1}^{2/3} \\ 0 & 0 & 0 & \Omega_b^{-2/3} & 0 \\ 0 & 0 & -c_1 c_2 q_2 q_\kappa s \bar{V}_s^2 \omega_{b1}^{2/3} & 0 & c_1 c_2 q_2 s \bar{V}_s^2 \omega_{b1}^{2/3}(1+q_\kappa) \end{bmatrix} \quad \textbf{(4-26)}$$

Therefore, the coupled unsymmetrical system is characterised by six parameters and one site classification. This allows performing an intensive study that explores a large number of generic cases. These parameters are listed as follows:

(i) The uncoupled lateral frequency of building 1 on a rigid base ω_{b1} (or $T_x = 2\pi/\omega_{b1}$).

(ii) Frequency ratio between buildings 1 and 2 $\Omega_b = \omega_{b1}/\omega_{b2}$.

(iii) Aspect ratio $s = h_1/b$ (for building 1).

(iv) The ratio between the uncoupled torsional to lateral frequencies $\Omega_\theta = \omega_\theta/\omega_{b1}$ (for building 1).

(v) The normalised inter-building distance ratio ζ.

(vi) Static eccentricity ratio e/b of building 1.

(vii) The soil class is defined by using the soil shear wave velocity of $V_s = 156[m/s]$, the Poisson's ratio of $\mu_s = 0.3$, and the soil density of $\rho_s = 1300[kg/m^3]$.

The system's linear viscous damping matrix **C** defined in equation (4-27) assumes that each natural mode $n \in [1,5]$ is damped at $\xi_n = 0.05$ of critical damping, $\boldsymbol{\phi}_n$ is the modal eigenvector of the mode *n*, and ω_n are the natural frequencies of the systems. These ω_n were calculated considering the completely elastic system. Thus, the Caughey orthogonal damping matrix **C** can be calculated as Chopra (2000) by equation (4-27).

$$\mathbf{C} = \mathbf{M}\left(\sum_{n=1}^{5} \frac{2\xi_n \omega_n}{\boldsymbol{\phi}_n^T \mathbf{M} \boldsymbol{\phi}_n} \boldsymbol{\phi}_n \boldsymbol{\phi}_n^T\right)\mathbf{M} \quad \textbf{(4-27)}$$

4.2.2 Finite Element Model validation

In order to validate the equations of motion described in equation (4-19), a qualitative comparison has been carried out between the proposed model and an analogue Finite Element (FE) system modelled on MidasGen+ (2019). This comparison can only be efficiently performed for a parameter set, as each different case requires a new Midas Gen model to be constructed. The following high order FE model shown in Figure 4.4 is developed.

The Finite Element model is a three-dimensional (3D) strain model with linear elastic underlying material conditions. The soil has loose soil elastic properties (unit weight $\rho_s = 12.75[kN/m^3]$, shear wave velocity $V_s = 156[m/s]$ and Poisson's ratio $\mu_s = 0.30$) and building properties described in section 4.2.1. Adjacent footings were modelled using 2D plate elements with a 1-m unit width and reinforced concrete with a modulus of elasticity $E_c = 23400[MPa]$, Poisson's ratio $\mu_c = 0.20$, and unit weight $\gamma_c = 23.5[kN/m^3]$. The buildings were modelled using beam elements with six DOFs per node. The foundations were modelled as a rigid block, i.e. chosen a large value for the elastic modulus (ten times the elastic modulus of the reinforced concrete). The soil was modelled using a symmetric mesh in all its dimensions. It has been recommended that FE mesh for shallow foundations of width b on isotropic homogeneous soil includes an area extending to about $5b$ laterally and $8b$ vertically, which is the area where most of the stress variations are expected to occur. Also, a sensitivity study to evaluate the mesh size was performed. This study reached a mesh size that allowed reasonable computing running time and also similar seismic response if smaller mesh sizes were used. The boundaries condition applied to the soil mesh correspond to (i) pin supports on the bottom face (bedrock) and (ii) horizontal springs proportional to the stiffness soil on the lateral faces. The torsional effect was considered as an eccentric mass on the top of building 1.

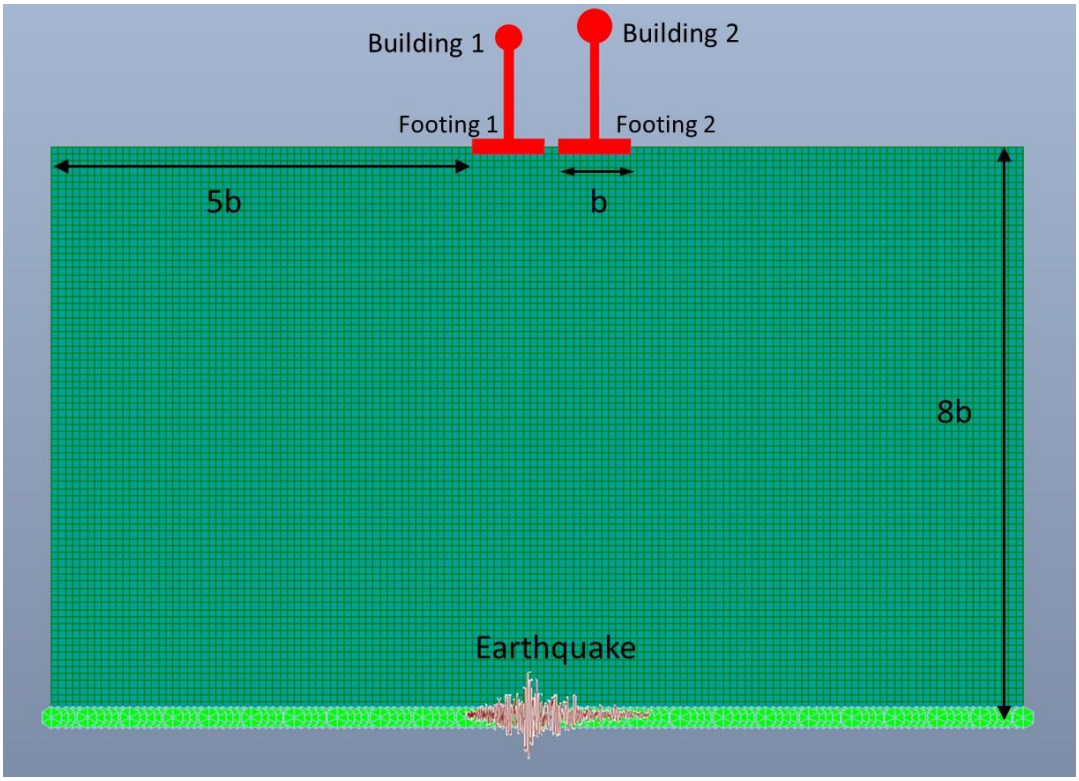

Figure 4.4 Evaluation of SSSI in unsymmetrical buildings using Finite Element (Midas Gen) model.

The validation is carried out for the different seismic events described in the next section. In this thesis, as an example of the good match, the results for the El Centro earthquake are presented in Figure 4.5 for a selected combination of parameters ($\omega_{b1} = 3.45$, $\Omega_b = 1.1$, $s = 2$, $\Omega_\theta = 1.3$, $\zeta = 0.2$ and $e/b = 0.05$). Figure 4.5 shows the high order FE model (blue line) and low-order model (red line) response for the upper DOF of building 1. Comparing the responses, in Figure 4.5 it is possible to observe that the response agrees very well for all time-history and the low-order model provides a good match in terms of peak and damping ratio estimates, despite the simplicity of the low-order model. Consequently, the discrete model captures reasonably well the main behaviour of SSSI in unsymmetrical buildings.

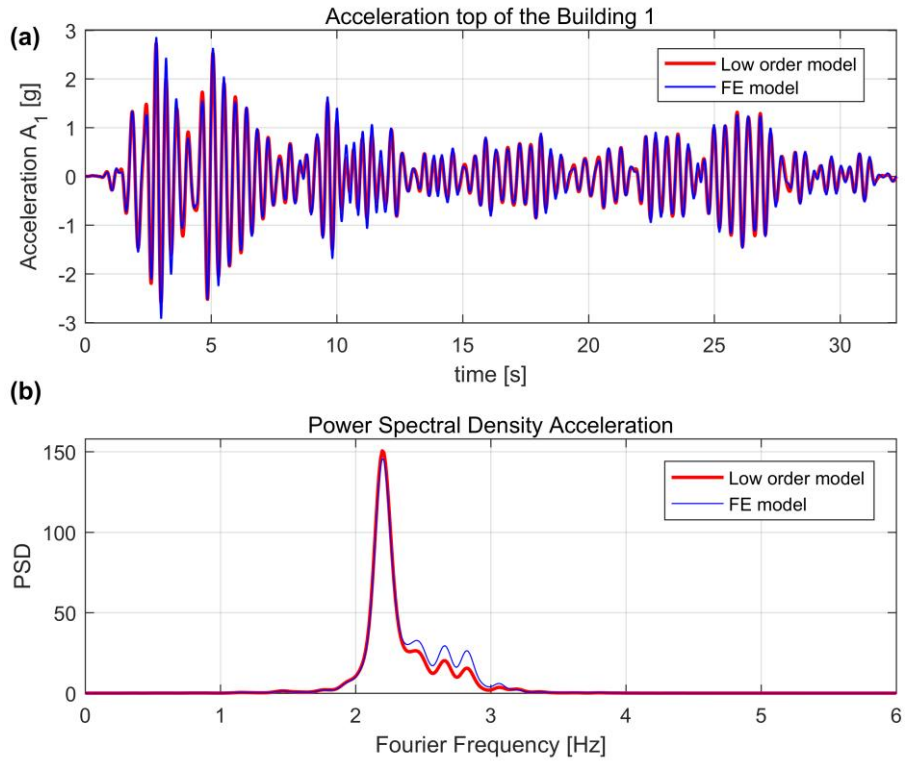

Figure 4.5 Evaluation of SSSI in unsymmetrical buildings using Finite Element (Midas Gen) model, (a) Total acceleration responses and (b) Power spectral density.

4.2.3 Quantities of interest

The main objective of this chapter is evaluating the effects of the torsion in buildings and the change in the response between the coupled (SSSI) and the uncoupled (soil-structure interaction, SSI) system. For this purpose, first it is calculated the solution of equation (4-19), for unsymmetrical-plan building 1 in the presence of building 2 (i.e. SSSI responses). Then, the responses of unsymmetrical-plan building 1 is evaluated in the absence of building 2 (i.e. SSI responses). The equation of motion (4-19) for the special case of uncoupled buildings (SSI responses) can be obtained either by (i) increasing the inter-building distance ζ to a very large value or (ii) setting $q_\kappa = 0$ and $q_2 = 1$. In this research to evaluate the SSI response (without coupled interaction), the rotational interaction spring κ equal to zero (i.e. $q_\kappa = 0$ and $q_2 = 1$) was employed.

In this chapter, two system performance measures are employed: (i) the relative displacement U_1 (horizontal + sway + torsion) at distance $\pm b/2$ from the CM (i.e. at the building's corners), and (ii) total acceleration A_1 (horizontal + sway + ground + torsion) at distance $\pm b/2$ from the CM for the top of the building 1, denoted by,

$$U_1 = x_1 - 3s\theta_{y1} \pm \frac{b}{2}\theta_{z1}, \qquad A_1 = \ddot{x}_1 + \ddot{x}_g - 3s\ddot{\theta}_{y1} \pm \frac{b}{2}\ddot{\theta}_{z1} \qquad \textbf{(4-28)}$$

Although displacements and accelerations for both locations at distance $+b/2$ and $-b/2$ from the CM were computed for each system, only results for the maximum response are presented since the response trends are similar in both cases. In addition, it is useful to define the change in total power caused by the buildings' interaction. So, the percentage change in total power, when using the uncoupled SSI analyses rather than coupled SSSI analyses is defined as follow,

$$\chi_1(U_1) = 100\left\{\frac{[E_s(U_1)]_{SSSI}}{[E_s(U_1)]_{SSI}} - 1\right\}, \qquad \ddot{\chi}_1(A_1) = 100\left\{\frac{[E_s(A_1)]_{SSSI}}{[E_s(A_1)]_{SSI}} - 1\right\} \tag{4-29}$$

where $E_s(U_1)$ or $E_s(A_1)$ are the total power spectral densities (which are based on all data points of response time series U_1) for the displacement and acceleration. The change of power χ_1 and $\ddot{\chi}_1$ will be zero if there is no difference between SSSI and SSI analysis. The power spectral density (PSD) is defined using Parseval's theorem according to equations (4-30) and (4-31).

$$E_s(U_1) = \int_{-\infty}^{\infty} |U_1(t)|^2 dt = \frac{1}{2\pi}\int_{-\infty}^{\infty} |U_1(\omega)|^2 d\omega \tag{4-30}$$

$$E_s(A_1) = \int_{-\infty}^{\infty} |A_1(t)|^2 dt = \frac{1}{2\pi}\int_{-\infty}^{\infty} |A_1(\omega)|^2 d\omega \tag{4-31}$$

where $U_1(\omega)$ is the continuous Fourier transform of $U_1(t)$ and $A_1(\omega)$ is the continuous Fourier transform of $A_1(t)$. Using total power as a comparative metric delivers a statistical estimate of magnitude that provides more information about the response than employing a single peak of the function.

4.2.4 Ground motion selection

The SSSI system is analysed with horizontal components of ground motions from 25 records that are taken from 15 events that occurred between 1971 and 2007 (see Table 4-1). Nine of them occurred in California (namely San Fernando, Imperial Valley, Coalinga, Morgan Hill, Whittier Narrows, Superstition Hills, Loma Prieta, Northridge and Parkfield) and six of them are taken from different places around the world (namely Kocaeli, Chi-Chi, Duzce, Tottori, Niigata and Chuetsu-oki). Each record has two horizontal components. Event magnitudes range from $M_w = 6.0$ to $M_w = 7.6$ with an average magnitude of $M_w = 6.6$. Values of their peak ground accelerations (PGAs) vary from 0.03g to 0.83g with a mean value of 0.175g. These ground motion data were obtained from the Pacific Earthquake Engineering Research (PEER) Center Database (PEER, 2014). All ground motions were recorded on weak soils, which correspond to sites of an average shear wave velocity of less than 180 m/s, according to the definition of

Eurocode 8 EN-1998 (2004), i.e. loose sand. Figure 4.6 displays the elastic response spectrum for all the records and their mean.

Table 4-1 Summary of Earthquake events

Record Name	PGA [m/s^2]	M_w	Record Name	PGA [m/s^2]	M_w
San Fernando, US	0.70	6.6	Parkfield, US	8.17	6.0
Imperial Valley, US	2.62	6.5	Kocaeli, Turkey	2.48	7.5
Coalinga, US	1.41	6.4	Chi-Chi, Taiwan	2.40	8.3
Morgan Hill, US	0.64	6.2	Duzce, Turkey	0.37	7.1
Whittier Narrows, US	1.08	6.0	Tottori, Japan	1.89	6.6
Superstition Hills, US	2.04	6.5	Niigata, Japan	2.01	6.6
Loma Prieta, US	2.79	6.9	Chuetsu, Japan	2.24	6.8
Northridge, US	0.90	6.7			

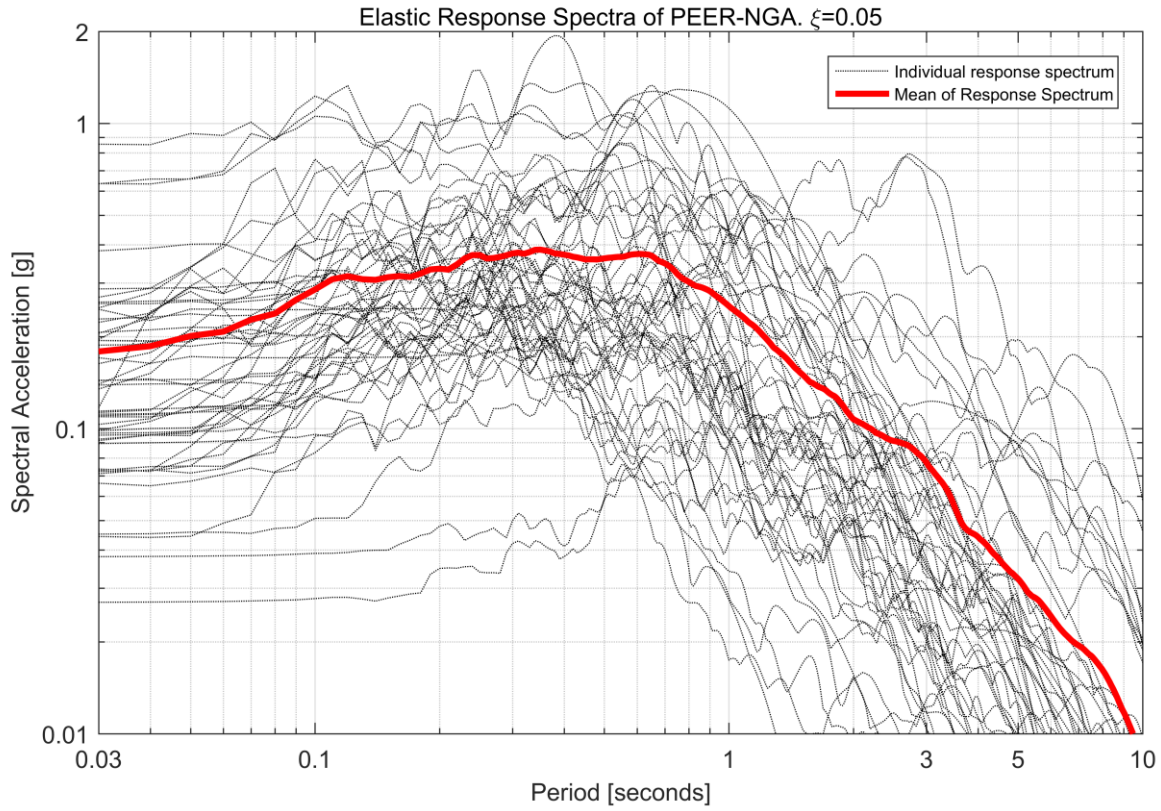

Figure 4.6 Elastic response spectra of horizontal ground motions

4.3 Change in the response of unsymmetrical buildings due to SSSI

The system analysed in this chapter corresponds to the case when the two buildings are placed in very close proximity to each other, at $\zeta = 0.1$, i.e. at a spacing distance equal to $0.1b$. It has been demonstrated that the inter-building distance is big enough to avoid pounding but close enough to maximise the SSSI effects (Alexander et al., 2013).

Due to the complexity of the problem and the large number of parameters considered in this study, the results for the unsymmetrical-plan building 1 are divided into five sections, as follows,

(i) Section 4.3.1 demonstrates beneficial and adverse cases of SSSI effect on unsymmetrical-plan building 1. Also, it is explored the torsional components of the building's responses explicitly.

(ii) Section 4.3.2 explores beneficial and adverse SSSI effects for different building aspect ratio and frequency ratios because previous studies (Aldaikh et al., 2015; Aldaikh et al., 2016) suggest that these are important parameters.

(iii) Section 4.3.3 explores the influence of the fundamental fixed-base frequency of building 1 on SSSI responses. These effects have not been reported in previous papers (Alexander et al., 2013; Aldaikh et al., 2016).

(iv) Section 4.3.4 explores whether the torsional frequency ratio Ω_θ is an important parameter in the SSSI responses of the buildings.

(v) Section 4.3.5 explores the influence of static eccentricity ratio e/b in the SSSI responses of the buildings.

4.3.1 Initial beneficial/adverse SSSI cases for unsymmetrical-plan building 1

In this section, initial results are presented for SSSI and SSI responses in unsymmetrical-plan buildings. The translation and rotation of building 1 are coupled because of the static eccentricity ratio $e/b = 0.05$, equation (4-19). This implies that the building 1 will simultaneously undergo translation and torsion when subjected to horizontal base motions. The analysis is carried out first for the Superstition Hill earthquake (11/24/1987, Imperial Valley Wildlife SH-02 Station) and for a selected combination of parameters as a starting example. Figure 4.7 shows the ground motion time series and the power spectral density of the record. The rigid base period of building 1 is $T_x = 2\pi/\omega_{b1} = 0.5$ seconds.

Figure 4.8(a) and Figure 4.8(b) show the uncoupled SSI (blue line) and coupled SSSI (red line) responses for the top of the building 1 (namely the displacement U_1 for Figure 4.8(a) and the total acceleration A_1 for Figure 4.8(b)) when it is adjoined by a 13.5% taller building (i.e. frequency ratio $\Omega_b = \omega_{b1}/\omega_{b2} =$

1.1) and building 1 has a height to width ratio equal to $s = h_1/b = 2$. The static eccentricity ratio is equal to $e/b = 0.05$ and the torsional to lateral frequency ratio is $\Omega_\theta = \omega_\theta/\omega_{b1} = 1.2$ (i.e. torsionally-stiff structure). Figure 4.8(c) shows the corresponding power spectral density (PSD) for the displacement and Figure 4.8(d) shows the PSD for the total acceleration of the building 1 considering the coupled (SSSI) and uncoupled (SSI) cases.

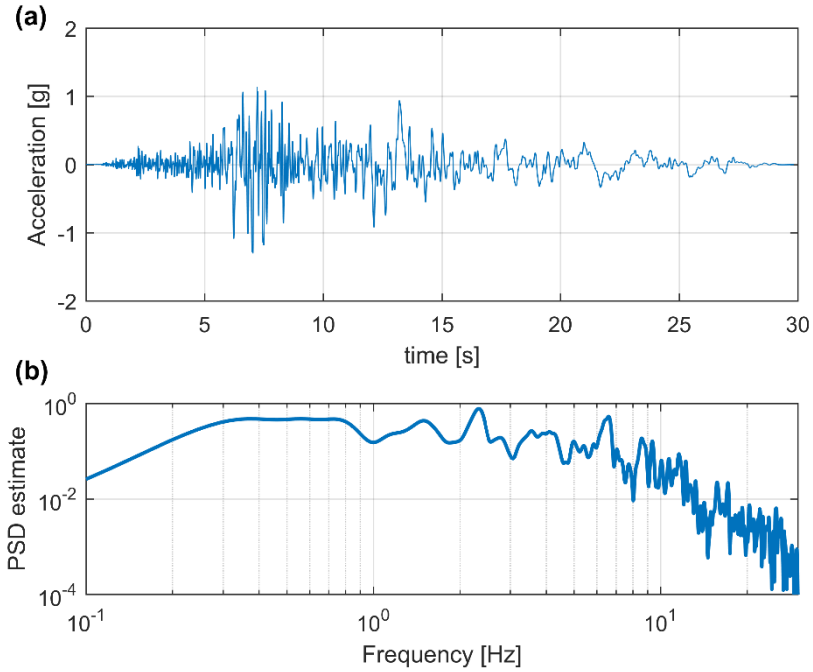

Figure 4.7 (a) Acceleration ground motion and (b) Power spectral density (Superstition Hill-02 24/11/1987)

Comparing the uncoupled and coupled responses, building 1's response appears to be significantly affected by the presence of the taller building in all the time-history. The change in power, defined in equation (4-29), is equal to $\chi_1 = 45.2\%$ for the displacement U_1 and $\ddot{\chi}_1 = 75.4\%$ for the acceleration A_1. The peak in the PSD of Figure 4.8(c) and (d) represents approximately the fundamental frequency of the system, where the frequency does not change very much between the SSI and SSSI systems (small shift of the PSD peaks).

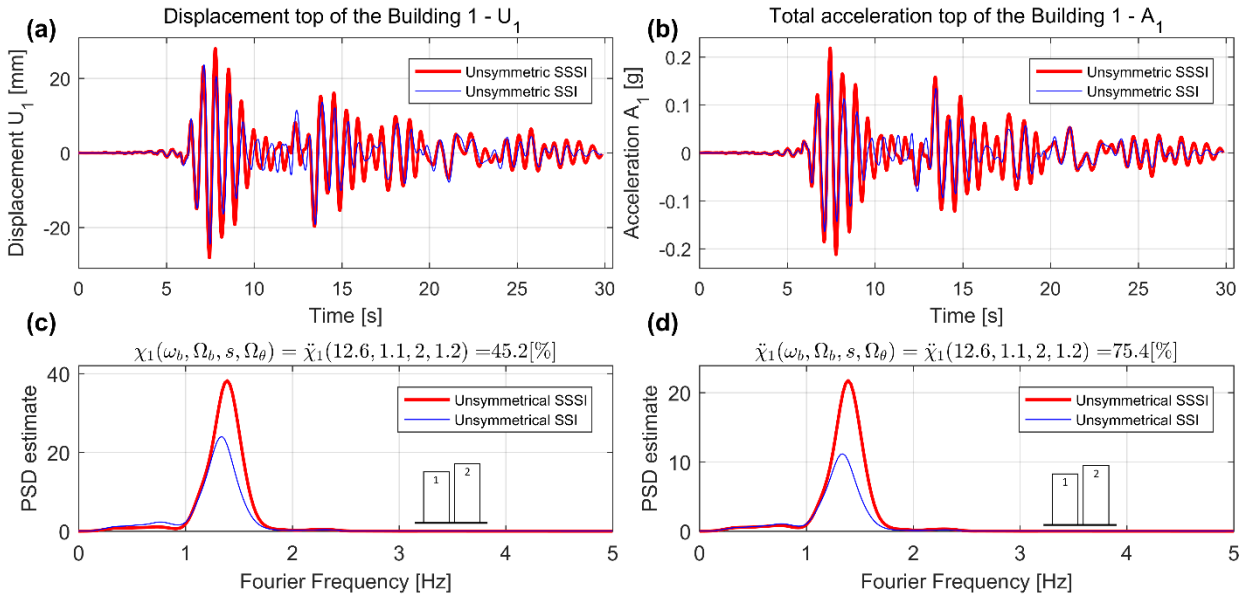

Figure 4.8 (a) Displacement and (b) Total acceleration responses, (c) Power spectral density of displacement and (d) PSD of total acceleration – Responses for the parameter set (T_x = 0.5s, Ω_b = 1.1, s = 2.0, e/b = 0.05, and Ω_θ = 1.2)

Figure 4.9 displays the response for a system where the second building is shorter than the first building (i.e. frequency ratio of $\Omega_b = 0.75$). The rest of the parameters are considered the same to those used in Figure 4.8, i.e. parameter set of $T_x = 0.5$ seconds, $s = 2$, $\Omega_\theta = 1.2$ and $e/b = 0.05$. Figure 4.9(a) and (b) show the uncoupled and coupled responses for the top of building 1, that is displacement U_1 and total acceleration A_1. Comparing the SSI and SSSI responses, there is a transfer of earthquake energy from building 1 to building 2. Building 1's total power response attenuates by $\chi_1 = -19.7\%$ for the displacement U_1 and $\ddot{\chi}_1 = -12.7\%$ for the acceleration A_1, as seen in Figure 4.9. Those results agree with past investigations (Aldaikh et al., 2015; Aldaikh et al., 2016).

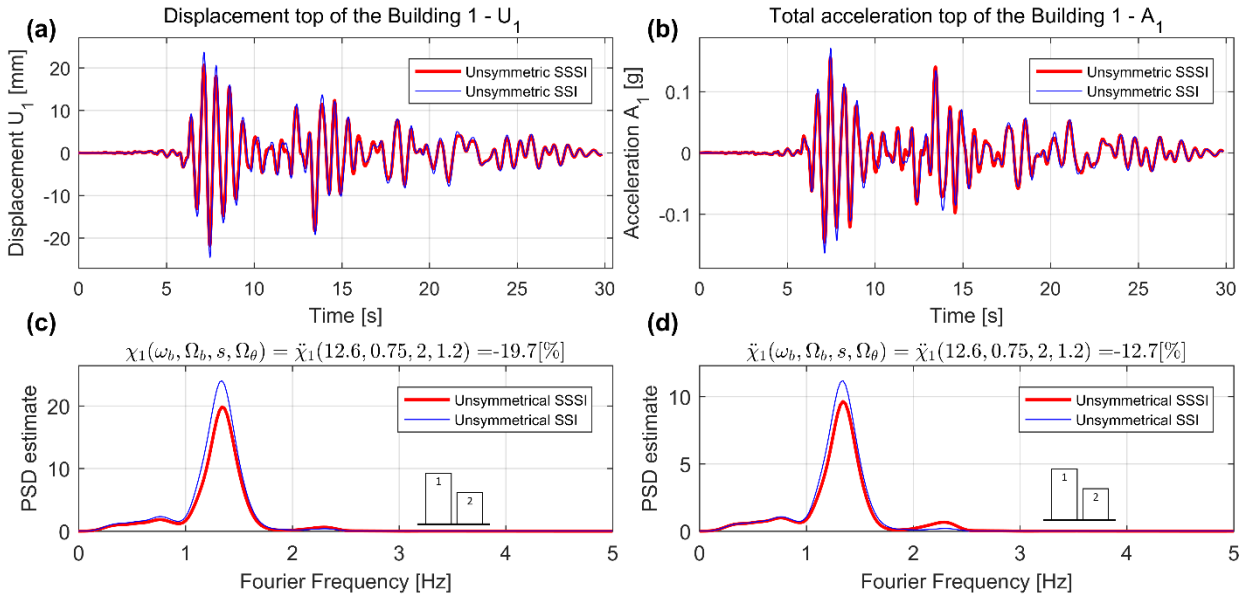

Figure 4.9 (a) Displacement and (b) Total acceleration responses, (c) Power spectral density of displacement and (d) PSD of total acceleration – Responses for the parameter set (T_x = 0.5s, Ω_b = 0.75, s = 2.0, e/b = 0.05, and Ω_θ = 1.2)

In order to isolate the influence of SSSI in the torsional response of unsymmetrical building 1, it is graphed in Figure 4.10(a) the torsional displacement $\frac{b}{2}\theta_{z1}$ and in Figure 4.10(b) the torsional acceleration $\frac{b}{2}\ddot{\theta}_{z1}$ for the building 1. Those results are for the set of parameters described in the previous figure (i.e. $T_x = 0.5$ seconds, $\Omega_b = 0.75$, $s = 2$, $\Omega_\theta = 1.2$ and $e/b = 0.05$). As seen in Figure 4.10(c) and (d), the torsional displacement $\frac{b}{2}\theta_{z1}$ and torsional acceleration $\frac{b}{2}\ddot{\theta}_{z1}$ of building 1 increases for the SSSI case in $\chi_1 = 43.6\%$ and $\ddot{\chi}_1 = 151\%$ respectively. So, the SSSI effects have a significant influence on the torsional response in building 1 for frequency ratios Ω_b lower than 1. This additional torsional interaction was not explored in the previous papers (Alexander et al., 2013; Aldaikh et al., 2015). Nevertheless, these detrimental influences are reduced if it is considered as a relevant variable the displacement U_1 (horizontal + sway + torsion) and acceleration A_1 (horizontal + sway + ground + torsion) in building 1, defined in equation (4-28), as it was shown in Figure 4.9.

Note that the examples shown in Figure 4.8 and Figure 4.9 also indicate similar time-histories for both displacement and acceleration responses. This is a particular feature of (i) this earthquake with a predominant frequency at approximately 2.4Hz and (ii) a system with the first two natural frequencies in range 1.3-2.4Hz. It is important to state that in general, the displacement and acceleration time-history responses will not be so similar.

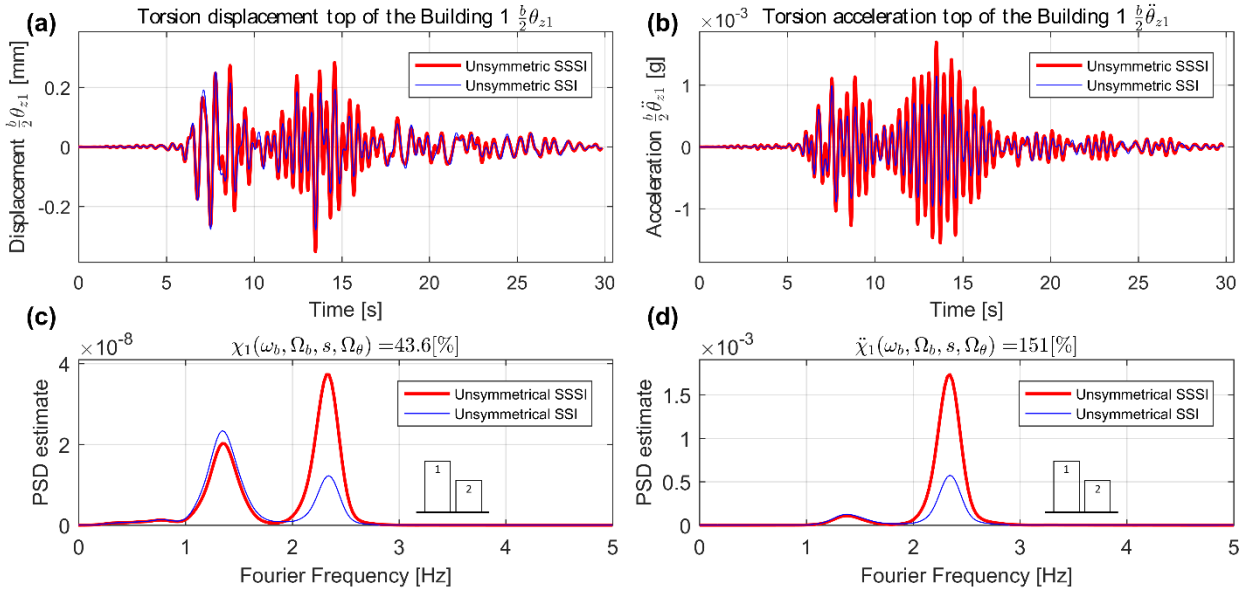

Figure 4.10 (a) Torsion displacement and (b) Torsion acceleration responses, (c) Power spectral density of torsion displacement and (d) PSD of torsion acceleration – Responses for the parameter set (T_x = 0.5s, Ω_b = 0.75, s = 2.0, e/b = 0.05, and Ω_θ = 1.2)

4.3.2 Change in power due to variation in aspect ratio s and frequency ratio Ω_b

The change in power, χ_1 and $\ddot{\chi}_1$, of the building 1 for the displacement U_1 and acceleration A_1 are analysed. These changes in power are defined in equation (4-29). These terms will be zero if there are no differences between the coupled (SSSI) and uncoupled (SSI) analysis.

Presented in this section are results for the variation of change in power of unsymmetrical buildings resulting from the SSSI. Results are presented for buildings with aspect ratio $s = h_1/b$ varying between 0.5 and 2.5; frequency ratio between the buildings $\Omega_b = \omega_{b1}/\omega_{b2}$ varying between 0.5 and 2; eccentricity ratio $e/b = 0.05$ and torsion to lateral frequency ratio equal to $\Omega_\theta = 1.2$ (i.e. torsionally-stiff systems). The system is subjected to all earthquake events and for its East-West and North-South components. The mean and mean-plus-one standard deviation values (of all earthquakes events) of the change in power are presented.

Contour plots in Figure 4.11 display the variation of change in power χ_1 for the displacement U_1 on top of building 1. The critical zones in the figure are in red, i.e. where the building's total response power is amplified by the presence of building 2. Blue indicates when the response power is reduced. In general, for frequency ratios greater than 1.0, i.e. when adjacent buildings are equal or taller, the response of building 1 is amplified. The maximum increase in total displacement power response occurs when the structure configuration lies around two different sections of the graph. First, for aspect ratio $s = 2.5$ and frequency ratio equal to $\Omega_b = 2.0$, and another peak close to the frequency ratio equal to $\Omega_b = 1.1$. As it

was discussed in Chapter 3, the significant change in power when there are large differences of heights between the buildings is because the taller building imposes a low-frequency 'rigid body rocking mode' on the shorter building. On average, the amplification reaches a value of $\chi_1 = 45\%$ and mean-plus-one standard deviation of 150%. Each contour plot presented in this chapter contains the results of 1,200,000 different time-histories analyses. The University of Bristol's supercomputer, BlueCrystal is employed, for these simulations and required approximately 3 hours run-time.

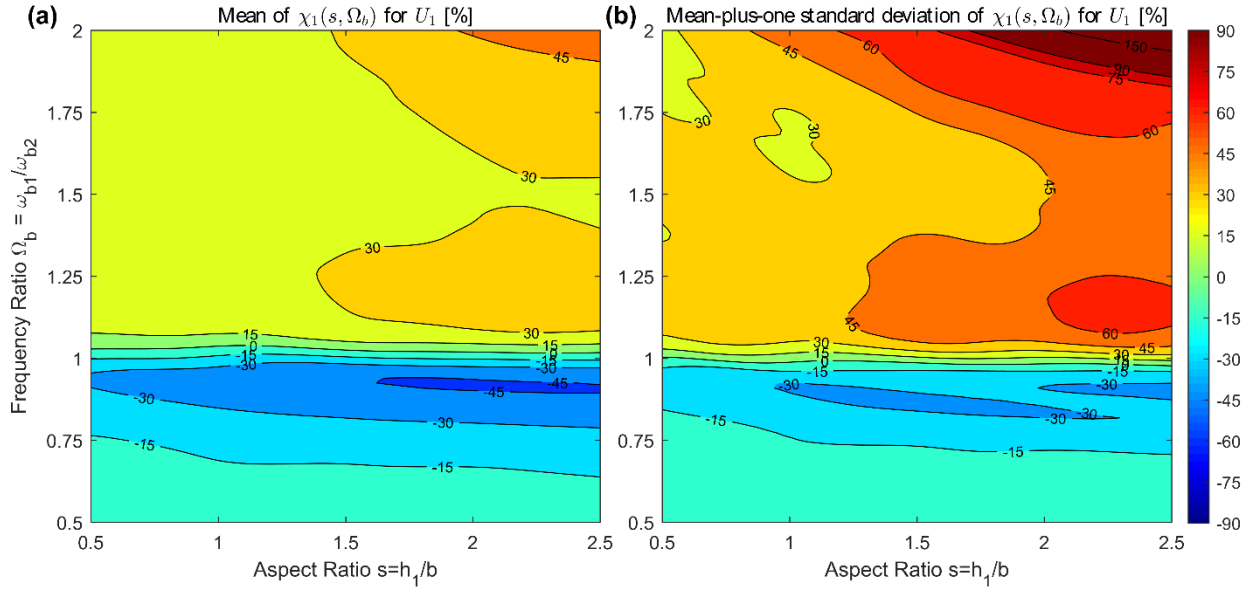

Figure 4.11 (a) Mean and (b) Mean-plus-one standard deviation of the change in displacement power $\chi_1(s,\Omega_b)$ for U_1 as a function of aspect ratio s = h_1/b and frequency ratio Ω_b - Response for the parameter set (T_x = 0.5s, e/b = 0.05, and Ω_0 = 1.2)

Contour plots in Figure 4.12 display the variation of change in power $\ddot{\chi}_1$ for the acceleration A_1 on top of building 1. In general, for frequency ratios greater than 1.0, i.e. when adjacent buildings are equal or taller, the response of building 1 is amplified. The maximum increase in total acceleration power response occurs when the structure configuration lies around aspect ratio $s = 2.3$ and frequency ratio equals to $\Omega_b = 1.1$. This result was observed in previous studies (Aldaikh et al., 2015; Aldaikh et al., 2016). On average, the amplification reaches a value of $\ddot{\chi}_1 = 60\%$ and mean-plus-one standard deviation of 90%. Thus, a very similar trend is observed in the change in power for all the earthquakes analysed in this research. In addition, the additional peaks for large frequency ratios ($\Omega_b \geq 1.75$) noted for displacements are not distinguished in Figure 4.12 because acceleration responses are, by definition, much less susceptible to low-frequency excitation.

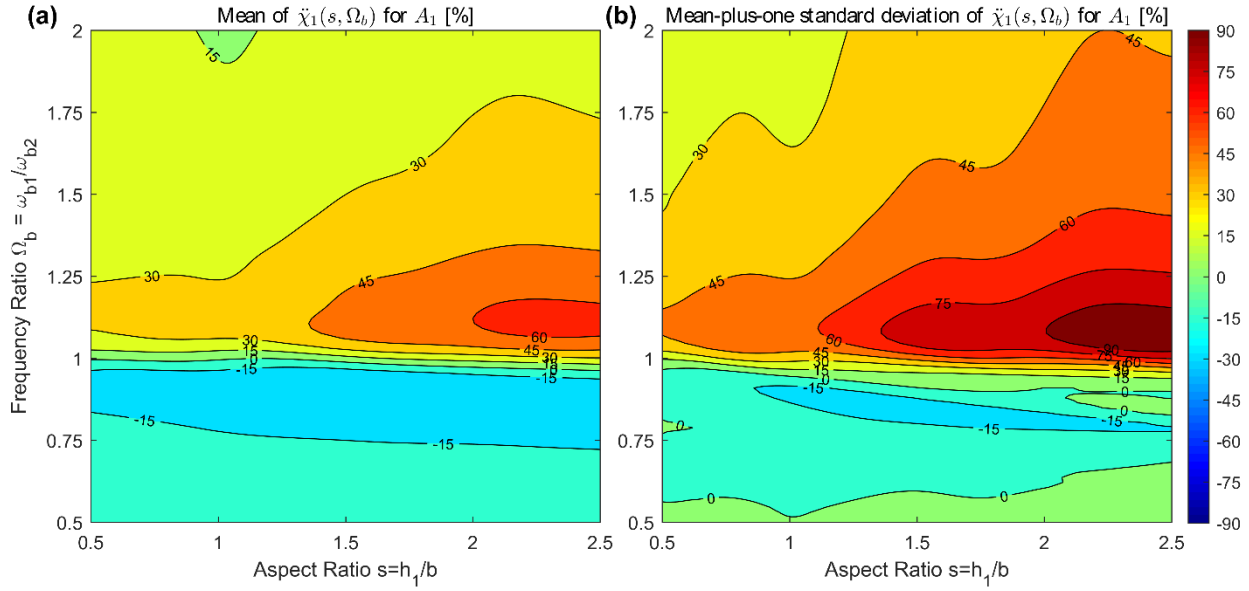

Figure 4.12 (a) Mean and (b) Mean-plus-one standard deviation of the change in acceleration power $\ddot{x}_1(s,\Omega_b)$ for A_1 as a function of aspect ratio s = h$_1$/b and frequency ratio Ω_b - Response for the parameter set (T_x = 0.5s, e/b = 0.05, and Ω_θ = 1.2)

Figure 4.13(a) shows the mean contour plot and Figure 4.13(b) shows the mean-plus-one standard deviation values of the change in power χ_1, for the torsional displacement θ_{z1}, considering all records. Unlike the contour plot of Figure 4.11, the detrimental effect of SSSI in unsymmetrical-plan structure is valid for a broader range of frequency ratio Ω_b, and not just for frequency ratios greater than 1. On average, the amplification reaches a value of $\chi_1 = 15\%$ and mean-plus-one standard deviation of 60% for taller torsionally irregular building adjacent to a small building ($\Omega_b < 1.0$).

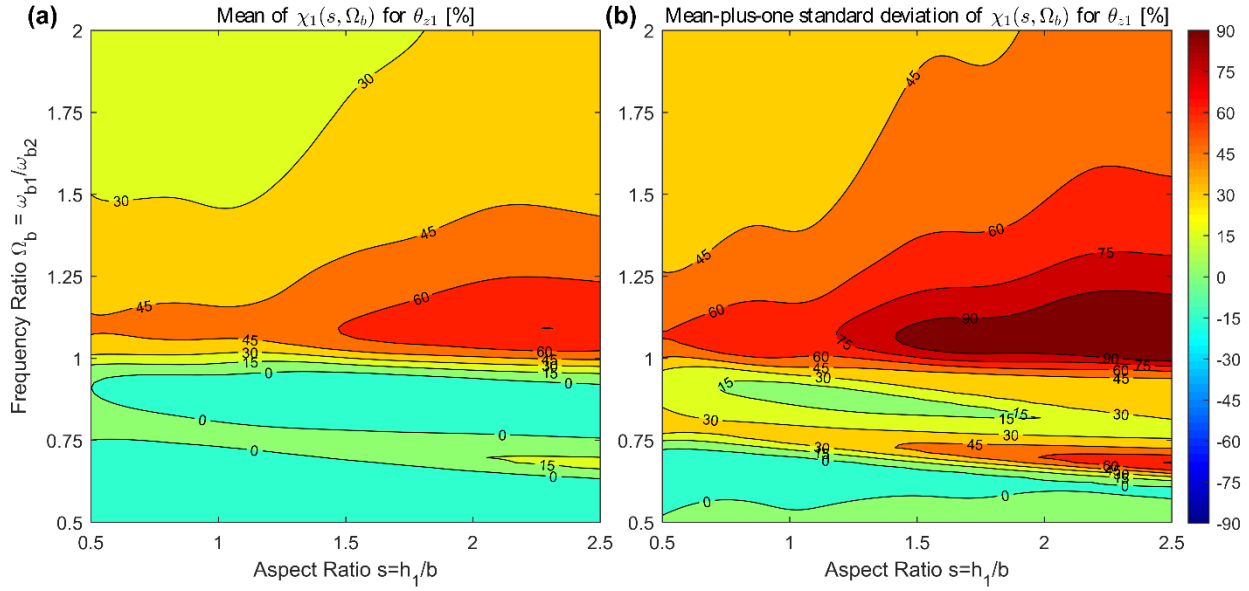

Figure 4.13 (a) Mean and (b) Mean-plus-one standard deviation of the change in displacement power $\chi_1(s,\Omega_b)$ for θ_{z1} as a function of aspect ratio s = h$_1$/b and frequency ratio Ω_b - Response for the parameter set (T_x = 0.5s, e/b = 0.05, and Ω_θ = 1.2)

Figure 4.14(a) shows the mean contour plot and Figure 4.14(b) shows the mean-plus-one standard deviation values of the change in power $\ddot{\chi}_1$, now for the torsional acceleration $\ddot{\theta}_{z1}$, considering all records. In the same way, the negative effect of SSSI in unsymmetrical-plan structure is valid for a wider variety of frequency ratios Ω_b, and not only for frequency ratios greater than 1. On average, the amplification reaches a value of $\ddot{\chi}_1 = 90\%$ and mean-plus-one standard deviation of 150% for a taller torsionally irregular building adjacent to a small building ($\Omega_b < 1.0$). These torsional effects on the building 1's response produce an additional amplification in displacement and acceleration responses, which was not presented in previous research (Aldaikh et al., 2015; Aldaikh et al., 2016).

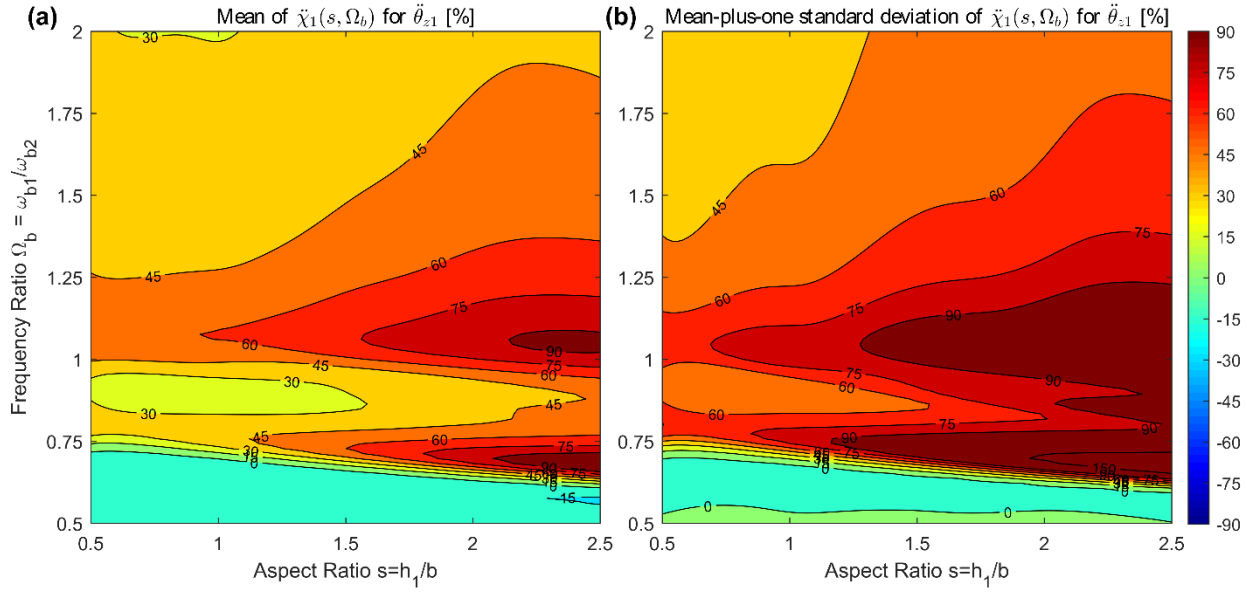

Figure 4.14 (a) Mean and (b) Mean-plus-one standard deviation of the change in acceleration power $\ddot{\chi}_1(s,\Omega_b)$ for $\ddot{\theta}_{z1}$ as a function of aspect ratio s = h$_1$/b and frequency ratio Ω_b - Response for the parameter set (T_x = 0.5s, e/b = 0.05, and Ω_θ = 1.2)

4.3.3 Change in power due to variation in period on rigid foundation of building 1 T_x and frequency ratio Ω_b

In this section, results are presented for the change in power χ_1 and $\ddot{\chi}_1$, corresponding to the displacement and acceleration of building 1 respectively. The dynamic response is for buildings with uncoupled vibration period $T_x = 2\pi/\omega_{b1}$ varying between 0.1 and 1.0 seconds; frequency ratio between the buildings $\Omega_b = \omega_{b1}/\omega_{b2}$ varying between 0.5 and 2; aspect ratio $s = 2.0$, eccentricity ratio $e/b = 0.05$ and torsion to lateral frequency ratio equal to $\Omega_\theta = 1.2$ (i.e. torsionally-stiff system). Shown in Figure 4.15 are the mean and mean-plus-one standard deviation of the contour plots of variation of change in power χ_1 for the displacement U_1. In this case, the maximum change of power lies around the frequency ratio equal to $\Omega_b = 2$ and another red zone close to $\Omega_b = 1.1$. The effect of the 'rigid body rocking mode' on building 1 for large frequency ratio, is more relevant for stiff structures (T_x for building 1 between 0.1s to 0.3s). On mean, the amplification reaches a value of 90% and mean-plus-one standard deviation of 200%.

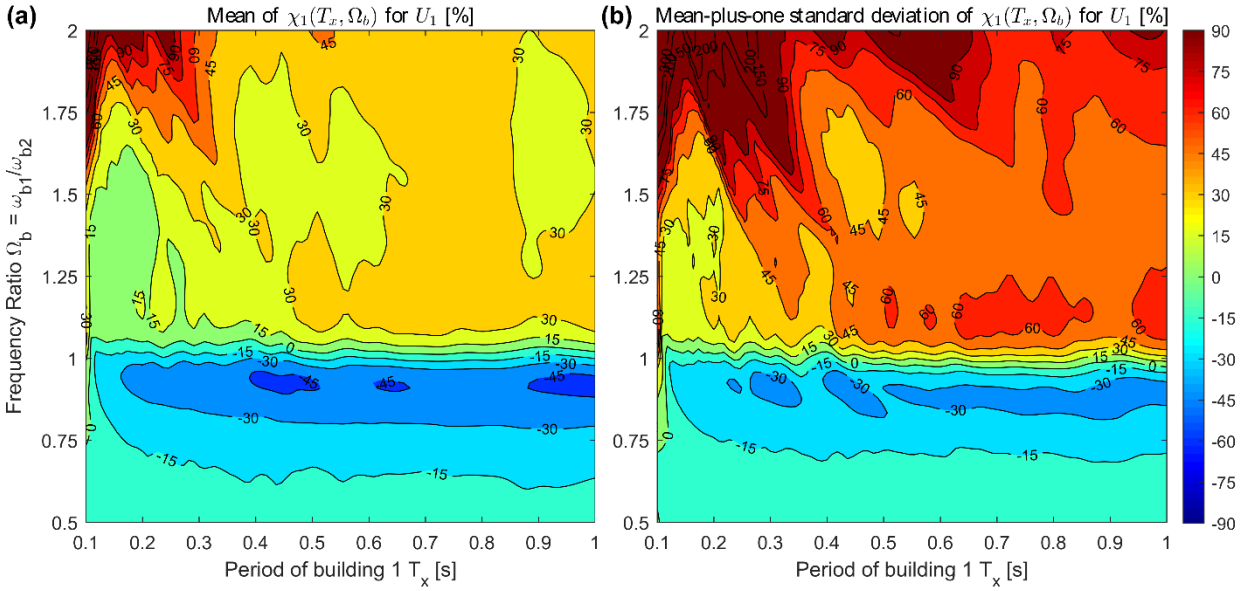

Figure 4.15(a) Mean and (b) Mean-plus-one standard deviation of the change in displacement power $\chi_1(T_x,\Omega_b)$ for U_1 as a function of natural period of the building on rigid foundation T_x and frequency ratio Ω_b - Response for the parameter set (s = 2.0, e/b = 0.05, and Ω_0 = 1.2)

Shown in Figure 4.16 are the mean and mean-plus-one standard deviation of the contour plots of variation of change in power $\ddot{\chi}_1$ for the acceleration A_1. In this case, the maximum change of power lies around the frequency ratio equal to $\Omega_b = 1.1$. On mean, the amplification reaches a value of $\ddot{\chi}_1 = 60\%$ and mean-plus-one standard deviation of 100%. Another interesting feature of this figure is that the change in power increases for structures that are more flexible.

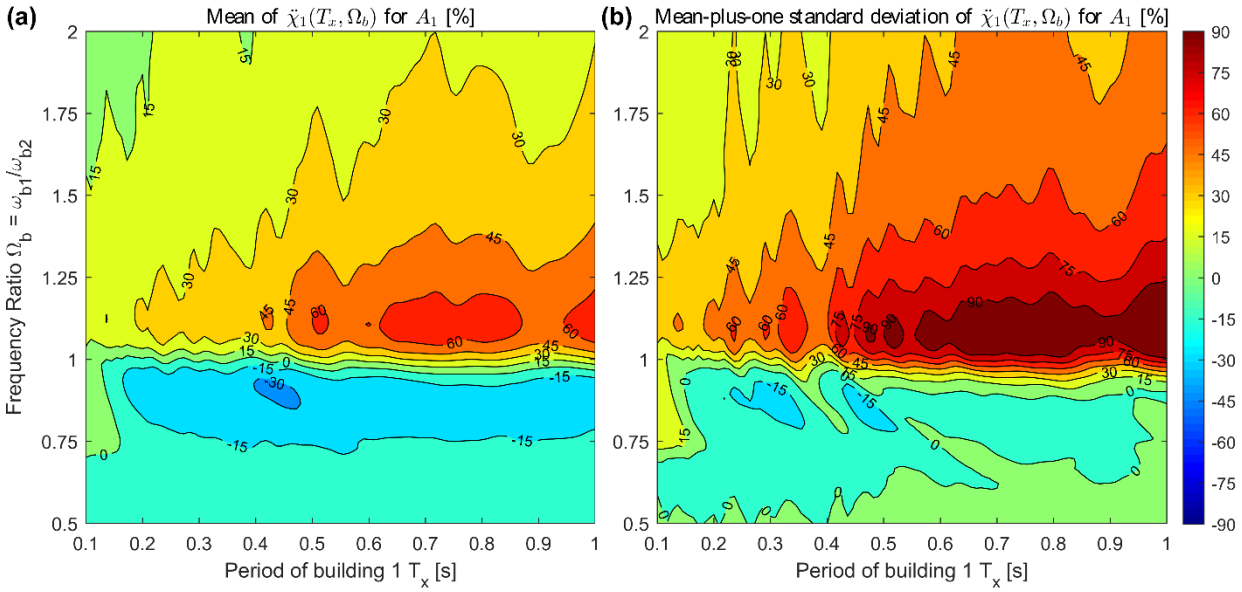

Figure 4.16(a) Mean and (b) Mean-plus-one standard deviation of the change in acceleration power $\ddot{\chi}_1(T_x,\Omega_b)$ for A_1 as a function of natural period of the building on rigid foundation T_x and frequency ratio Ω_b - Response for the parameter set (s = 2.0, e/b = 0.05, and Ω_0 = 1.2)

4.3.4 Change in power due to variation in torsional frequency ratio Ω_θ and period on rigid foundation of building 1 T_x

Mean and mean-plus-one standard deviation values of the change in power χ_1 for the displacement U_1 are shown in Figure 4.17 for a wide range of torsional to lateral frequency ratio $\Omega_\theta = [0.8 - 1.6]$ (covering torsionally-flexible and torsionally-stiff structures) and three different values of the natural period of the building 1 on rigid base $T_x = 2\pi/\omega_{b1} = 0.1$, 0.3 and 0.5 seconds. The frequency ratio $\Omega_b = 1.1$ and aspect ratio $s = 2.0$ are considered constant. The increase in displacement response resulting from the SSSI effects is insensitive to changes in the frequency torsional ratio Ω_θ unless the building is very flexural stiff (i.e. T_x is less than 0.3 seconds, with a maximum of $\chi_1 = 60\%$). This observation also applies to the mean-plus-one standard deviation results.

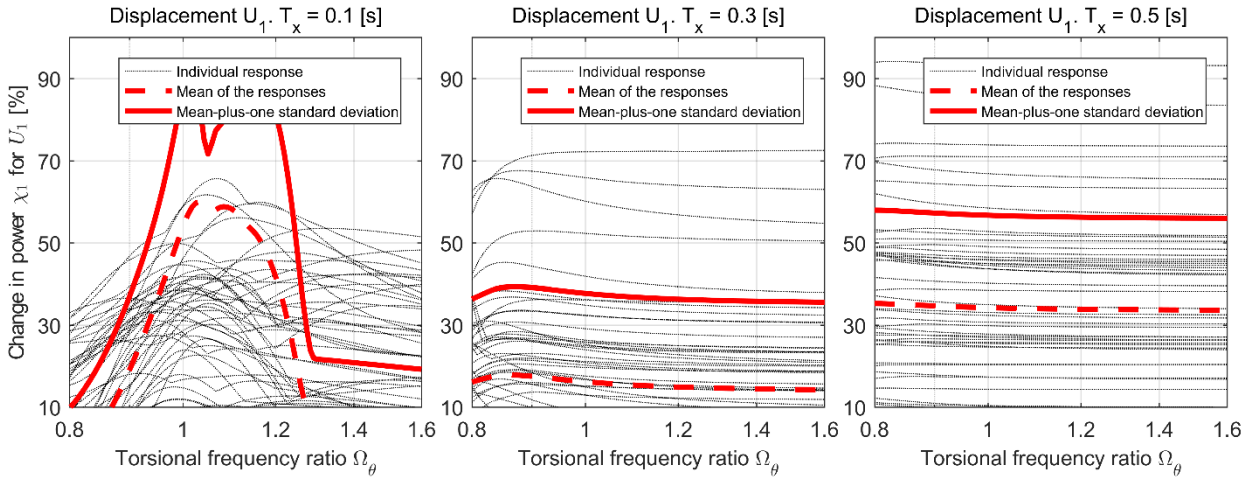

Figure 4.17 Variation of change in displacement power $\chi_1(\Omega_\theta, T_x)$ with the torsional to lateral frequency ratio Ω_θ using three different natural periods of the building 1 on rigid foundation T_x - Response for the parameter set (s = 2.0, e/b = 0.05, and Ω_b = 1.1)

Mean and mean-plus-one standard deviation values of the change in power $\ddot{\chi}_1$ for the acceleration A_1 are shown in Figure 4.18. As with the displacement, the increase in acceleration response is insensitive to changes in the frequency torsional ratio Ω_θ unless the building is very flexural stiff. On mean, the amplification reaches a value of $\ddot{\chi}_1 = 60\%$ and mean-plus-one standard deviation of 90%, for T_x equal to 0.5 seconds.

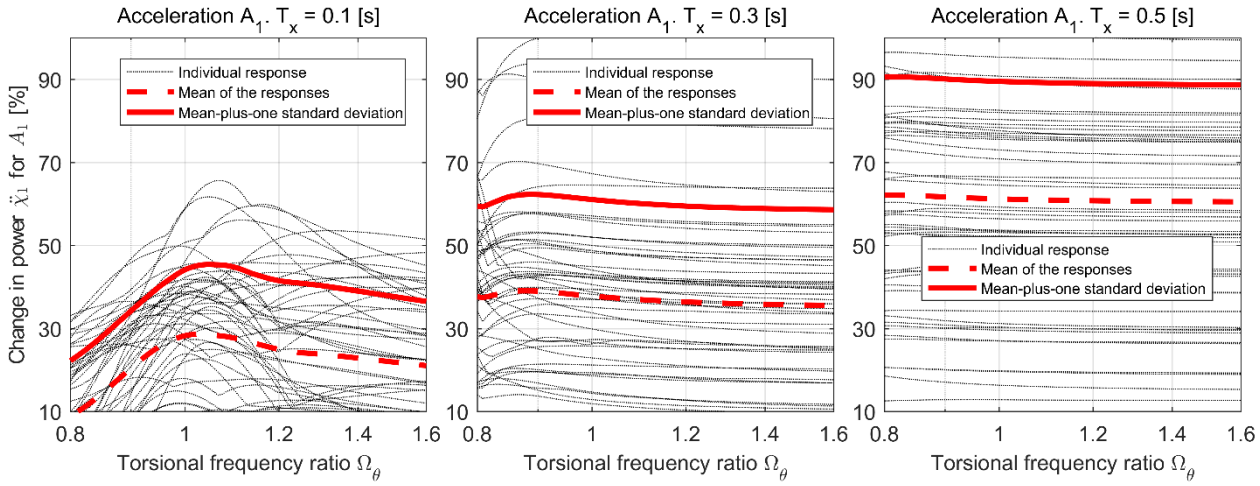

Figure 4.18 Variation of change in acceleration power $\ddot{x}_1(\Omega_0, T_x)$ with the torsional to lateral frequency ratio Ω_0 using three different natural periods of the building 1 on rigid foundation T_x - Response for the parameter set (s = 2.0, e/b = 0.05, and Ω_b = 1.1)

4.3.5 Change in power due to variation in static eccentricity ratio e/b and period on rigid foundation of building 1 T_x

Figure 4.19 shows the mean and mean-plus-one standard deviation values of the change in power χ_1 for the displacement U_1 on the top of building 1. Figure 4.20 shows the mean and mean-plus-one standard deviation values of the change in power $\ddot{\chi}_1$ for the acceleration A_1 on the top of building 1. Results are presented for a wide range of eccentricity ratios, varying between $e/b = [0,0.2]$, and fixed values for the natural period of the building 1 $T_x = 2\pi/\omega_{b1} = 0.1$, 0.3 and 0.5 seconds. The frequency ratio is $\Omega_b = 0.7$ and aspect ratio equal to $s = 2.0$.

As a general trend, Figure 4.19 shows a reduction in the displacement response (i.e. negative values for χ_1) for low static eccentricity ratios ($e/b \leq 0.05$) and a stiffer building 1 ($T_x = 0.1s$). For a more flexible building 1 ($T_x = 0.3s$ and $T_x = 0.5s$), the reduction is for a broader range of eccentricity ratios.

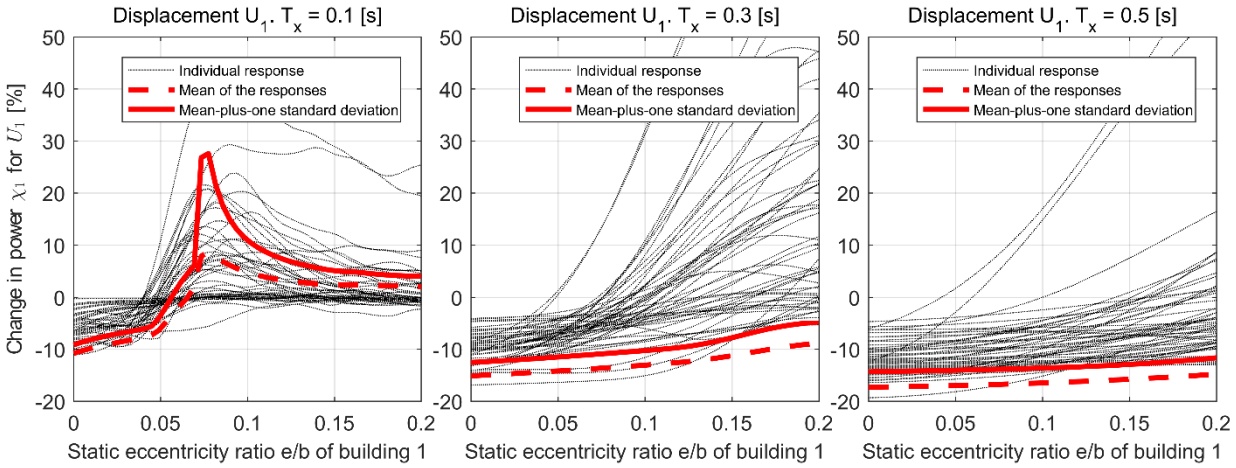

Figure 4.19 Variation of change in displacement power χ_1(e/b,T_x) with the static eccentricity ratio e/b using three different natural periods of the building 1 on rigid foundation T_x - Response for the parameter set (s = 2.0, Ω_b = 0.7, and Ω_0 = 1.2)

Figure 4.20 shows that for low static eccentricity ratios (i.e. $e/b \leq 0.05$) there are favourable effects in the accelerations, where the seismic risk is reduced in building 1 by the presence of a smaller building 2 (i.e. negative values for $\ddot{\chi}_1$). On the other hand, for higher eccentricity ratios (i.e. $e/b > 0.05$) the effects of SSSI are detrimental, producing an increase in the response of up to 40%. This result was not observed in previous studies (Aldaikh et al., 2015; Aldaikh et al., 2016). In most cases, the increase in the response resulting from the eccentricity is larger for stiff structures (low period), compared to flexible structures.

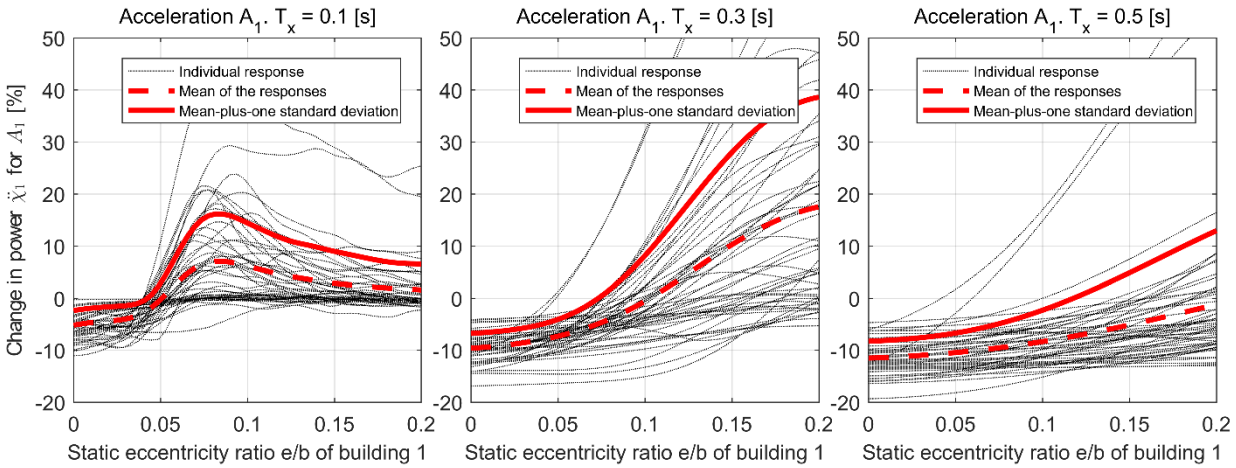

Figure 4.20 Variation of change in acceleration power $\ddot{\chi}_1$(e/b,T_x) with the static eccentricity ratio e/b using three different natural periods of the building 1 on rigid foundation T_x - Response for the parameter set (s = 2.0, Ω_b = 0.7, and Ω_0 = 1.2)

Finally, contour plots in Figure 4.21 and Figure 4.22 display the variation of change in power χ_1 and $\ddot{\chi}_1$, for the displacement U_1 and acceleration A_1 respectively, on top of the building 1. In these graphs, the static eccentricity ratios varying between $e/b = [0,0.2]$ and frequency ratio between the buildings $\Omega_b = \omega_{b1}/\omega_{b2}$ varying between 0.5 and 2.

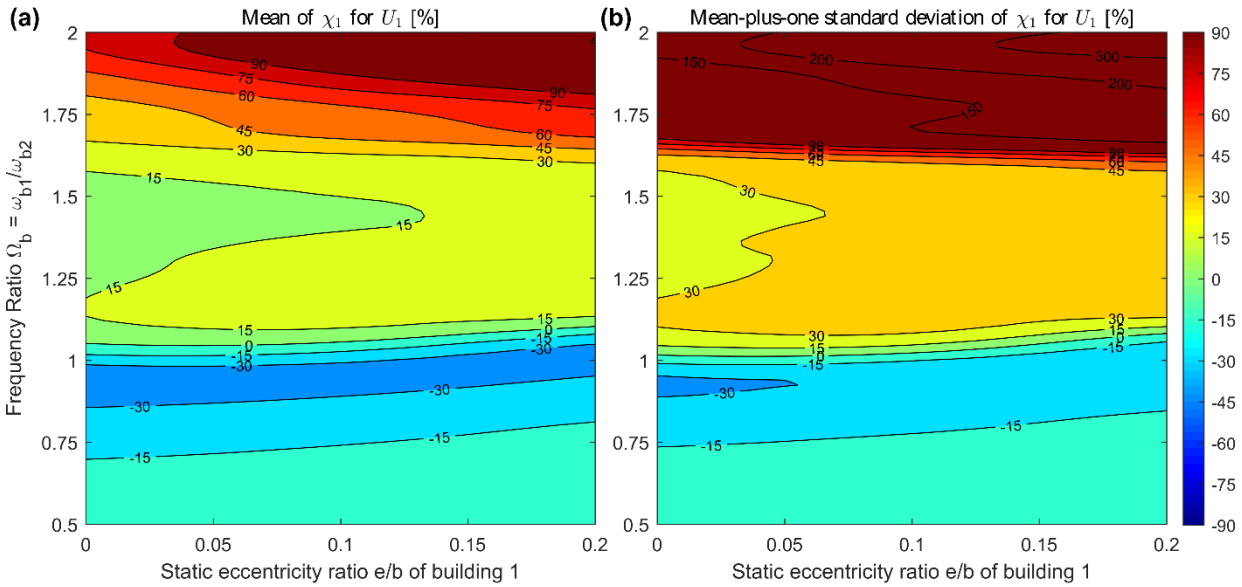

Figure 4.21 (a) Mean and (b) Mean-plus-one standard deviation of the change in displacement power χ_1(e/b,Ω_b) for U_1 as a function of static eccentricity ratio e/b and frequency ratio Ω_b - Response for the parameter set (s = 2.0, T_x = 0.3s, and Ω_0 = 1.2)

As was discussed before, the detrimental effect of SSSI in unsymmetrical-plan structures is significant for (i) frequency ratios greater than 1.0 with any static eccentricity ratios e/b, and (ii) frequency ratio near to 0.7 for torsionally eccentric structures $e/b > 0.1$. On average, the amplification reaches a value of $\ddot{\chi}_1 = 15\%$ and mean-plus-one standard deviation of 35%.

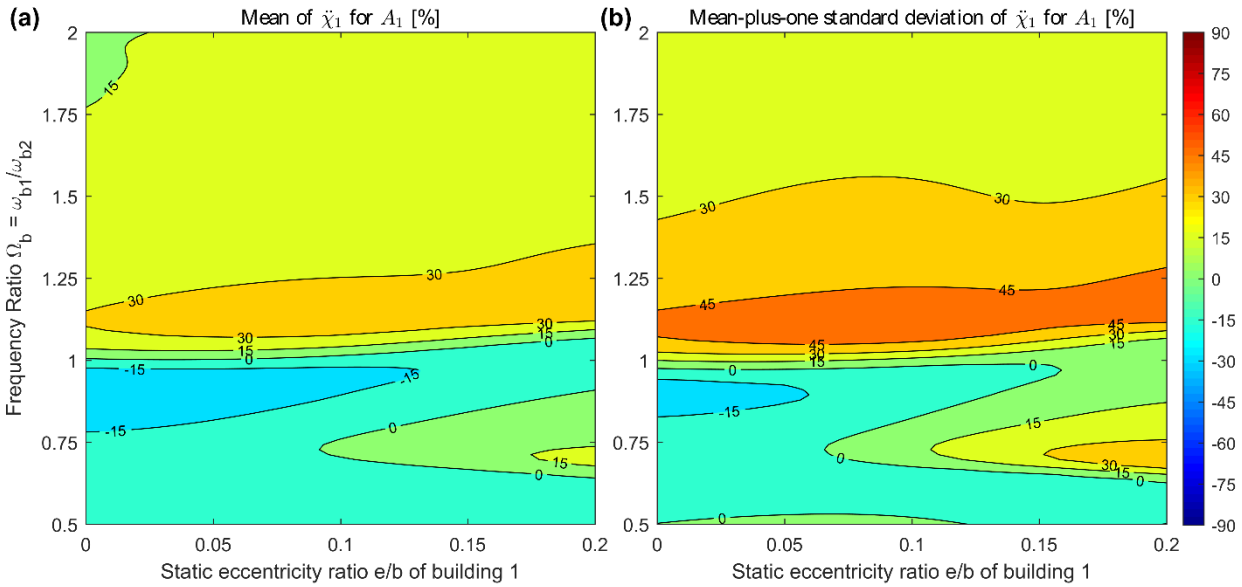

Figure 4.22 (a) Mean and (b) mean-plus-one standard deviation of the change in acceleration power $\ddot{x}_1$(e/b,Ω_b) for A_1 as a function of static eccentricity ratio e/b and frequency ratio Ω_b - Response for the parameter set (s = 2.0, T_x = 0.3s, and Ω_0 = 1.2)

4.4 Summary

In this chapter, a theoretical formulation for Structure-Soil-Structure Interaction (SSSI) between adjacent buildings is presented, that are coupled through the soil in 2D. All results are predicated on the assumptions made in this chapter and cannot be taken as generalizable to all configurations. It is used this two-dimensional reduced-order model to evaluate the effects of torsion upon unsymmetrical structures. 15 strong ground motion events selected from the PEER-NGA have been employed. A single horizontal component of seismic excitation is considered. The parametric exploration undertaken in this research explores the system response behaviour for a large range of buildings' parameters. These dynamic simulations involve over 3 million time-history analyses. The research presented in this chapter has led to the following principal findings:

- The SSSI effect on a tall unsymmetrical building adjacent to a smaller building (i.e. for frequency ratios $\Omega_b < 1.0$) can be adverse (35% increase in the seismic response) or beneficial (-15% reduction). This change in the response depends on the dynamic characteristics of the structure adjacent to the building under consideration. The amplification in building 1's response can be seen as the interaction between the first torsional/sway mode of unsymmetrical building 1 with the first sway mode of the second building when the natural frequencies are close.

- Regardless of the earthquake event, it is found that the most adverse interaction effect occurred when the unsymmetrical building 1 (shorter period) was adjacent to a more flexible building (longer period, $\Omega_b = \omega_{b1}/\omega_{b2} \approx 1.1$). The amplification in the total change in power

(displacement and acceleration) can be as high as 110%. This conclusion is consistent with previous research (Alexander et al., 2013; Aldaikh et al., 2018).

- The SSSI effect has a significant influence on the torsional response in building 1 for a broad range of frequency ratios Ω_b, varying between 0.6 and 2.0 for a static eccentricity ratio equal to $e/b = 0.05$. On average, there is an increase in the torsional response of up to 150%. These effects cannot be observed in symmetric plan buildings considered in previous research (Alexander et al., 2013; Aldaikh et al., 2015; Aldaikh et al., 2016).

- An increase in the buildings' responses resulting from SSSI is insensitive to changes in the torsional frequency ratio Ω_θ. That is to say, the torsionally stiff and flexible structures explored in this chapter behave in a qualitatively similar manner.

- There is evidence to suggest that the power of the earthquake can be passed from the shorter structure to the taller torsionally irregular structure (i.e. for frequency ratios $\Omega_b < 1.0$). This is for static eccentricity ratios larger than $e/b \geq 0.1$. The amplification in response total power of the unsymmetrical building 1 can be as high as 35%.

4.5 Nomenclature

The units correspond to those defined by the International System of Units, where the abbreviations represent [M] mass, [T] time, [L] length and [rad] radians.

α_1	Ratio of soil/foundation to building mass of the building 1 []
α_2	Ratio between the building' mass 2 to building mass 1 []
ϵ_r	Ratio of eccentricity to the radius of gyration ratio for building 1 []
θ_{y1}, θ_{y2}	Rotational degrees of freedom at the base of the buildings 1 and 2 respectively []
θ_{z1}	Rotational degrees of freedom of the building 1's rigid diaphragm []
μ_s	Poison's ratio of the soil []
μ_c	Poison's ratio of the reinforced concrete []
ξ_n	Ratio of critical damping of the system []
ρ_b, ρ_s	Average densities of the buildings and the soil respectively [ML^{-3}]
$\boldsymbol{\Phi}_n$	Modal eigenvector of the linear system []
χ_1	Change in displacement power when moving from uncoupled to coupled state for the building 1 [%]
$\ddot{\chi}_1$	Change in acceleration power when moving from uncoupled to coupled state for the building 1 [%]
ω_{b1}, ω_{b2}	Modal circular frequency parameters for the buildings 1 and 2 respectively [$radT^{-1}$]
ω_s	Circular frequency of soil/foundation for the buildings 1 and 2 [$radT^{-1}$]
ω_θ	Torsional frequency of the building 1 [$radT^{-1}$]
ω_{y12}	Interaction circular frequency ratio parameter [$radT^{-1}$]
ω	Fourier frequency [rad T^{-1}]
ω_n	Natural frequencies of the linear system [rad T^{-1}]
Ω_{y12}	Ratio of interaction frequency parameter to building 1 (ω_{b1}) circular frequency []
Ω_b	Ratio of building 1 (ω_{b1}) to building 2 (ω_{b2}) circular frequencies []
Ω_s	Ratio of soil/foundation frequency to building 1 (ω_{b1}) circular frequency []
Ω_θ	Ratio of the torsional frequency of building 1 to building 1 (ω_{b1}) circular frequency []
A_1	Total acceleration on top of the building 1 [LT^{-2}]
b	Foundation's width for the buildings 1 and 2 [L]
$\mathbf{C}$	Damping matrix of the system in its final form [MT^{-1}]
$\hat{\mathbf{C}}$	Damping matrix of the system [MT^{-1}]
c_1	Density ratio (soil to buildings) parametric constant []
c_2	Soil parametric constant []
C_t	Dimensional factor for the calculation of the natural period of a structure, Eurocode 8 (2004) []
E_s	Total power spectral density []

E_c	Elasticity modulus of the reinforced concrete [$ML^{-1}T^{-2}$]
e	Static eccentricity of the building 1 [L]
G_s	Shear modulus of the soil [$ML^{-1}T^{-2}$]
h_1, h_2	Total heights of the buildings 1 and 2 respectively [L]
I_p	Polar moment of inertia of the building 1 [L^4]
$\mathbf{K}$	Stiffness matrix of the system in its final form [MT^{-2}]
$\widehat{\mathbf{K}}$	Stiffness matrix of the system [MT^{-2}]
K_{b1}, K_{b2}	Total lateral stiffnesses of buildings 1 and 2 respectively [MT^{-2}]
K_θ	Torsional stiffness of building 1 with respect to the center of mass [$M\ L^2T^{-2}$]
$K_{\theta R}$	Torsional stiffness of building 1 with respect to the center of stiffness [$M\ L^2T^{-2}$]
k_s	Soil/foundation rotational stiffness in absence of buildings interaction [ML^2T^{-2}]
k_{y1}, k_{y2}	Rotational soil stiffnesses of the soil beneath the buildings 1 and 2 respectively [ML^2T^{-2}]
k_{y12}	Inter-building soil rotational spring between the buildings 1 and 2 [ML^2T^{-2}]
$\bar{k}_{xi}, \bar{k}_{yi}$	Lateral stiffness for the *i*th resisting element in the *x*-direction and *y*-direction respectively [MT^{-2}]
$\mathbf{M}$	Mass matrix of the system in its final form [M]
$\widehat{\mathbf{M}}$	Mass matrix of the system [M]
M_w	Moment magnitude scale of the earthquake
m_{b1}, m_{b2}	Total modal masses of the buildings 1 and 2 respectively [M]
m_{s1}, m_{s2}	Soil/foundation masses of the buildings 1 and 2 respectively [M]
N_x, N_y	Number of resisting elements in each direction for the buildings 1 and 2 respectively []
$\mathbf{p}$	Force vector of the system in its final form [M]
$\widehat{\mathbf{p}}$	Force vector of the system [M]
q_2, q_κ	Interaction functions that depend on the inter-building distance ζ []
r_1, r_2	Soil/foundation mass radius of gyration for the buildings 1 and 2 respectively [L]
r_{z1}	Radius of gyration of the system plan about the vertical axis for the building 1 [L]
s	Aspect ratio. Height to width ratio of the building 1 []
T_E	System kinematic energy [ML^2T^{-2}]
T_x	Fundamental period of the structure on a rigid foundation [T]
t	Time [T]
U_1	Total displacements on top of building 1 [L]
U_E	System potential energy [ML^2T^{-2}]
$U_1(\omega)$	Fourier transform of $U_1(t)$
V_s	Shear wave velocity of the soil [LT^{-1}]
$\bar{V}_s$	Normalised shear wave velocity of the soil []
x_1, x_2	Horizontal displacement (degrees of freedom) of the top of buildings 1 and 2 respectively [L]

x_g Horizontal ground displacement time series [L]

x_s Separation between the resisting elements [L]

$\bar{x}_i$ Distance from the CM of the building 1 for the resisting elements '*i*' [L]

$\ddot{x}_g$ Horizontal acceleration ground motion [LT^{-2}]

$\mathbf{x}$ Degrees of freedom (vector) of the system [L]

$\bar{y}_i$ Distance from the CM of the building 1 for the resisting elements '*i*' [L]

ζ Inter-building distance coefficient []

Chapter 5

Dynamic interaction between adjacent buildings through nonlinear soil during earthquakes

---

The contents of this chapter have been adapted from that published in:

Vicencio, F., and Alexander, N.A. (2018a). Dynamic interaction between adjacent buildings through nonlinear soil during earthquakes. *Soil Dynamics and Earthquake Engineering,* 108, 130-141.

Part of the introduction has been removed and included in Chapter 2 - Literature Review.

5.1 Introduction to nonlinear analysis

The interchange of energy between the soil and the structure during nonlinear dynamical responses is an essential issue in earthquake engineering. The soil/foundation has complex dynamic characteristics and plays an important role in determining the seismic loads on a structure. It has a nonlinear stress-strain relation (constitutive model) under cyclic loading conditions, i.e. backbone curve or cyclic degradation of the shear modulus and energy dissipation (Kramer, 1996). Laboratory tests have shown that soil stiffness is influenced by cyclic strain amplitude, mean principal effective stress, and the number of loading cycles, among other factors. Although the equivalent linear type of analysis is the most popular, it has some well-known limitations for the case of large magnitude earthquake excitation. Several researchers, like Pedretti (1998), Cremer et al. (2001, 2002), and Gajan et al. (2005) among others, have extensively investigated Soil-Structure Interaction (SSI) by explicitly considering the soil-foundation modelling through nonlinear macro-elements. However, this analysis does not consider the interaction of adjacent buildings via the underlying soil during an earthquake.

Experimental tests of specific building/foundation configurations and computational models have been used in the study of SSSI considering the nonlinear behaviour of soil and structure. For a complete bibliographic review, please refer to Chapter 2. However, modelling a whole class of building configurations, in a large-scale parametric nonlinear study, is very difficult in general. Thus, large-scale parametric explorations of this problem require a different approach that prioritizes computational efficiency. The alternative is to use SSSI models, with a relatively limited number of degrees of freedom (DOFs), for a complete parametric nonlinear study. These low-order models (i) capture the most significant dynamic behaviour, (ii) have a relatively small number of system parameters, and (iii) are computationally simple enough for exploring a vast number of generic cases. These parametric studies should be viewed as an initial exploration of the problem. They are not meant to replace advanced computational models and experimental work of specific cases.

5.1.1 Aims

In this chapter, the previous linear study on the SSSI of two buildings presented in the paper of Alexander et al. (2013) is extended, to the case of nonlinear soil behaviour underneath buildings using the phenomenological Bouc-Wen model (Baber and Wen, 1981). In addition, seismic ground motions rather than the Kanai-Tajimi artificial ground motion are now employed. In this new parametric study, over 20 thousand different nonlinear systems are explored. This model spans an extensive range of geometric cases, and three different soil classes are considered. This computationally challenging study required the High-Performance Computing (HPC) machine, BlueCrystal, belonging to the Advance Computing Research Centre (ACRC) at the University of Bristol. The code used in this study was developed in MATLAB

(2016). The stiff nonlinear equations of motion for each model were solved using MATLAB's ode15s (solver for stiff ordinary differential equations) integrator. To prevent the substantial computational costs that are produced when solving the nonlinear equations, a single spectrally matched ground motion is employed (to the Eurocode 8 elastic response spectrum) rather than multiple ground motion records, for the nonlinear time-history analyses. Additionally, the cases where inelastic behaviour occurs in the soil directly underneath the building's foundations are considered rather than within the buildings. Also, the building structures are considered to act linearly.

The aims of this chapter are to answer the following questions.

(i) Does the introduction of soil nonlinearity reduce the size of adverse/beneficial SSSI effects to a level at which it can be safely neglected?

(ii) Is there evidence to suggest significant differences between nonlinear SSSI (the coupled building case) and nonlinear SSI (the uncoupled building case) analyses?

5.2 A theoretical nonlinear reduced-order model for SSSI

5.2.1 Non-dimensional equations of motion

The system shown in Figure 5.1 is described in terms of four generalised coordinates (or degrees of freedom, DOFs) namely x_j for the translational DOFs and θ_j for the rotational DOFs, with $j \in [1,2]$. A known ground displacement field x_g is applied at both foundations, i.e. wave passage effects and spatially heterogeneous ground displacements are neglected in the present work. The effects of the horizontal and vertical stiffness of the foundations are not considered in this chapter, mainly because they are not relevant in the SSSI phenomenon (Aldaikh et al., 2015). The kinetic energy T_E and potential energy U_E for this system are given by the equations (5-1) and (5-2) respectively. The total kinetic energy can be specified as the sum of (i) the translational kinetic energy of each building's mass and (ii) the rotational energy of each soil/foundation mass. The potential energy is the sum of (i) the internal work due to the buildings' deformation, (ii) the nonlinear energy of the foundation springs underneath the buildings, and (iii) the differential rotation between the buildings.

$$T_E = \frac{1}{2}\sum_{j=1}^{2}\left(m_{bj}\left(\dot{x}_j + \dot{x}_g - h_j\dot{\theta}_j\right)^2 + m_{sj}r_j^2\theta_j^2\right) \quad \textbf{(5-1)}$$

$$U_E = \sum_{j=1}^{2} \left(\frac{1}{2} k_{bj} x_{j1}^2 + \int M_j d\theta_j \right) + \frac{1}{2} \kappa (\theta_2 - \theta_1)^2 \quad \textbf{(5-2)}$$

where h_1 and h_2 are the heights, and m_{b1} and m_{b2} are the structure' lumped masses (i.e. the generalised masses of the fundamental modes) of the buildings 1 and 2 respectively. The terms m_{s1} and m_{s2} are the soil/foundation masses underneath buildings 1 and 2, r_j are the soil/foundation mass's radii of gyration, $m_{sj} r_j^2$ are the soil/foundation mass polar second moments of area (moments of inertia). k_{bj} are the linear building lateral stiffnesses (i.e. the generalised stiffnesses of the fundamental modes), κ is the stiffness of inter-building soil rotational spring, ζb_1 is the inter-building distance, and b_j are the foundations' widths.

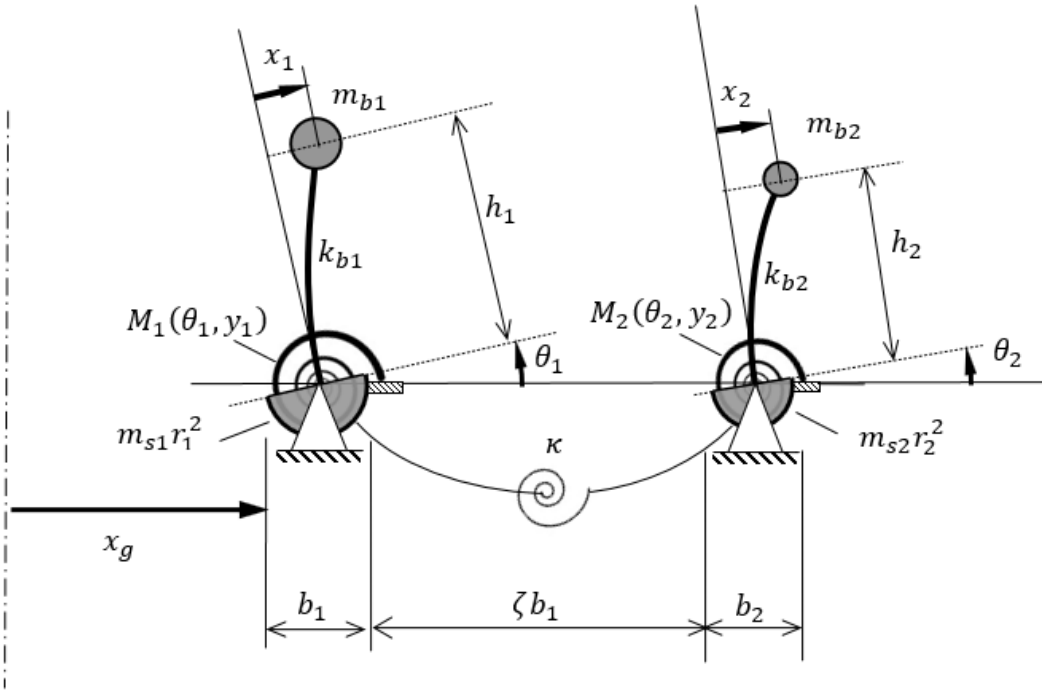

Figure 5.1 Structural model of a two-building system subjected to horizontal ground motion

The terms $M_j(\theta_j(t), y_j(t))$ are the nonlinear moments at the support springs. These springs are related to the rotational spring stiffnesses of soil beneath buildings 1 and 2. The terms $y_j(t)$ are the internal hysteretic rotations (history-dependent of rotations θ_j) at time t, that controls the nonlinear response of the soil. In this thesis, it is assumed that the stiffness associated with the inter-building interaction κ through the soil is linear. The rationale behind this is that the soil strains between buildings are likely to be far smaller than those directly under the footing. Hence, the system's nonlinear behaviour is presumed encapsulated by a nonlinear Bouc-Wen spring model for the footings alone, and a linear interaction spring model between the foundations of the type of Alexander et al. (2013). At the moment, there does not exist a discrete nonlinear interaction spring model in the literature. Nevertheless, the effects of non-linearity on soil response between the buildings due to earthquake size could be incorporated within the linear coupling

using a reduced G_s value, even though this option was not done in this research. It is also worth noting that an analytical formulation for the linear interaction spring between the buildings in two dimensions has been derived by Aldaikh et al. (2018). Note that an updated and extended 3D version of the coupled springs will be calculated in Chapter 6.

The Euler-Lagrange equation of motion that defines the dynamics of the discretised system can be derived in the standard way by calculus and is written, in matrix form, as follows,

$$\widehat{\mathbf{M}}\ddot{\mathbf{x}} + \hat{\mathbf{C}}\dot{\mathbf{x}} + \widehat{\mathbf{K}}\mathbf{x} + \hat{\mathbf{q}}(\theta, y) = \hat{\mathbf{f}}\ddot{x}_g \tag{5-3}$$

where the system matrices $\widehat{\mathbf{M}}$, $\widehat{\mathbf{K}}$, and the vectors $\hat{\mathbf{q}}$, $\hat{\mathbf{f}}$, and $\mathbf{x}$ are defined as follows,

$$\widehat{\mathbf{M}} = \begin{bmatrix} m_{b1} & -m_{b1}h_1 & 0 & 0 \\ -m_{b1}h_1 & m_{b1}h_1^2 + m_{s1}r_1^2 & 0 & 0 \\ 0 & 0 & m_{b2} & -m_{b2}h_2 \\ 0 & 0 & -m_{b2}h_2 & m_{b2}h_2^2 + m_{s2}r_2^2 \end{bmatrix} \tag{5-4}$$

$$\widehat{\mathbf{K}} = \begin{bmatrix} k_{b1} & 0 & 0 & 0 \\ 0 & \kappa & 0 & -\kappa \\ 0 & 0 & k_{b2} & 0 \\ 0 & -\kappa & 0 & \kappa \end{bmatrix} \tag{5-5}$$

$$\hat{\mathbf{q}}(\theta, y) = \begin{bmatrix} 0 \\ B_1 k_{s1}\theta_1 \\ 0 \\ B_2 k_{s2}\theta_2 \end{bmatrix} + \begin{bmatrix} 0 \\ (1-B_1)k_{s1}y_1 \\ 0 \\ (1-B_2)k_{s2}y_2 \end{bmatrix}, \quad \hat{\mathbf{f}} = \begin{bmatrix} -m_{b1} \\ m_{b1}h_1 \\ -m_{b2} \\ m_{b2}h_2 \end{bmatrix}, \quad \mathbf{x} = \begin{bmatrix} x_1 \\ \theta_1 \\ x_2 \\ \theta_2 \end{bmatrix}, \tag{5-6}$$

where y_j are the internal degrees of freedom that control the nonlinear response of the soil, $0 \leq \mathrm{B}_j \leq 1$ is the ratio of linear to nonlinear response (defined below according to the Bouc-Wen model). If the term B_j is considered equal to one, the vector $\hat{\mathbf{q}}(\theta, y)$ becomes linear, in the same way as the rest of the structural system. The rotational stiffnesses k_{sj} defined in equation (5-7) are obtained by using an empirical formula deducted by Pais and Kausel (1988), for the rotational stiffness coefficients of soil beneath buildings 1 and 2. G_s is the initial tangent shear modulus of the soil (typically called $G_0 = \rho_s V_s^2$ in the literature, Kramer (1996)), ρ_s is the soil density, and μ_s is the Poisson's ratio of the soil.

$$k_{sj} = \frac{1}{2}\frac{G_s b_j^3}{1-\mu_s} \tag{5-7}$$

The dimensional form of the equation (5-3) contains too many system parameters for a large nonlinear parametric study. Therefore, a reduction of the number of parameters through a process of removing all system dimensions is required. The nonlinear moment/rotation function $M_j(\theta_j(t), y_j(t))$ shall be replaced

by the following term described in equation (5-8), where $q_j(\theta_j(t), y_j(t))$ is a non-dimensional nonlinear moment/rotation functions of the soil/foundation and k_{sj} are the initial linear rotational stiffnesses of soil beneath buildings, when the rotation $\theta_j = 0$ at time $t = 0$.

$$M_j\left(\theta_j(t), y_j(t)\right) = k_{sj} q_j\left(\theta_j(t), y_j(t)\right) \tag{5-8}$$

The following non-dimensional parameter groups can be introduced as follows,

$$\eta_j = \frac{h_j}{r_j}, \quad \alpha_j = \frac{m_{sj}}{m_{bj}}, \quad \beta = \frac{r_1}{r_2}, \quad \lambda = \frac{m_{b2} r_2^2}{m_{b1} r_1^2} \tag{5-9}$$

where η_j are the height to radius of gyration ratios, α_j are the soil to building mass ratios, β is the radius of gyration ratio, and λ is the mass polar moment of inertia ratio. The frequency parameters of the system are given as,

$$\omega_{b1}^2 = \frac{k_{b1}}{m_{b1}}, \quad \omega_{s1}^2 = \frac{k_{s1}}{m_{s1} r_1^2}, \quad \omega_{b2}^2 = \frac{k_{b2}}{m_{b2}}, \quad \omega_{s2}^2 = \frac{k_{s2}}{m_{s2} r_2^2}, \quad \varpi^2 = \frac{\kappa}{m_{b1} r_1^2} \tag{5-10}$$

In the same way, the frequency ratios normalised by ω_{b1} are introduced,

$$\Omega_b = \frac{\omega_{b2}}{\omega_{b1}}, \quad \Omega_{s1} = \frac{\omega_{s1}}{\omega_{b1}}, \quad \Omega_{s2} = \frac{\omega_{s2}}{\omega_{b1}}, \quad \Omega_0 = \frac{\varpi}{\omega_{b1}} \tag{5-11}$$

The fundamental natural period of a structure T_x in seconds, on a rigid foundation (i.e. with no soil/foundation rotation, equivalent to $\theta_1 = \theta_2 = 0$), is equal to the empirical relationship $T_x = n_s/10\ [s]$. This relationship is calculated according to the SEAOC Bluebook (1976), where n_s is the number of storeys of the buildings. The height of the buildings is taken in meters and the average storey height equals 3.2m. The period has a relationship with the lateral frequency of the building as $\omega_{b1} = 2\pi/T_x$. Therefore, the fundamental natural frequencies on a rigid base are defined in equation (5-12) for buildings 1 and 2 in terms of the buildings' heights.

$$\omega_{b1} \approx \frac{200}{h_1}, \quad \omega_{b2} \approx \frac{200}{h_2} \tag{5-12}$$

Finally, the following change of variables presented in equation (5-13) are introduced, that completes the full non-dimensionalisation of the problem. Where ω_{b1} is the modal circular frequency on a fixed base (i.e. with no soil/foundation rotation) of the building 1, u_j are non-dimensional relative displacements of buildings to ground, and u_g is the non-dimensional horizontal ground displacement (absolute).

$$x_j = r_j u_j, \;\; x_g = r_1 u_g, \;\; \tau = \omega_{b1} t \tag{5-13}$$

Therefore, after some calculus, the Euler-Lagrange equations of motion can be stated thus,

$$\mathbf{M\ddot{u}} + \mathbf{C\dot{u}} + \mathbf{Ku} + \mathbf{q}(\theta, y) = \mathbf{f}\ddot{u}_g \tag{5-14}$$

where Newtonian dots above now indicate derivatives with respect to scaled time τ, i.e. $(\dot{\bullet}) = \partial \bullet / \partial \tau$ and $(\ddot{\bullet}) = \partial^2 \bullet / \partial \tau^2$.

The matrices **M**, **K**, and vectors **u**, and **f** for the equation (5-14) are stated as follows,

$$\mathbf{M} = \begin{bmatrix} 1 & -\eta_1 & 0 & 0 \\ -\eta_1 & \alpha_1 + \eta_1^2 & 0 & 0 \\ 0 & 0 & \lambda & -\eta_2 \lambda \\ 0 & 0 & -\eta_2 \lambda & \lambda(\alpha_2 + \eta_2^2) \end{bmatrix}, \qquad \mathbf{u} = \begin{bmatrix} u_1 \\ \theta_1 \\ u_2 \\ \theta_2 \end{bmatrix} \tag{5-15}$$

$$\mathbf{K} = \begin{bmatrix} 1 & 0 & 0 & 0 \\ 0 & \Omega_0^2 & 0 & -\Omega_0^2 \\ 0 & 0 & \lambda \Omega_b^2 & 0 \\ 0 & -\Omega_0^2 & 0 & \Omega_0^2 \end{bmatrix}, \qquad \mathbf{f} = \begin{bmatrix} -1 \\ \eta_1 \\ -\lambda \beta \\ \eta_2 \lambda \beta \end{bmatrix} \tag{5-16}$$

The system's linear viscous damping matrix **C** defined in equation (5-14) assumes that each natural mode $n \in [1,4]$ is damped at $\xi_n = 0.05$ of critical damping, $\boldsymbol{\phi}_n$ is the modal vector of the mode *n*, and ω_n are the natural frequencies of the linear systems. These ω_n were calculated considering the completely elastic system described in Alexander et al. (2013). Thus, the Caughey damping matrix **C** can be calculated as equation (5-17), according to Chopra (2000),

$$\mathbf{C} = \mathbf{M}\left(\sum_{n=1}^{4} \frac{2\xi_n \omega_n}{\boldsymbol{\phi}_n^T \mathbf{M} \boldsymbol{\phi}_n} \boldsymbol{\phi}_n \boldsymbol{\phi}_n^T \right) \mathbf{M} \tag{5-17}$$

This viscous model includes the linear contribution to damping. Additional nonlinear contributions to damping of the soil are provided by the Bouc-Wen hysteretic model. The nonlinearity in the equation (5-14) is contained in the non-dimensional version of the vector $\mathbf{q}(\theta_j, y_j)$, that is defined as,

$$\mathbf{q}(\theta_j, y_j) = \begin{bmatrix} 0 \\ B_1 \Omega_{s1} \theta_1 \\ 0 \\ B_2 \Omega_{s2} \theta_2 \end{bmatrix} + \begin{bmatrix} 0 \\ (1 - B_1) \Omega_{s1} y_1 \\ 0 \\ (1 - B_2) \Omega_{s2} y_2 \end{bmatrix} \tag{5-18}$$

Note that both linear and nonlinear support rotational moment/rotation relationships are contained in the vector $\mathbf{q}(\theta, y)$. If $B_j = 1$, then this system reduces to a linear system described in the reference Alexander et al. (2013).

5.2.2 Bouc-Wen model for nonlinear soil rotational springs

The Bouc-Wen hysteretic model, in all its various forms, Bouc (1967), Wen (1976), Baber and Wen (1981), Baber and Noori (1986), Ma et al. (2004), and Ismail et al. (2009), is widely used in the literature for systems that exhibit inelastic behaviour under severe cyclic loads. The attractiveness of this approach is that it employs a first-order differential equation in terms of an 'internal hysteretic' variable y_j to describe, qualitatively the phenomenological nonlinear hysteretic behaviour. The model reproduces the nonlinear hysteretic behaviour of a variety of soils, and it is capable of representing complex patterns such as stiffness and strength degradation with cycling loading. This approach contrasts with the "rule-based" hysteretic models of Takeda et al. (1970), Ramberg and Osgood (1943), and others that require more complex coding than the Bouc-Wen model.

The non-dimensional nonlinear moment/rotation function, of *j*th building foundation, is described by the following Bouc-Wen nonlinear differential equation.

$$\dot{y}_j = \frac{1}{\gamma_y}\frac{D_j\dot{\theta}_j - \upsilon(E)\left(\varsigma_j|\dot{\theta}_j||y_j|^{n_j}\mathrm{sgn}(y_j) + \psi_j\dot{\theta}_j|y_j|^{n_j}\right)}{\eta(E)} \qquad \textbf{(5-19)}$$

In the above expression, γ_y is the soil strain at the initiation of nonlinear behaviour in the soil. This value has been defined by various studies in the literature, e.g. the papers of Hardin and Drnevich (1972), Ishibashi and Zhang (1993), and Tatsuoka et al. (1993), among others. In these nonlinear analyses presented here, the typical value of $\gamma_y = 10^{-4}$ for sand is adopted. The terms $[D_j, \varsigma_j, \psi_j, n_j]$ represent the dimensionless Bouc-Wen parameters that define the shape of the hysteretic stress-strain loops. The parameter B_j is the ratio of linear to nonlinear response, δ_v is the strength degradation parameter and δ_η is the stiffness degradation parameter. The terms $\nu(E)$ and $\eta(E)$ defined in equation (5-20) characterise the degradation shape functions that are dependent on the dissipated hysteretic energy $E(\tau)$ from initial time $\tau = 0$ to the present time τ.

$$E(\tau) = \int_0^\tau y\dot{\theta}\,d\tau\,,\ \ \upsilon(E) = 1 + \delta_v E(\tau),\ \ \eta(E) = 1 + \delta_\eta E(\tau) \qquad \textbf{(5-20)}$$

In this chapter dedicated to nonlinear analysis, the values for Bouc-Wen parameters originally proposed by Gerolymos and Gazetas (2005) and validated by Gerolymos and Gazetas (2007) and Drosos et al. (2012) are used. The numerical values of these parameters are listed in Table 5-1.

Table 5-1 Bouc-Wen nonlinear soil model parameters

Soil	γ_y	D_j	B_j	ς_j	ψ_j	δ_v	δ_η	n_j
Sand	10^{-4}	1	0.02	0.5	0.5	0.01	0.01	0.6

These parameters' values give a reasonable shape for soil spring and damping stress-strain curves for all examined soil profiles (different types of sands, dense, medium, and loose). In addition, these values provide a good representation of the complex nonlinear characteristics of the cyclic behaviour of the soil element. The process of parameter calibration consists of an optimization method to fit the Bouc-Wen response with the shear modulus reduction and damping curves obtained from i) laboratory experimental tests, ii) in situ tests, and iii) recorded free-field response, iv) centrifuge or large shaking table soil response. Note that the Bouc-Wen model do not represent any physically system, so the identification and calibration of the model parameters is a compulsory task. This calibration was already performed by Gerolymos and Gazetas (2005) and validated by Gerolymos and Gazetas (2007) and Drosos et al. (2012) for different types of soils (clays and sands). Figure 2.11 and Figure 2.12 depicted the good fit of the calibration prevously performed by Gerolymos and Gazetas (2005). Due to a reduced set of soils (sand with different densities and shear velocities) is being used in this research and that does not represent any particular site or experimental observations; the calibration is considered acceptable given the properties of the soil used.

5.2.3 Reduced parametric form

Equation (5-14) is expressed in terms of ten linear system parameters η_1, η_2, α_1, α_2, λ, Ω_0, Ω_b, Ω_{s1}, Ω_{s2}, and ω_{b1} plus the eight constants that define the Bouc-Wen model. Additionally, the ground excitation has its own statistical descriptors which can be viewed as further system parameters. Therefore, there have an extremely large system parameter space to explore for a comprehensive nonlinear parametric study. To reduce this number, the procedure described by Alexander et al. (2013) is followed, where the scope of this analysis is limited by assuming that:

(v) The same soil profile exists under both buildings, this means $k_{s1} = k_{s2}$.

(vi) Both buildings have a similar square plan area and raft foundations of b^2, this means $m_{s1} = m_{s2}$ and $r_1 = r_2 = 0.33b$.

(vii) Both buildings have the same average density of ρ_b.

(viii) The buildings can be of different heights, h_j.

(ix) The buildings are spaced at some arbitrary distance from each other, ζb, where ζ is the non-dimensional inter-building distance.

(x) The mean system response to a set of ground motion time series is estimated by using a single spectrally matched ground motion time series.

The parameters η_1, η_2 can be contracted into two geometric parameters, the Height ratio $\varepsilon = h_2/h_1$ and the Aspect ratio $s = h_1/b$.

$$\eta_1 = 3s, \;\; \eta_2 = 3\varepsilon s, \;\; \varepsilon = \frac{h_2}{h_1}, \;\; s = \frac{h_1}{b} \qquad \textbf{(5-21)}$$

Newmark and Rosenblueth (1971) proposed that the dynamic mass of soil beneath buildings is equal to $m_s = 0.35b^3\rho_s$, for a square base building. The mass of the buildings can be calculated as $m_{bj} = \rho_b h_j b^2$, where ρ_s and ρ_b are the densities of soil and building respectively. Based on typical spans and floor loading, the average building density is $\rho_b = 400 - 800[kg/m^3]$. Therefore, the proportionality constant c_1 is defined in equation (5-22). In the same way, the parameters α_1, α_2 are rewritten as specified in equation (5-22). The numerical values of c_1 are indicated in Table 5-2 for the different soil classes.

$$c_1 = 0.35\frac{\rho_s}{\rho_b}, \;\; \alpha_1 = \frac{c_1}{s}, \;\; \alpha_2 = \frac{c_1}{\varepsilon s} \qquad \textbf{(5-22)}$$

The interaction spring κ is modelled using an inverse cube relationship between κ and k_{s1}, by Alexander et al. (2013). Note that the function $q_2(\zeta)$ expresses the stiffening of the rotational soil stiffnesses k_{s1} and k_{s2} as the building foundations move closer together. The term $q_\kappa(\zeta)q_2(\zeta)$ represent the stiffening of the negative interaction spring κ as building foundations move close together. These functions are depicted in Figure 5.2.

$$\kappa = q_k(\zeta)q_2(\zeta)k_s, \;\; k_{s1} = q_2(\zeta)k_s, \;\; q_k(\zeta) = \frac{-0.25}{(1+\zeta)^3}, \;\; q_2(\zeta) = 1 + \frac{0.5}{(1+\zeta)^3} \qquad \textbf{(5-23)}$$

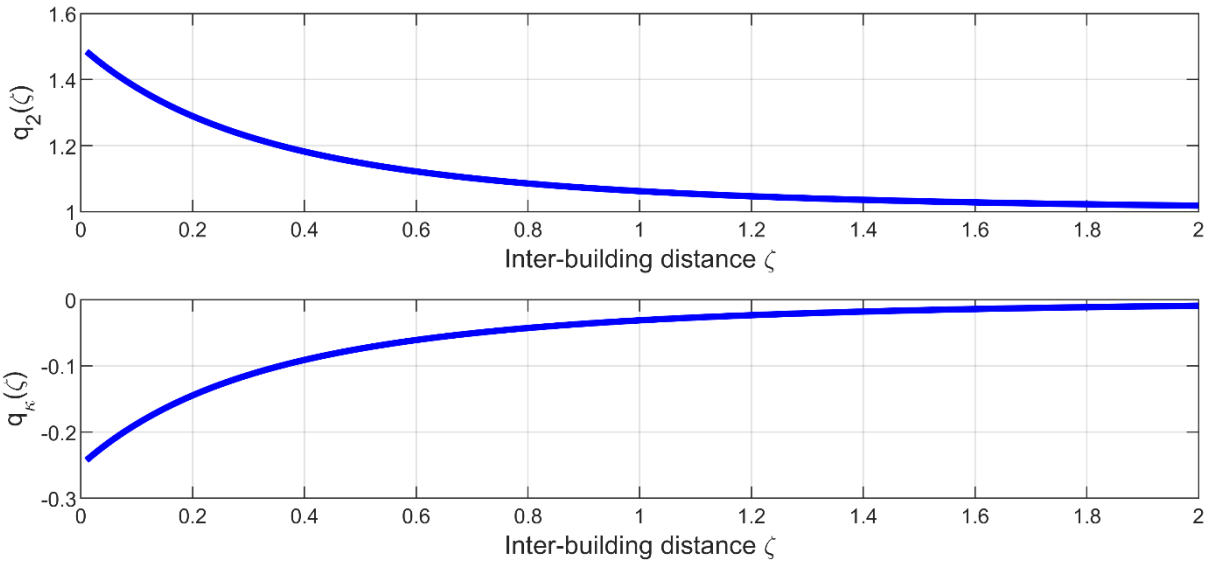

Figure 5.2 Variation of the coefficient $q_2(\zeta)$ and $q_\kappa(\zeta)$ with the inter-building distance ζ

In Chapter 6 an updated 3D version for the values of the interaction spring κ and the rotational soil stiffnesses of soil k_{s1} was presented.

The soil frequency ratios can be expressed as,

$$\omega_{s1}^2 = \omega_{s2}^2 = \frac{k_{s1}}{m_{s1} r_1^2} = \frac{\frac{1}{21-\mu_s} G_s b^3 q_2}{(0.35 b^3 \rho_s)(0.33b)^2} = 13.1 \times 10^6 \frac{1}{1-\mu_s} \frac{1}{b^2} q_2 \overline{V}_s^2 \qquad \textbf{(5-24)}$$

where $\overline{V}_s$ is the normalised non-dimensional shear wave velocity (to a reference of 1000 m/s) and V_s is shear wave velocity of the soil in [m/s]. The ratio of foundation radii of gyration β and the ratio of foundation mass polar moments of inertia λ are contracted and re-expressed in terms of,

$$V_s^2 = \frac{G_s}{\rho_s}, \quad \overline{V}_s = \frac{V_s}{1000}, \quad \lambda = \varepsilon, \quad \beta = \frac{r_2}{r_1} = 1 \qquad \textbf{(5-25)}$$

The frequency ratio parameters Ω_0, Ω_b, Ω_{s1} and Ω_{s2} can be express as,

$$\Omega_{s1}^2 = \Omega_{s2}^2 = \frac{\omega_{s1}^2}{\omega_{b1}^2} = \frac{13.1 \times 10^6 \frac{1}{1-\mu_s} \frac{1}{b^2} q_2 \overline{V}_s^2}{\left(\frac{200}{h_1}\right)^2} = c_2 q_2 s^2 \overline{V}_s^2, \qquad \Omega_b = \frac{1}{\varepsilon} \qquad \textbf{(5-26)}$$

$$\Omega_0^2 = \frac{\kappa}{\omega_{b1}^2 m_{b1} r_1^2} = \frac{\frac{1}{21-\mu_s} G_s b^3 q_2 q_\kappa}{\left(\frac{200}{h_1}\right)^2 (h_1 b^2 \rho_b)(0.33b)^2} = c_1 c_2 q_2 q_\kappa s \overline{V}_s^2 \qquad \textbf{(5-27)}$$

where the term $c_2 = 327.5/(1-\mu_s)$. The shear wave velocity V_s of the soil and the soil constant c_2 are defined in Table 5-2 for the different soil classes. The values of Poisson's ratio were obtained from the values suggested by Bowles (1997).

Table 5-2 Linear elastic stiffness parameters for soil classes

Soil Class (sand)	$\rho_s[kg/m^3]$	μ_s []	c_1 []	c_2 []	V_s $[m/s]$
Dense	2000	0.35	1.17	503.8	325
Medium	1600	0.30	0.93	468	250
Loose	1300	0.30	0.76	468	156

Therefore, the system matrices (5-14) are re-expressed in terms of three geometric non-dimensional parameters and one site classification. This reduction of parameters allows performing an intensive study that explores a huge range of generic cases. These parameters are listed as follows:

(i) The aspect ratio $s = h_1/b$ (for building 1).

(ii) The height ratio $\varepsilon = h_2/h_1$ between the buildings 2 to 1.

(iii) The normalised inter-building distance ratio ζ (the ratio of distance between buildings to buildings' width).

(iv) The soil class that is defined using c_1, c_2, $\bar{V}_s$, ρ_s and μ_s (see Table 5-2).

Therefore, the matrices and vectors for the equation (5-14) can be stated as follows,

$$\mathbf{M} = \begin{bmatrix} 1 & -3s & 0 & 0 \\ -3s & c_1 s^{-1} + 9s^2 & 0 & 0 \\ 0 & 0 & \varepsilon & -3\varepsilon^2 s \\ 0 & 0 & -3\varepsilon^2 s & c_1 s^{-1} + 9\varepsilon^3 s^2 \end{bmatrix} \tag{5-28}$$

$$\mathbf{K} = \begin{bmatrix} 1 & 0 & 0 & 0 \\ 0 & \Omega_0^2 & 0 & -\Omega_0^2 \\ 0 & 0 & \varepsilon^{-1} & 0 \\ 0 & -\Omega_0^2 & 0 & \Omega_0^2 \end{bmatrix}, \quad \mathbf{f} = \begin{bmatrix} -1 \\ 3s \\ -\varepsilon \\ 3\varepsilon^2 s \end{bmatrix} \tag{5-29}$$

The nonlinear vector $\mathbf{q}(\theta, y)$ in its non-dimensional form can be evaluated as:

$$\mathbf{q}(\theta, y) = B_1 c_1 c_2 q_2 s\overline{V}_s^2 \begin{bmatrix} 0 & 0 & 0 & 0 \\ 0 & 1 & 0 & 0 \\ 0 & 0 & 0 & 0 \\ 0 & 0 & 0 & 1 \end{bmatrix} \begin{bmatrix} u_1 \\ \theta_1 \\ u_2 \\ \theta_2 \end{bmatrix} + (1 - B_1) c_1 c_2 q_2 s\overline{V}_s^2 \begin{bmatrix} 0 & 0 & 0 & 0 \\ 0 & 1 & 0 & 0 \\ 0 & 0 & 0 & 0 \\ 0 & 0 & 0 & 1 \end{bmatrix} \begin{bmatrix} u_1 \\ y_1 \\ u_2 \\ y_2 \end{bmatrix} \quad \textbf{(5-30)}$$

5.2.4 Defining system performance measures

This research aims to evaluate the change in the response between the coupled (SSSI) and uncoupled (SSI) systems. For this purpose, the solution of the equation of motion (5-14) is calculated. Then, the responses of buildings 1 and 2 without the coupled effects are evaluated. To obtain the uncoupled system response (SSI case) could be computed through either (i) set the rotational interaction spring κ equal to zero (i.e. $q_\kappa = 0$ and $q_2 = 1$) or (ii) increasing the inter-building distance ζ to a very large value. In this research to evaluate the SSI response (without coupled interaction), the rotational interaction spring κ equal to zero was employed.

In this research the following performance measures are employed,

$$U_j = u_j - 3\frac{h_j}{b}\theta_j, \qquad A_j = \ddot{u}_j + \ddot{u}_g - 3\frac{h_j}{b}\ddot{\theta}_j \quad \textbf{(5-31)}$$

where U_j are the relative (horizontal sway + rocking) displacements, and A_j are the total (horizontal sway + ground + rocking) accelerations of buildings "j" in non-dimensional form. Additionally, it is useful to define the change in total power χ_j caused by building interactions when moving from the uncoupled (SSI) to the coupled (SSSI) case. Therefore, the percentage change in total power is defined as follow,

$$\chi_j = 100\left\{\frac{\left[E_s(U_j)\right]_{SSSI}}{\left[E_s(U_j)\right]_{SSI}} - 1\right\}, \qquad \ddot{\chi}_j = 100\left\{\frac{\left[E_s(A_j)\right]_{SSSI}}{\left[E_s(A_j)\right]_{SSI}} - 1\right\} \quad \textbf{(5-32)}$$

where $E_s(U_j)$ and $E_s(A_j)$ are the total power spectral density (which is based on all data points of response time series U_j and A_j) for the displacement and acceleration. The change in power χ_j and $\ddot{\chi}_j$ will be zero if there is no difference between SSSI and SSI analysis. The power spectral density is defined as follows, using Parseval's theorem,

$$E_s(U_j) = \int_{-\infty}^{\infty} \left|U_j(\tau)\right|^2 d\tau = \frac{1}{2\pi}\int_{-\infty}^{\infty} \left|U_j(\omega)\right|^2 d\omega, \quad \textbf{(5-33)}$$

$$E_s(A_j) = \int_{-\infty}^{\infty} \left|A_j(\tau)\right|^2 d\tau = \frac{1}{2\pi}\int_{-\infty}^{\infty} \left|A_j(\omega)\right|^2 d\omega \quad \textbf{(5-34)}$$

By using the Fourier transform of $U_j(\tau)$ (Clough and Penzien, 1993) the power spectral density function $U_j(\omega)$ are obtained. In the same way, the $A_j(\omega)$ is the continuous Fourier transform of $A_j(\tau)$. Using the equations (5-33) and (5-34) as a comparative metric, delivers a statistical estimate of magnitude that provides more information about the response than employing a single peak of the function. In the same way, the PSD relates to cumulative damage in inelastic systems and is complementary information about the single peak of the seismic response.

5.2.5 Ground Motion Selection

In order to determine the effect of SSSI on the system equation (5-14), it is analysed considering a horizontal component of ground motion matched with a specific target response spectra. In this way, it is significantly reduced the number of nonlinear time-history analyses performed while approximating the mean system response to a set of ground motion time series that are compatible with the EC8 elastic spectrum. The original ground motion time series is from the event in Imperial Valley California, USA, in 1979 with a magnitude of M_w=6.5 and a peak ground acceleration (PGA) equal to a_{gr} = 0.37g. This ground motion was obtained from the Pacific Earthquake Engineering Research (PEER) Center Database (PEER, 2014). This time series was recorded on weak soil with a shear wave velocity equal to 175 m/s.

The target horizontal elastic response spectrum $S_a(T)$ chosen in this study was the response spectra defined in Eurocode 8, Part 1 (Eurocode 8 EN-1998, 2004). It is considered a design ground acceleration equal to a_g = 0.6g and a ground type equal to "D" (i.e. deposit of loose to medium cohesionless soil with a shear wave velocity V_s< 180 m/s). A viscous damping ratio of the structure ξ = 5% (damping correction factor equal to η_s=1) and the magnitude of the earthquake corresponds to type 1 (the earthquake had a surface-wave magnitude M_s > 5.5.) are used. The design ground acceleration represents a high seismic zone, with a magnitude of M_w=7.5 and an epicentre distance of 8km, according to the Joint Research Centre (JRC) of the European Commission (EUR 23563 EN-2008, 2008). This high earthquake excitation produces a significant nonlinear response in the soil beneath the buildings.

The Reweighted Volterra Series Algorithm (RVSA) proposed by Alexander et al. (2014) is employed, to calculate the spectrally matched seismic ground motion. This spectral matching process is stable and robust because it converges to any reasonable response spectrum for any suitable seed time series and keeps the non-stationary characteristics (e.g. timing of the main pulse, the variation of frequency content with time and general envelope) of the original record. Note that the EC8 spectrum is extended from 4s to 10s. This extension to the target spectrum enables the RVSA spectral matching process to significantly reduce the low-frequency content of the spectrally matched time series. The RVSA re-express the ground motion time series as a discrete Volterra series. Then, using a complete multinomial mixing of the first-order kernel functions the higher-order Volterra kernels are estimated. Finally, the optimal weighting of each term within each Volterra kernel is obtained using the Levenberg-Marquardt approach. The matched, target and

original response spectra are shown in Figure 5.3(a). Figure 5.3(b) shows the original (seed) and matched seismic ground motions. The time series shown in Figure 5.3 validates that the matched time-series maintains the overall envelope and locations of pulses of the original time series while matching much more closely the target spectrum.

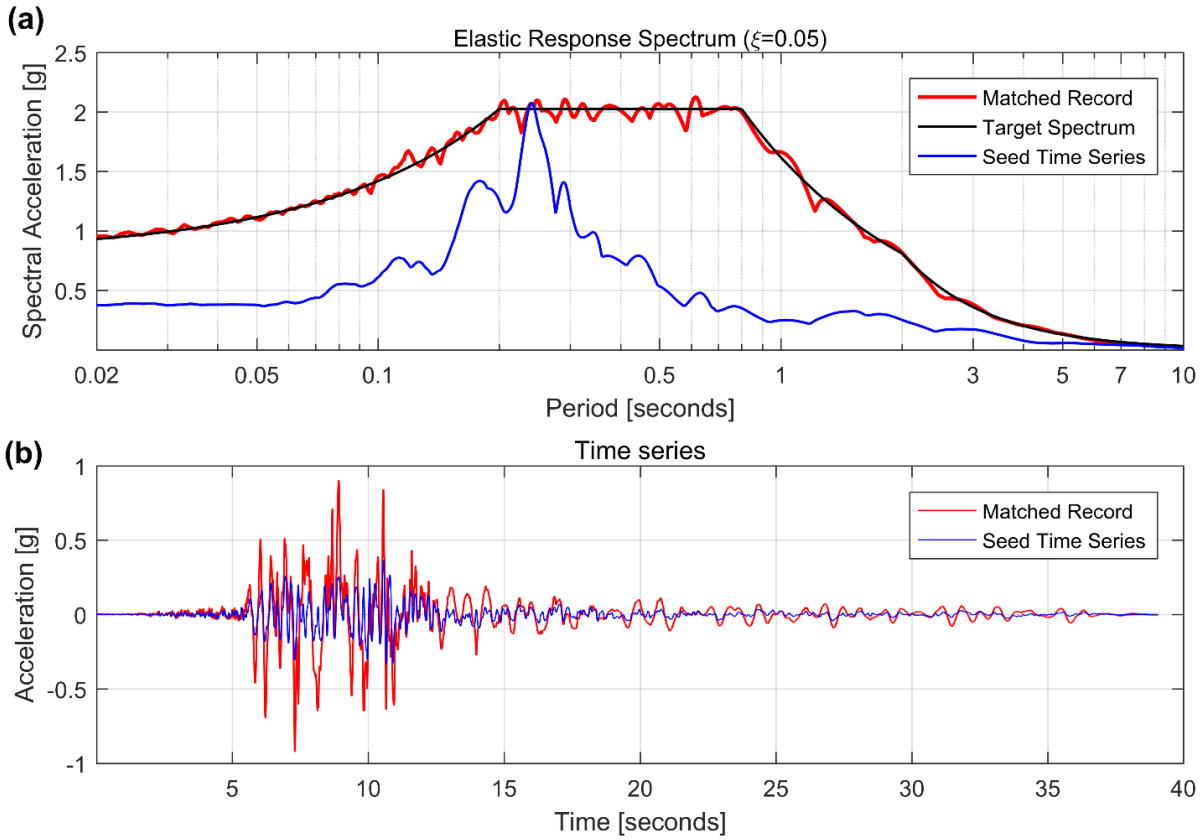

Figure 5.3 (a) Matched, target and seed response spectra (ξ=0.05), (b) Matched and seed (original) time series

5.3 Change in the response of adjacent buildings due to SSSI

In this parametric study, the dynamic response of the system depends on the aspect ratio $s = h_1/b$, height ratio $\varepsilon = h_2/h_1$, soil type and inter-building distance ζ. The Bouc-Wen parameters are assumed constant for the three soil types and are defined above in Table 5-1. Due to the complexity of the problem and the number of parameters considered, the results are divided into four sections, as follows,

(i) Section 5.3.1 explores the differences in the seismic response of linear/nonlinear SSSI and linear/nonlinear SSI problems for a test case of loose soil and closely spaced buildings. Alexander et al. (2013) suggested that the largest percentage change (SSI to SSSI) occurs for loose soil and closely spaced buildings, therefore, loose soil and inter-building case $\zeta = 0.1$ are adopted as a test case.

(ii) Section 5.3.2 explores beneficial and adverse SSSI effects for different buildings' height ratio ε and aspect ratio s. Alexander et al. (2013) and Aldaikh et al. (2015) suggest that these parameters are important in the SSSI behaviours.

(iii) Section 5.3.3 explores the influence of the soil class in the SSSI nonlinear responses of buildings.

(iv) Section 5.3.4 explores the influence of inter-building spacing ζ in the SSSI nonlinear responses of buildings.

5.3.1 Initial beneficial/adverse SSSI cases for linear and nonlinear soil

The differences in the dynamic response between the linear and nonlinear cases considering the dynamic coupling of adjacent buildings are investigated. For this, the case when two buildings are very close to each other are examined, i.e. at a spacing distance equal to $\zeta = 0.1$ of building's base width b, fixed base frequency of the building 1 equal to $\omega_{b1}/2\pi = 4.0$Hz, aspect ratio $s = 1.5$ and height ratio $\varepsilon = 1.5$ (i.e. the second building is 50% taller than the first building and building one has a height to width ratio of 1.5).

Figure 5.4(a) shows the linear (blue line) and nonlinear (red line) response of the buildings 1 and 2 considering the coupled effect (SSSI) in terms of the displacement U_1 and U_2, respectively. When comparing the responses, it is observed that the maximum displacement of the buildings increases when the nonlinear behaviour in the soil is included. Figure 5.4(b) depicts the linear and nonlinear response of the buildings for the uncoupled case (SSI) in terms of the displacement U_1 and U_2. Likewise, in Figure 5.4(b) is noticed that the maximum displacement of the buildings 1 and 2, for the uncoupled (SSI) case, increases when nonlinear behaviour in the soil (red line) is assumed. This difference in the behaviour is expected since the structural system becomes softer at the point where soil strain exceeds the threshold of $\gamma_y = 10^{-4}$. Therefore, the rotational spring stiffness decreases in each subsequent large-amplitude cycle.

Figure 5.4(c) shows the power spectral density for the displacements considering four cases: (i) coupled elastic response (linear SSSI), (ii) uncoupled elastic response (linear SSI), (iii) coupled nonlinear response (nonlinear SSSI), and (iv) uncoupled nonlinear response (nonlinear SSI). When comparing the linear and nonlinear responses, it is observed that building 1 is significantly affected by the nonlinear behaviour of the soil. Building 1's response power increases by $\chi_1 = 323\%$, for the nonlinear SSSI case, in the presence of the taller building 2. Conversely, its response power only increases by $\chi_1 = 34.6\%$, for the linear SSSI case. Equivalently, building 2 has a more significant reduction in response power with $\chi_2 = -57.7\%$ in the nonlinear SSSI case, in comparison with the linear SSSI case $\chi_2 = -20.6\%$. Thus, it is observed that both adverse and beneficial effects of the SSSI in building 1 can be found more significant in nonlinear SSSI cases.

The nonlinear SSSI displacement time series display on Figure 5.4(a) does not return to zero at the end of the seismic excitation. This behaviour is highlighted by the power spectral density in Figure 5.4(c), where the DC term (the zero-frequency component) is 75dB/Hz, 12dB/Hz and 1.5dB/Hz for the coupled (nonlinear SSSI), uncoupled (nonlinear SSI) and uncoupled (linear SSI) cases respectively in the building 1. This DC term is proportional to the mean of the time series (Chatfield, 2003). This suggests that the nonlinear SSSI analyses may exhibit seriously greater asymmetric oscillations than nonlinear SSI analyses. Therefore, there is a significantly higher probability of the buildings coming to rest leaning at some angle if a nonlinear SSSI analysis is performed.

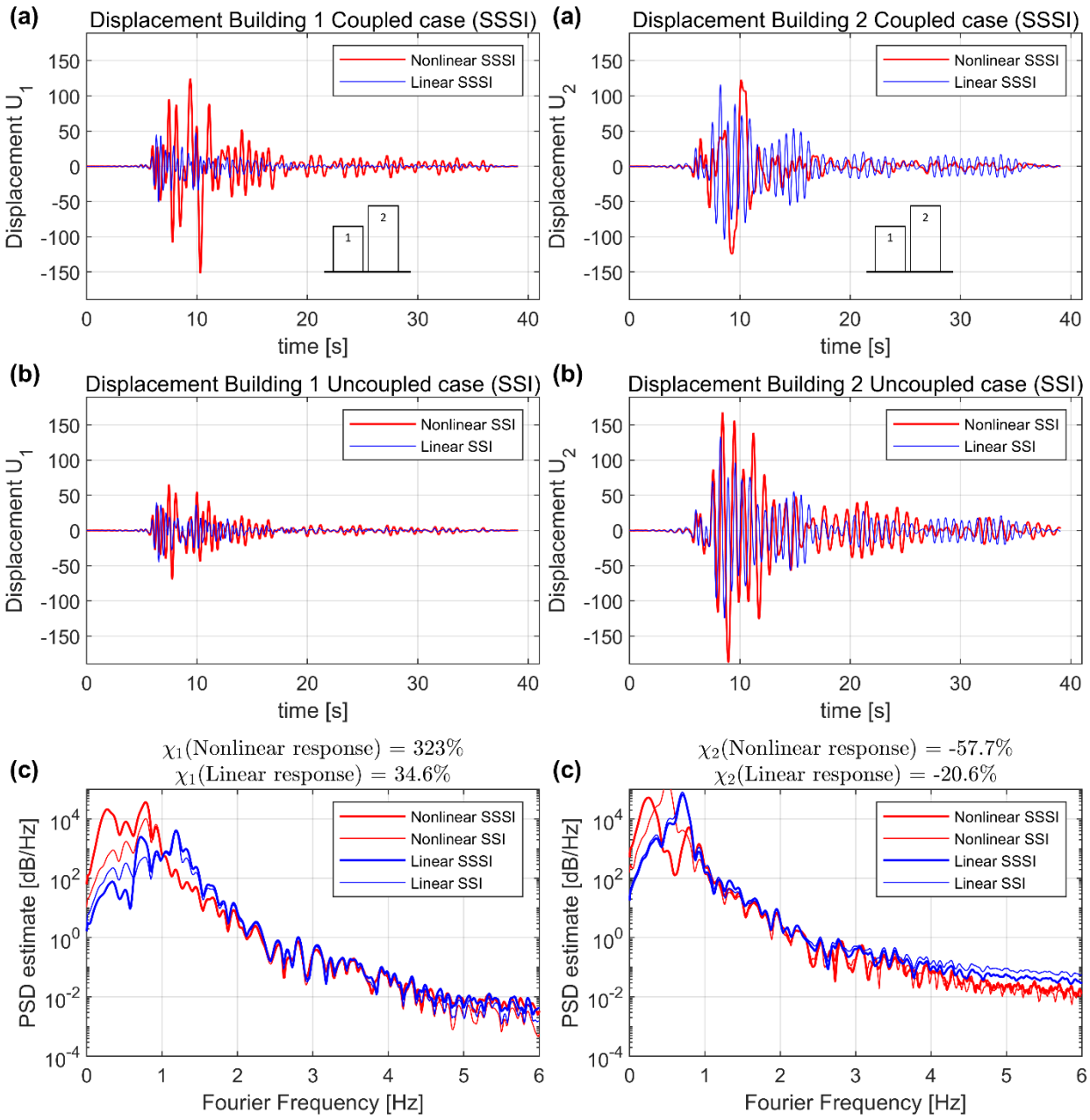

Figure 5.4 (a) Displacement responses coupled case (SSSI), (b) Displacement responses uncoupled case (SSI), (c) Power spectral density for all cases – Responses on loose soil for the parameter set (T_x = 0.25s, ε = 1.5, s = 1.5, and ζ = 0.1)

Figure 5.5(a) shows the linear/nonlinear SSSI total acceleration A_1 and A_2 responses of the buildings 1 and 2, respectively. Figure 5.5(b) displays the acceleration of buildings 1 and 2 for the uncoupled (SSI) case. It is observed that from these four graphs that, in general, the total accelerations of the buildings are reduced with the introduction of nonlinear behaviour, which is expected.

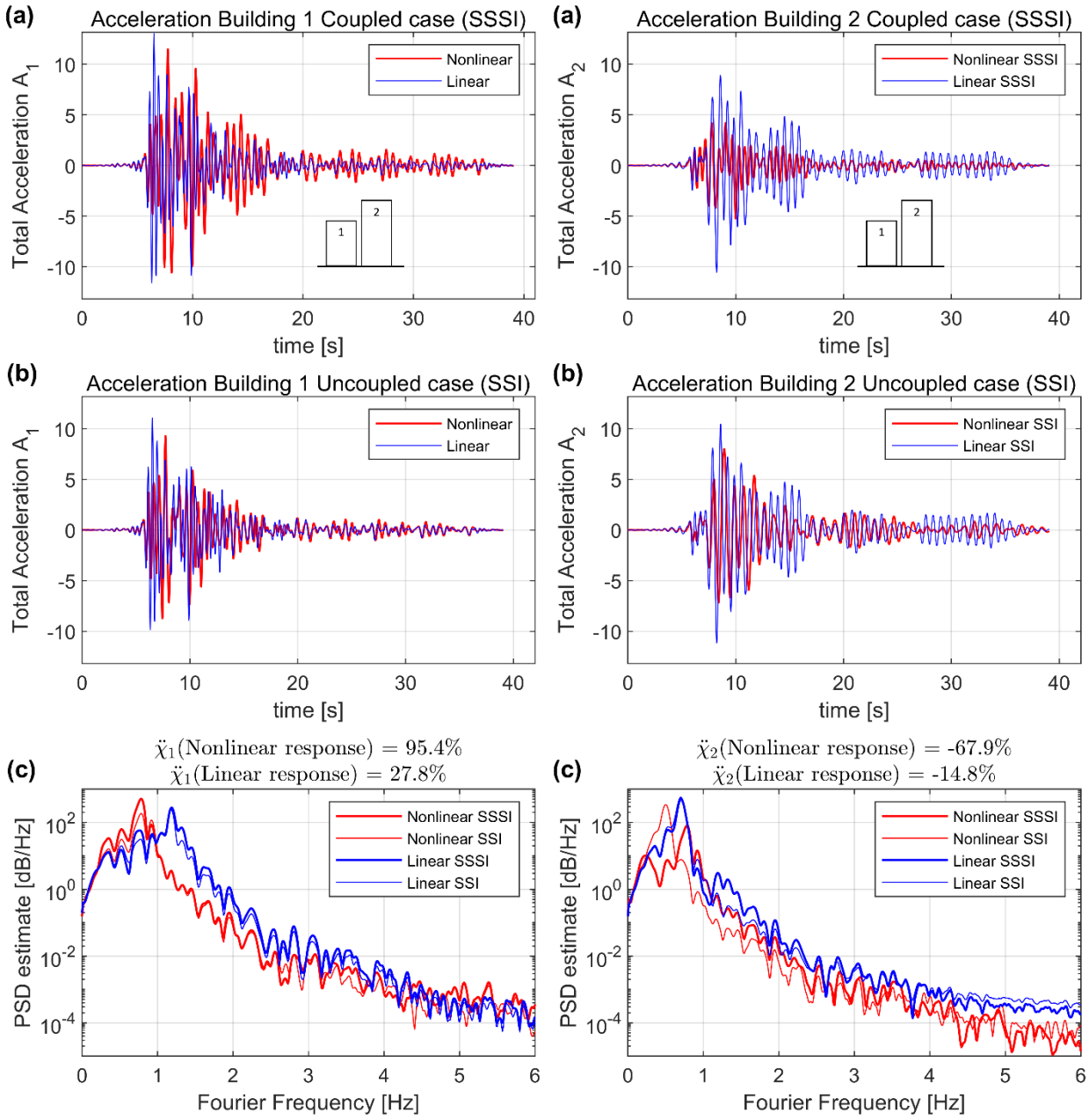

Figure 5.5 (a) Total acceleration responses coupled case (SSSI), (b) Total acceleration responses uncoupled case (SSI), (c) Power spectral density for all cases – Responses on loose soil for the parameter set (T_x = 0.25s, ε = 1.5, s = 1.5, and ζ = 0.1)

Figure 5.5(c) shows the corresponding power spectral density for the total acceleration and the percentage change in total response power $\ddot{\chi}_1$, considering the four cases. For both cases respectively, linear and nonlinear, it can be observed that building 1's total response power increases by about $\ddot{\chi}_1 = 27.8\%$ (linear response) and $\ddot{\chi}_1 = 95.4\%$ (nonlinear response) and building 2's reduces by $\ddot{\chi}_2 = -14.8\%$ (linear

response) and $\ddot{\chi}_2 = -67.9\%$ (nonlinear response). It is noted that, unlike displacement, the DC terms are close to zero (with a value of 0.15dB/Hz) suggesting that the mean total accelerations are negligible. In addition, Figure 5.5(c) illustrates the drop in the peak of the frequency system response between the linear (1.2Hz) and nonlinear case (0.8Hz). This is a typical behaviour of softening nonlinear systems.

Figure 5.6 depicts the hysteresis cycles in the soil/foundation of the buildings 1 and 2 under the seismic action, computed by using the Bouc-Wen model. The moment-rotation loops are consistent with the shear modulus and damping curves of the literature (please see Section 2.4.2) and have a good correspondence to the hysteretic soil behaviour experimentally observed by Gerolymos and Gazetas (2005).

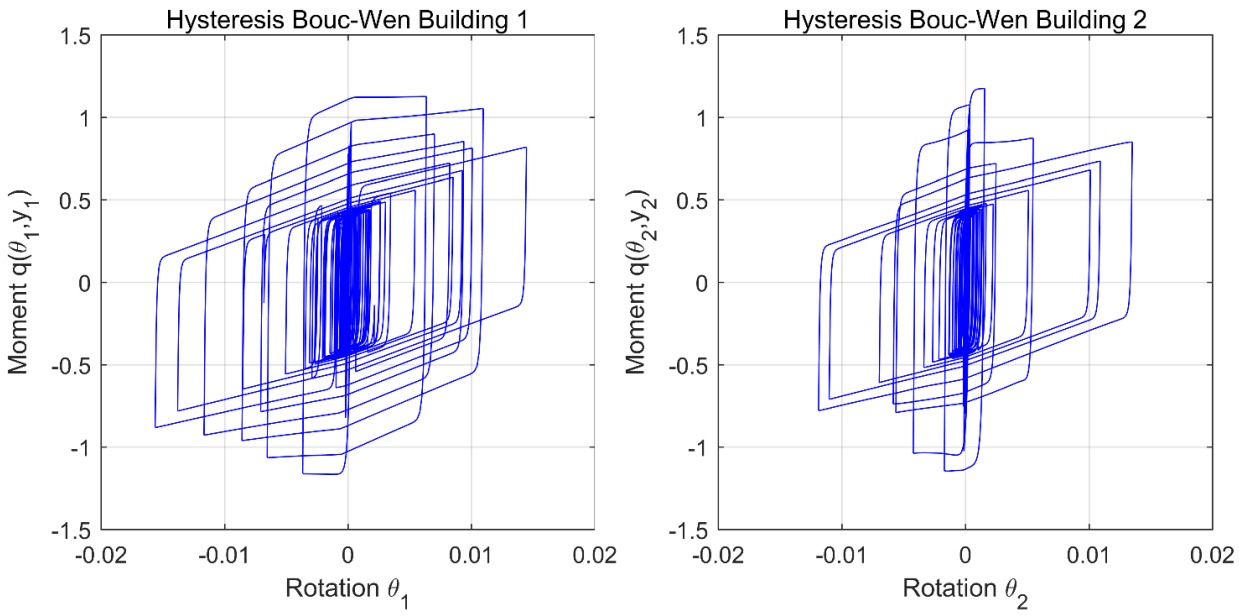

Figure 5.6 Hysteresis loops for the soil beneath buildings 1 and 2 (nonlinear SSSI) – Responses on loose soil for the parameter set (T_x = 0.25s, ε = 1.5, s = 1.5, and ζ = 0.1)

5.3.2 Change in power considering nonlinear analyses for loose soil due to variation in aspect ratio s and height ratio ε

To begin with, the variation of change of power $\chi_1(s,\varepsilon)$ of building 1 for the case considering linear behaviour of the soil is analysed, i.e. be setting the Bouc-Wen parameter $B_j = 1$. Therefore, later the linear and nonlinear responses are compared for a broader range of parameters. The aspect ratio $s = h_1/b$ varying between 0.25 and 4, and the height ratio $\varepsilon = h_2/h_1$ varying between 0.5 and 2. Loose soil and inter-building distance case equal to $\zeta = 0.1$ are considered. Figure 5.7 displays the contour plots of $\chi_1(s,\varepsilon)$ and $\ddot{\chi}_1(s,\varepsilon)$ for the displacement U_1 and acceleration A_1 of building 1 respectively. The critical zones in the figure are in red, i.e. where the building 1's total response power is amplified by the presence of building 2, and in blue when the response is reduced. The worst possible building parametric

configuration lies around $\chi_1(0.25,1.3) = 65\%$ and $\ddot{\chi}_1(2.0,1.2) = 85\%$ for the displacement and acceleration respectively.

Each contour plot presented in this chapter contains the results of ten thousand different time-histories nonlinear analyses. For that, it required approximately 600 hours run-time on BlueCrystal, the High-Performance Computing (HPC) machine belonging to the Advance computing research centre at the University of Bristol.

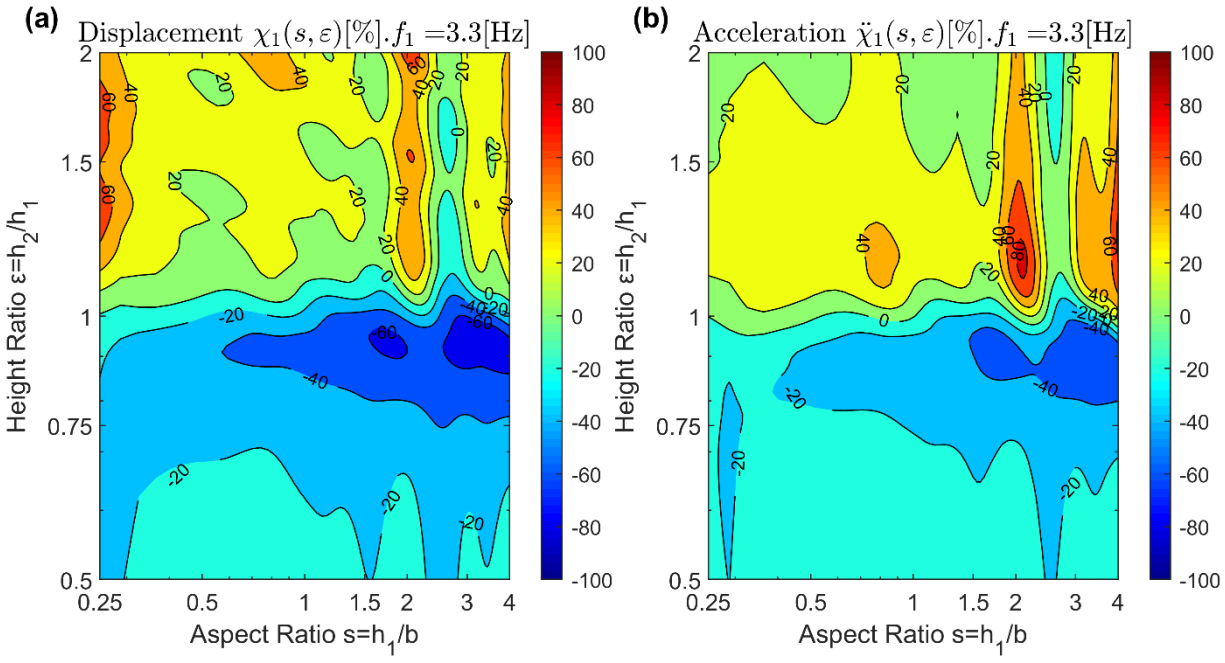

Figure 5.7 (a) Change in displacement power $\chi_1(s,\varepsilon)$ and (b) Change in acceleration power $\ddot{\chi}_1(s,\varepsilon)$ with the variation in aspect ratio s = h_1/b and height ratio ε = h_2/h_1 – Linear response on loose soil and inter-building distance ζ = 0.1

Now the results for the variation of change in power of building 1 for the nonlinear case are presented. The aspect ratio $s = h_1/b$ varying between 0.25 and 4, and the height ratio $\varepsilon = h_2/h_1$ varying between 0.5 and 2. Contour plots in Figure 5.8(a) show the variation of change of power $\chi_1(s,\varepsilon)$ for the displacement of building 1, U_1. With the aim of making the figure more readable, the change in the colour contour is shown up to a value of 100% and for larger values only the contour line is marked. In general, it can be observed that the power of the earthquake passes from the taller building to the smaller building. This amplification increases dramatically when the height ratio is greater than 1.5, reaching values above $\chi_1 = 400\%$ of amplification. As shown earlier in Figure 5.4(c), this large amplification is due to significant low-frequency content of the response.

Large asymmetrical oscillations of the building increase the probability of a large residual rotation of building 1 after the earthquake shaking has finished. To exemplify this effect, the contour plots of Figure 5.9 depict the residual rotation of the building 1, with a maximum value of 0.73 degrees and 0.26 degrees

for the nonlinear SSSI (Figure 5.9(a)) and the nonlinear SSI (Figure 5.9(b)) respectively. The residual rotation is more relevant for large aspect ratio ($s \geq 2.0$) values of the buildings.

Comparing Figure 5.7(a) and Figure 5.8(a) suggests that including nonlinearity smooths out the parametric variation in total power responses due to the limiting value of soil-spring capacity assumed in the Bouc-Wen model. In addition, the nonlinear analysis could produce more substantial favourable and unfavourable interaction effects, when it is compared with the linear analysis.

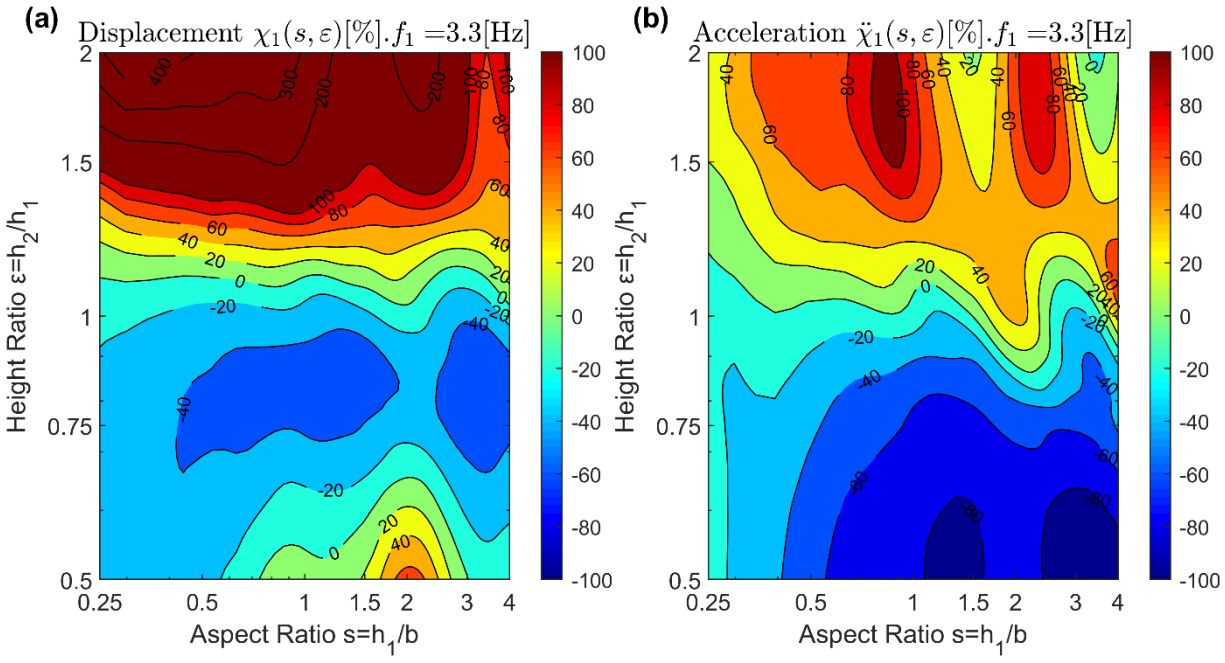

Figure 5.8 (a) Change in displacement power $\chi_1(s,\varepsilon)$ and (b) Change in acceleration power $\ddot{\chi}_1(s,\varepsilon)$ with the variation in aspect ratio $s = h_1/b$ and height ratio $\varepsilon = h_2/h_1$ – Nonlinear response on loose soil and inter-building distance $\zeta = 0.1$

Thus, the interaction effect between the buildings increases when the nonlinear behaviour in the soil is considered. This highlights the importance of considering the dynamic coupling (nonlinear SSSI) of adjacent buildings when the structures are very close, especially when extreme seismic loads produce predominantly nonlinear behaviour in the system. On the other hand, the reduction of the response is limited to a maximum value of $\chi_1(0.75,0.75) = -45\%$ for a height ratio $\varepsilon < 1.0$. Unlike the linear SSSI response shown in Figure 5.7, this reduction does not apply for the entire range of aspect ratios.

Figure 5.8(b) displays the change of power $\ddot{\chi}_1(s,\varepsilon)$ for the total acceleration of the building 1 A_1 where, unlike the previous case, the maximum amplification is limited to certain values of height and aspect ratio. In this case, the worst possible configuration is when the second building is 75% taller than the first and the foundation width of the buildings is 1.1 times the height of the building 1, $\ddot{\chi}_1(0.9,1.75) = 110\%$. For both figures (Figure 5.7 and Figure 5.8), a 100x100 grid of parametric values for the height and aspect ratio are considered.

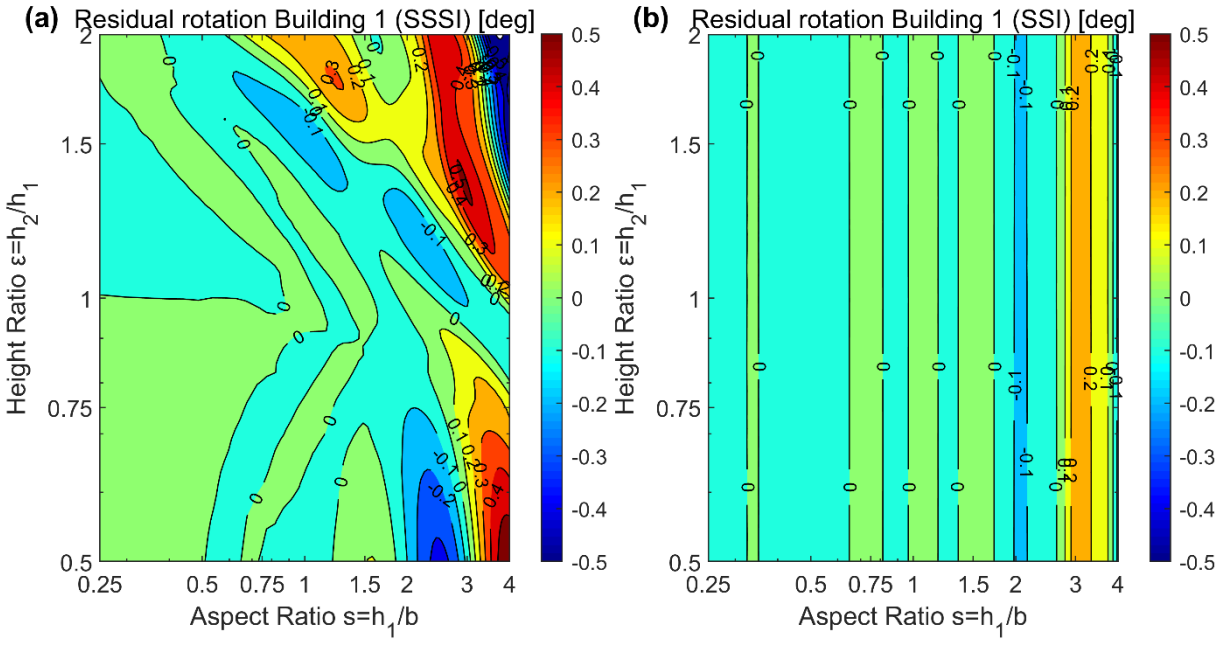

Figure 5.9 (a) Residual rotation of coupled case (nonlinear SSSI) and (b) Residual rotation uncoupled case (nonlinear SSI) with the variation in aspect ratio s = h_1/b and height ratio ε = h_2/h_1 – Nonlinear response on loose soil and inter-building distance ζ = 0.1

5.3.3 Change in power considering nonlinear analyses for dense soil due to variation in aspect ratio s and height ratio ε

Figure 5.10 displays the previous nonlinear analysis but for the case of dense sand (i.e. dense soil). In this parametric configuration, the amplification or reduction in the change of power is more limited. The most adverse configuration produces a change of power for the displacement and acceleration of $\chi_1(2.0,2.0) = 250\%$ and $\ddot{\chi}_1(3.0,1.8) = 45\%$ respectively. This suggests that the worst seismic interaction conditions occur on loose soil. The same can be observed in the linear case (Alexander et al., 2013).

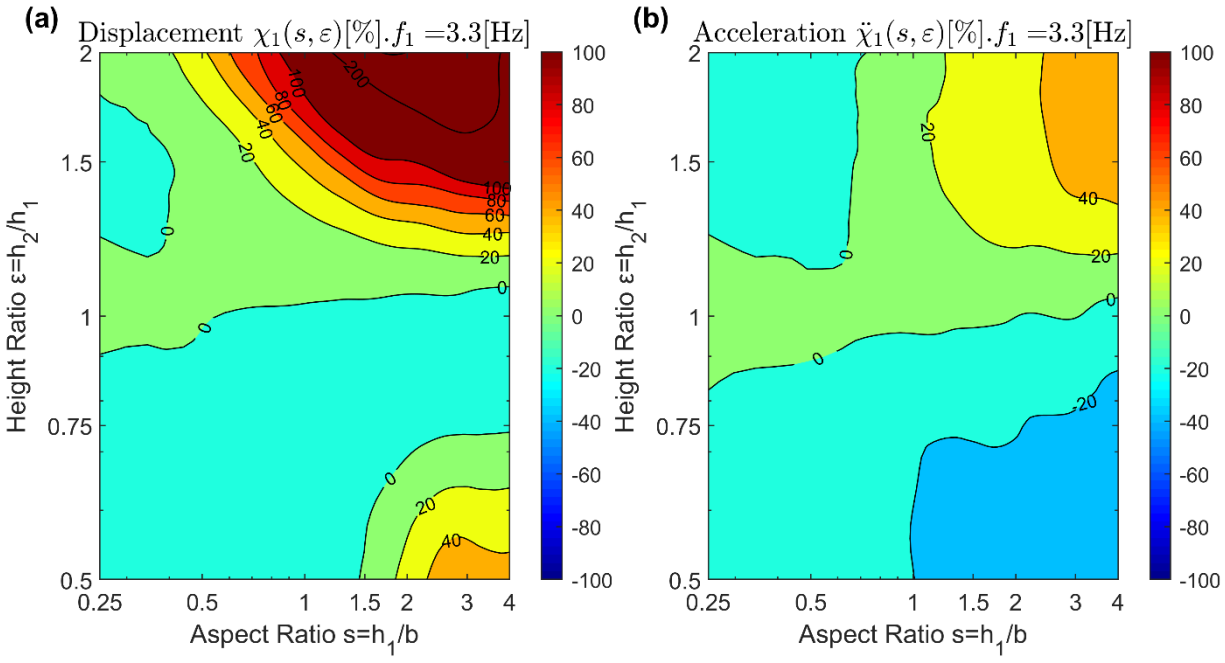

Figure 5.10 (a) Change in displacement power $\chi_1(s,\varepsilon)$ and (b) Change in acceleration power $\ddot{\chi}_1(s,\varepsilon)$ with the variation in aspect ratio s = h_1/b and height ratio ε = h_2/h_1 – Nonlinear response on dense soil and inter-building distance ζ = 0.1

5.3.4 Change in power considering nonlinear analyses for loose soil due to variation in height ratio ε and inter-building spacing ζ

In this section, results are presented for buildings with height ratio $\varepsilon = h_2/h_1$ varying between 0.5 and 2 and inter-building spacing ζ varying between 0.1 and 4. The aspect ratio was set equal to $s = 3.0$. Figure 5.11(a) shows the variation of power $\chi_1(s,\varepsilon,\zeta)$ for the displacement. As expected, the effects of SSSI decrease when increasing the inter-building spacing. At a distance between foundations equal to b, the SSSI is practically negligible $\chi_1(3.0,\varepsilon,1.0) = 21.5\%$. This reduction in the interaction, for large inter-building distances, happens for any value of aspect ratio s. As discussed above, there is a sharp increase in the change in power for height ratios greater than 1.5. Therefore, as not to distort the Figure 5.11, the colour contour is only shown up to 100%.

Figure 5.11(b) repeats the previous analysis for the change of power $\ddot{\chi}_1(s,\varepsilon,\zeta)$ corresponding to the accelerations. Similarly, the interaction effect drops more sharply when increasing the inter-building spacing to a value of $\ddot{\chi}_1(3.0,\varepsilon,1.0) = 22.5\%$.

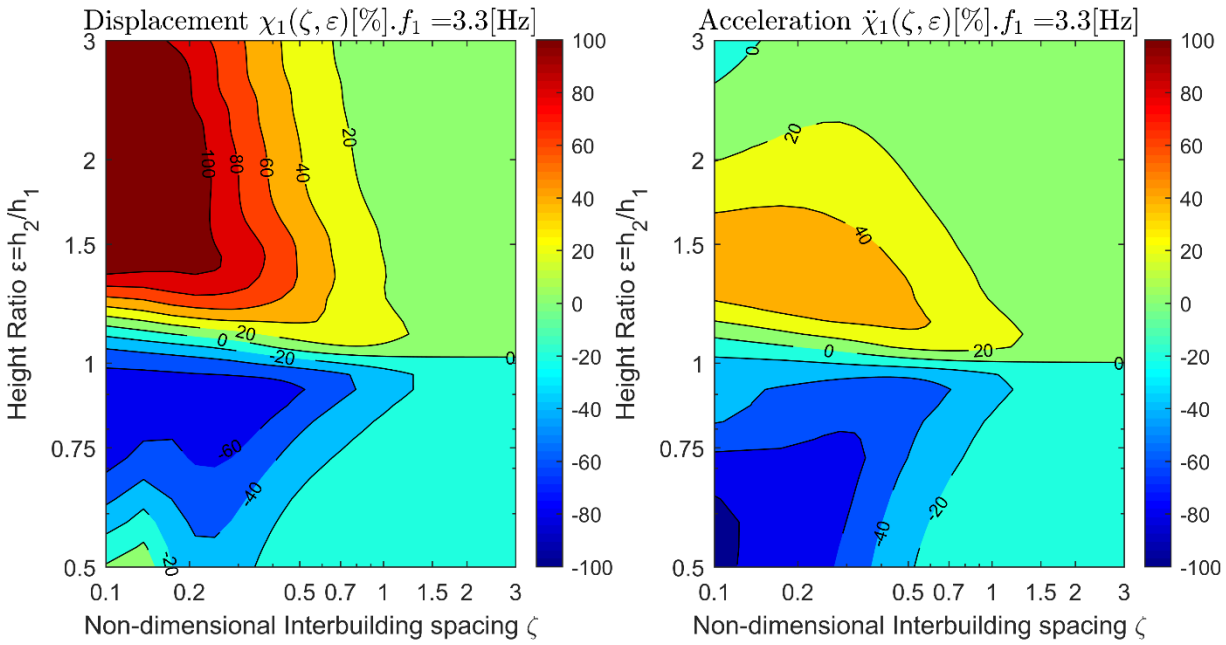

Figure 5.11 (a) Change in displacement power $\chi_1(\zeta,\varepsilon)$ and (b) Change in acceleration power $\ddot{x}_1(\zeta,\varepsilon)$ with the variation in height ratio $\varepsilon = h_2/h_1$ and inter-building spacing ζ – Nonlinear response on loose soil and aspect ratio s = 3.0

5.4 Summary

In this chapter, a theoretical formulation for the 2D SSSI between two buildings that are coupled through the soil is presented. A nonlinear phenomenological Bouc-Wen model for the soil underneath the foundations was employed. The seismic ground motion employed was spectrally matched with the EC8 elastic spectra. This model in its linear state was validated with Finite Element Analysis by Alexander et al. (2013) and using a small scale physical experimental test at the University of Bristol's shaking table (Aldaikh et al., 2016). The research presented in this chapter has led to the following principal findings:

- The nonlinear SSSI parametric study showed that there are significant differences in the seismic response compared with the linear SSSI analysis. It is found that the nonlinear SSSI can produce a greater range of beneficial and adverse behaviour for displacement responses when it is compared with the linear SSSI. This highlights the importance of considering the nonlinear SSSI between buildings.

- There are significant differences between the nonlinear SSSI (coupled building analysis) and nonlinear SSI (uncoupled building analysis) responses. The most adverse effects on building displacement, occurs when there is a big difference of height between the buildings (height ratio $\varepsilon > 1.5$). In this case, the displacement power of building 1 can be amplified up to $\chi_1 = 450\%$, i.e. the power of the earthquake passed from the taller structure to the small structure. In this

case, nonlinear SSSI analysis indicated a very large residual rotation of building 1 at the end of the earthquake. This effect cannot be quantified with traditional elastic analyses and is much less significant in nonlinear uncoupled (SSI) analysis.

- For the case of a smaller building 1 (flanked by a taller building 2), the amplification in nonlinear SSSI acceleration responses can be as high as $\ddot{\chi}_1 = 110\%$. Results also indicate that there is a beneficial effect for the taller building 2, with a maximum change in power of $\ddot{\chi}_1 = -45\%$ for the acceleration responses. This reduction does not apply for the entire range of aspect ratios considered in this study.

- The linear SSSI suggests that the adverse/beneficial effects boundary seems to be relevant when building 1 and building 2 natural frequencies are close (i.e. height ratio between the buildings close to 1.1). Meanwhile nonlinear SSSI presents a more complex picture with interactions across a broader range of frequencies between the buildings.

- Results from analyses of well-spaced building i.e. around one time the building base width, show that the SSSI seismic response energy amplification noticeable decreases. Also, for dense soil, the results show that the SSSI interaction is less relevant than for the case of loose soil. Therefore, the interaction effects increase when considering loose soil and closely spaced buildings.

- There is evidence presented that including the presence of nonlinearity in the soil can increase the size of adverse/beneficial SSSI effects, so it should not be neglected. Additionally, the evidence suggests significant differences between nonlinear SSSI (coupled building case) and nonlinear SSI (uncoupled building case) analyses.

5.5 Nomenclature

The units correspond to those defined by the International System of Units, where the abbreviations represent [M] mass, [T] time, [L] length and [rad] radians.

α_1, α_2	Ratios of soil/foundation to building masses of the buildings 1 and 2 respectively []
β	Ratio of soil/foundation radii of gyration (building 1 to 2) []
ς_1, ς_2	Bouc-Wen parameters that describe the shape and amplitude for the buildings 1 and 2 []
ψ_1, ψ_2	Bouc-Wen parameters that describe the shape and amplitude for the buildings 1 and 2 []
γ_y	Strain at the initiation of nonlinear soil behaviour []
δ_η	Stiffness degradation parameter of Bouc-Wen model []
δ_ν	Strength degradation parameter of Bouc-Wen model []
ε	Height ratio between the buildings 2 to 1 []
η_1, η_2	Height to the radius of gyration ratios for the buildings 1 and 2 respectively []
$\eta(E)$	Degradation shape function of the Bouc-Wen model []
η_s	Damping correction factor of the Eurocode 8 elastic spectrum []
θ_1, θ_2	Rotational degrees of freedom at the base of the buildings 1 and 2 respectively []
κ	Inter-building soil rotational spring between the buildings 1 and 2 [ML^2T^{-2}]
λ	Ratio of building 2 to building 1 mass (square of the radii of gyration) []
μ_s	Poison's ratio of the soil []
$\nu(E)$	Degradation shape function of the Bouc-Wen model []
ξ_n	Ratio of critical damping of the system []
ρ_b, ρ_s	Average densities of the buildings and the soil respectively [ML^{-3}]
τ	Scaled time []
$\boldsymbol{\phi}_n$	Modal eigenvector of the linear system for the mode "n" []
χ_j	Change in displacement power when moving from uncoupled to coupled state for the building *j* [%]
$\ddot{\chi}_j$	Change in acceleration power when moving from uncoupled to coupled state for the building *j* [%]
ω_{b1}, ω_{b2}	Modal circular frequencies (on a rigid base) for the buildings 1 and 2 respectively [$radT^{-1}$]
ω_{s1}, ω_{s2}	Circular frequencies of soil/foundation for the buildings 1 and 2 respectively [$radT^{-1}$]
ω	Fourier frequency [$radT^{-1}$]
ω_n	Natural frequencies of the linear system [$radT^{-1}$]
ϖ	Interaction circular frequency ratio parameter [$radT^{-1}$]
Ω_0	Ratio of interaction frequency parameter to building 1 (on a rigid base) circular frequency []
Ω_b	Ratio of building 2 (on a rigid base) frequency to building 1 (on a rigid base) circular frequency []
Ω_{s1}	Ratio of building 1 soil/foundation frequency to building 1 (on a rigid base) circular frequency []

Ω_{s2}	Ratio of building 2 soil/foundation frequency to building 1 (on a rigid base) circular frequency []
A_1, A_2	Total acceleration on top of the buildings 1 and 2 respectively []
a_g	Peak ground acceleration (PGA) of the elastic response spectrum [MT^{-2}]
a_{gr}	Peak ground acceleration (PGA) of the ground motion record [MT^{-2}]
B_1, B_2	Linear to nonlinear response ratios of the building 1 and 2 respectively []
b_1, b_2	Foundation widths for the buildings 1 and 2 respectively [L]
$\boldsymbol{C}$	Non-dimensional damping matrix of the linear system []
c_1	Density ratio (soil/buildings) parametric constant []
c_2	Soil parametric constant []
D_1, D_2	Bouc-Wen parameters that describe the shape and amplitude for the buildings 1 and 2 []
$E(\tau)$	Dissipated hysteretic energy []
E_s	Total power spectral density []
$\mathbf{f}$	Non-dimensional force vector of the system []
$\hat{\mathbf{f}}$	Dimensional force vector of the system [M]
G_s	Initial tangent shear modulus of the soil [$ML^{-1}T^{-2}$]
h_1, h_2	Heights of the buildings 1 and 2 respectively [L]
$\boldsymbol{K}$	Non-dimensional stiffness matrix of the system []
$\widehat{\boldsymbol{K}}$	Dimensional stiffness matrix of the system [MT^{-2}]
k_s	Soil/foundation rotational stiffness in the absence of inter-buildings interaction [ML^2T^{-2}]
k_{b1}, k_{b2}	Lateral modal stiffnesses of the buildings 1 and 2 respectively [MT^{-2}]
k_{s1}, k_{s2}	Rotational soil/foundation stiffnesses of the soil beneath the buildings 1 and 2 [ML^2T^{-2}]
$\boldsymbol{M}$	Non-dimensional mass matrix of the system []
$\widehat{\boldsymbol{M}}$	Dimensional mass matrix of the system [M]
M_1, M_2	Nonlinear moments at the base of the buildings 1 and 2 respectively [ML^2T^{-2}]
M_s	Surface wave magnitude scale of the earthquake
M_w	Moment magnitude scale of the earthquake
m_{b1}, m_{b2}	Modal masses of the buildings 1 and 2 respectively [M]
m_{s1}, m_{s2}	Soil/foundation masses of the buildings 1 and 2 respectively [M]
n_1, n_2	Bouc-Wen parameters that describe the shape and amplitude for the buildings 1 and 2 []
n_s	Number of storeys of the buildings []
q_1, q_2	Non-dimensional nonlinear functions of soil at the base of the buildings 1 and 2 respectively []
$q_2(\zeta)$	Interaction function that depend on the inter-building distance ζ []
$q_\kappa(\zeta)$	Interaction function that depend on the inter-building distance ζ []
$\boldsymbol{q}$	Nonlinear moment/rotation vector of the system []
r_1, r_2	Soil/foundation mass radius of gyration for the buildings 1 and 2 [L]

S_a	Horizontal elastic response spectra of the Eurocode 8 [MT^{-2}]
s	Aspect ratio. Height to width ratio of the building 1 []
T_x	Fundamental period of the structure on a rigid foundation [T]
T_E	System kinematic energy [ML^2T^{-2}]
T_B, T_c, T_D	Elastic response spectra parameters that depend on the soil type []
t	Time [T]
U_1, U_2	Non-dimensional displacements on top of the buildings 1 and 2 respectively []
$U_j(\omega)$	Fourier transform of $U_j(\tau)$
U_E	System potential energy [ML^2T^{-2}]
u_1, u_2	Non-dimensional relative displacement to ground of the buildings 1 and 2 respectively []
u_g	Non-dimensional horizontal ground displacement time series []
$\ddot{u}_g$	Non-dimensional acceleration ground motion []
$\boldsymbol{u}$	Non-dimensional degrees of freedom (vector) of the system []
V_s	Shear wave velocity of the soil [LT^{-1}]
$\bar{V}_s$	Normalised shear wave velocity of the soil []
x_1, x_2	Horizontal displacement (degrees of freedom) of the top of buildings 1 and 2 respectively [L]
x_g	Horizontal ground displacement time series [L]
$\ddot{x}_g$	Horizontal acceleration ground motion [LT^{-2}]
$\mathbf{x}$	Degrees of freedom (vector) of the system [L]
y_1, y_2	Internal (DOFs) hysteretic rotations of the buildings 1 and 2 respectively []
ζ	Inter-building distance coefficient []

Chapter 6

Method to evaluate the dynamic Structure-Soil-Structure Interaction of 3-D buildings arrangement due to seismic excitation

---

The contents of this chapter have been adapted from the paper under review in:

Vicencio, F., and Alexander, N.A. (2021). Method to evaluate the dynamic Structure-Soil-Structure Interaction of 3-D buildings arrangement due to seismic excitation. *Soil Dynamics and Earthquake Engineering*, 141, 106494.

Part of the introduction has been removed and included in Chapter 2 - Literature Review.

6.1 Introduction to multiple SSSI among a group of buildings

Population growth and enhanced land costs have produced an increase in city building surface density, i.e. more closely spaced buildings. While it is common practice to determine the seismic response of buildings as single structures, the high surface density inevitably results in the possibility of interaction and coupling effects via the underlying soil. This phenomenon is referred to as Structure-Soil-Structure Interaction (SSSI) and it can either magnify or attenuate the seismic response of a building.

Lumped parameter models (or reduced-order models) with a limited number of DOFs have been well recognized and effectively applied in the evaluation of the SSSI effects on the dynamic response of buildings (see Chapter 2, Literature Review). In these mechanical models, it was considered that all masses, springs, and dashpots are lumped into a single mass, single spring, and single damping constant for each mode of vibration. Also, frequency-independent lumped masses, springs and dampers are assumed. The coupled effects were incorporated into the solution by means of empirical stiffness coefficients. These previous works highlight how that dynamic loading, e.g. seismic ground motion, can affect the response of the structures, and this influence can either magnify or attenuate the structural response of a building.

A related problem that has been addressed recently is Site-City Interaction (SCI) or city effects, where the seismic free-field ground motion is affected by building clusters in dense urban areas. Several studies have been undertaken in the last decades (for a complete list of references see Chapter 2, Literature Review). These works have shown that (i) the SCI effect is influenced by the separation/size of the structures and the relative stiffness to the soil, (ii) a part of the seismic energy transmitted to the buildings is redistributed in their neighbourhood through multiple interaction between the soil foundation and the buildings, and (iii) the ground motion is affected by the presence of a large group of structures, producing a spatial variation of the ground acceleration.

6.1.1 Aims

The objective of this work is to introduce a novel framework for producing an efficient reduced-order mathematical formulation, so multiple SSSI among a group of buildings on a city-block under seismic excitation in 3D are evaluated. Additionally, this reduced-order model is not reliant on the creation of any initial full 3D FEA analysis of the soil. Thus, it is proposing a new methodology that avoids the necessity of using any FEA of the soil. It relies solely on defining auto-rotational and inter-rotational spring coefficients for the elastic half-space. The only input information required to define the reduced-order model is (i) the soil class and (ii) the height, footprint dimensions and the planar coordinates of the buildings. The approach defines the problem in terms of a small number of system parameters and degrees of freedom. Note that this method is limited to linear soil behaviour, and if the earthquake is large enough to generate significant inelastic strain, a non-linear FEA to produce an accurate seismic response is

required. Therefore, it is computationally simple and efficient enough for an extensive exploration of the problem of multiple buildings interacting. The rocking spring stiffnesses of the soil-foundation (auto-rotational spring stiffnesses) and the coupling spring stiffnesses between the buildings (inter-rotational spring stiffnesses) are determined by using a least-squares inverse system identification. A number of load cases of static applied moments at foundations are employed, along with their implied surficial displacement fields, to determine all the individual stiffness coefficients of the system matrix. The implied surficial displacement field is obtained by using an empirical formulation (loosely based on a form derived from a Boussinesq elastic half-space approximation that was calibrated against 3D FEA). Also, frequency-independent lumped masses, springs and dampers are assumed. All code used in this study was developed in the software MATLAB (2016).

Finally, it is worth stating that the reduced-order model has only 4*n* DOFs (where *n* is the number of buildings) rather than perhaps hundreds of millions of DOFs for a full 3D FE analysis of simple buildings and their underlying elastic half-space and hence does not require any full 3D FE analyses.

6.2 A theoretical reduced-order model for SSSI between multiple buildings in 3D

6.2.1 General preamble and limitations

The reduced-order model derived in this chapter consists of a set of n buildings belonging to a city block, distributed over the ground surface, as shown in Figure 6.1. No attempt is made to model all inter-building interactions, only the significant rotational ones as in the research of Alexander et al. (2013), Aldaikh et al. (2016, 2018), and the previous chapters. This system can be viewed as an assemblage of individual buildings coupled through the common homogeneous linear elastic soil medium. Thus, each building's foundation has two orthogonal auto-rotational springs k_{xi} and k_{yi}, and a large number of inter-rotational springs $\boldsymbol{\kappa}_{ij}$ (i.e. the coupling effect between buildings "i" and "j"). The planar mesh of rotational springs k_{xi}, k_{yi}, and $\boldsymbol{\kappa}_{ij}$ can be viewed as a complete replacement (master-slave condensation, sub-structuring) of the ground, where only rotational DOFs at the foundation θ_{xi}, θ_{yj} are retained. Note that due to the 3-dimensional nature of the problem, the inter-rotational springs matrix $\boldsymbol{\kappa}_{ij}$ should be viewed as a small matrix with inter-rotational stiffness coefficients in the x-direction κ_{xij}, in the y-direction κ_{yij}, and the cross-coupled term κ_{xyij}.

Each building's superstructure has 2 DOFs, x_i and y_i, and it is assumed regular (i.e. only plan-symmetric buildings are considered, unlike the cases discussed in Chapter 4). The sway-flexural (modal) stiffness in both *x* and *y* directions of building "*i*" is defined by k_{bi}. The lumped mass (the effective fundamental modal

mass) of the building "i" in both x and y directions is m_{bi}, and the foundation/soil mass underneath the building "i" is m_{si}. The soil/foundation system for building "i" has two rotational DOFs at the foundation levels θ_{xi} and θ_{yi}. The term "modal" used here refers to the first fundamental mode of this characteristic multiple degrees of freedom building.

Thus, the total system only contains 4*n* DOFs, where *n* is the number of buildings.

As an initial problem exploration, it is assumed that all buildings are simultaneously excited only in the *x*-direction. A known ground displacement field x_g is applied at all foundations, i.e. wave passage effects and spatially heterogeneous ground displacements are neglected in the presented work. Nevertheless, this unidirectional spatially coherent ground motion produces vibration in the two horizontal directions due to the unsymmetrical arrangement of foundations. Note that this model formulation is already set-up to include a ground displacement y_g (i.e. 2D planar excitation), although only 1D excitation was used. It is assumed that each building's response could be affected by any building of the system, and the magnitude of these interactions mainly depend on the inter-building distance, as was stated in the previous chapters. This means that it is taken into account multiple structure-soil-structure interactions through the soil. Note that building pounding is not permitted as the inter-building spacing is assumed large enough to avoid pounding.

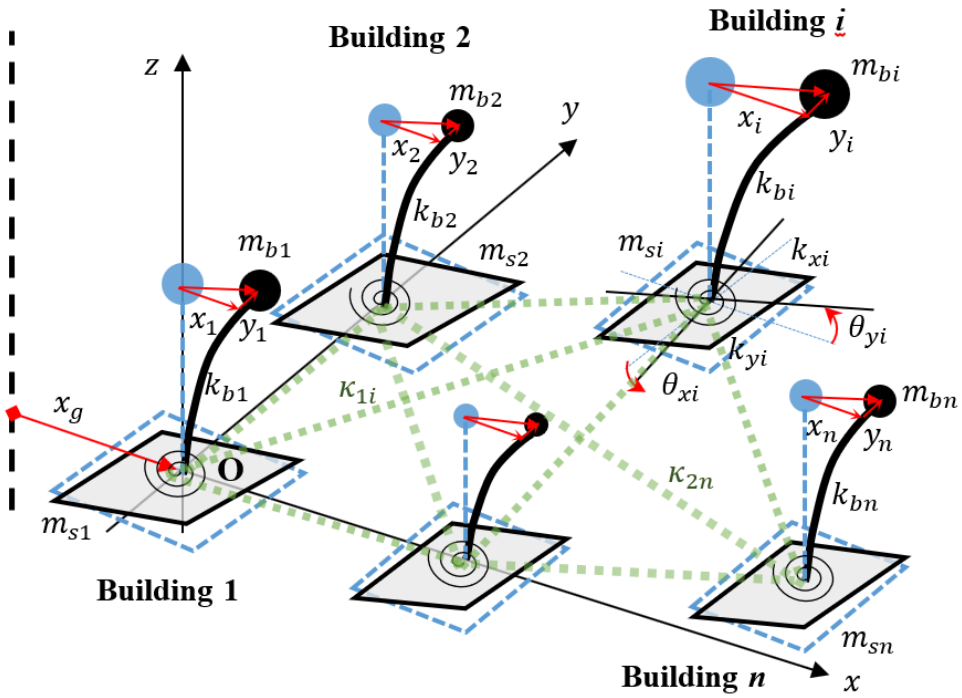

Figure 6.1 Idealization of the multi-buildings SSSI model in a 3D arrangement

6.2.2 How are the stiffness coefficients of all ground rotational springs obtained?

In order to determine the inter-rotational springs $\boldsymbol{\kappa}_{ij}$ and the auto-rotational spring stiffnesses of the soil beneath each buildings k_{xi} and k_{yi}, the procedure described by Aldaikh et al. (2018) is extended to the three-dimensional case. This technique considers a reduced-order model of the soil and the foundations. In addition, this formulation is calibrated using FEM.

The geometry and nomenclature for the 3D foundation-soil-foundation system studied in this chapter are shown in Figure 6.2. Each of these foundations are coupled with the other foundations by the inter-rotational springs $\boldsymbol{\kappa}_{ij}$ between buildings "i" and "j". The term κ_{xij} corresponds to the component in the x-direction, κ_{yij} in the y-direction, and κ_{xyij} is the cross-coupled part that takes into account the vibration in the two horizontal directions due to the unsymmetrical arrangement of foundations. All the foundations are assumed square, i.e. $k_{xi} = k_{yi}$, but buildings can have different plan-size foundations i.e. k_{xi} is not necessarily equal to k_{xj}.

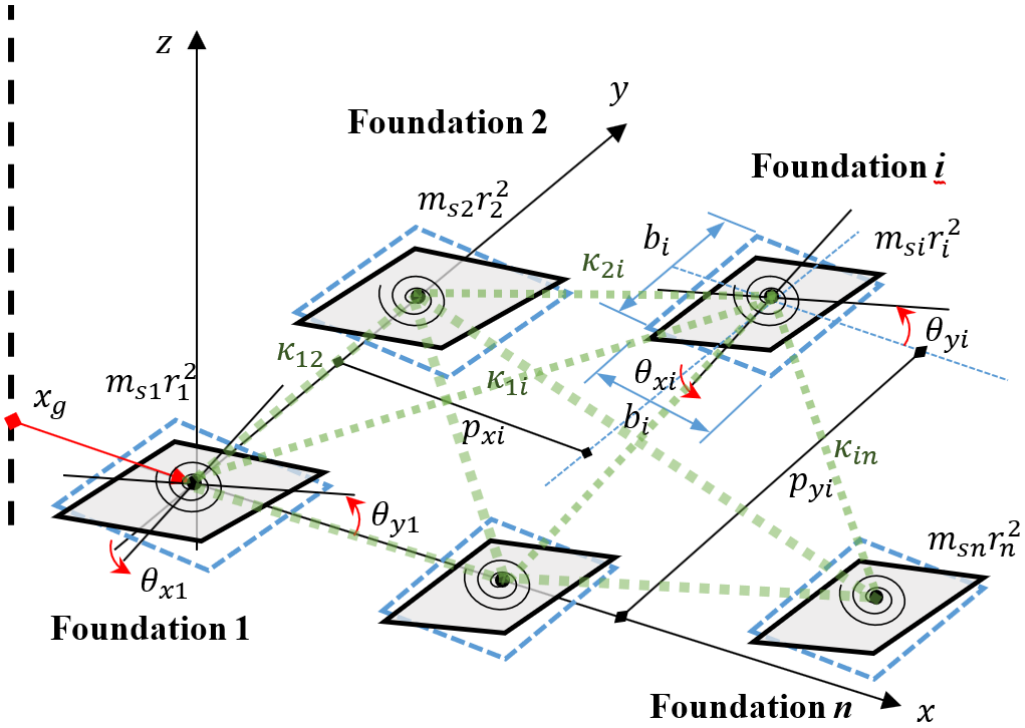

Figure 6.2 Spatial distribution of multiple foundations and their interaction in 3D

The potential energy U_E of the system is given by equation (6-1). It is calculated by the sum of (i) the external work of applied static moments μ_{xi} and μ_{yi} (summation term 1 in equation (6-1)), (ii) the internal work due to auto-rotational springs (summation term 2 in equation (6-1)), and (iii) the internal work due

to inter-rotational springs κ_{xij}, κ_{yij} and the cross-coupled term κ_{xyij}, where $\kappa_{xij} = \kappa_{xji}$ and $\kappa_{yij} = \kappa_{yji}$ (double summation term 3 in equation (6-1)). Hence,

$$U_E = -\sum_{i=1}^{n}\left(\mu_{xi}\theta_{xi} + \mu_{yi}\theta_{yi}\right) + \frac{1}{2}\sum_{i=1}^{n}\left(k_{xi}\theta_{xi}^2 + k_{yi}\theta_{yi}^2\right) + \cdots + \frac{1}{2}\sum_{i=1}^{n-1}\sum_{j=i+1}^{n}\left(\kappa_{xij}\left(\theta_{xj} - \theta_{xi}\right)^2 + \kappa_{yij}\left(\theta_{yj} - \theta_{yi}\right)^2 + \kappa_{xyij}\left(\theta_{yj} - \theta_{xi}\right)^2\right) \quad \textbf{(6-1)}$$

where n is the number of buildings, k_{xi} and k_{yi} are the rotational spring stiffnesses of each foundation and b_i are the width of the building's foundation. The Euler-Lagrange formulation provides a set of $2n$ linear equations that relate the external moments and their implied rotations (associated with the surface rotation field). These equations written in matrix form are formulated in equation (6-2).

$$\boldsymbol{\mu} = \mathbf{K}\boldsymbol{\Theta} \quad \textbf{(6-2)}$$

where the moment vector $\boldsymbol{\mu}$, rotation vector $\boldsymbol{\Theta}$, and the stiffness matrix $\mathbf{K}$ are,

$$\boldsymbol{\mu} = \begin{bmatrix} \mu_{x1} \\ \vdots \\ \mu_{xi} \\ \vdots \\ \mu_{yn} \end{bmatrix}, \qquad \boldsymbol{\Theta} = \begin{bmatrix} \theta_{x1} \\ \vdots \\ \theta_{xi} \\ \vdots \\ \theta_{yn} \end{bmatrix} \quad \textbf{(6-3)}$$

$$\mathbf{K} = \begin{bmatrix} k_{x1} + \kappa_{x1i} + \cdots + \kappa_{xy1n} & \cdots & -\kappa_{x1i} & \cdots & -\kappa_{xy1n} \\ \vdots & \ddots & \vdots & \ddots & \vdots \\ -\kappa_{xi1} & \cdots & k_{xi} + \kappa_{xi1} + \cdots + \kappa_{xyin} & \cdots & -\kappa_{xyin} \\ \vdots & \ddots & \vdots & \ddots & \vdots \\ -\kappa_{xyn1} & \cdots & -\kappa_{xyni} & \cdots & k_{yn} + \kappa_{yn1} + \cdots + \kappa_{xyni} \end{bmatrix} \quad \textbf{(6-4)}$$

Therefore, to determine the stiffness coefficients, i.e. the entire matrix $\mathbf{K}$ of equation (6-2), it is made use of the extended relationship between applied surface moments $\boldsymbol{\mu}$ and surficial rotations $\boldsymbol{\Theta}$, as in the 2D formulation of Aldaikh et al. (2018). In this chapter, two approaches are used to develop an empirical applied moment-surficial rotation relationship, (i) a formulation based entirely on Boussinesq's approximation of elastic half-space behaviour and (ii) a 3D FEA calibrated empirical relationship loosely based on a Boussinesq form. Then, these results with previous 2D works of Alexander et al. (2013) and Aldaikh et al. (2018) are compared.

For small deformations, i.e. a linear elastic soil half-space, the surface displacement field $U_z(x, y)$ is specified in equation (6-5), where θ_{y0} corresponds to the rotation of the rigid foundation about the y-axis, and $\Delta(x, y)$ is the decay function. The shape of the decay function is depicted in Figure 6.3 and is defined

for any (x, y) arbitrary coordinate, located in the free surface plane. This function is valid only for points outside the foundation, i.e. valid for $(|x| \geq b/2) \wedge (|y| \geq b/2)$, where b is the foundation width. The equation (6-5) can be nondimensionalized by the definition of the length $x = \xi_x b$ and $y = \xi_y b$, where ξ_x and ξ_y are the non-dimensional coordinates. Also, it can be stated that the non-dimensional surface vertical displacement $u_z(\xi_x, \xi_y)b = U_z(x, y)$.

$$U_z(x,y) = \frac{b}{2}\Delta(x,y)\theta_{y0} \quad \therefore \; u_z(\xi_x,\xi_y) = \frac{1}{2}\Delta(\xi_x,\xi_y)\theta_{y0} \tag{6-5}$$

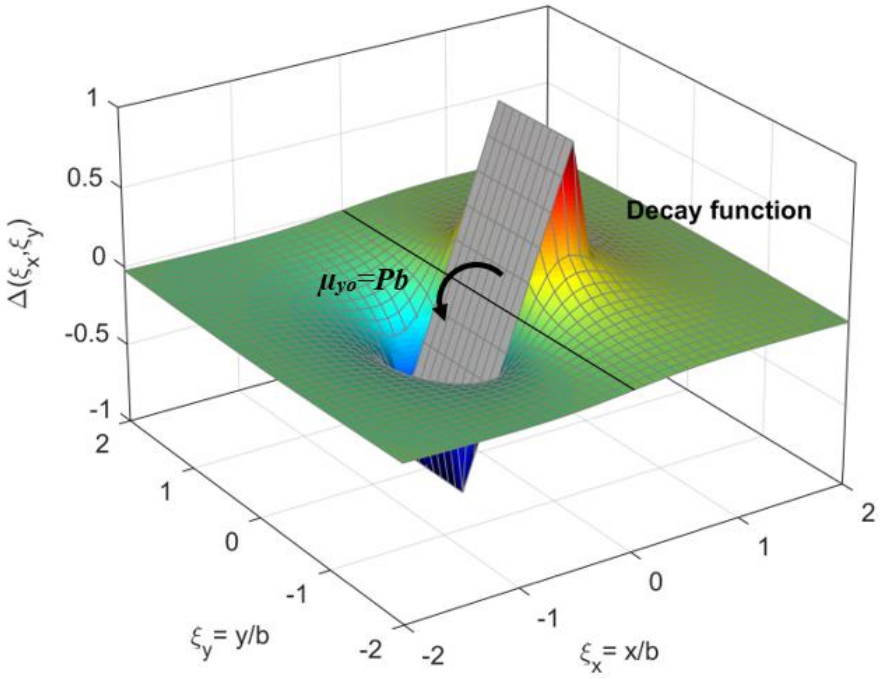

Figure 6.3 Decay function $\Delta(\xi_x,\xi_y)$ for the surface displacement field in 3D

By differentiating the previous equation (6-5), the surface rotation field in x and y directions can be calculated as,

$$\theta_y(\xi_x,\xi_y) = \frac{\partial u_z(\xi_x,\xi_y)}{\partial \xi_x} = \frac{1}{2}\theta_{y0}\frac{\partial \Delta(\xi_x,\xi_y)}{\partial \xi_x}, \qquad \left(|\xi_x| \geq \frac{1}{2}\right) \wedge \left(|\xi_y| \geq \frac{1}{2}\right) \tag{6-6}$$

$$\theta_x(\xi_x,\xi_y) = \frac{\partial u_z(\xi_x,\xi_y)}{\partial \xi_y} = \frac{1}{2}\theta_{y0}\frac{\partial \Delta(\xi_x,\xi_y)}{\partial \xi_y}, \qquad \left(|\xi_x| \geq \frac{1}{2}\right) \wedge \left(|\xi_y| \geq \frac{1}{2}\right) \tag{6-7}$$

6.2.3 Method 1: Applied moment-surficial rotation, using only Boussinesq's approximation.

The Boussinesq surficial displacement field ρ_z due to presence of a vertical point load P applied at the origin of an elastic (linear and homogeneous) half-space is defined as,

$$\rho_z(x,y) = \frac{P}{\pi}\frac{(1-\nu_s^2)}{E_s}\frac{1}{\sqrt{x^2+y^2}} \tag{6-8}$$

where ν_s is the Poisson's ratio, E_s is the elastic modulus of the soil, and (x,y) represent the Cartesian coordinates between the load and any point in the half-space surface. Now, if it is had a rigid square footing of length b, the equation (6-8) can be used by applying a pair of equal and opposite point loads P along the axis x at the locations $x = b/2$ and $x = -b/2$. These loads produce a moment about the y-axis equal to $\mu_{y0} = Pb$. Thus, an approximation of the surface vertical displacement function $U_z(x,y)$ in 3D, due to the moment μ_{y0} can be derived through the sum of the two vertical loads as follows,

$$U_z(x,y) = \rho_z\left(x-\tfrac{b}{2},y\right) - \rho_z\left(x+\tfrac{b}{2},y\right)$$

$$U_z(x,y) = \frac{\mu_{y0}}{\pi}\frac{(1-\nu_s^2)}{E_s b}\left\{\frac{1}{\sqrt{\left(x-\frac{b}{2}\right)^2+y^2}} - \frac{1}{\sqrt{\left(x+\frac{b}{2}\right)^2+y^2}}\right\} \tag{6-9}$$

The relationship between the applied moment μ_{y0} and the rotation of the foundation θ_{y0} can be defined by using the empirical formulae deduced by Pais and Kausel (1988).

$$\mu_{y0} = \frac{1}{2}\frac{G_s b^3}{(1-\nu_s)}\theta_{y0} = \frac{1}{4}\frac{E_s b^3}{(1-\nu_s^2)}\theta_{y0}, \qquad G_s = \frac{E_s}{2(1+\nu_s)} \tag{6-10}$$

where G_s is the shear modulus of the half-space. Then, using the equation (6-10), the surface vertical displacement $U_z(x,y)$ can be written as,

$$U_z(x,y) = \frac{b^2}{4\pi}\left\{\frac{1}{\sqrt{\left(x-\frac{b}{2}\right)^2+y^2}} - \frac{1}{\sqrt{\left(x+\frac{b}{2}\right)^2+y^2}}\right\}\theta_{y0} \tag{6-11}$$

The non-dimensional coordinates are defined as $x = \xi_x b$ and $y = \xi_y b$, where the term $U_z(x,y) = u_z(\xi_x,\xi_y)b$ of the equation (6-11) becomes,

$$u_z(\xi_x,\xi_y)=\frac{1}{4\pi}\left\{\frac{1}{\sqrt{\left(\xi_x-\frac{1}{2}\right)^2+\xi_y^2}}-\frac{1}{\sqrt{\left(\xi_x+\frac{1}{2}\right)^2+\xi_y^2}}\right\}\theta_{y0}=\frac{1}{2}\Delta(\xi_x,\xi_y)\theta_{y0} \qquad \textbf{(6-12)}$$

Therefore, the decay function $\Delta(\xi_x,\xi_y)$ can be defined as,

$$\Delta(\xi_x,\xi_y)=\frac{1}{2\pi}\left\{\frac{1}{\sqrt{\left(\xi_x-\frac{1}{2}\right)^2+\xi_y^2}}-\frac{1}{\sqrt{\left(\xi_x+\frac{1}{2}\right)^2+\xi_y^2}}\right\},\quad \left(|\xi_x|\gg\frac{1}{2}\right)\wedge\left(|\xi_y|\gg\frac{1}{2}\right) \qquad \textbf{(6-13)}$$

The surficial slopes are given by partial differentiation of equation (6-13) as follows,

$$\theta_y(\xi_x,\xi_y)=\frac{\partial\Delta(\xi_x,\xi_y)}{\partial\xi_x}=\frac{1}{4\pi}\left\{-\frac{2\xi_x-1}{\left(\left(\xi_x-\frac{1}{2}\right)^2+\xi_y^2\right)^{3/2}}+\frac{2\xi_x+1}{\left(\left(\xi_x+\frac{1}{2}\right)^2+\xi_y^2\right)^{3/2}}\right\} \qquad \textbf{(6-14)}$$

$$\theta_x(\xi_x,\xi_y)=\frac{\partial\Delta(\xi_x,\xi_y)}{\partial\xi_y}=\frac{1}{2\pi}\left\{-\frac{\xi_y}{\left(\left(\xi_x-\frac{1}{2}\right)^2+\xi_y^2\right)^{3/2}}+\frac{\xi_y}{\left(\left(\xi_x+\frac{1}{2}\right)^2+\xi_y^2\right)^{3/2}}\right\} \qquad \textbf{(6-15)}$$

The limitations of this formulation, equation (6-13) are: (i) the displacement field for the position $\xi_x=1/2\,,\xi_y=0$ gives a singularity point $\Delta(1/2\,,0)=\infty$, (ii) for small inter-building distances, where the SSSI is important, the vertical deformation is less accurate, and (iii) it does not completely include the constraining effects of the rotation of the rigid footing itself, as discussed by Aldaikh et al. (2018).

6.2.4 Method 2: Applied moment-surficial rotation, using a 3D FEA calibrated empirical fit

The weakness of Method 1 (Boussinesq approach) is that it predicts accurate vertical deformations only far away from the foundation. Therefore, a Finite Element solution that provides a more accurate response is required. The following high-order FE model, shown in Figure 6.4, using the MATLAB Finite Element CALFEM toolbox (developed by Austrell et al. (2004)) is performed. The soil was modelled considering a fine mesh of 8-node isoparametric solid linear elastic elements and a 3-D formulation. Note that Figure 6.4 for a single-footing case employed millions of DOFs. The foundation is modelled as a perfectly rigid plate element. Note that a sensitivity study to evaluate the mesh size was performed. This study reached a mesh size that allowed reasonable computing running time and also similar seismic response if smaller mesh sizes were used.

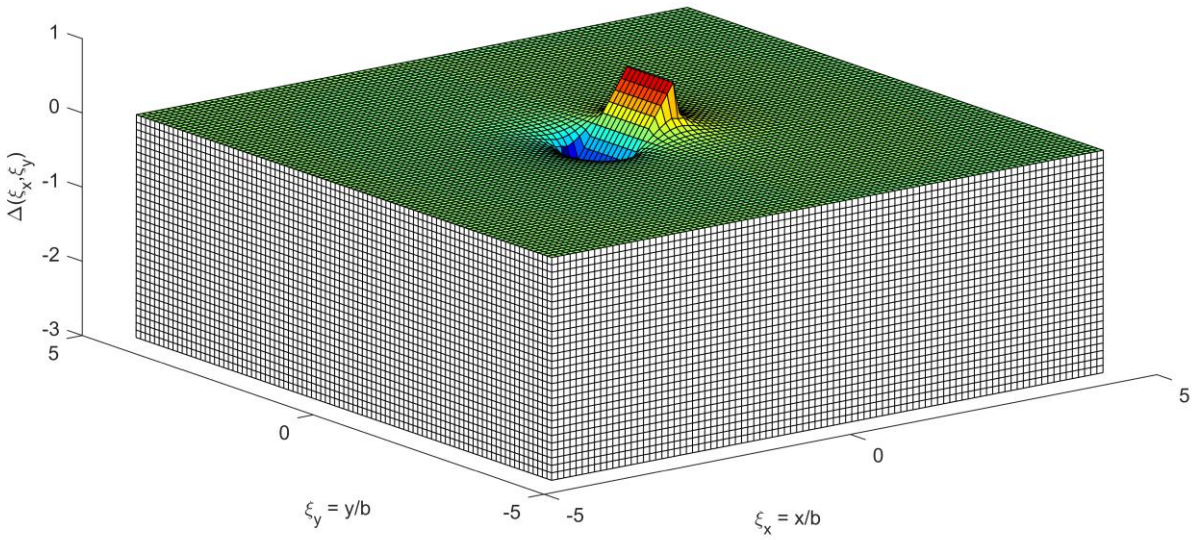

Figure 6.4 Evaluation of surface deformation field in 3D due to the rotation of a rigid foundation using a Finite Element model (Calfem, Austrell et al. (2004))

The empirical form of the decay function $\Delta(\xi_x, \xi_y)$ that is loosely based on the form in method 1, is defined as follows,

$$\Delta(\xi_x, \xi_y) = \frac{p_1}{\sqrt{(\xi_x - p_2)^2 + (p_3\xi_y)^2}} - \frac{p_1}{\sqrt{(\xi_x + p_2)^2 + (p_3\xi_y)^2}} \quad \textbf{(6-16)}$$

The optimal p_1, p_2, and p_3 coefficients that result from the least-squares fitting of equation (6-16) to the full 3D FEA simulation shown in Figure 6.4 are the follows, $p_1 = 0.3555$, $p_2 = 0.2453$, and $p_3 = 0.8049$. The goodness of fit is very high with a coefficient of determination of $R^2 = 0.956$. It is worth noting that equation (6-13) is identical to equation (6-16) when the coefficients are equal to $p_1 = 0.159$, $p_2 = 0.5$, and $p_3 = 1$.

This equation (6-16) represents an inverse power relationship between the decay function $\Delta(\xi_x, \xi_y)$ and the distances ξ_x and ξ_y. By differentiating the equation (6-16) the surface rotation function in both directions are estimated as follows,

$$\theta_y(\xi_x, \xi_y) = \frac{\partial\Delta(\xi_x, \xi_y)}{\partial\xi_x} = -\frac{p_1(\xi_x - p_2)}{\left((\xi_x - p_2)^2 + (p_3\xi_y)^2\right)^{3/2}} + \frac{p_1(\xi_x + p_2)}{\left((\xi_x + p_2)^2 + (p_3\xi_y)^2\right)^{3/2}} \quad \textbf{(6-17)}$$

$$\theta_x(\xi_x,\xi_y)=\frac{\partial\Delta(\xi_x,\xi_y)}{\partial\xi_y}=-\frac{p_1\xi_y p_3^2}{\left((\xi_x-p_2)^2+(p_3\xi_y)^2\right)^{3/2}}+\frac{p_1\xi_y p_3^2}{\left((\xi_x+p_2)^2+(p_3\xi_y)^2\right)^{3/2}} \quad \textbf{(6-18)}$$

Figure 6.5(a) displays the comparison for the surface decay function $\Delta(\xi_x,\xi_y)$ between Method 1 (Boussinesq's approximation, equation (6-13)), and Method 2 (3D FEM empirical fit, equation (6-16)). In general, the forms of both surfaces are very similar. Nevertheless, Method 2 is more accurate at small inter-building distances, mainly because the FEA empirical fit constrains the value of the vertical deformation at the corners of the foundation. Instead, Method 1 gives a singular point at the end of the foundation $\xi_x = 1/2\,, \xi_y = 0$, with a value of $\Delta(1/2\,,0)=\infty$.

Figure 6.5(b) displays the comparison for the surface rotations, derivative of the function $\Delta_x(\xi_x,\xi_y)$, between Method 1 (Boussinesq's approximation, equation (6-14)) and Method 2 (3D FEM empirical fit, equation (6-17)).

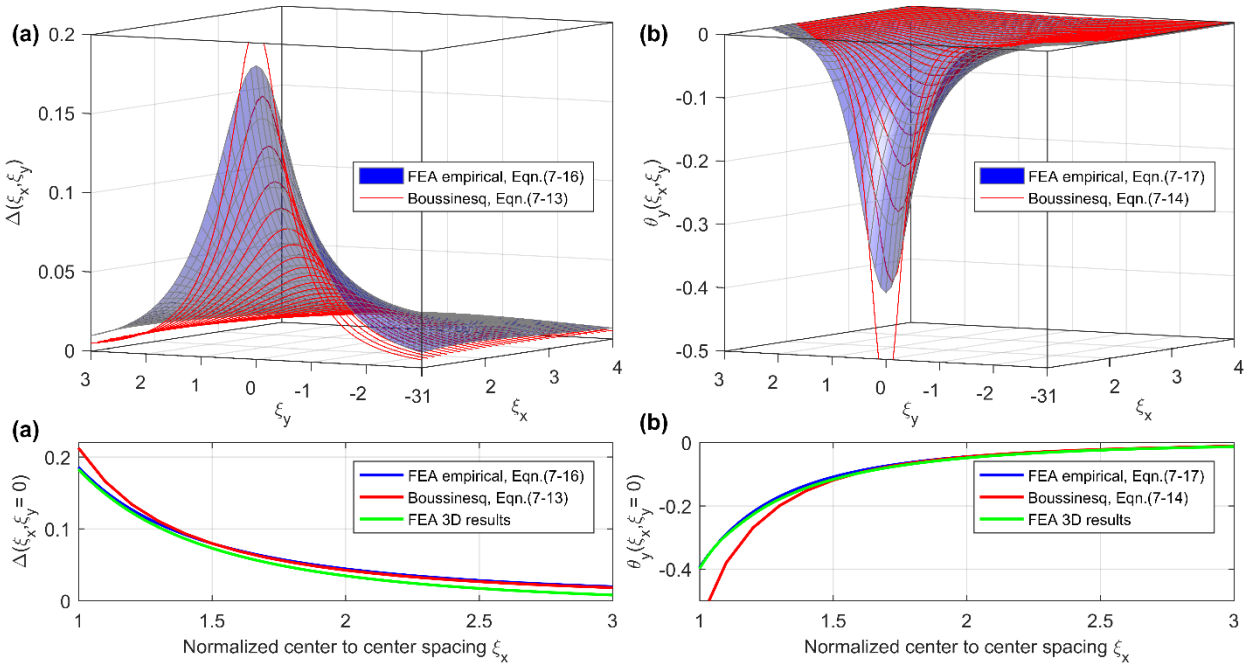

Figure 6.5 Comparison between the FEA empirical function results and Boussinesq results for (a) Surface decay function $\Delta(\xi_x,\xi_y)$ and (b) Surface rotation function $\theta_y(\xi_x,\xi_y)$

The FEA (Method 2) calibrated empirical model loosely based on Boussinesq's approximation removes the errors at small inter-building distances of Method 1 so is proposed as favourable and is used in all subsequent analyses.

6.2.5 Using static moment-surficial rotation field to determine global stiffness coefficients of K matrix

Once the surface decay and rotation functions are obtained, it is possible to estimate the stiffness matrix **K** of the foundation-soil-foundation system by defining different load cases. The numbers of unknown coefficients in the symmetric stiffness matrix **K,** defined in equation (6-2), are $2n^2 + n$ (from the upper triangle of the symmetric matrix $\mathbf{K} \in \mathbb{R}^{2n \times 2n}$). In equation (6-2), for a particular load case, it is known both the applied moments $\boldsymbol{\mu}$ at foundations and their associated foundation rotation $\boldsymbol{\theta}$ (from equations (6-14) and (6-17)), this would result in $2n$ equations. Thus, many independent load cases are needed to produce a rank sufficient system of algebraic equations in order to fully determine all the coefficients of **K**. Each load case i represents $2n$ algebraic equations in terms of these $2n^2 + n$ unknowns. Hence, at least q load cases are needed, where q is,

$$q \geq n + \frac{1}{2}, \quad q \in \mathbb{N} \tag{6-19}$$

The presence of the term (1/2) in equation (6-19) suggests that it is difficult to avoid an overdetermined system. However, using more load cases than are absolutely necessary can help, via averaging, to produce more stable results. Therefore, the least-squares method is used (Woodgate, 1998), to determine the stiffness coefficients **K**, by minimizing the error ε in the following expression,

$$\varepsilon = \min \|\boldsymbol{\mu} - \mathbf{K}\boldsymbol{\Theta}\|_2, \quad \boldsymbol{\mu} = \left[\boldsymbol{\mu}_1, \cdots, \boldsymbol{\mu}_q\right], \quad \boldsymbol{\theta} = \left[\boldsymbol{\theta}_1, \cdots, \boldsymbol{\theta}_q\right] \tag{6-20}$$

where moments $\boldsymbol{\mu}_i$ and rotations $\boldsymbol{\theta}_i$ are defined for the different load case "*i*". The suggestion in this research is that only one footing should have one applied moment on it. Therefore $\boldsymbol{\mu}_i$ is a single-entry vector. Each footing could have 2 load cases (for *x* and *y*-directions) and hence a total of $q = 2n$ load cases are proposed. The rotation vectors $\boldsymbol{\theta}_i$ are determined by making use of equations (6-17) and (6-18), thus $\boldsymbol{\theta}_i$ contains all non-zero elements.

The weakness of equation (6-20) is that for large building arrangements, the method becomes a little computationally time-consuming. This is mainly because all the buildings are connected with each other, so the number of unknowns grows quadratically. Therefore, for a large cluster of buildings, the approach presented below can be followed, based on Kronecker products.

6.2.6 Stiffness matrix estimate using the theory of Kronecker products

A different approach for the same problem is using the theory of Kronecker products for inverse system identification. Given that there is, in principle, a unique solution to this inverse problem, it has left with

the problem of rearranging equations (6-2) into a form that is easily tractable. This is a set of algebraic equations where, non-typically, the unknowns are in a matrix rather than a vector. The theory of Kronecker products enables this kind of problem to be solved. Consider the following matrix equation,

$$\mathbf{AXB} = \mathbf{C} \tag{6-21}$$

In which it wants to determine all terms in matrix $\mathbf{X}$. Consider a vectorisation function $\mathrm{vec}(\bullet)$ which is an isomorphism (a linear transformation) that converts a matrix into a vector, (Petersen and Pedersen, 2007). The vectorization function $vec(\bullet)$ is performed in MATLAB (2016) using the *reshape( )* function. When this vectorization function is applied to equation (6-21) is obtained,

$$(\mathbf{B}^T \otimes \boldsymbol{A})\mathrm{vec}(\boldsymbol{X}) = \mathrm{vec}(\mathbf{C}) \tag{6-22}$$

where the symbol $\otimes$ is the Kronecker product (using the *kron( )* function in MATLAB). Hence, the following solution can be stated,

$$\widetilde{\mathbf{X}} = \mathrm{vec}^{-1}\big((\mathbf{B}^T \otimes \mathbf{A})^{+}\mathrm{vec}(\mathbf{C})\big) \tag{6-23}$$

where $\mathrm{vec}^{-1}(\bullet)$ is the inverse vectorization isomorphism and $(\bullet)^{+}$ is the Moore-Penrose pseudo-inverse (which can be determined using a singular-value decomposition in MATLAB using the backslash operator). Thus, for equations (6-2) it is substituted $\mathbf{A} = \mathbf{I}, \widetilde{\mathbf{X}} = \widetilde{\mathbf{K}}, \mathbf{B} = \boldsymbol{\Theta}$, and $\mathbf{C} = \boldsymbol{\mu}$ into equation (6-23) and therefore,

$$\widetilde{\mathbf{K}} = \mathrm{vec}^{-1}\big((\boldsymbol{\Theta}^T \otimes \mathbf{I})^{+}\mathrm{vec}(\boldsymbol{\mu})\big) \tag{6-24}$$

This is achieved by the following one line of MATLAB (2016) script

```
Kest = reshape(kron(Theta', eye(n)) \ reshape(mu, q*n, 1) ,n, n)
```

The weakness of this method is that it does not enforce symmetry in $\widetilde{\mathbf{K}}$. This must be imposed through averaging. Additionally, this method does not constrain the zero elements of equation (6-2) to be exactly zero. Thus, the methods presented in equation (6-20) and (6-24) are fundamentally both least squares approaches. However, equation (6-20) adds additional constraints which are not explicitly present in equation (6-24). Nevertheless, the differences between both approaches should be considered second order effects, with equation (6-24) being significantly quicker computationally.

In the following section, the moment surficial rotation method presented in Section 6.2.5 (by employing the least-squares method) is used.

6.2.7 Comparison of 3D Method 2 with the 2D solutions presented by Aldaikh et al. (2018)

In order to verify the method presented here, the stiffness coefficients k_{y1} and κ_{y12} are compared with the values calculated in previous research of Aldaikh et al. (2018), for two foundations located with different centre to centre distances ξ_x and ξ_y. The matrices of the relationship, equation (6-2), between the applied moment $\boldsymbol{\mu}$ and the rotation $\boldsymbol{\Theta}$ in a two-building system simplifies to the following,

$$\boldsymbol{\mu} = \begin{bmatrix} \mu_{x1} \\ \mu_{y1} \\ \mu_{x2} \\ \mu_{y1} \end{bmatrix}, \qquad \boldsymbol{\Theta} = \begin{bmatrix} \theta_{x1} \\ \theta_{y1} \\ \theta_{x2} \\ \theta_{y1} \end{bmatrix} \tag{6-25}$$

$$\mathbf{K} = \begin{bmatrix} k_{x1} + \kappa_{x12} + \kappa_{xy12} & 0 & -\kappa_{x12} & -\kappa_{xy12} \\ 0 & k_{y1} + \kappa_{y12} + \kappa_{xy12} & -\kappa_{xy12} & -\kappa_{y12} \\ -\kappa_{x12} & -\kappa_{xy12} & k_{x2} + \kappa_{x12} + \kappa_{xy12} & 0 \\ -\kappa_{xy12} & -\kappa_{y12} & 0 & k_{y2} + \kappa_{y12} + \kappa_{xy12} \end{bmatrix} \tag{6-26}$$

Aldaikh et al. (2018) performed a Finite Element analysis in the software PLAXIS 2D for two identical footings spaced at different distances. This model is a plane strain model in 2D (per unit length in the out-of-plane direction) with linear elastic materials. The soil was modelled using an unstructured mesh of 15-node triangular elements. It is termed here as "Empirical 2D Aldaikh et al. (2018)". In addition, Aldaikh et al. (2018) performed a physical experiment for the case of two adjacent rigid foundations, here termed "Experimental results Aldaikh et al. (2018)".

Figure 6.6(a) shows the variation of foundation stiffness auto-rotational coefficients k_{y1} (with a neighbouring footing) relative to the stiffness of a singleton, completely isolated, footing k_s. Figure 6.6(b) depicts the variation of the inter-rotational stiffness κ_{y12} (normalized by k_{y1}) with the non-dimensional center to center distances ξ_x and ξ_y. It is termed "empirical 3D, equation (6-16)" in this chapter. In general, the results of the FEA empirical 3D agree very well with both FEA empirical 2D and experimental data, for center to center spacing $\xi_y = 0$ (i.e. 2D case).

The increase of the auto-rotational stiffness k_{y1} reaches a maximum value of 125% of k_s, Figure 6.6(a). The auto-rotational stiffness k_{y1} is different from the stiffness of a completely isolated footing k_s because it includes the additional stiffening effect of the adjacent footings. Instead, the inter-rotational stiffness k_{y12} is -20% of k_{y1} at the same distance $\xi_x = 1, \xi_y = 0$, Figure 6.6(b).

The interaction between the buildings is practically negligible at a spacing larger than 2.5 times the foundation's width (i.e. the auto-rotational stiffness coefficients equal to $k_{y1} \approx k_s$ and the inter-rotational stiffness equal to $\kappa_{y12} \approx 0$).

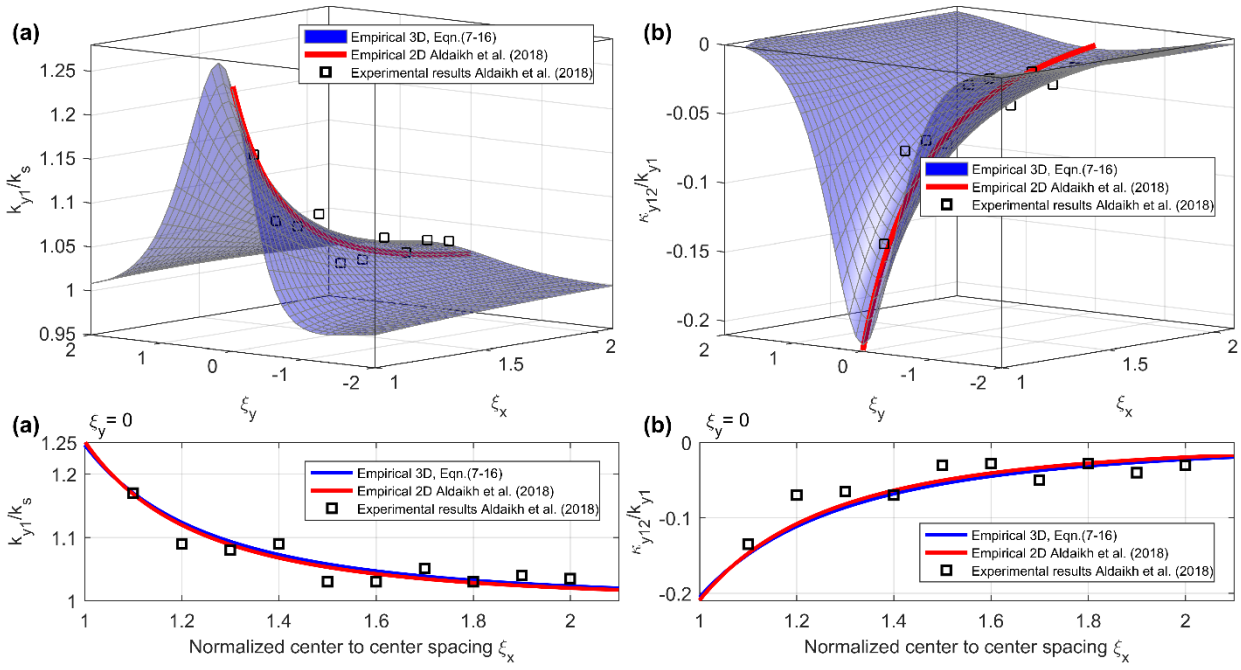

Figure 6.6 Comparison of the FEA empirical 3D analysis, FEA empirical 2D analysis (Aldaikh et al., 2018) and experimental data (Aldaikh et al., 2018) for: (a) Foundation stiffness relative to a single footing and (b) Rotational interaction springs relative to individual footing stiffness

Using Method 2 (the FEA calibrated empirical 3D form, equation (6-16)) it is possible to calculate the cross-coupled interaction stiffness κ_{yx12}, and κ_{yx12} is plotted in Figure 6.7. The value of κ_{xy12} decreases as the footing spacing increases and it is zero at a spacing equal to $\xi_y = 0$, because the rotation θ_{xi} and θ_{yi} are decoupled in this position. The cross-coupled interaction stiffness κ_{yx12} reaches a value of only 8.6% of the auto-rotational spring stiffness k_{y1} (at $\xi_x = 1, \xi_y = \pm 0.5$). Thus, it is demonstrated that the cross-coupling inter-rotational springs κ_{yxij} are likely to only produce second order effects.

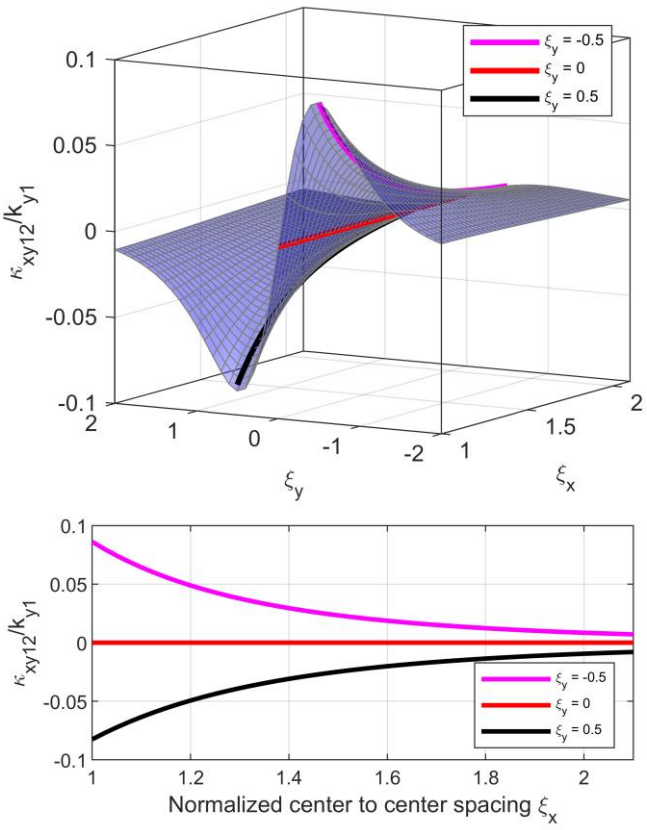

Figure 6.7 Variation of cross-coupled interaction stiffness with the normalized centre to centre spacing

6.2.8 Equation of motion of the complete system

Employing Euler-Lagrange energy mechanics, the equations of motion describing the dynamics of the discretised system of Figure 6.1 is formulated. The kinetic energy T_E and the potential energy U_E for this system are written respectively as follows,

$$T_E = \frac{1}{2}\sum_{i=1}^{n}\left(m_{bi}\left(\dot{x}_i + \dot{x}_g - h_i\theta_{yi}\right)^2 + m_{bi}(\dot{y}_i - h_i\theta_{xi})^2 + m_{si}r_i^2\left(\theta_{xi}^2 + \theta_{yi}^2\right)\right) \quad \textbf{(6-27)}$$

$$U_E = \frac{1}{2}\sum_{i=1}^{n}\left(k_{bi}x_i^2 + k_{bi}y_i^2 + k_{xi}\theta_{xi}^2 + k_{yi}\theta_{yi}^2\right) + \cdots$$
$$+\frac{1}{2}\sum_{i=1}^{n-1}\sum_{j=i+1}^{n}\left(\kappa_{xij}\left(\theta_{xj} - \theta_{xi}\right)^2 + \kappa_{yij}\left(\theta_{yj} - \theta_{yi}\right)^2 + \kappa_{xyij}\left(\theta_{yj} - \theta_{xi}\right)^2\right) \quad \textbf{(6-28)}$$

where h_i is the height, m_{bi} is the total lumped modal mass of building i and m_{si} is the foundation/soil mass underneath building i. k_{bi} is the modal building lateral stiffness and r_i is the soil/foundation mass radius of gyration. κ_{xij}, κ_{yij} are the stiffness coefficients of the inter-rotational springs between buildings i and j, κ_{xyij} are the cross-coupled coefficients, and k_{xi} and k_{yi} are the auto-rotational spring stiffnesses

of the soil beneath each building. Hence, the Euler-Lagrange equations of motion describing the dynamics of the discretised system can be derived in the standard way, by calculus, and is written in matrix form, as follows,

$$\mathbf{M}\ddot{\mathbf{x}} + \mathbf{C}\dot{\mathbf{x}} + \mathbf{K}\mathbf{x} = \mathbf{p}\ddot{x}_g \tag{6-29}$$

where the mass matrix **M**, the damping matrix **C**, the stiffness matrix **K**, the force vector **p** and the DOFs vector **x** correspond to the complete system of n buildings, and are defined as follows,

$$\mathbf{M} = \begin{bmatrix} \widehat{\mathbf{M}}_1 & \cdots & 0 & \cdots & 0 \\ \vdots & \ddots & \vdots & \ddots & \vdots \\ 0 & \cdots & \widehat{\mathbf{M}}_i & \cdots & 0 \\ \vdots & \ddots & \vdots & \ddots & \vdots \\ 0 & \cdots & 0 & \cdots & \widehat{\mathbf{M}}_n \end{bmatrix}, \quad \mathbf{K} = \begin{bmatrix} \widehat{\mathbf{K}}_1 & \cdots & \widehat{\boldsymbol{\kappa}}_{\mathbf{1}\boldsymbol{i}} & \cdots & \widehat{\boldsymbol{\kappa}}_{\mathbf{1}\boldsymbol{n}} \\ \vdots & \ddots & \vdots & \ddots & \vdots \\ \widehat{\boldsymbol{\kappa}}_{\boldsymbol{i}\mathbf{1}} & \cdots & \widehat{\mathbf{K}}_i & \cdots & \widehat{\boldsymbol{\kappa}}_{\boldsymbol{i}\boldsymbol{n}} \\ \vdots & \ddots & \vdots & \ddots & \vdots \\ \widehat{\boldsymbol{\kappa}}_{\boldsymbol{n}\mathbf{1}} & \cdots & \widehat{\boldsymbol{\kappa}}_{\boldsymbol{n}\boldsymbol{i}} & \cdots & \widehat{\mathbf{K}}_n \end{bmatrix} \tag{6-30}$$

$$\mathbf{p} = [\widehat{\mathbf{p}}_1 \quad \cdots \quad \widehat{\mathbf{p}}_i \quad \cdots \quad \widehat{\mathbf{p}}_n]^T, \quad \mathbf{x} = [\hat{\mathbf{x}}_1 \quad \cdots \quad \hat{\mathbf{x}}_i \quad \cdots \quad \hat{\mathbf{x}}_n]^T \tag{6-31}$$

$$\mathbf{C} = \mathbf{M}\left(\sum_{j=1}^{4n} \frac{2\zeta_j \omega_j}{\boldsymbol{\phi}_j^T \mathbf{M} \boldsymbol{\phi}_j} \boldsymbol{\phi}_j \boldsymbol{\phi}_j^T\right)\mathbf{M} \tag{6-32}$$

The system's linear viscous damping matrix **C** assumes that each natural mode is damped at $\zeta_j = 0.05$ of the critical damping, $\boldsymbol{\phi}_j$ is the modal eigenvector of the mode j, and ω_j are the natural frequencies of the system. Thus, the Caughey orthogonal damping matrix **C** can be calculated as Clough and Penzien (1993), by equation (6-32).

The global mass matrix **M** corresponds to a diagonal block matrix, where the different blocks $\widehat{\mathbf{M}}_i$ represent the mass matrix for each building i, as follows.

$$\widehat{\mathbf{M}}_i = \begin{bmatrix} m_{bi} & 0 & -m_{bi}h_i & 0 \\ 0 & m_{bi} & 0 & -m_{bi}h_i \\ -m_{bi}h_i & 0 & m_{bi}h_i^2 + m_{si}r_i^2 & 0 \\ 0 & -m_{bi}h_i & 0 & m_{bi}h_i^2 + m_{si}r_i^2 \end{bmatrix} \tag{6-33}$$

The global stiffness matrix **K** includes the interaction effects between all the buildings. So, the diagonal block term $\widehat{\mathbf{K}}_i$ is the stiffness matrix for each building i, including the additional stiffening effect of the adjacent footings.

$$\widehat{\mathbf{K}}_i = \begin{bmatrix} k_{bi} & 0 & 0 & 0 \\ 0 & k_{bi} & 0 & 0 \\ 0 & 0 & k_{xi} + \sum_{j=1}^{n} \left(\kappa_{xij} + \kappa_{xyij}\right) & 0 \\ 0 & 0 & 0 & k_{yi} + \sum_{j=1}^{n} \left(\kappa_{yij} + \kappa_{xyij}\right) \end{bmatrix} \quad \textbf{(6-34)}$$

The off-diagonal block terms $\widehat{\boldsymbol{\kappa}}_{ij}$ represent the interaction between the buildings i and j and is defined in equation (6-35).

$$\widehat{\boldsymbol{\kappa}}_{1i} = \begin{bmatrix} 0 & 0 & 0 & 0 \\ 0 & 0 & 0 & 0 \\ 0 & 0 & -\kappa_{x1i} & -\kappa_{xy1i} \\ 0 & 0 & -\kappa_{xy1i} & -\kappa_{y1i} \end{bmatrix} \quad \textbf{(6-35)}$$

Finally, the global excitation vector **p** is assembled by the block vector $\widehat{\boldsymbol{p}}_i$ of each building i, and the degrees of freedom vector **x** is assembled by the vector $\hat{\mathbf{x}}_i$ according to equation (6-36).

$$\widehat{\mathbf{p}}_i = [-m_{bi} \quad 0 \quad -m_{bi}h_i \quad 0]^{\boldsymbol{T}}, \quad \hat{\mathbf{x}}_i = [x_i \quad y_i \quad \theta_{yi} \quad \theta_{xi}]^{\boldsymbol{T}} \quad \textbf{(6-36)}$$

In this chapter, the dynamic properties of the building "i" required for equation (6-29) are calculated according to the following assumptions,

(i) For the fundamental natural period of the structure on a rigid foundation (i.e. with no foundation/soil rotation), it is adopted the approximate empirical relationship proposed by the Eurocode 8 EN-1998 (2004), $T_{xi} = T_{yi} = T_i = c_0 h_i^{3/4}$. In this formulation the height of the building is taken in metres and the factor is equal to $c_0 = 0.075$ for reinforced concrete moment resisting frames.

(ii) Newmark and Rosenblueth (1971) consider that the volume of soil mass beneath a square base building is approximately equal to $m_{si} = 0.35\rho_s b_i^3$.

(iii) The mass of the building can be approximated as $m_{bi} = \rho_b b_i^2 h_j$.

(iv) The radius of gyration is calculated according to the Newmark's empirical expression $r_i = 0.33 b_i$.

(v) It has been demonstrated that SSSI on structures supported on loose soil may exhibit significant interaction (Alexander et al., 2013; Aldaikh et al., 2015) so the soil properties used correspond

to loose sand, where the soil density is $\rho_s = 1300[kg/m^3]$, the shear wave velocity is $V_s = 156[m/s]$ and the Poisson's ratio of the soil is $\nu_s = 0.3$.

(vi) The average building density can be considered as $\rho_b = 600[kg/m^3]$.

6.2.9 Response performance measures of interest

This chapter intends to evaluate the change in the response between the coupled (Structure-Soil-Structure Interaction, SSSI) and the uncoupled (Soil-Structure Interaction, SSI) systems. First the coupled solution of equation (6-29) is determined through time-history analysis. Then, the uncoupled response of each buildings (i.e. SSI response) are computed similarly. The equations of motion for the special case of uncoupled buildings response (SSI) are obtained by completely removing all coupling springs and their stiffening effects. As a measure of change in the response between SSSI and SSI, the relative displacement U_1 (horizontal sway + rocking) and the total acceleration A_1 (horizontal sway + ground + rocking) for the top of the building i are employed, denoted by,

$$U_i = x_i - h_i\theta_{yi}, \qquad A_i = \ddot{x}_i + \ddot{x}_g - h_i\ddot{\theta}_{yi} \tag{6-37}$$

In addition, it is valuable to characterize the change in total power caused by the multiple SSSI among the buildings. So, the percentage change in total power χ_i and $\ddot{\chi}_i$ for the building i, when using the uncoupled SSI analyses rather than coupled SSSI analyses is expressed in terms of the total power spectral densities $E_{PSD}(U_i)$ and $E_{PSD}(A_i)$,

$$\chi_i = 100\left\{\frac{[E_{PSD}(U_i)]_{SSSI}}{[E_{PSD}(U_i)]_{SSI}} - 1\right\}, \qquad \ddot{\chi}_i = 100\left\{\frac{[E_{PSD}(A_i)]_{SSSI}}{[E_{PSD}(A_i)]_{SSI}} - 1\right\} \tag{6-38}$$

where $E_{PSD}(U_i)$ and $E_{PSD}(A_i)$ are based on the Fourier Transform of all data points of the response displacement U_i and acceleration time series A_i, respectively. The change of power χ_i and $\ddot{\chi}_i$ would be zero if there is no difference in overall response power between SSSI and SSI analyses.

6.3 Numerical studies

In this section the approach described previously is applied (the reduced-order model equation (6-29)), to explore some multi-building SSSI 3D cases. These anecdotal cases are designed to explore the performance of the reduced order model equation (6-29) rather than explore a full parametric, geometric and ground motion variation of the multi-building SSSI 3D phenomenology, as this is beyond the scope of this current research.

First, results for a two-foundation system in 3D with different inter-building distances (case 1) are presented. Subsequently, the solution for a set of seven buildings in an L shape arrangement (case 2) is analysed. Lastly, a city block of 12 buildings (case 3) is examined. These analyses are carried out for the Superstition Hill earthquake (11/24/1987, Imperial Valley Wildlife SH-02 Station). This particular record was selected because the SSSI effects (amplifications and reductions) are representative of mean for all record set presented in Table 3-2 and Table 3-3.

Figure 6.8 shows the ground motion time series and the power spectral density of the record. The record data were obtained from the Pacific Earthquake Engineering (PEER) Research Center Database (PEER, 2014). The ground motion was recorded on weak soil, where the average shear wave velocity is less than $180[m/s]$, i.e. loose sand (Eurocode 8 EN-1998, 2004).

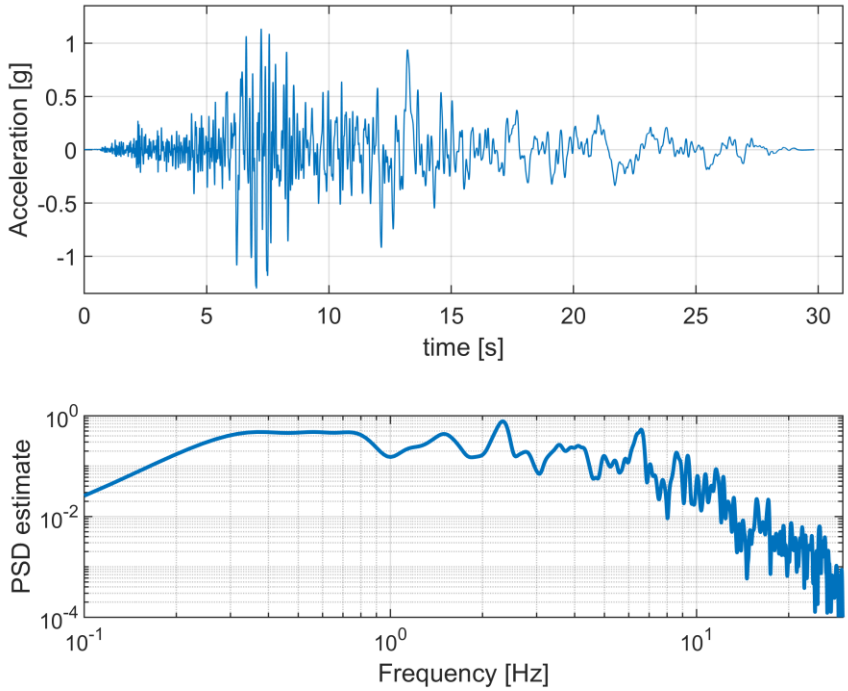

Figure 6.8 Acceleration ground motion and power spectral density (Superstition Hills-02 24/11/1987)

6.3.1 Case 1: A comparison between 2D and 3D seismic analyses for two adjacent buildings

In order to compare the differences between 2D and 3D analyses, the system of two buildings shown in Figure 6.9 is considered. Building 2 can be in any centre to centre distances ξ_x, ξ_y respect to building 1. Both buildings have a similar square plan area of b^2 and raft foundations.

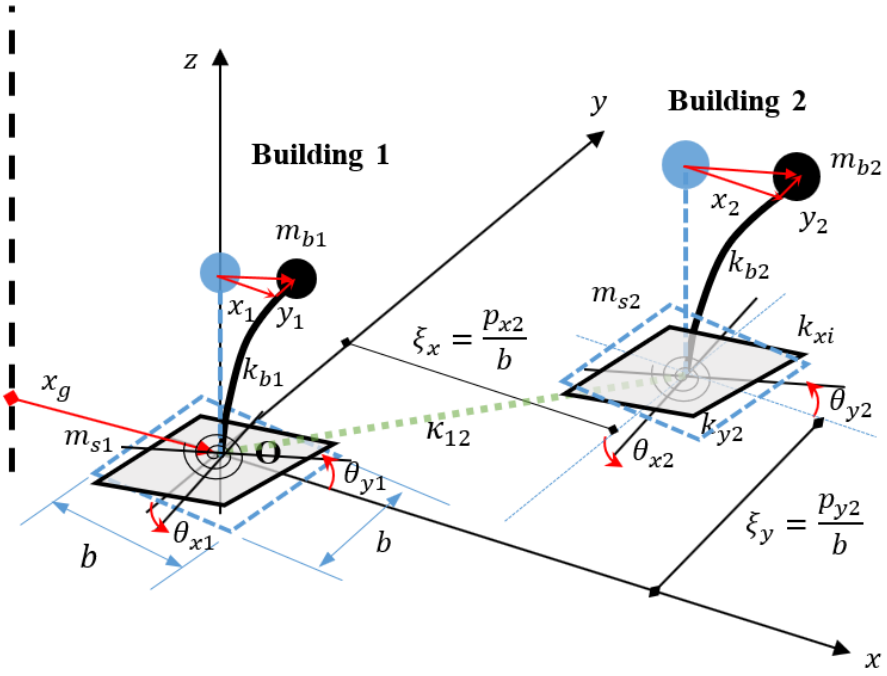

Figure 6.9 Multi buildings SSSI model in 3D

Figure 6.10(a) and Figure 6.10(b) show the uncoupled SSI (blue line) and coupled SSSI (red line) responses for the top of building 1 (namely the displacement U_1 for Figure 6.10(a) and total acceleration A_1 for Figure 6.10(b)), when the inter-building distances are equal to $\xi_x = 1.1$ and $\xi_y = 0$. The rigid base period is $T_1 = 0.6s$ of building 1 and $T_2 = 0.66s$ for building 2 (i.e. the second building is approximately 13.5% taller than the first building). Building 1 has a height to width ratio equal to $h_1/b = 1.6$. Figure 6.10(c) shows the corresponding power spectral density (PSD) for the displacement and Figure 6.10(d) shows the PSD for the total acceleration for building 1 considering the coupled (SSSI) and uncoupled (SSI) cases. Comparing the uncoupled and coupled responses, building 1's response appears to be significantly affected by the presence of the taller building in all of the time-history. The change in power, defined in equation (6-38), is equal to $\ddot{\chi}_1 = 26.7\%$ $\ddot{\chi}_1 = 37.4\%$ for the displacement and acceleration respectively.

Figure 6.11 displays the variation of change in power for the displacement $\chi_1(U_1)$ on the top of the building 1, where the centre to centre inter-building spacing ξ_x, ξ_y varies between -3.0 and 3.0. Note, building 1 is smaller than building 2. The critical zones in this figure are in red, i.e. where the building 1's total response power is amplified by the presence of building 2. Blue indicates when the response power is reduced. The inner black rectangle indicates the footprint of building 1, while the outer black rectangle highlights the touching centre to centre distances between buildings 1 and 2.

The maximum increase in the response occurs when building 2 is close to building 1 and aligned to the direction of the earthquake (i.e. $|\xi_y| \approx 0$), where the change in power are $\chi_1 = 32\%$ for the displacement. As expected, the effects of SSSI diminish as the inter-building distance increases, being practically negligible at $\xi_x, \xi_y \geq 2.5$.

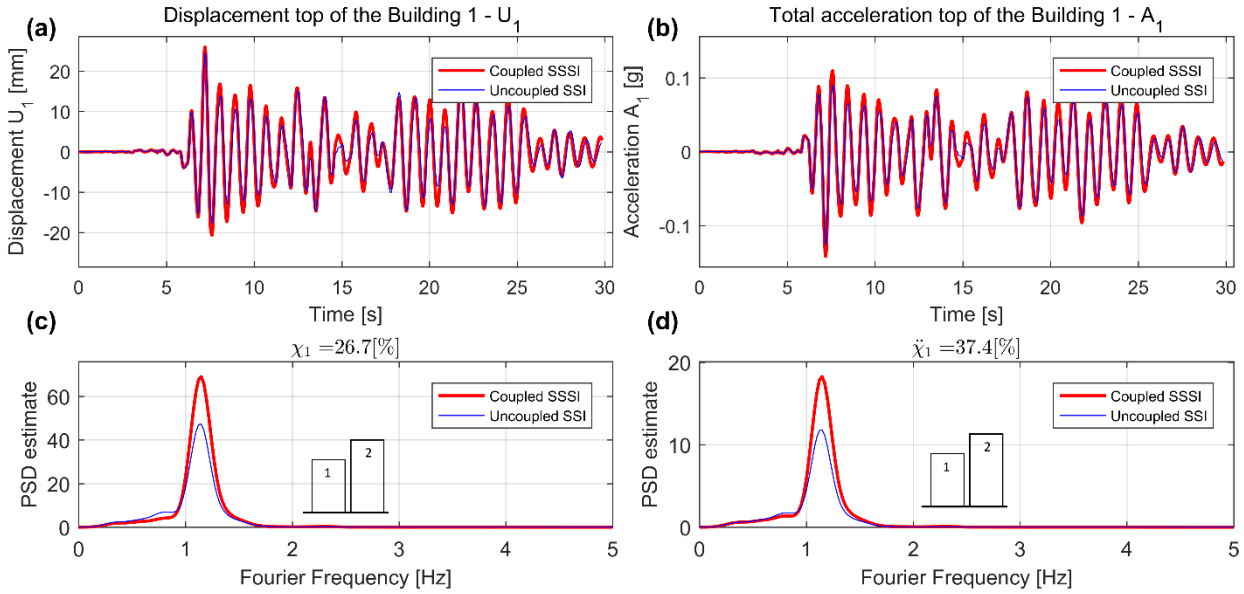

Figure 6.10 (a) Displacement and (b) Total acceleration responses, (c) Power spectral density of displacement and (d) Total acceleration – Building 1 smaller than building 2, (T_1 = 0.6s, T_2 = 0.66s, h_1/b = 1.6)

On the other hand, for the position of building 2 out of plane XZ (i.e. $|\xi_y| \geq 1.1$), building 1's total power response attenuates, with a maximum of $\chi_1 = -16.5\%$ for the displacement when the buildings are close together. This reduction on the response was not explored in the previous papers (Alexander et al., 2013; Aldaikh et al., 2015; Aldaikh et al., 2016), because these papers performed 2D analysis.

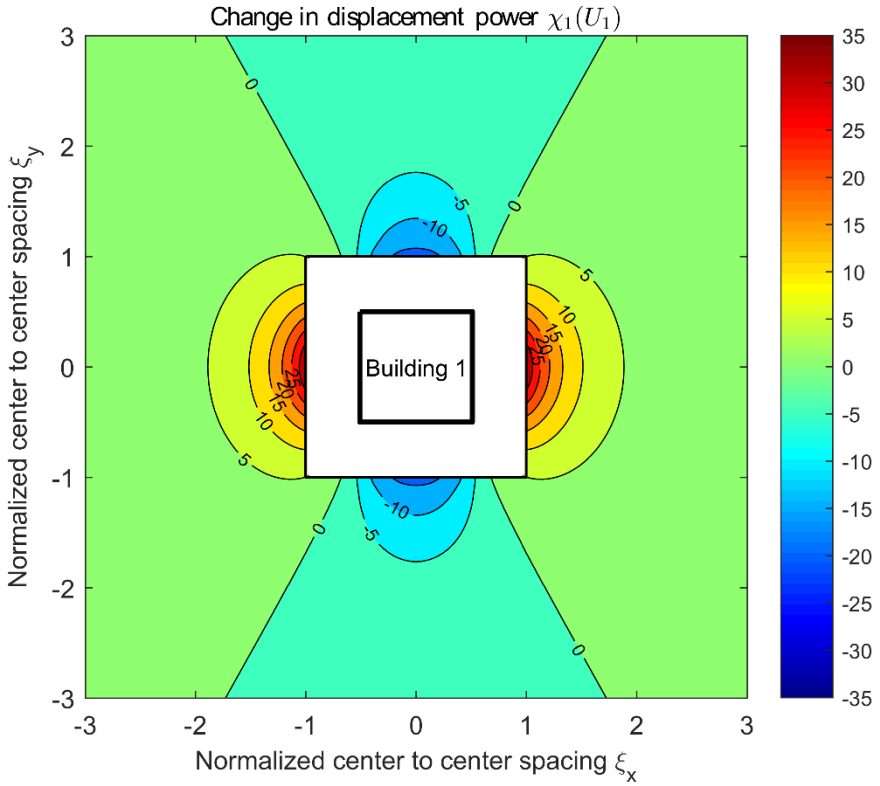

Figure 6.11 Change in displacement power χ_1 for building 1 as a function of the position of building 2, when building 1 is smaller than building 2 – Parameter set (T_1 = 0.6s, T_2 = 0.66s, h_1/b = 1.6)

Figure 6.12 displays the variation of change in power for the acceleration $\ddot{\chi}_1(A_1)$ on the top of the building 1, where the centre-to-centre inter-building spacing ξ_x, ξ_y varies between -3.0 and 3.0. As with the displacement, the maximum increase in the acceleration response occurs when building 2 is close to building 1 and aligned to the direction of the earthquake (i.e. $|\xi_y| \approx 0$), where the change in power is $\ddot{\chi}_1 = 50\%$. The effects of SSSI is small at $\xi_x, \xi_y \geq 2.5$. For the position of building 2 equal to $|\xi_y| \geq 1.1$, the building 1's total power response attenuates with a maximum of $\ddot{\chi}_1 = -22.5\%$ for the acceleration.

Therefore, while the 2D analysis seems to capture the worst case (the largest detrimental effect of SSSI), it does not allow a complete understanding of the SSSI effects between two adjacent buildings, especially the cases of out-of-plane adjacency that produce beneficial effects here.

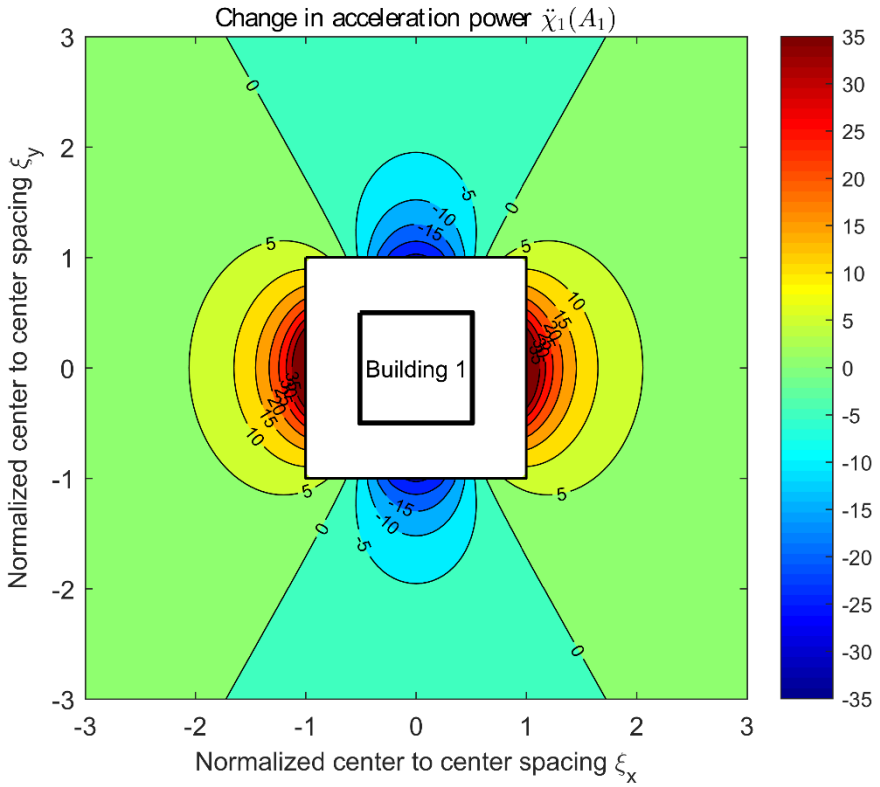

Figure 6.12 Change in acceleration power $\ddot{\chi}_1$ for building 1 as a function of the position of building 2, when building 1 is smaller than building 2 – Parameter set (T_1 = 0.6s, T_2 = 0.66s, h_1/b = 1.6)

Figure 6.13 displays the variation of change in power for the displacement χ_1 at the top of building 1 for the case where building 1 is taller than building 2. These results correspond to the case where the rigid base period of building 1 is $T_1 = 0.6[s]$ and $T_2 = 0.54[s]$ for building 2 (i.e. the second building is 13.1% smaller than the first building). Building 1 has a height to width ratio equal to $h_1/b = 1.6$. Unlike the previous figure, the position of the red peaks shifts between the graphs, where the maximum increase in the response ($\chi_1 = 20\%$) corresponds to the position of building 2 equal to $|\xi_y| = 1.1$ and $\xi_x = 0$. The maximum decrease in the response occurs when building 2 is close to building 1 and aligned to the direction of the earthquake (i.e. $|\xi_y| \approx 0$), where the change in power is $\chi_1 = -40\%$ for the acceleration.

Thus, again the 2D analysis developed by Alexander et al. (2013), Aldaikh et al. (2015), and Aldaikh et al. (2016), highlights the extreme case (the largest beneficial effect of SSSI) and it does not capture the cases of out-of-plane adjacency that produce detrimental effects here.

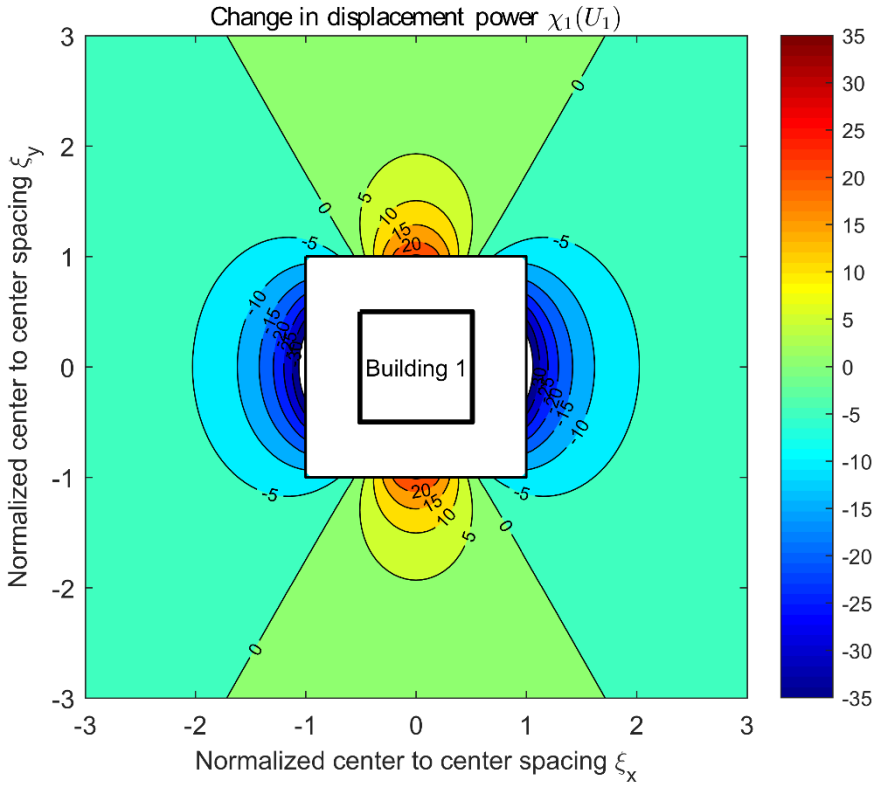

Figure 6.13 Change in displacement power χ_1 for building 1 as a function of the position of building 2, when building is 1 taller than building 2 – Parameter set (T_1 = 0.6s, T_2 = 0.54s, h_1/b = 1.6)

Figure 6.14 displays the variation of change in power for the acceleration $\ddot{\chi}_1$ at the top of building 1 for the case where building 1 is taller than building 2. The maximum increase in the change of power is $\ddot{\chi}_1 = 15\%$ (position of building 2 equal to $|\xi_y| = 1.1$ and $\xi_x = 0$). The maximum decrease in the response corresponds to $\ddot{\chi}_1 = -36\%$, when the building 2 is close to building 1 and aligned to the direction of the earthquake (i.e. $|\xi_y| \approx 0$).

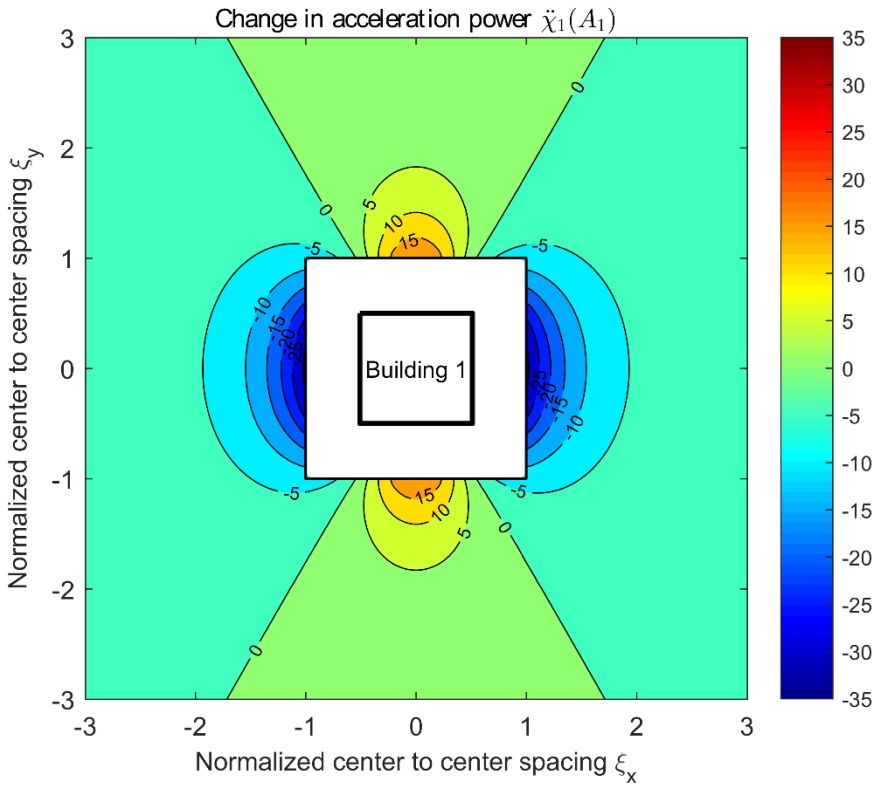

Figure 6.14 Change in acceleration power $\ddot{\chi}_1$ for building 1 as a function of the position of building 2, when building 1 is taller than building 2 – Parameter set (T_1 = 0.6s, T_2 = 0.54s, h_1/b = 1.6)

6.3.2 Case 2: L shape arrangement of identical equispaced buildings

In this section, a selected L shape arrangement is presented in order to measure the influence of multi-building SSSI in 3D. All the buildings are identical, having a rigid base period of $T_i = 0.5s$, the same square plan area and buildings have a height to width ratio equal to $h_i/b = 1.5$. The centre-to-centre inter-building distances are equispaced at $\xi_x = 1.2, \xi_y = 1.2$. Figure 6.15 displays the variation of change in power for the acceleration on top of the buildings. The maximum increase in total acceleration power response occurred on the buildings aligned with the earthquake, with a maximum of $\ddot{\chi}_3 = 64\%$ for the acceleration on building 3. In addition, there is reduction in the response for some buildings, with a maximum for the building 1 ($\ddot{\chi}_1 = -17.6\%$). The change in displacement and acceleration power have a similar trend when the height of the buildings are the same. So, the change in acceleration power is only presented from now on.

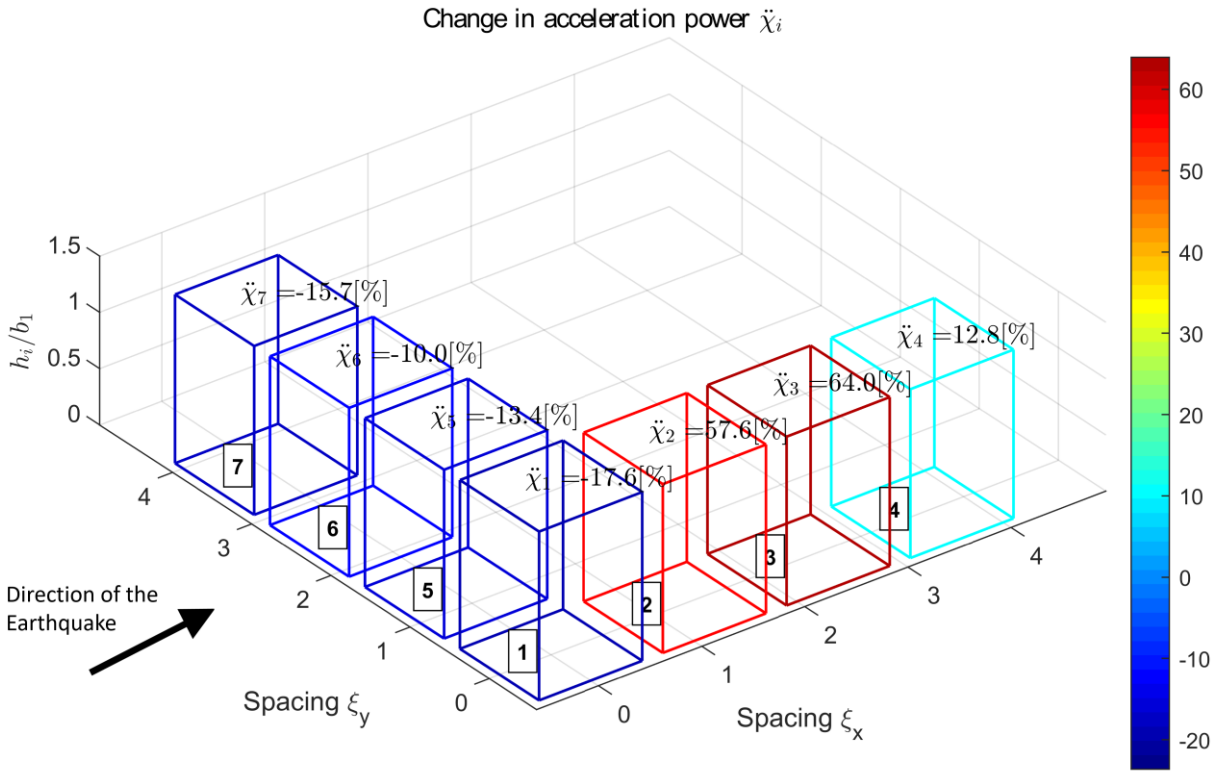

Figure 6.15 Change in acceleration power due to 3D SSSI for L shape arrangement. Equispaced identical buildings – Parameter set (T_i = 0.5s, h_i/b = 1.5, ξ_x = 1.2, ξ_y = 1.2)

Figure 6.16(a) and (b) show the uncoupled SSI (blue line) and coupled SSSI (red line) response for the top of the building 1 and 3 and Figure 6.16(c) and (d) show the corresponding power spectral density for the total acceleration for these buildings. Comparing the uncoupled and coupled responses, building 3's response appears to be significantly affected by the presence of the adjacent buildings. The change in power, is equal to $\ddot{\chi}_3 = 64\%$ for the acceleration. On the other hand, for building 1, there is a reduction of the seismic response, with a change of power equal to $\ddot{\chi}_1 = -17.6\%$.

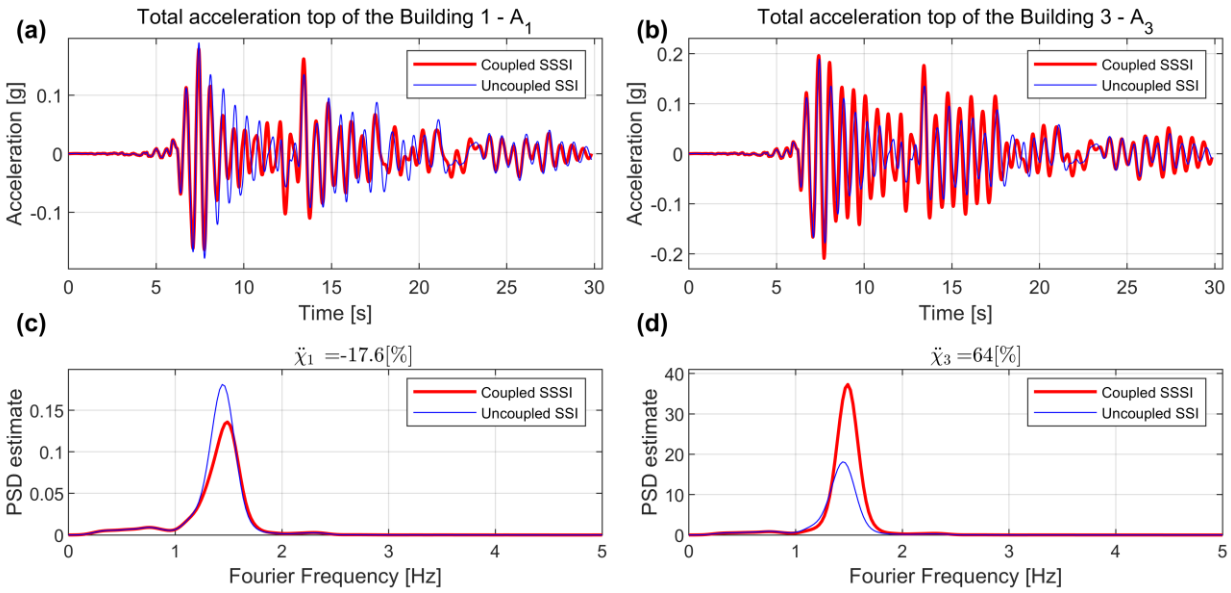

Figure 6.16 L plan of equispaced identical buildings. Total acceleration responses for (a) Building 1 and (b) Building 3, and Power spectral density of acceleration for (c) Building 1 and (d) Building 3 – Responses for the parameter set (T_i = 0.5s, h_i/b = 1.5, ξ_x = 1.2, ξ_y = 1.2)

6.3.3 Case 3: A city block arrangement of identical equispaced buildings

Figure 6.17 shows the variation of change in power for the acceleration at the top of the buildings, for a city block of twelve identical equispaced buildings. All the buildings have a rigid base period equal to $T_i = 0.5s$ and the buildings have a height to width ratio equal to $h_i/b = 1.6$. The centre-to-centre inter-building distance are the same between the adjacent buildings, $\xi_x = 1.2, \xi_y = 1.2$. The maximum increase in total acceleration power response occurred in the central buildings, with a maximum of $\ddot{\chi}_{10} = 65.1\%$ for the acceleration on building 2, 3, 10 and 11. Due to the symmetry of the buildings' arrangement, the change in the seismic response is also symmetric.

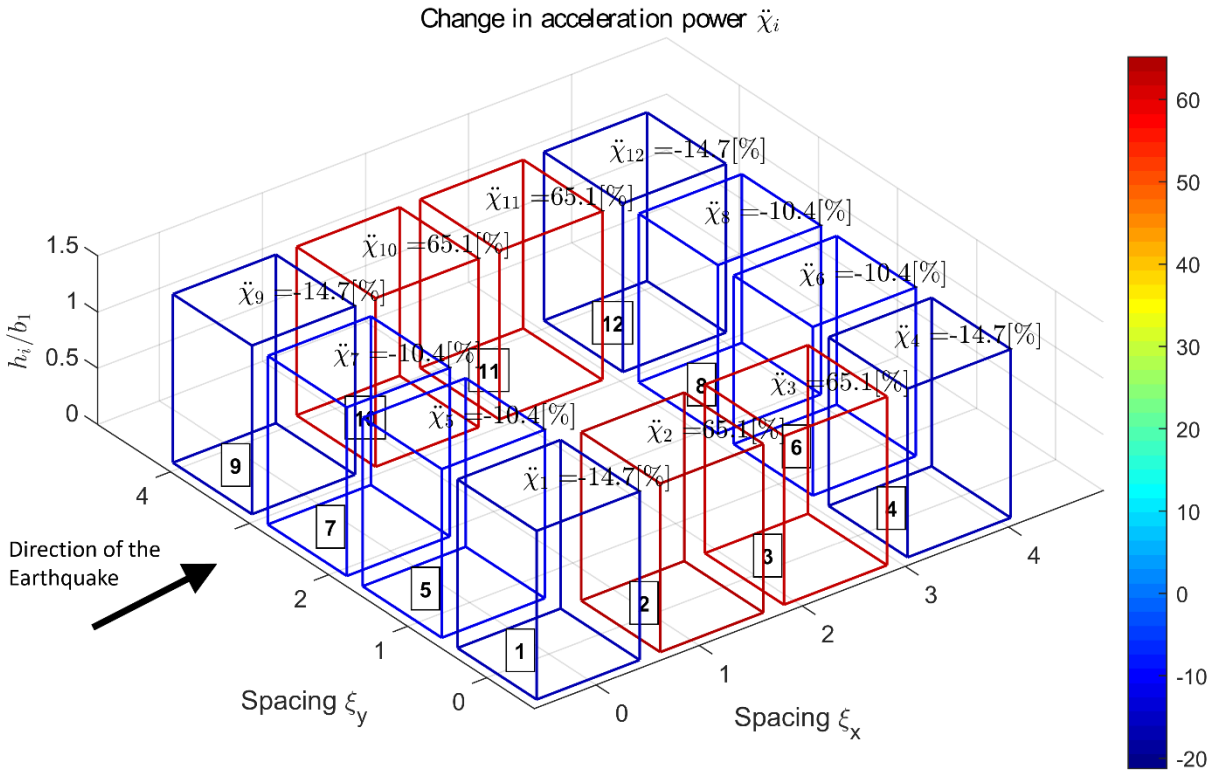

Figure 6.17 Change in acceleration power due to 3D SSSI for a city block of twelve equispaced identical buildings – Parameter set (T_i = 0.5s, h_i/b = 1.5, ξ_x = 1.2, ξ_y = 1.2)

Figure 6.18(a) and (b) show the acceleration response for the top of the building 5 and 10, and Figure 6.18(c) and (d) show the corresponding power spectral density for these buildings. Comparing the uncoupled and coupled responses, building 10's response appears to be significantly affected by the presence of the adjacent buildings. The change in power, is equal to $\ddot{\chi}_{10} = 65\%$ for the acceleration. On the other hand, for building 5, there is a reduction of the seismic response, with a change of power equal to $\ddot{\chi}_5 = -10.4\%$.

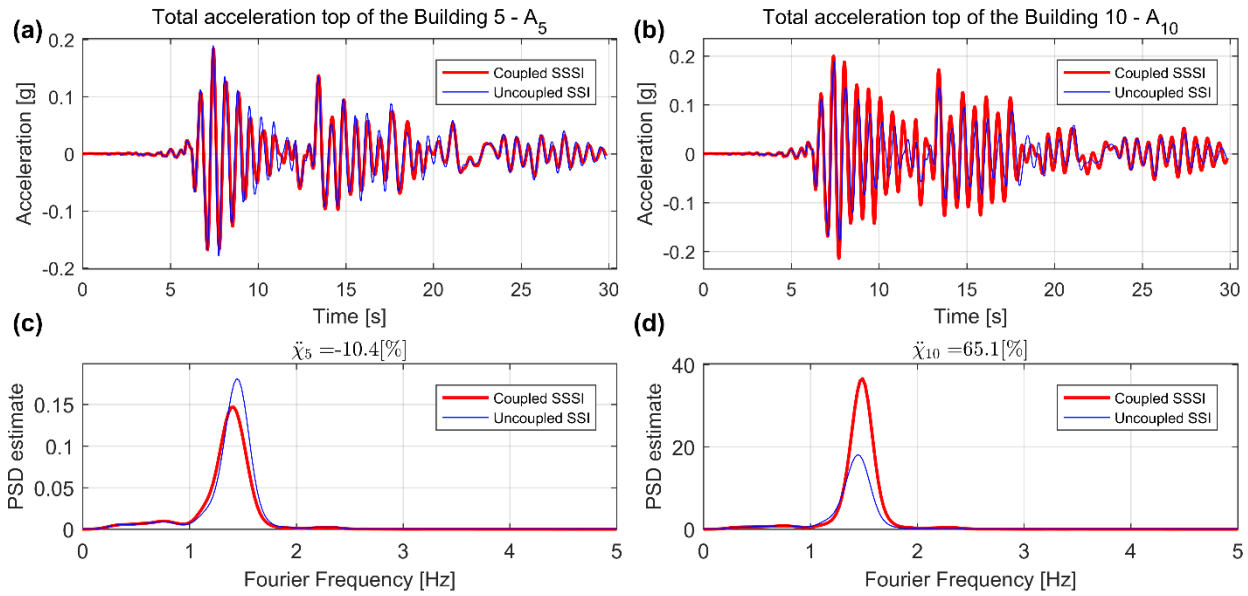

Figure 6.18 City block of twelve equispaced identical buildings. Total acceleration responses for (a) Building 5 and (b) Building 10, and Power spectral density of acceleration for (c) Building 5 and (d) Building 10 – Responses for the parameter set (T_i = 0.5s, h_i/b = 1.5, ξ_x = 1.2, ξ_y = 1.2)

6.4 Summary

In this chapter, a theoretical formulation (a reduced-order model) for the evaluation of Structure-Soil-Structure interaction between several buildings in a three-dimensional arrangement is presented, that are coupled through the soil. The buildings can have different sizes, properties, and inter-building spacing. This conceptual model reduces the number of DOFs from perhaps hundreds of millions in a conventional full 3D FEA to 4*n* (where *n* is the number of buildings). Thus, city-site and city block seismic time history analyses are far more tractable. The key computational stage is to assign values to all the auto-rotational and inter-rotational soil/foundations spring stiffnesses. A novel approach for estimating these stiffnesses is presented that makes use of least-square inverse system identification based on an FEA calibrated empirical relationship between applied surficial moments and rotations.

The research presented in this chapter has led to the following principal findings:

- Two different numerical methods are explored for determining stiffness coefficients using (i) the explicit symmetrical form of the stiffness matrix (using a least squares toolbox) and (ii) based on the theory of Kronecker products and Moore-Penrose pseudo inverse (which is far more computationally efficient but doesn't completely guarantee symmetry). Results indicate that both methods, which are conceptually least-squares approaches, produce very similar results.

- The proposed FEA calibrated empirical fit for the surficial displacement field (loosely based on a Boussinesq form) showed excellent agreement with 3D FEA and experimental results. In

addition, the auto-rotational and inter-rotational soil spring stiffness coefficients showed excellent agreement with previous FEA 2D and experimental data in the literature.

- Results indicate that the hitherto unused (in 2D) cross-coupled inter-rotational soil spring stiffnesses κ_{yxij} may have only second order effects on system responses. However, it is included in the analyses.

- Three numerical cases are presented to explore the performance of the reduced-order model. These cases were anecdotal and designed to explore the versatility of the algorithm rather than an extensive exploration of the phenomenology of 3D SSSI. Case 1 compared the differences between 2D and 3D SSSI for the case of two similar but not identical buildings. Results suggest that the 2D analysis seems to capture the extreme case (the largest detrimental or largest beneficial effect of SSSI). However, it does not tell the whole story. Two buildings that are out-of-plane adjacent behave completely differently to those adjacent in plane. Case 2 and Case 3 explore a set of equispaced identical buildings in a L plan configuration and a square block configuration, respectively. Both cases indicate that large detrimental effects are possible for buildings within a group parallel to the main seismic direction of excitation and suggest that corner buildings do not suffer the most detrimental effects in the case that the soil behaviour is elastic. Note that corner buildings can be vulnerable to permanent tilt if the soil has a non-linear elasto-plastic behaviour.

6.5 Nomenclature

The units correspond to those defined by the International System of Units, where the abbreviations represent [M] mass, [T] time, [L] length and [rad] radians.

ε	Error in the estimation of the stiffness coefficients using the least-square method []
θ_{xi}, θ_{yi}	Rotational degrees of freedom at the base of the buildings *i* about the *x* and *y*-axis respectively []
$\boldsymbol{\Theta}$	Rotational degrees of freedom (vector) at the base of the building []
θ_{y0}	Rotation of the rigid foundation about the *y*-axis []
$\boldsymbol{\kappa}_{ij}$	Inter-rotational stiffness coefficient matrix between the foundations *i* and *j* [ML^2T^{-2}]
$\widehat{\boldsymbol{\kappa}}_{ij}$	Inter-rotational stiffness coefficient matrix between the buildings *i* and *j* [ML^2T^{-2}]
κ_{xij}	Inter-rotational stiffness coefficients in the *x*-direction between the buildings *i* and *j* [ML^2T^{-2}]
κ_{yij}	Inter-rotational stiffness coefficients in the *y*-direction between the buildings *i* and *j* [ML^2T^{-2}]
κ_{xyij}	Inter-rotational cross-coupled stiffness coefficients between the buildings *i* and *j* [ML^2T^{-2}]
μ_{xi}, μ_{yi}	Static moments applied to the foundation *i* about the *x* and *y*-axis respectively []
μ_{y0}	Static moment applied to the foundation about the *y*-axis []
$\boldsymbol{\mu}$	Static moment vector [ML^2T^{-2}]
ν_s	Poison's ratio of the soil []
ζ_j	Ratio of critical damping of the system for the mode *j* []
ξ_x, ξ_y	Non-dimensional center to center distances between buildings in the *x* and *y*-direction respectively []
ρ_b, ρ_s	Average densities of the buildings and the soil respectively [ML^{-3}]
$\rho_z(x, y)$	Boussinesq's surface vertical displacement field [L]
$\boldsymbol{\phi}_n$	Modal eigenvector of the linear system []
χ_i	Change in displacement power when moving from uncoupled to coupled state for the building *i* [%]
$\ddot{\chi}_i$	Change in acceleration power when moving from uncoupled to coupled state for the building *i* [%]
ω	Fourier frequency [rad T^{-1}]
ω_n	Natural frequencies of the linear system [radT^{-1}]
$\Delta(x, y)$	Decay function of the surface displacement field []
A_i	Total acceleration on top of the buildings *i* [LT^{-2}]
b_i	Foundation widths of the buildings *i* [L]
$\mathbf{C}$	Damping matrix of the system [MT^{-1}]
E_s	Elastic modulus of the soil [$ML^{-1}T^{-2}$]
E_{PSD}	Total power spectral density []
G_s	Shear modulus of the soil [$ML^{-1}T^{-2}$]
h_i	Total heights of the buildings *i* [L]

$\mathbf{K}$	Stiffness matrix of the system [MT^{-2}]
$\widehat{\mathbf{K}}_i$	Stiffness matrix of the building *i* [MT^{-2}]
$\widetilde{\mathbf{K}}$	Stiffness matrix estimation of the system using the theory of Kronecker products [MT^{-2}]
k_s	Soil/foundation rotational stiffness in absence of buildings interaction [ML^2T^{-2}]
k_{bi}	Lateral stiffnesses of the building *i* [MT^{-2}]
k_{xi}, k_{yi}	Auto-rotational spring stiffnesses of the soil beneath the building *i* in the *x* and *y*-direction [ML^2T^{-2}]
$\mathbf{M}$	Mass matrix of the system [M]
$\widehat{\mathbf{M}}_i$	Mass matrix of the building *i* [M]
M_w	Moment magnitude scale of the earthquake
m_{bi}	Total modal mass of the buildings *i* [M]
m_{si}	Soil/foundation mass of the buildings *i* [M]
n	Number of buildings belonging to a city block []
P	Vertical point load applied at the origin of the half-space soil [MLT^{-2}]
$\mathbf{p}$	Force vector of the system [MLT^{-2}]
$\widehat{\mathbf{p}}_i$	Force vector of the building *i* [MLT^{-2}]
p_1, p_2, p_3	Least-square fitting coefficients for the 3D FEA analysis []
q	Number of load cases defined to the foundation-soil-foundation system []
r_i	Soil/foundation mass radius of gyration of the buildings *i* [L]
T_E	System kinematic energy [ML^2T^{-2}]
T_{xi}, T_{yi}	Fundamental natural period of the structure *i* on a rigid foundation in *x* and *y*-direction [T]
t	Time [T]
$u_z(\xi_x, \xi_y)$	Non-dimensional surface vertical displacement field [L]
U_i	Total displacements on top of the buildings *i* []
U_E	System potential energy [ML^2T^{-2}]
$U_z(x, y)$	Surface vertical displacement field [L]
V_s	Shear wave velocity of the soil [LT^{-1}]
x_i	Horizontal displacement (degrees of freedom) of the building *i* in the *x*-direction [L]
x_g	Horizontal ground displacement time series [L]
$\ddot{x}_g$	Horizontal acceleration ground motion [LT^{-2}]
$\mathbf{x}$	Degrees of freedom (vector) of the system [L]
$\hat{\mathbf{x}}_i$	Degrees of freedom (vector) of the buildings *i* [L]
x, y	Arbitrary coordinate in the *x*-direction and *y*-direction respectively [L]
y_i	Horizontal displacement (degrees of freedom) of the building *i* in the *y*-direction [L]

Chapter 7

A parametric study on the effect of rotational ground motions on building structural response

---

The contents of this chapter have been adapted from that published in:

Vicencio, F., and Alexander, N.A. (2019a). A parametric study on the effect of rotational ground motions on building structural responses. *Soil Dynamics and Earthquake Engineering*, 118, 191-206.

This chapter has no direct relationship with the SSSI effects. Still, it should be viewed as an initial exploration of the effect of rotational ground motion in the structures, and its future extension to the SSSI problem.

7.1 Introduction to rotational ground motions and building response

The rotational components of earthquake ground motions have been discussed in the literature for more than 40 years. Nevertheless, in most cases, seismic analysis and design of buildings do not include the effect of rotational ground motion. In fact, seismic structural responses are evaluated using only three translational components as system inputs. They neglect the three rotational pitch, roll, yaw components of the ground motion. This is mainly due to the limited recorded data on the rotational components. The seismic loading due to rotational components is not considered by most seismic design codes, with the exception of Eurocode 8 part 6: Towers, masts and chimneys (Eurocode 8 EN-1998, 2005), due in part to the difficulty of recording the rotational accelerations with strong motion accelerometers. In the last few years, it has been possible to measure rotational ground motion by modern technologies such as fibre optical gyros, solid-state devices, or ring laser sensors. These technologies are described in the works of Nigbor (1994), Takeo (1998), Liu et al. (2009), and Yin et al. (2016). However, these new technologies are not currently available in large-scale seismic networks as they are not included in standard strong-motion accelerometers.

There is evidence that rotational components are responsible for different kinds of structural damage during seismic excitations. Earthquake rotational effects have been observed in various types of structures for centuries, according to Kozak (2009) and Sargeant and Musson (2009). These effects were detected on simple vertical structures such as chimneys, obelisks and gravestones. Cucci and Tertulliani (2011) and Cucci and Tertulliani (2013) described the earthquake-induced rotational effects in structures during recent earthquakes in the near-fault region. However, due to the lack of direct data recorded from these structures, it is difficult to isolate the influence of the translational ground motion input with that of the rotational ground motion.

A number of researchers have investigated the effect of the rotational ground motions on structural responses using mathematical/computational models. As reported by Rutenberg and Heidebrecht (1985), Gupta and Trifunac (1988), Gupta and Trifunac (1990), Gupta and Trifunac (1991), and Zembaty and Boffi (1994), the rocking component of the ground shaking may be critical for the safety of multi-storey buildings and slender towers. Kalkan and Graizer (2007) studied the effects of the tilt component in ground motions on a single degree of freedom oscillator, considering the secondary P-Δ effects. Trifunac (2009) explored the role of near earthquake faults in the rotational responses. Jalali and Trifunac (2011) evaluated the effects of wave-passage (excited by SH wave earthquake pulses) in out-of-plane response of long structures, and Jalali et al. (2013) studied the linear and nonlinear responses of a two-story building model excited by near-source fault-normal pulse and fault-parallel displacement. Falamarz-Sheikhabadi (2014) reported that the contribution of rocking excitation is sensitive to structural irregularity, structural height, and seismic excitation.

Different methods of extracting the rotational components using a single station have been developed in the last years. The pioneering work of Penzien and Watabe (1975) showed that most of the earthquake energy travels to the station through a principal plane and then it is possible to decompose the three recorded acceleration time series into body and surface waves. Several researchers extended the work of Penzien and Watabe (1975) to estimate the rotational ground motion using a single station, including Trifunac (1982), Lee and Trifunac (1987), Castellani and Boffi (1996), Li et al. (2004), Zembaty (2009), and Basu et al. (2012). These methods are based on a series of assumptions, such as: (i) plane wave propagation, (ii) horizontal homogeneity of the soil, (iii) the existence of a principal plane passing through the hypocentre, (iv) a frequency-dependent angle of incidence, (v) the effect of wave dispersion, and (vi) the seismic ground motions can be decomposed into body and surface waves.

A different approach to the single station method involves the use of data from several stations, i.e. data from closely spaced or dense arrays. There are a variety of methods that use acceleration time series recorded by multiple stations. Niazi (1986) estimates the rotational ground motions in a long rigid foundation from the data recorded in a linear array, the El Centro Differential Array in Southern California. One common practice of estimating the rotational ground motion, obtained from a dense array, is to make use of a finite-difference scheme. Oliveira and Bolt (1989) used the strong motion array in Taiwan, SMART-1, to estimate the rotational ground motion, and Castellani (2017) proposes a procedure to calculate the rotational ground motion around any axis using the SMART-1 array. Huang (2003) analysed the 1999 Chi-Chi Taiwan strong motion, recorded in a dense array near to the fault and derived the rotational ground motion. In the same way, Chayamghamian and Nouri (2007) examined the properties of the rotational ground motion using the Chiba dense array data. Paolucci and Smerzini (2008) and Smerzini et al. (2009) derived the earthquake-induced rotations of Parkway Valley, New Zealand and the UPSAR, California array through the spatial interpolation of the records and a numerical finite-difference method.

On the other hand, Spudich et al. (1995) proposed the Geodetic Method, which is an extension of the work of Niazi (1986) and was expressed in terms of a displacement-gradient matrix, that was assumed to be constant and small over the footprint of the array. Basu et al. (2013) proposed the Acceleration Gradient Method capable of capturing higher frequency content in the rotational ground motions and does not require any site-specific data. The Surface Distribution Method by Basu et al. (2015) is capable of capturing high frequencies but requires site information for the calculation and several assumptions that are rarely satisfied by the data recorded in a seismic array. Lee and Trifunac (2009) proposed a simple approximate algorithm for generating torsional and rocking Fourier spectral amplitudes from the corresponding translational motions and Jalali and Trifunac (2009) illustrated that the pseudo-relative spectral velocity of an equivalent oscillator can be extended to describe the spectral velocity excited by horizontal, vertical and rocking components of ground motion.

In this chapter, the multi-station interpolation procedures are used to calculate the rotational ground motion (pitch and roll components) through a high order finite difference scheme that uses a biharmonic spline spatial interpolation of real vertical acceleration records. This approach makes no additional assumptions about wave mechanics and the spatial variation in site soil characteristics, i.e. no assumption about site homogeneity are made. To this end, data from the SMART-1 (1991) dense accelerometer array in Taiwan, in which the separation distances among accelerometers vary from 105m to 1050m, are employed. The array consisted of 37 force-balance triaxial stations configured in three concentric circles of radii 200m, 1000m and 2000m, and a central station. The effect of torsional ground motion (yaw component) in the structure is neglected in the present work because i) the rocking ground motion tends to be less relevant in comparison with the rotational ground motion (Hao (1996) and Yin et al. (2016)), ii) the torsional springs for the foundations is stiffer compared with the rocking springs, and iii) the effects of rocking ground motion on buildings is important for base-isolated buildings (Falamarz-Sheikhabadi (2014) and Basu et al. (2015)).

7.1.1 Aim

To examine the possible effects of the rotational ground motion on the time-history response of buildings, a simple parametric model is proposed. This reduced-order model has some advantages over Finite Element Analysis. It captures the most significant soil/structure behaviour while including a relatively small number of system parameters. Thus, it is computationally simple enough for exploring a huge number of generic cases. To find the contribution from the rotational components in the response of a structure, a complete set of equations of motion is developed including the combined effects of translation and rotational ground motions. The code used in this study was developed in MATLAB (2016). There are of the order of 1.6 million different full time-history analyses in this chapter, with a set of more than five thousand different horizontal-rotational ground motion time-histories employed. The large scope of these analyses made use of the High-Performance Computing (HPC) machine, BlueCrystal, belonging to the Advance computing research centre at the University of Bristol.

The objective of this chapter is to answer the following questions.

(i) Is there evidence that rotational ground motion can produce a significant increase in the response of building structures?

(ii) Is the influence of the rotational ground motion frequency dependent?

(iii) Does the peak vertical ground motion to peak horizontal ground motion ratio correlate with cases where the rotational ground motion is significant?

7.2 Reduced-order model for Soil-Structure-Interaction (SSI) including rotational ground excitation

7.2.1 Non-dimensional equations of motion

The model shown in Figure 7.1, was described in terms of four degrees of freedom (DOFs). The building has one rotational DOF at the foundation level θ_s, one translational DOF for the foundation mass x_s, and two translational DOFs for the building masses (x_1 and x_2) relative to the ground. A known ground displacement x_g and ground rotational θ_g fields are applied. The impact of the vertical ground motion and P-Δ effects in the structures' response is neglected in the present work, i.e. only small lateral displacements are considered. The kinetic energy T_E and potential energy U_E for this system are given by equations (7-1) and (7-2), respectively. The first term of the kinetic energy in equation (7-1) describes the inertial forces on building masses due to flexure, soil spring motion and support translation/rotation respectively. The second term in (7-1) describes the translation and rotational kinetic energies of the soil/foundation mass. The potential energy (equation (7-2)) is the sum of internal work due to building deformation, rotation of the foundation spring underneath the building and deformation of the foundation translational spring. Thus,

$$T_E = \tfrac{1}{2}\sum_{j=1}^{2}\left(\tfrac{1}{2}m_b\left(\dot{x}_j + \dot{x}_s + \dot{x}_g - \tfrac{j}{2}h(\dot{\theta}_g+\dot{\theta}_s)\right)^2\right) + \tfrac{1}{2}\left\{m_s\left(\left(\dot{x}_g + \dot{x}_s\right)^2 + r^2\left(\dot{\theta}_g + \dot{\theta}_s\right)^2\right)\right\} \qquad \textbf{(7-1)}$$

$$U_E = \tfrac{1}{2}(k_b x_1^2 + k_b(x_2 - x_1)^2 + k_s x_s^2 + k_\theta \theta_s^2) \qquad \textbf{(7-2)}$$

where h is the total height of the building, m_b is the total building mass, m_s is the soil/foundation mass underneath the building, r is the soil/foundation mass-radius of gyration, and $m_s r^2$ is the soil/foundation mass moments of inertia. k_b is the building lateral horizontal stiffness (constant throughout the height), k_s is the lateral horizontal stiffness of the soil/foundation, k_θ is the rotational stiffness of the soil/foundation, and b is the foundation' width. Note here that it does not employ a complex (real and imaginary) frequency dependent rotational stiffness k_θ in this research. Nevertheless, this static stiffness formulation is reasonable (see Luco and Westmann (1972) and Gazetas (1983)) if the non-dimensional parameter $a_0 = \pi f b/V_s < 1.0$, where b is the foundation width, V_s is the shear wave velocity of the soil, and f is the excitation frequency. For the SMART-1 array location data, this criterion for most cases is met when the aspect ratio is $h/b > 1$. In addition, it is worth noting that the inclusion of an appropriate soil/foundation mass and damping does generate a dynamic stiffness (in the frequency domain) that is frequency dependent and conceptually equivalent with the complex frequency dependent stiffness of Luco and Westmann (1972).

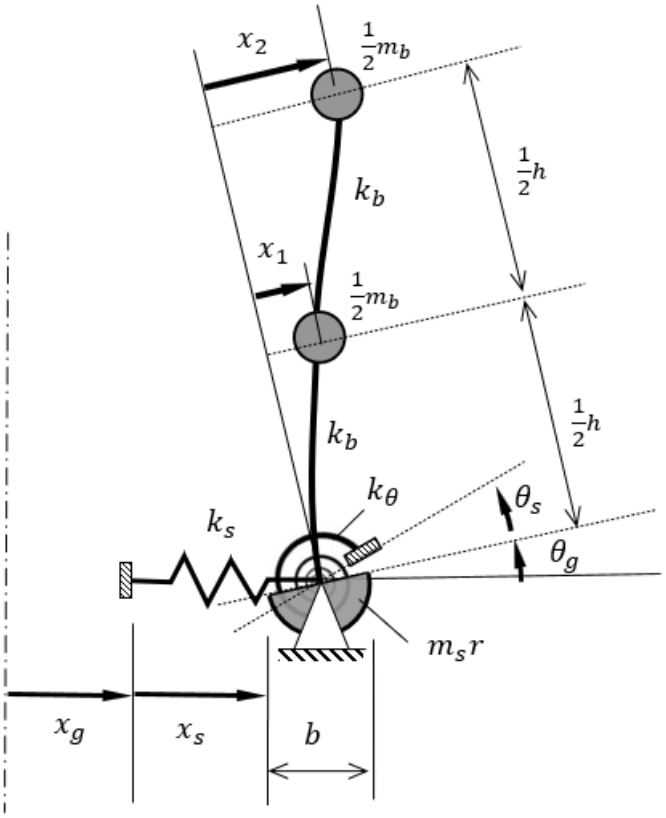

Figure 7.1 Structural model of a building subjected to horizontal and rotational ground motion

The Euler-Lagrange equations of motion describing the dynamics of the discretized system can be derived in the standard way by variational calculus, and is formulated in the matrix equations of motion (7-3).

$$\widehat{\mathbf{M}}\ddot{\mathbf{x}} + \hat{\mathbf{C}}\dot{\mathbf{x}} + \widehat{\mathbf{K}}\mathbf{x} = \hat{\boldsymbol{p}}_1\ddot{x}_g + \hat{\boldsymbol{p}}_2\ddot{\theta}_g \tag{7-3}$$

where system matrices are defined as follows,

$$\widehat{\mathbf{M}} = \begin{bmatrix} \frac{1}{2}m_b & 0 & \frac{1}{2}m_b & -\frac{1}{4}m_b h \\ 0 & \frac{1}{2}m_b & \frac{1}{2}m_b & -\frac{1}{2}m_b h \\ \frac{1}{2}m_b & \frac{1}{2}m_b & m_b + m_s & -\frac{3}{4}m_b h \\ -\frac{1}{4}m_b h & -\frac{1}{2}m_b h & -\frac{3}{4}m_b h & \frac{5}{8}m_b h^2 + m_s r^2 \end{bmatrix}, \widehat{\mathbf{K}} = \begin{bmatrix} 2k_b & -k_b & 0 & 0 \\ -k_b & k_b & 0 & 0 \\ 0 & 0 & k_s & 0 \\ 0 & 0 & 0 & k_\theta \end{bmatrix} \tag{7-4}$$

$$\hat{\mathbf{p}}_1 = \begin{bmatrix} -\frac{1}{2}m_b \\ -\frac{1}{2}m_b \\ -m_b - m_s \\ \frac{3}{4}m_b h \end{bmatrix}, \hat{\mathbf{p}}_2 = \begin{bmatrix} \frac{1}{4}m_b h \\ \frac{1}{2}m_b h \\ \frac{3}{4}m_b h \\ -\frac{5}{8}m_b h^2 - m_s r^2 \end{bmatrix}, \mathbf{x} = \begin{bmatrix} x_1 \\ x_2 \\ x_s \\ \theta_s \end{bmatrix} \tag{7-5}$$

The dimensional form of system (7-3) contains too many system parameters. Hence, a parameter reduction through a process of removing all dimensional terms is performed. Thereby, the following frequency parameters are introduced,

$$\omega_b^2 = \frac{k_b}{m_b}, \quad \omega_s^2 = \frac{k_s}{m_s}, \quad \omega_\theta^2 = \frac{k_\theta}{m_s r^2} \tag{7-6}$$

and the following non-dimensional parameter groups,

$$\eta = \frac{h}{r}, \quad \alpha = \frac{m_s}{m_b}, \quad \Omega_s = \frac{\omega_s}{\omega_b}, \quad \Omega_\theta = \frac{\omega_\theta}{\omega_b} \tag{7-7}$$

The frequency parameter ω_{b} of the building can be estimated using the natural frequency of a rigid base system ω_{rb} (i.e. with no soil/foundation rotation, equivalent to $\theta_s = 0$). The first modal circular frequency ω_{rb} of this rigid system (as shown in Section 3.2.1, equation (3-10)) can be obtained by the solution of its resulting eigenvalue problem, as follows,

$$\omega_{rb} = 0.874\sqrt{\frac{k_b}{m_b}} = 0.874\omega_b \tag{7-8}$$

In this chapter, the first building frequency ω_{rb} is approximated by the empirical relationship suggested in the SEAOC Bluebook (1976) for the natural period of a structure on rigid foundation $T_x = n_s/10$. The fundamental natural period of a structure is T_x (in [s]) and n_s is the number of storeys based on a fixed 3.2m average storeys height (for $n_s \leq 12$). So, the total height of the building (in [m]) is equal to $h = 3.2n_s$ and the period is $T_x = h/32$. The period has a relationship with the circular frequency thus $\omega_{rb} = 2\pi/T_x$. Therefore, the fundamental natural frequencies, on a rigid base, results in $\omega_{\mathrm{rb}} \approx 200/h$. Thus, the frequency parameter described in the equation (7-6) is re-expressed for the building in terms of the building height, as follows,

$$\omega_b \approx \frac{228.83}{h} \tag{7-9}$$

Newmark and Rosenblueth (1971) proposed that the dynamic mass of the soil beneath buildings is approximately equal to $m_s = 0.35b^3\rho_s$. The mass of the buildings can be calculated as $m_b = \rho_b h b^2$, where ρ_s and ρ_b are the densities of soil and building respectively. Based on typical spans and floor loading, the average building density is $\rho_b = 400 - 800[kg/m^3]$, while typical soil density ranges within $\rho_s = 1200 - 2100[kg/m^3]$. Hence, the density ratio c_1 (defined in equation (7-10)) lies between 0.7 and 1.8 approximately. The soil/building density ratio stated in Table 7-1 refers to an average building of

density $\rho_b = 600[kg/m^3]$. The radius of gyration of the soil semi-cylinder, based on Newmark's empirical results, is $r \approx 0.33b$. Parameters α and η are contracted into the Aspect ratio *s*.

$$s = \frac{h}{b}, \quad \alpha = \frac{m_s}{m_b} = 0.35\frac{\rho_s}{\rho_b}\frac{b}{h} = \frac{c_1}{s}, \quad c_1 = 0.35\frac{\rho_s}{\rho_b}, \quad \eta = \frac{h}{r} = 3s \tag{7-10}$$

The soil/foundation rotational stiffness k_θ and the soil/foundation translational stiffness k_s are obtained by using the empirical formulae (deduced by Pais and Kausel (1988) and shown in equation (7-11)) for the stiffness spring coefficients of the soil beneath the building. In addition, the rotational stiffness was validated using Finite Element Models (Alexander et al., 2013; Aldaikh et al., 2018) and physical experimental models (Aldaikh et al., 2015; Aldaikh et al., 2016). G_s is the elastic shear modulus of the soil, V_s is the shear wave velocity of the soil in [m/s], and μ_s is the Poisson's ratio of the soil. In this analysis, three types of soil class are employed (properties of the soil described in Table 7-1).

$$k_\theta = \frac{1}{2}\frac{G_s b^3}{1-\mu_s}, \quad k_s = 4.6\frac{G_s b}{2-\mu_s}, \quad V_s^2 = \frac{G_s}{\rho_s} \tag{7-11}$$

Table 7-1 Linear elastic stiffness parameters for soil classes

Soil Class	$\boldsymbol{\rho_s[kg/m^3]}$	$\boldsymbol{\mu_s}$ []	$\boldsymbol{V_s}$ $[\boldsymbol{m/s}]$	$\boldsymbol{c_1}$ []
Very Dense	2100	0.35	380	1.23
Dense	2000	0.35	325	1.16
Medium	1600	0.30	250	0.93

Finally, the change of variable from equation (7-12) is introduced, where u_1 and u_2 are the non-dimensional relative displacements of the building DOFs to the ground, u_s is the non-dimensional horizontal displacement of the foundation, and u_g is the non-dimensional horizontal ground displacement (absolute).

$$x_1 = u_1 r, \quad x_2 = u_2 r, \quad x_s = u_s r, \quad x_g = u_g r \tag{7-12}$$

Therefore, after some calculus, the Euler-Lagrange equations of motion can be re-stated thus,

$$\mathbf{M\ddot{u} + C\dot{u} + Ku} = \mathbf{p_1}\ddot{x}_g + \mathbf{p_2}\ddot{\theta}_g \tag{7-13}$$

The matrices and vectors for the above equation (7-13) are stated as follows,

$$\mathbf{M}=\begin{bmatrix} \frac{1}{2} & 0 & \frac{1}{2} & -\frac{3}{4}s \\ 0 & \frac{1}{2} & \frac{1}{2} & -\frac{3}{2}s \\ \frac{1}{2} & \frac{1}{2} & 1+\frac{c_1}{s} & -\frac{9}{4}s \\ -\frac{3}{4}s & -\frac{3}{2}s & -\frac{9}{4}s & \frac{45}{8}s^2+\frac{c_1}{s} \end{bmatrix},\quad \mathbf{K}=\omega_b^2\begin{bmatrix} 2 & -1 & 0 & 0 \\ -1 & 1 & 0 & 0 \\ 0 & 0 & \frac{c_1}{s}\Omega_s^2 & 0 \\ 0 & 0 & 0 & \frac{c_1}{s}\Omega_\theta^2 \end{bmatrix} \tag{7-14}$$

$$\mathbf{p}_1=\begin{bmatrix} -\frac{1}{2} \\ -\frac{1}{2} \\ -1-\frac{c_1}{s} \\ \frac{9}{4}s \end{bmatrix},\quad \mathbf{p}_2=\begin{bmatrix} \frac{3}{4}s \\ \frac{3}{2}s \\ \frac{9}{4}s \\ -\frac{45}{8}s^2-\frac{c_1}{s} \end{bmatrix},\quad \mathbf{u}=\begin{bmatrix} u_1 \\ u_2 \\ u_s \\ \theta_s \end{bmatrix} \tag{7-15}$$

The system's linear viscous damping matrix $\mathbf{C}$ defined in equation (7-13) assumes that each natural mode $n \in [1,4]$ is damped at $\xi_n = 0.05$ of critical damping, $\boldsymbol{\phi}_n$ is the modal eigenvector of the mode n, and ω_n are the natural frequencies of the systems. These ω_n were calculated considering the completely elastic system. Thus, the Caughey orthogonal damping matrix $\mathbf{C}$ can be calculated as Chopra (2000) by equation (7-16).

$$\mathbf{C}=\mathbf{M}\left(\sum_{n=1}^{4}\frac{2\xi_n\omega_n}{\boldsymbol{\phi}_n^T\mathbf{M}\boldsymbol{\phi}_n}\boldsymbol{\phi}_n\boldsymbol{\phi}_n^T\right)\mathbf{M} \tag{7-16}$$

7.3 Determination of system inputs, rotational-translational ground motion time series

7.3.1 The SMART-1 accelerograph array database

Strong motion data recorded at the SMART-1 dense accelerometer array in Taiwan have been used to calculate the rotational ground motion by employing a biharmonic spline interpolation and a high-order finite difference scheme. The SMART-1 array was one of the largest digital strong-motion seismographs in the world, specially designed to record near-field ground motion. It was located at the northeast corner of Taiwan, near to the city of Lotung on the Lanyang Plain (Abrahamson et al., 1987). The array consisted of 41 stations (force-balanced triaxial accelerometers), where the main stations were located in three concentric circles of twelve equally spaced stations, with a central station (C). The inner ring (I) was positioned with a radius of 200 meters, the middle ring (M) had a radius of 1000 meters and the outer ring (O) had a radius of 2000 meters. The distances between station pairs vary from 105m to 1050m (see Figure 7.2). The final two stations (E-01 and E-02) were added several kilometres to the south of the ring in June

1983 and two more stations (E-03 and E-04) were added to the north of the ring in June 1987. These four stations had no geometric relation to the other stations, so have not been used in this study.

In 1991, The SMART-1 array was replaced by the SMART-2 array which is located further to the south (SMART-1, 1991). The array SMART-1 was located in a large valley, fifteen kilometres wide and eight kilometres long approximately. The topography of the surface was very flat. The near-surface geology under the array is predominantly recently laid alluvial deposits. The soils beneath the array consist of 3 to 18 meters of grey sandy silt and silty sand with some gravel over recent alluvium, down to 50m. The P-wave velocities are between 430 to 760 m/s in the soils (Abrahamson et al., 1987). The water table was at or near the surface.

During its operational life, the SMART-1 array detected a total of 60 events, that included 4296 individual strong-motion accelerograms (Abrahamson et al., 1987). These range in local magnitude from M_L= 3.6 to M_L= 7.0. However, SMART-1 was designed to record earthquakes much larger than this. The dynamic range of the triaxial forced-balanced instrument, SA-3000, was ±1*g* suggesting events of local magnitude of greater than M_L= 8.0 were permissible without clipping. However, no earthquakes occurred near this upper amplitude limit. The largest earthquake used a third of the available amplitude range. Thus, for events with low PGA noticeable quantisation errors were impressed on the data. Consequently, a set of the three larger events detected by the array is considered. The three earthquakes studied are listed in Table 7-2 with numerical designation #39, #43 and #45. They are among the largest events recorded by the array and cover a range of magnitudes, depth, and epicentral distances.

The largest earthquake recorded at SMART-1 was event #45, which occurred on 14 November 1986 (Abrahamson et al., 1987). Event #39 had a local magnitude of 6.5 and produced a peak acceleration of 314 [cm/s^2] in the vertical axis. However, event #43 on 30 July 1986 was the only earthquake that triggered all 39 stations in the array. The epicentre of event #43 was nearly directly beneath the array: it was 6 kilometres distance away and 2 kilometres below the surface. The stations I-10, O-06 and O-11 in the event #39 and the stations I-10, M-08 and O-05 in the event #45 failed to record any meaningful data. Hence, the component of these stations was estimated by interpolating across the entire array.

Table 7-2 Characteristics of the earthquake events used from the SMART-1 array

Event	Date	Magnitude M_L	Depth [km]	Distance [km]	Azimuth (N-E)	PGA Horiz. [cm/s^2]	Station	PGA Vert. [cm/s^2]	Station
#39	16/01/1986	6.5	10.2	22	64°	375	M-04	314	I-12
#43	30/07/1986	6.2	1.5	6	150°	283	O-04	224	O-08
#45	14/11/1986	7.0	15.0	79	175°	238	O-01	104	O-07

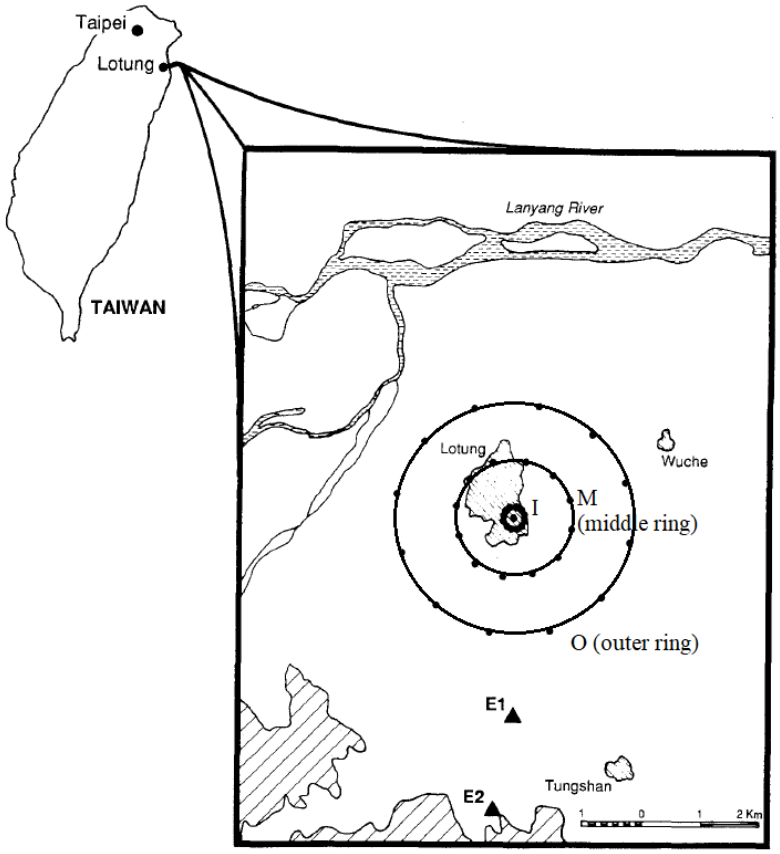

Figure 7.2 Geographic location of SMART-1 array in northeast Taiwan, after (Abrahamson et al., 1987)

7.3.2 Data processing and calculation of rotational ground accelerations

Each station accelerometer in the SMART-1 array recorded three time series for each earthquake, two in the horizontal direction (East-West $\ddot{x}_g(t)$ and North-South $\ddot{y}_g(t)$ components) and one in the vertical direction $\ddot{z}_g(t)$. The records were processed using the methodology described in Alexander (2008), to remove glitches, replace data dropouts and remove the DC baseline. A low pass five-pole, zero-phase, Butterworth filter (*filtfilt* MATLAB function), with a cut-off frequency of 25 Hz was used. In addition, noise has been removed from each of the accelerograms using a wavelet denoising algorithm using *db8* wavelet decomposition down to five levels (Channerly and Alexander, 2007), a standard single degree of freedom instrument deconvolution and a bandpass fourth-order Butterworth filter with a pass-band of 0.25-25 Hz. Figure 7.3 displays all the corrected horizontal (East-West and North-South components) and vertical spectrum accelerations and their respective means, from stations C-00 to O-12 for events #39, #43 and #45.

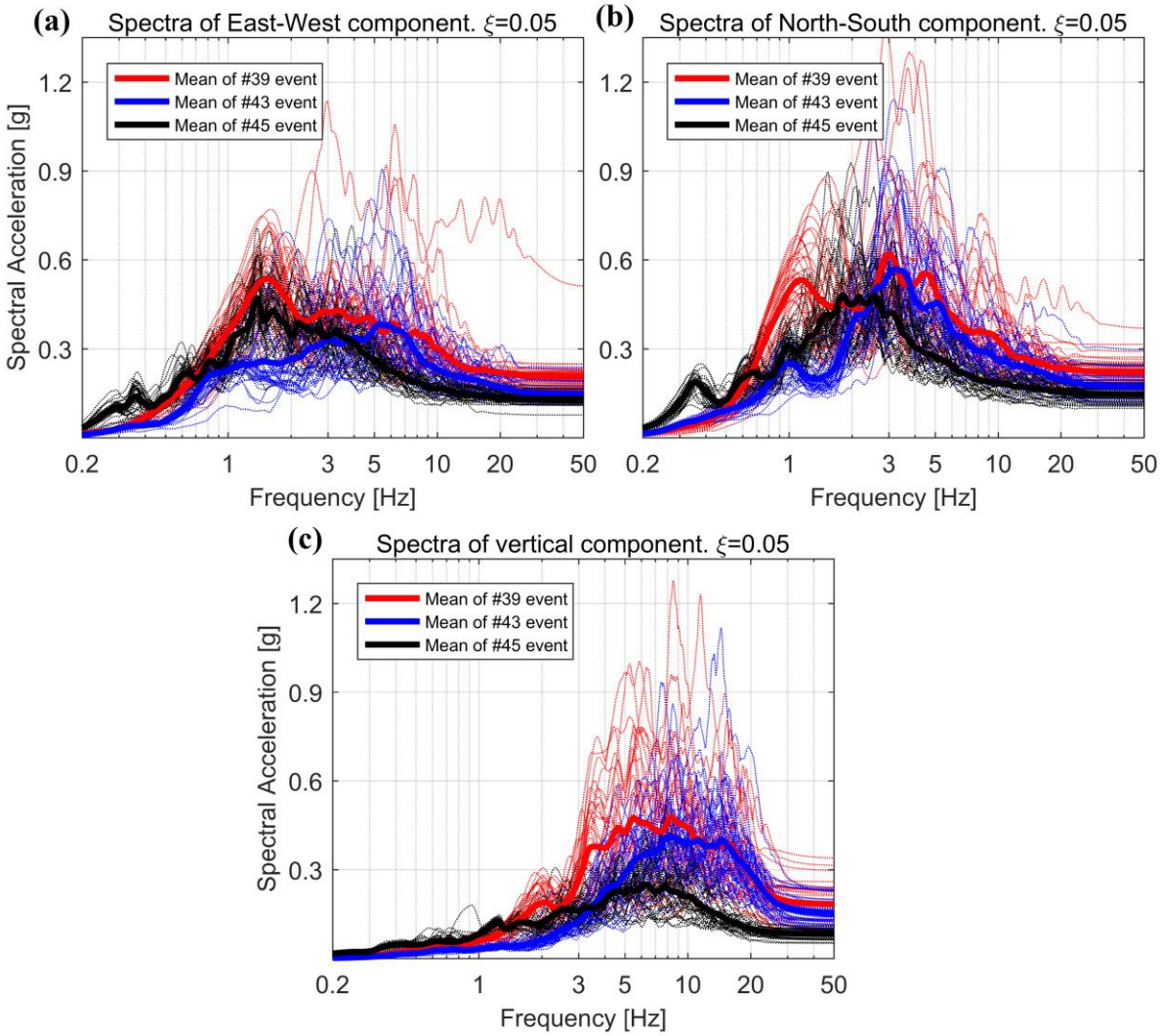

Figure 7.3 Elastic response spectra from stations C-00 to I-12 for (a) East-West, (b) North-South and (c) Vertical components.

To obtain a qualitative understanding of the ground motion, a biharmonic cubic spline interpolation algorithm (Sandwell, 1987) has been employed to find the complete spatial variation of vertical and horizontal acceleration at any point across the array.

This method is implemented in a MATLAB code (*griddata* function, MATLAB (2016)) and produces a smooth surface which does not have any discontinuities. In addition, it does not produce any unexpected maxima and it is twice continuously differentiable C^2. The disadvantages of using biharmonic spline interpolation are: (i) in the corners of the grid the data is extrapolated rather than interpolated and (ii) areas of most movement occur directly around the data points (i.e. the positions of the different stations), so between the stations of the middle and the outer rings the activity is low. As it is noted in Figure 7.2, the inner ring stations are much more closely spaced than the middle and outer rings. Therefore, this work focuses on the inner ring responses only. Essentially, the interpolation is most accurate for the inner ring, and the data from the outer rings are used to ensure that the boundary effects at the edges of the inner ring data are kept to a minimum.

Figure 7.4 shows an example of the spatial variation of the vertical ground acceleration $\ddot{z}_g(t)$ across the inner array for the event #43 at one instant in time (t = 5.98s). As indicated, the surface displayed is based on a biharmonic cubic spline interpolation algorithm. There are important differential variations in vertical acceleration from the centre to the edge of the inner ring. For example, considering stations C-00 and I-12, there is a difference of 1.3 [m/s^2]. This suggests that there exists a significant spatial variation in rotational ground acceleration across the array due to vertical surface distortions.

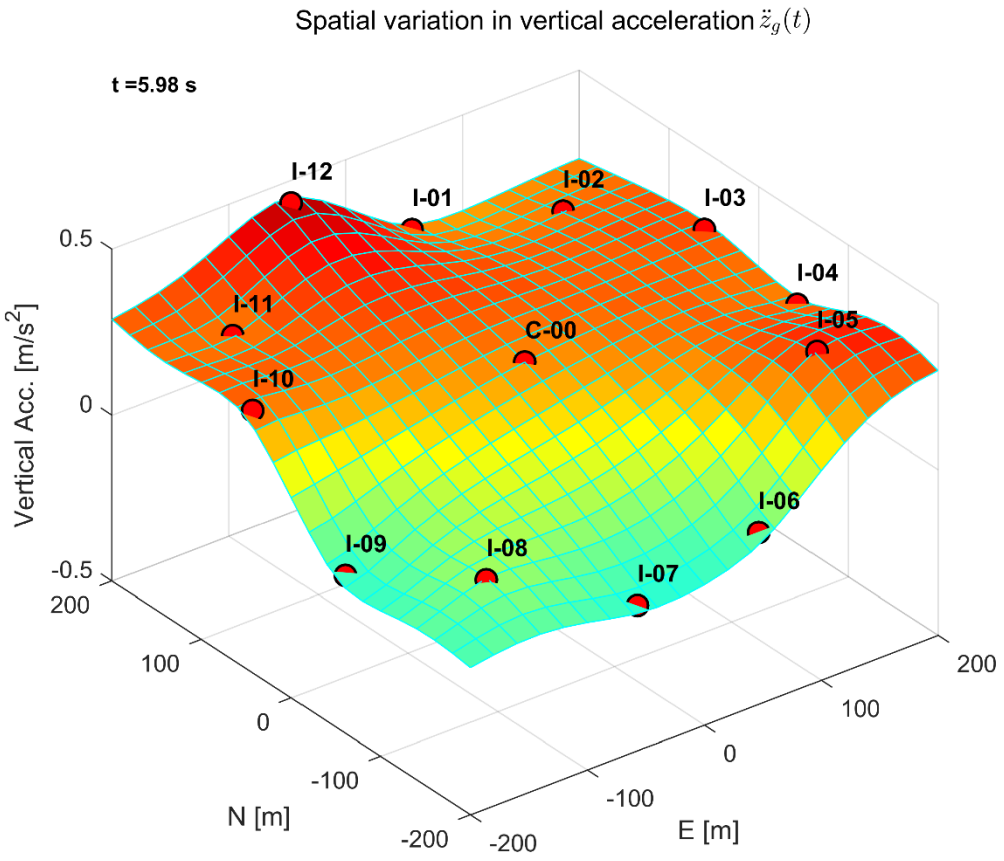

Figure 7.4 Example of spatial variation in vertical ground acceleration for event #43 at t=5.98[s]

To solve the equations of motion (7-13), a known rotational ground motion is needed. This rotation was not recorded by the strong motion seismometer of SMART-1. So, an indirect method to extract the rotational component using multiple stations is employed.

The accuracy of such a spatial interpolation scheme, when employed to determine rotational accelerations is discussed in the next section.

7.3.2.1 Frequency dependent error in vertical and rotational acceleration estimate when using spatial interpolation

A travelling wave field can be defined as,

$$z(t,x) = \sum_i z_i(t,x), \quad z_i(t,x) = a_i \sin\left(\omega_i t + \frac{\omega_i}{V}x + \phi_i\right) \tag{7-17}$$

where $z(t,x)$ is the normal (vertical) acceleration which is a function of time t and a spatial coordinate x. This $z(t,x)$ is composed of a Fourier series of components $z_i(t,x)$ of amplitude a_i, frequency ω_i, phase angle ϕ_i and group velocity V. Consider a single component z_i. Its contribution to the spatial slope $\theta_i(t,x)$ of $z_i(t,x)$ are obtained by differentiation, thus,

$$\theta_i(t,x) = \frac{\partial z_i(t,x)}{\partial x} = \frac{a_i\omega_i}{V}\cos\left(\omega_i t + \frac{\omega_i}{V}x + \phi_i\right) \tag{7-18}$$

The amplitude of the acceleration A_{zi} and the slope $A_{\theta i}$ at any spatial coordinate x is hence,

$$A_{zi} = \|z_i(t,x)\|_2 = a_i, \quad A_{\theta i} = \|\theta_i(t,x)\|_2 = \frac{a_i\omega_i}{V} \tag{7-19}$$

Now, let assume that spatially discrete estimates of $z_i(t,x)$ are only obtained at three locations $x = -L$, $x = 0$, and $x = L$. From these discrete estimates, it is fitted a quadratic equation using the following,

$$\hat{z}_i = \left(\frac{z_i(t,-L) - 2z_i(t,0) + z_i(t,L)}{2L^2}\right)x^2 - \left(\frac{z_i(t,-L) - z_i(t,L)}{2L}\right)x + z_i(t,0) \tag{7-20}$$

Hence, the estimated (interpolated) vertical acceleration $\hat{z}_i$, from the three stations above, is given as follows,

$$\hat{z}_i = \frac{xa_i}{L}\left(\sin\left(\frac{\omega_i L}{V}\right)\cos(\omega_i t + \phi_i) + \frac{x}{L}\cos\left(\frac{\omega_i L}{V}\right)\sin(\omega_i t + \phi_i)\right) \tag{7-21}$$

The estimated amplitude of acceleration $\hat{A}_{zi}$ is as follows (after some algebraic manipulation),

$$\hat{A}_{zi} = \|\hat{z}_i\|_2 = \frac{xa_i}{L}\left(\left(\frac{x^2}{L^2} - 1\right)\cos^2\left(\frac{\omega_i L}{V}\right) + 1\right)^{\frac{1}{2}} \tag{7-22}$$

From the interpolated estimate $\hat{z}_i$ of component z_i, it is spatially differentiated to determine an estimate of the slope as follows,

$$\hat{\theta}_i = \frac{\partial \hat{z}_i}{\partial x} = \frac{a_i}{L^2}\left(\sin\left(\frac{\omega_i L}{V}\right)\cos(\omega_i t + \phi_i)\, L + 2x\left(\cos\left(\frac{\omega_i L}{V}\right) - 1\right)\sin(\omega_i t + \phi_i)\right) \qquad \textbf{(7-23)}$$

The amplitude of this slope interpolation estimates at any spatial point x is

$$\hat{A}_{\theta i} = \left\|\hat{\theta}_i\right\|_2 = \frac{a_i}{L}\left(\sin^2\left(\frac{\omega_i L}{V}\right) + \left(\frac{2x}{L}\right)^2\left(\cos^2\left(\frac{\omega_i L}{V}\right) - 1\right)^2\right)^{\frac{1}{2}} \qquad \textbf{(7-24)}$$

Thus, the mean relative error in acceleration ε_{zi} and in slope $\varepsilon_{\theta i}$ (over our interpolated range $x \in [-L, L]$) are defined as follows,

$$\varepsilon_{zi} = \frac{1}{2L}\int_{-L}^{L}\left(\frac{\hat{A}_{zi}}{A_{zi}} - 1\right)\mathrm{d}x = 0, \qquad \varepsilon_{\theta i} = \frac{1}{2L}\int_{-L}^{L}\left(\frac{\hat{A}_{\theta i}}{A_{\theta i}} - 1\right)\mathrm{d}x \qquad \textbf{(7-25)}$$

By inspection or by using a computational algebra package it is observe that the mean relative error ε_{zi} in the acceleration interpolation formula (7-21) is zero. This does not imply that there are never interpolation errors, only that on average, these errors are zero. The mean relative error $\varepsilon_{\theta i}$ in the slope interpolation formula (7-23) is defined by the following closed form solution, as follows,

$$\varepsilon_{\theta i} = \frac{1}{8\zeta_0}\left(-\zeta_3\left(\ln\left(\frac{\zeta_1 + 2\zeta_2}{\zeta_1 - 2\zeta_2}\right)\right) + 4\zeta_1 - 8\zeta_0\right) \qquad \textbf{(7-26)}$$

where,

$$\zeta_0 = \frac{\omega_i L}{V}, \quad \zeta_1 = \sqrt{3(\cos\zeta_0)^2 + 5 - 8\cos\zeta_0}, \quad \zeta_2 = \cos\zeta_0 - 1, \quad \zeta_3 = \cos\zeta_0 + 1 \qquad \textbf{(7-27)}$$

For the SMART-1 array, the minimum accelerometer spatial distance L is 100m and the apparent horizontal wave velocity V is 1000m/s (Abrahamson et al., 1987). Therefore, in Figure 7.5 is plotted the variation of mean relative error $\varepsilon_{\theta i}$ in the estimated slope $\hat{\theta}_i$, using equation (7-26) and calibrated for the SMART-1 array geometry.

Consequently, the general trend in the mean is an increasing negative error in interpolated slope estimates with wave frequency. The interpolation formula (7-23) underestimates (on average) the slope at higher frequencies. In this case, the Nyquist wavelength is $2L$ and hence the Nyquist (Aliasing) frequency is $f_{nyq} = V/2L = 5Hz$ (Brigham, 1988). So, the recommendation in this chapter is to only use a range of

0Hz to 5Hz frequency for slope estimates and acknowledge that the most accurate estimates of slopes are likely to be in the range from 0Hz to 2.5Hz.

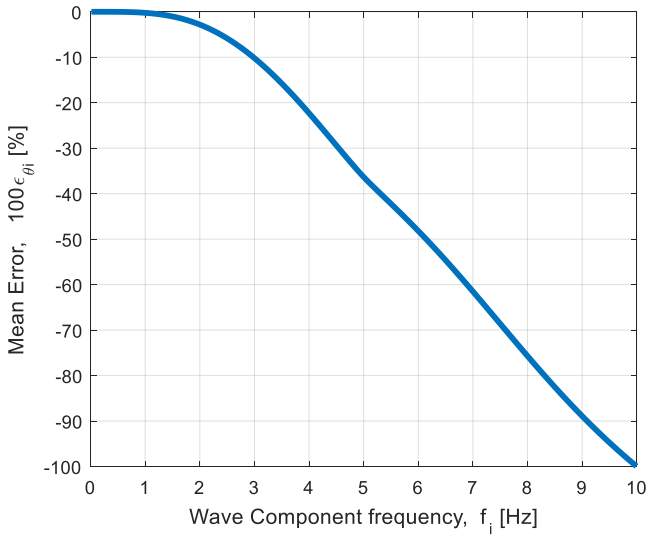

Figure 7.5 Variation of mean error in spatially interpolated slope formula with wave frequency

The previous analysis indicates that the inter-station spacing is critical to calculating the rotational ground motion. Spatial sampling results in aliasing (Loh, 1985) with an equivalent approximate Nyquist frequency of 5Hz at the inner ring perimeter of the SMART-1 array. Thus, to use interpolation above 5Hz, particularly for rotational acceleration estimation, is inadvisable. In other words, any estimate of the rotational ground acceleration (from the SMART-1 array) above 5Hz, is likely to be noise rather than a true description of the real rotational ground motion. In addition, on average slope estimates via interpolation are underestimates with the most reliable range from 0 to 2.5Hz. Therefore, is high-cut (zero-phase) filtered the vertical acceleration before using them to obtain estimates of rotational accelerations.

Using the interpolated vertical ground acceleration $\ddot{z}_g(t)$ of any 'x, y' position, it is possible to estimate the rotational component of the ground motion $\ddot{\theta}_g(t)$ for any point 'x, y' within the SMART-1 array, by using the 5-point high-order central difference method, according to equations (7-28) and (7-29). This method is graphically depicted in Figure 7.6. The equations (7-28) and (7-29) are a fifth-order estimate, so by making the step size Δx and Δy small, the neglected error terms $O(\Delta x^5)$ and $O(\Delta y^5)$ decrease sharply. Thus, a step size of 1 [mm] has been used (which was found to be accurate enough after a sensitivity analysis). The rotational ground accelerations $\ddot{\theta}_g(t)$ are essentially first partial derivatives (with respect to horizontal *x* and *y* coordinates) of the vertical accelerations in the East-West and the North-South directions. So, at any point, there are two different rotational ground motions, (pitch and roll), one in the East-West direction $\ddot{\theta}_{gy}(t)$ and another in the North-South direction $\ddot{\theta}_{gx}(t)$. This distinction becomes important when the total response of the structure is calculated, once considering the combined effects of horizontal and rotational ground accelerations.

$$\ddot{\theta}_{gx} = \frac{\partial \ddot{z}_g}{\partial y} = \frac{1}{\Delta y}\left\{\frac{1}{12}\ddot{z}_g(x, y - 2\Delta y) - \frac{2}{3}\ddot{z}_g(x, y - \Delta y) + \frac{2}{3}\ddot{z}_g(x, y + \Delta y) - \frac{1}{12}\ddot{z}_g(x, y + 2\Delta y)\right\} + O(\Delta y^5) \quad \textbf{(7-28)}$$

$$\ddot{\theta}_{gy} = \frac{\partial \ddot{z}_g}{\partial x} = \frac{1}{\Delta x}\left\{\frac{1}{12}\ddot{z}_g(x - 2\Delta x, y) - \frac{2}{3}\ddot{z}_g(x - \Delta x, y) + \frac{2}{3}\ddot{z}_g(x + \Delta x, y) - \frac{1}{12}\ddot{z}_g(x + 2\Delta x, y)\right\} + O(\Delta x^5) \quad \textbf{(7-29)}$$

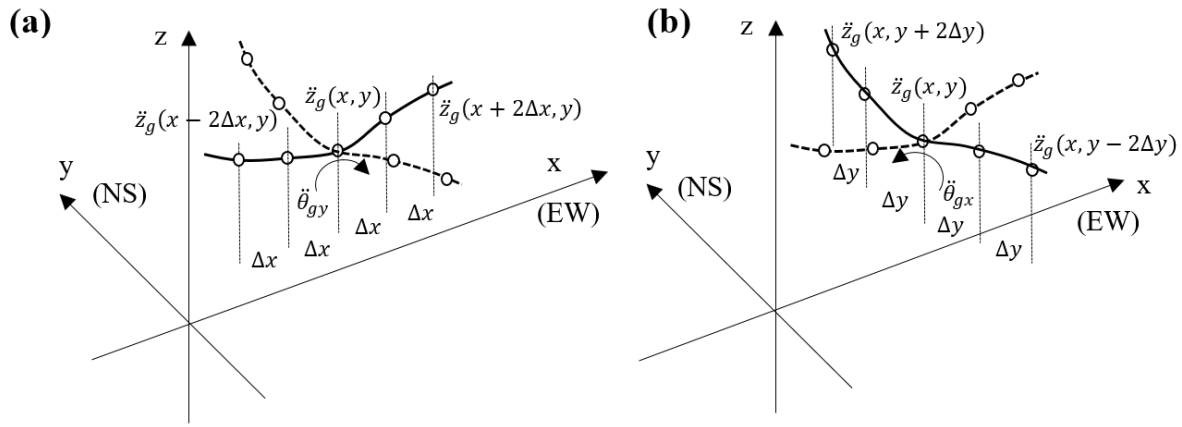

Figure 7.6 Rotational ground component in "x,y" position of the array (a) East-West and (b) North-South direction

Figure 7.7 shows the reconstructed estimate for the rotational acceleration $\ddot{\theta}_{gy}(t)$ with and without the 5Hz high-cut zero-phase filter. It is postulated that much of the signal above the cut-off frequency is interpolation induced noise rather than reliable estimates of rotational acceleration. Note that in this chapter, all structure systems have critical modal frequencies well below 5Hz hence these high-frequency rotational components are not significant for the flexible structures considered here.

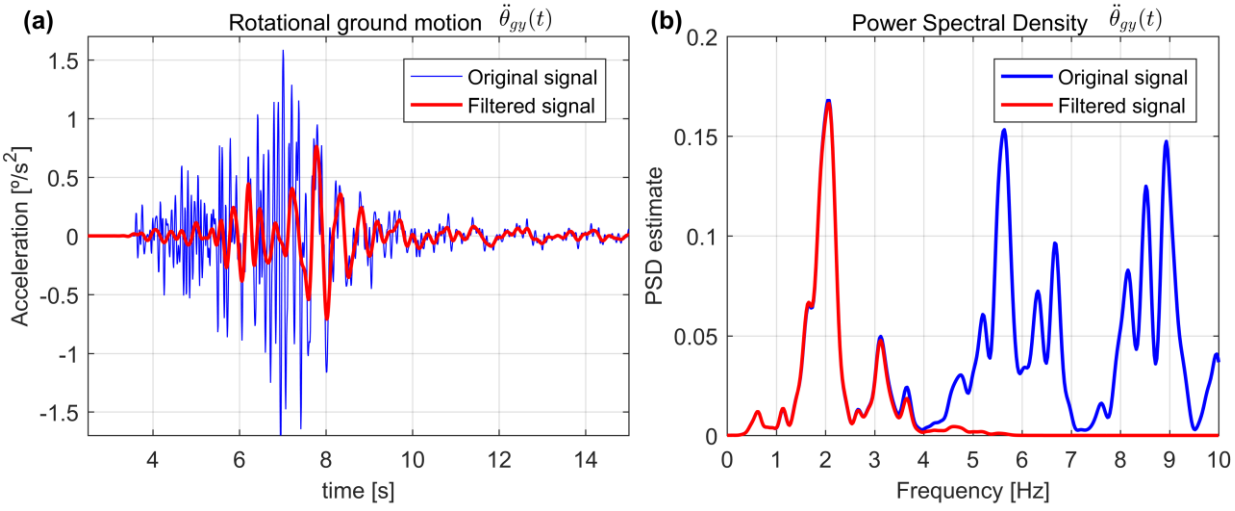

Figure 7.7 Comparison between the original and filtered signal for (a) Rotational ground motion and (b) Power spectral density for rotational ground motion

The Euclidian norms of the rotational ground acceleration for each position in the array are calculated in equation (7-30). Figure 7.8 depicts the spatial variation of the rotational ground motion norm within the inner array for the event #43. It shows that there is a significant variation in rotational acceleration, reaching values of 0.19 [deg/s^2] (0.0033 [rad/s^2]) close to the stations I-11 and I-12. Note that Figure 7.8 is for a particular time point of t = 5.98[s].

$$\left\|\ddot{\theta}_g(t)\right\|_2 = \sqrt{\ddot{\theta}_{gx}^2(t) + \ddot{\theta}_{gy}^2(t)} \qquad \textbf{(7-30)}$$

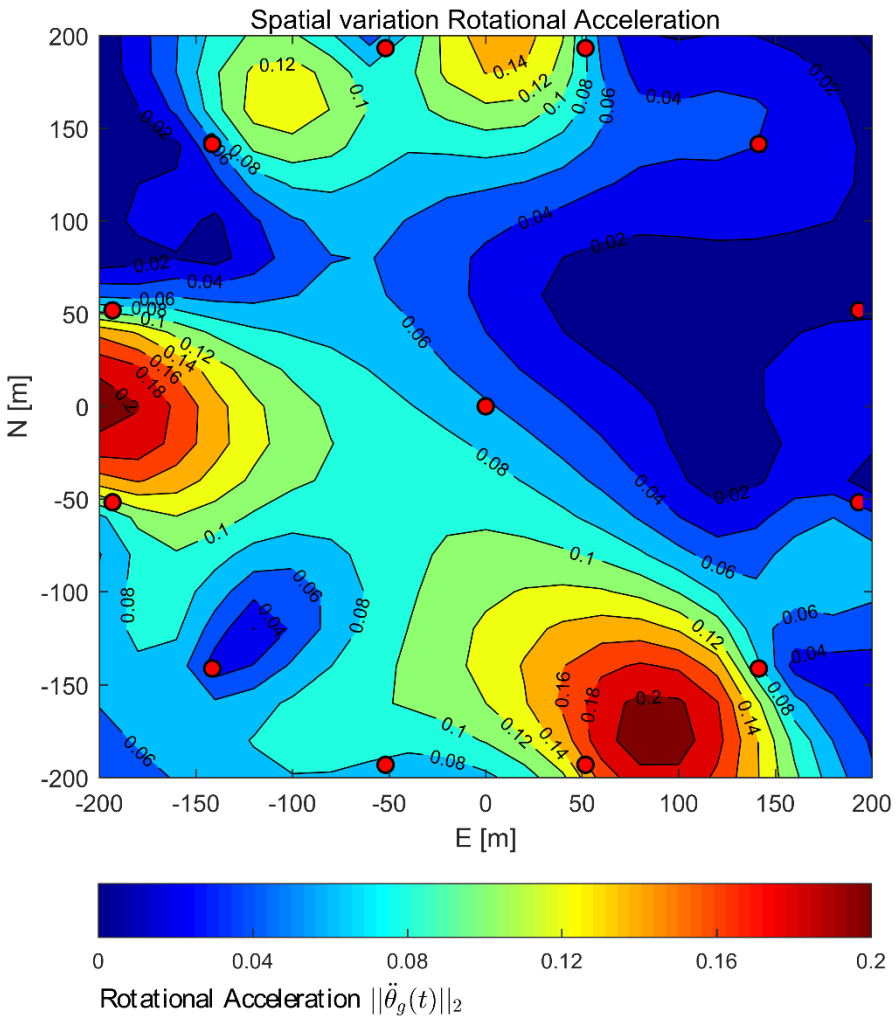

Figure 7.8 Example of spatial variation in norm rotational ground motion. (Event #43 at t=5.98[s], Rotational units: [degrees/s^2]).

In the same way, it is possible to calculate the Peak Rotational Ground Acceleration, known hereafter as *PRGA*, according to equation (7-31), for all data points of the time series, in each position of the SMART-1 array.

$$PRGA = \max_t \left\| \ddot{\theta}_g(t) \right\|_2, \quad PRGA_x = \max_t \left| \ddot{\theta}_{gx}(t) \right|, \quad PRGA_y = \max_t \left| \ddot{\theta}_{gy}(t) \right| \tag{7-31}$$

This information is significant in choosing an appropriate set of horizontal-rotational ground motions for the calculation of the structure's response. As explained above, it is possible to calculate the peak ground acceleration for each East-West ($\max|\ddot{\theta}_{gy}|$) and North-South ($\max|\ddot{\theta}_{gx}|$) direction. Figure 7.9 displays the contour plots of peak ground rotation acceleration *PRGA* for the event #39. These coloured contours express the magnitude of the peak rotational acceleration, with a maximum value of 0.86 [deg/s^2] (0.015 [rad/s^2]) close to the stations I-01 and I-12. The quiver plot represents the vectors $\vec{v}(x, y)$ as arrows, with each component keeping the sign of the rotation.

$$\vec{v}(x, y) = \left\{ \max_t |\ddot{\theta}_{gy}| \operatorname{sgn}(\ddot{\theta}_{gy}(\arg\max_t |\ddot{\theta}_{gy}|)), \max_t |\ddot{\theta}_{gx}| \operatorname{sgn}(\ddot{\theta}_{gx}(\arg\max_t |\ddot{\theta}_{gx}|)) \right\} \tag{7-32}$$

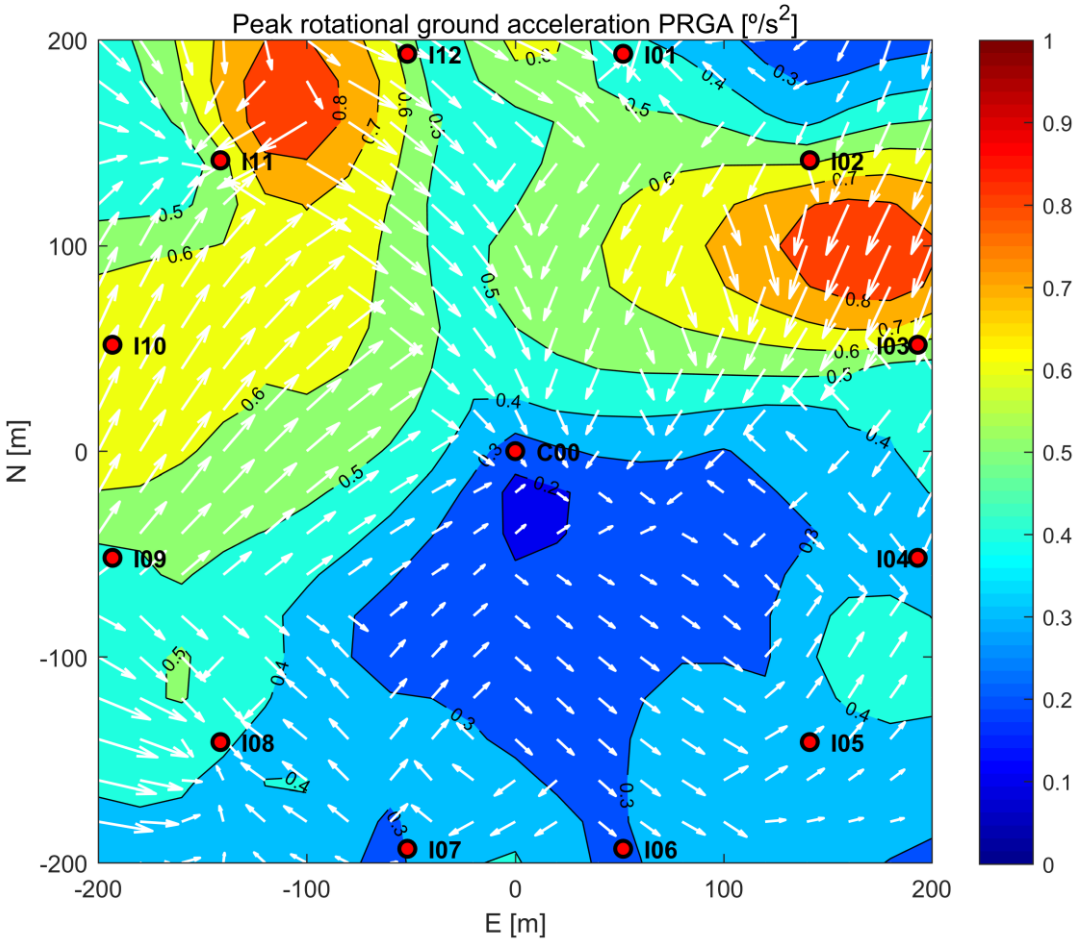

Figure 7.9 Maximum ground rotational acceleration *PRGA* for event #39

7.3.3 Selection of horizontal-rotational ground acceleration set

Once the rotational ground accelerations are estimated, a set of horizontal-rotational ground acceleration components are assembled. The horizontal-rotational set can be calculated for the East-West direction $(\ddot{x}_g, \ddot{\theta}_{gy})$ and North-South direction $(\ddot{y}_g, \ddot{\theta}_{gx})$. In this chapter, the main topic is to evaluate the effect of the rotational ground motion in the structure's response. Therefore, a set of accelerations that produce the greatest amplification in the structural responses is looked. Castellani et al. (2012) suggested that the relevance of the rotational component on structures is largely dependent on the vertical to horizontal ground motion amplitude ratio.

The hypothesis is that at the spatial location where a maximum vertical acceleration is found, the maximum rotational acceleration (pitch/roll) will occur at some delay in time due to wave passage. This is completely credible for individual Fourier components of the travelling wave. Additionally, the hypothesis is that the magnitude of rotational accelerations and vertical accelerations are correlated. The equation (7-19) suggests that there is a correlation but that it is frequency dependent. Therefore, Castellani et al. (2012) suggested using peak vertical ground acceleration (*PVGA*) to peak horizontal ground acceleration (*PHGA*) as a proxy for peak rotational ground acceleration (*PRGA*) to *PHGA*. Note that if this correlation were validated and strong it would provide some method of estimating the likely peak rotational ground acceleration indirectly. Therefore, the evidence is sought that supports or rejects this hypothesis.

To explore this hypothesis, the ratio of Peak Vertical Ground Acceleration (or *PVGA*) to the Peak Horizontal Ground Acceleration (or *PHGA*) is defined, where *PVGA* and *PHGA* are defined in equation (7-33). Note that there are two Peak Horizontal Ground Accelerations, one for each horizontal direction (East-West and North-South).

$$PVGA = \max_t \left|\ddot{z}_g(t)\right|, \quad PHGA_x = \max_t \left|\ddot{x}_g(t)\right|, \quad PHGA_y = \max_t \left|\ddot{y}_g(t)\right| \tag{7-33}$$

Figure 7.10 shows the ratio of the three events, (a) for East-West component $PVGA/PHGA_x$ and (b) for North-South component $PVGA/PHGA_y$.

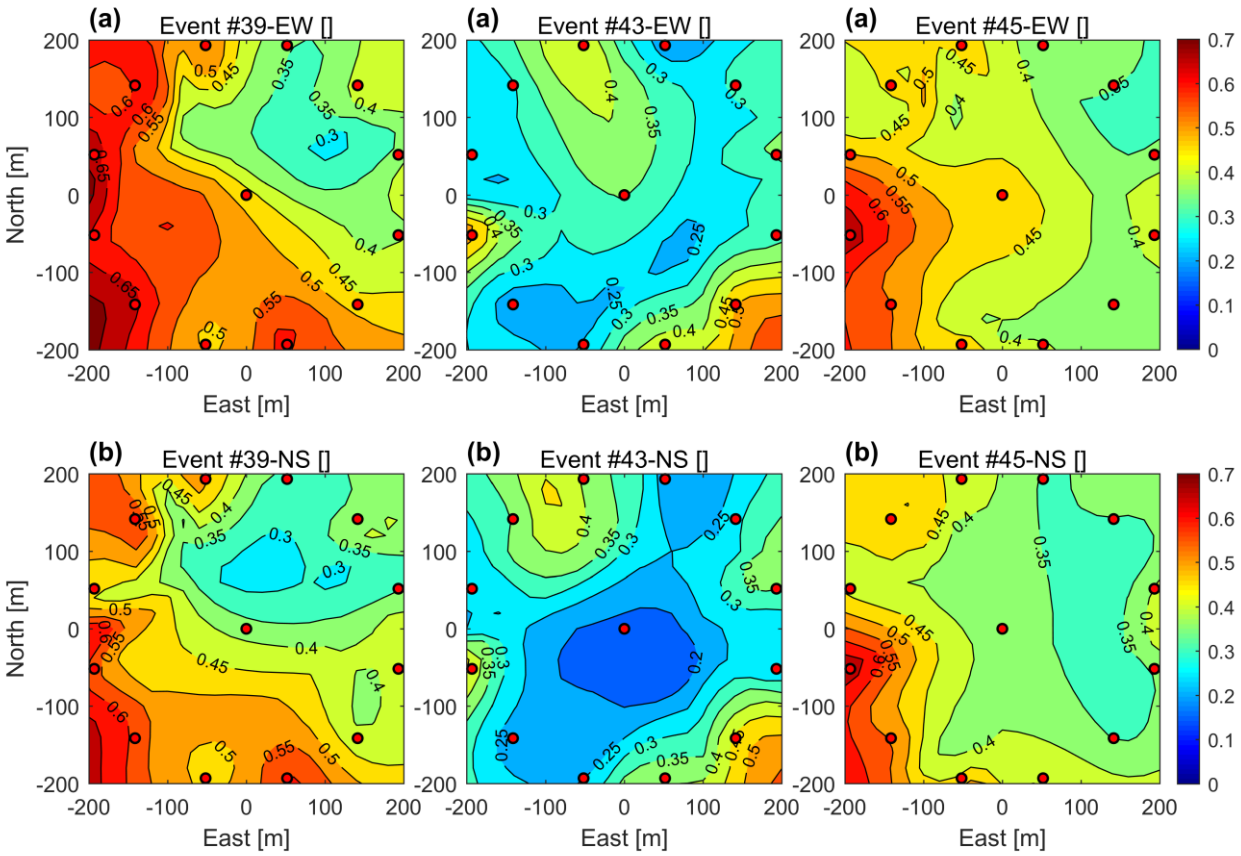

Figure 7.10 Ratio of the peak vertical to peak horizontal ground accelerations for the three events (a) East-West component ($PVGA/PHGA_x$) (b) North-South component ($PVGA/PHGA_y$)

On the other hand, given that is successfully estimated the rotational ground motion directly, it is possible to determine the ratio of Peak Rotational Ground Acceleration (*PRGA*) to Peak Horizontal Ground Acceleration (*PHGA*). Then is compared the utility of using the ratio *PVGA/PHGA* (shown in Figure 7.10) as a proxy for the ratio *PRGA/PHGA* (shown in Figure 7.11). It is clear that the locations where the maximum values of *PVGA/PHGA* and *PRGA/PHGA* are not coincident in the array.

This is underlined by Figure 7.12 which shows the correlation of *PVGA/PHGA* ratio with *PRGA/PHGA* ratio (for all three events and all points in the inner ring of the SMART-1 array). While there is some small statistically significant (R^2 value equal to 0.12, 0.25 and 0.48 for the events #39, #43 and #45 respectively) correlation in this plot, there is also a large degree of scatter. Hence, here is not recommend the postulated hypothesis, as the correlations are weak. Additionally, the direct use of *PVGA/PHGA* as a method of locating critical spatial locations where the maximum rotational to horizontal ground motions occur is unreliable. Therefore, Figure 7.11 was used later to select the set $(\ddot{x}_g, \ddot{\theta}_{gy})$ (in the East-West direction) or $(\ddot{y}_g, \ddot{\theta}_{gx})$ (in the North-South direction), for the time-history analyses of the structures.

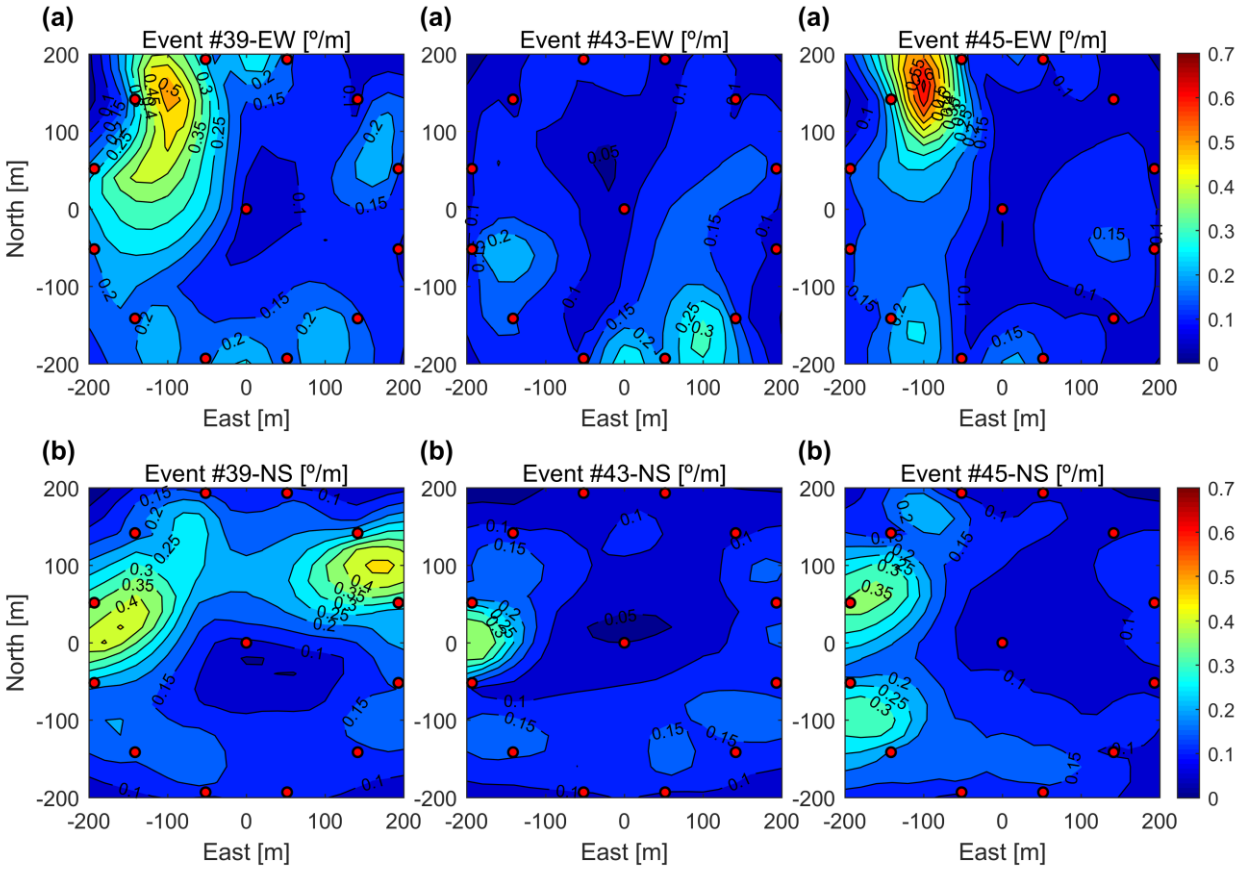

Figure 7.11 Ratio of the Peak Rotational Ground Acceleration to Peak Horizontal Ground Acceleration (*PRGA*/*PHGA*) for the three events (a) East-West component $\ddot{x}_g$ (b) North-South component $\ddot{y}_g$

The ratio shown in Figure 7.11 has units of [degree/m]. A non-dimensionalized version of the ratio *PRGA/PHGA* could be performed by using radians for the angle and multiplying the ratio by the predominant Rayleigh wavelength $\lambda = v_f/f$ of the SMART-1, where this wavelength is a property of the site. For example, the site average surface Rayleigh wave velocity is $v_f = 2.35$ [km/s] and its average frequency is f=1.17Hz (Loh, 1985). Therefore, the site average wavelength is approximately equal to λ=2000 [m]. For all cases, the shape of Figure 7.11 is the same. The non-dimensional version of ratio *PRGA/PHGA* would enable a more systematic comparison of the rotational to horizontal accelerations at a range of different geographic sites. Nevertheless, in this analysis, there is only a single site, and therefore it is not present the data in this form.

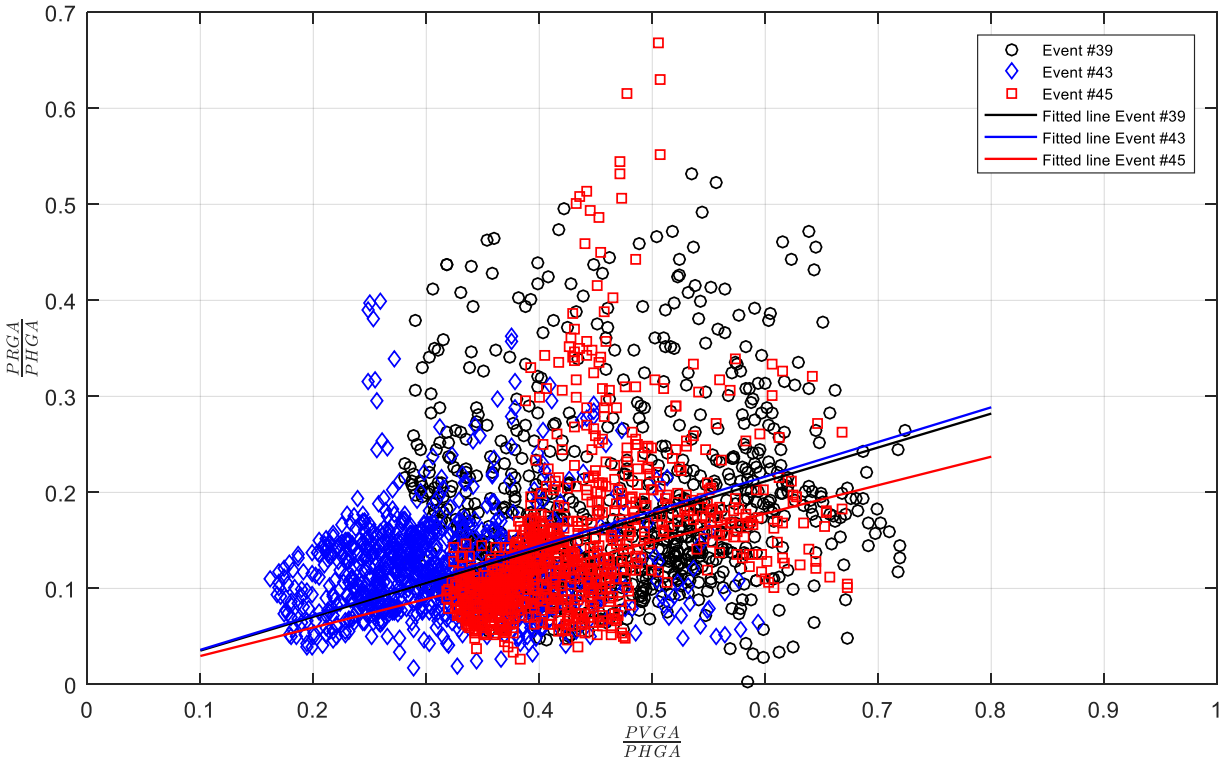

Figure 7.12 *PRGA*/*PHGA* ratio v/s *PVGA*/*PHGA* ratio for all three events and all points in the inner ring of the SMART-1 array

7.4 Numerical studies

7.4.1 Defining system performance measures

The main objective of this chapter is evaluating the effects of the rotational ground motion on buildings. For this purpose, first it is calculated the total solution of equation (7-13), hereafter referred as the response Including Ground Rotation (*IGR*). Then it is evaluated the response Neglecting Ground Rotation (*NGR*). The *NGR* is calculated when $\mathbf{p}_2=0$ in equation (7-13). As a measure of change in the response between *IGR* and *NGR*, the following performance measures are used,

$$U_1 = u_s + u_2 - 3s\theta_s \tag{7-34}$$

$$A_1 = \ddot{u}_s + \ddot{u}_2 + \ddot{u}_g - 3s\left(\ddot{\theta}_s + \ddot{\theta}_g\right) \tag{7-35}$$

where U_1 and A_1 are respectively the relative (horizontal + sway + rotational) displacement and total (horizontal + sway + ground + rotational) acceleration for the top of buildings in non-dimensional form, and $s = h/b$ is the aspect ratio of the building. Note that the horizontal displacement of the foundation is included u_s on the total response. Nevertheless, at the moment of calculate the difference in the response

effectively cancels between the two systems. The difference in the response total power, when using the response *IGR* (Including Ground Rotation) rather than *NGR* (Neglecting Ground Rotation) is defined as follows,

$$\chi_1(s, T_x, c_1) = 100\left(\frac{[E_s(U_1)]_{IGR}}{[E_s(U_1)]_{NGR}} - 1\right), \quad \ddot{\chi}_1(s, T_x, c_1) = 100\left(\frac{[E_s(A_1)]_{IGR}}{[E_s(A_1)]_{NGR}} - 1\right) \qquad \textbf{(7-36)}$$

where c_1 is the soil to building density ratio, both defined in equation (7-10). T_x is the fundamental natural period of a structure on a rigid base. $E_s(U_1)$ is the total power spectral density (based on all data points of response time series U_1), which is defined using Parseval's theorem according to equation (7-37).

$$E_s(U_1) = \int_{-\infty}^{\infty} |U_1(t)|^2 dt = \frac{1}{2\pi} \int_{-\infty}^{\infty} |U_1(\omega)|^2 d\omega \qquad \textbf{(7-37)}$$

where $U_1(\omega)$ is the continuous Fourier transform of $U_1(t)$. Using total power as a comparative metric delivers a statistical estimate of magnitude that provides more information about the change in the response than employing a single peak of the function.

7.4.2 Initial results for a set of parameters

The analysis is carried out first for the seismic event #39 and for a selected combination of parameters as a starting example. For this, the case when the building has a first natural period on rigid foundation equal to $T_x = 0.5s$, the soil to building density ratio equal to $c_1 = 1.16$ (see Table 7-1) and dense soil is examined. Then, the three seismic events are considered, and a broader range of system parameters are explored.

Figure 7.13(a) shows the East-West component of the horizontal ground motion and the rotational acceleration time series $\ddot{\theta}_{gy}(t)$ calculated using equation (7-29). This component represents the highest rotational/horizontal ground motion ratio (*PRGA/PHGA*) for event #39. The position of this record within the array can be observed in the red zone of Figure 7.11(a), close to the stations I-11 and I-12. Figure 7.13(b) shows the power spectral density for the horizontal and rotational ground motions, respectively. Figure 7.13(c) depicts the time-frequency plot for the horizontal and rotational ground motions, respectively.

Figure 7.14(a) shows the response Including Ground Rotation (*IGR*, red line) and the response Neglecting Ground Rotation (*NGR*, blue line) for the upper DOF of the building, namely displacement U_1 and the total acceleration A_1. This time series was calculated for a set of parameters: $s = h/b = 2.0$, $T_x = 0.5s$, $c_1 = 1.16$, dense soil and the set of horizontal-rotational ground motion shown in Figure 7.13.

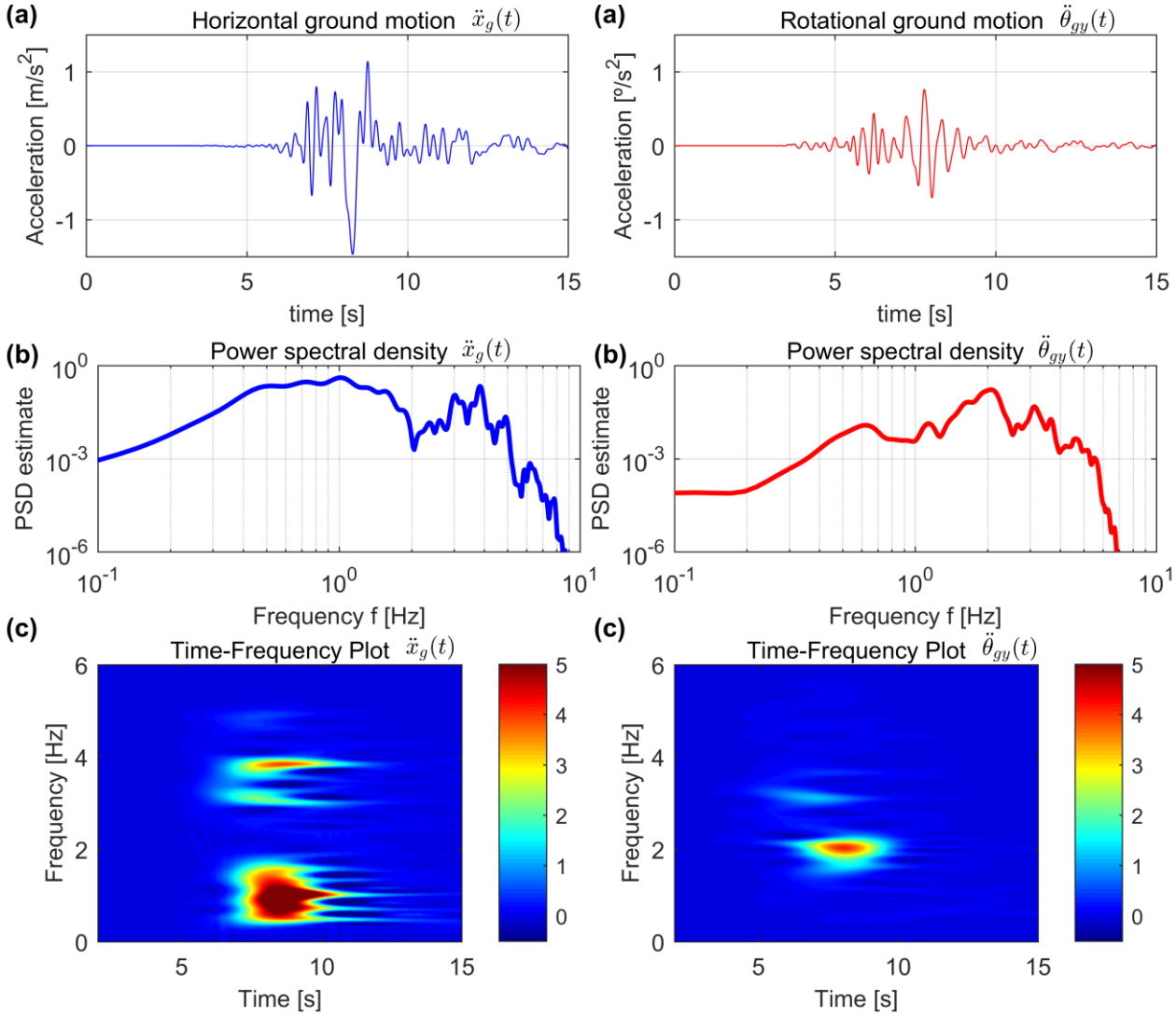

Figure 7.13 (a) Horizontal and rotational ground motions (b) Power spectral density for these horizontal and rotational ground motions and (c) Time-Frequency plot of these horizontal and rotational ground motions – Event #39 E-W component

Comparing the *IGR* (Including Ground Rotation) and *NGR* (Neglecting Ground Rotation), the maximum displacement increases when the rotational ground motion is considered as well as the total acceleration, throughout the earthquake duration. Figure 7.14(b) depicts the corresponding power spectral density for the displacement and total acceleration, respectively. Comparing the *IGR* and *NGR*, the structure is affected by the rotational ground motion, for a Fourier frequency nearly equal to 1.8[Hz] (which represents approximately the building's first natural frequency). The building's displacement response power increases by $\chi_1 = 13.6\%$ and there is an amplification in acceleration response power of $\ddot{\chi}_1 = 15.1\%$. It is important to note that, both these amplifications (change in displacement and acceleration power) have a similar value. In this study it was found that the change in the displacement and acceleration have a similar trend in the whole range of system parameters.

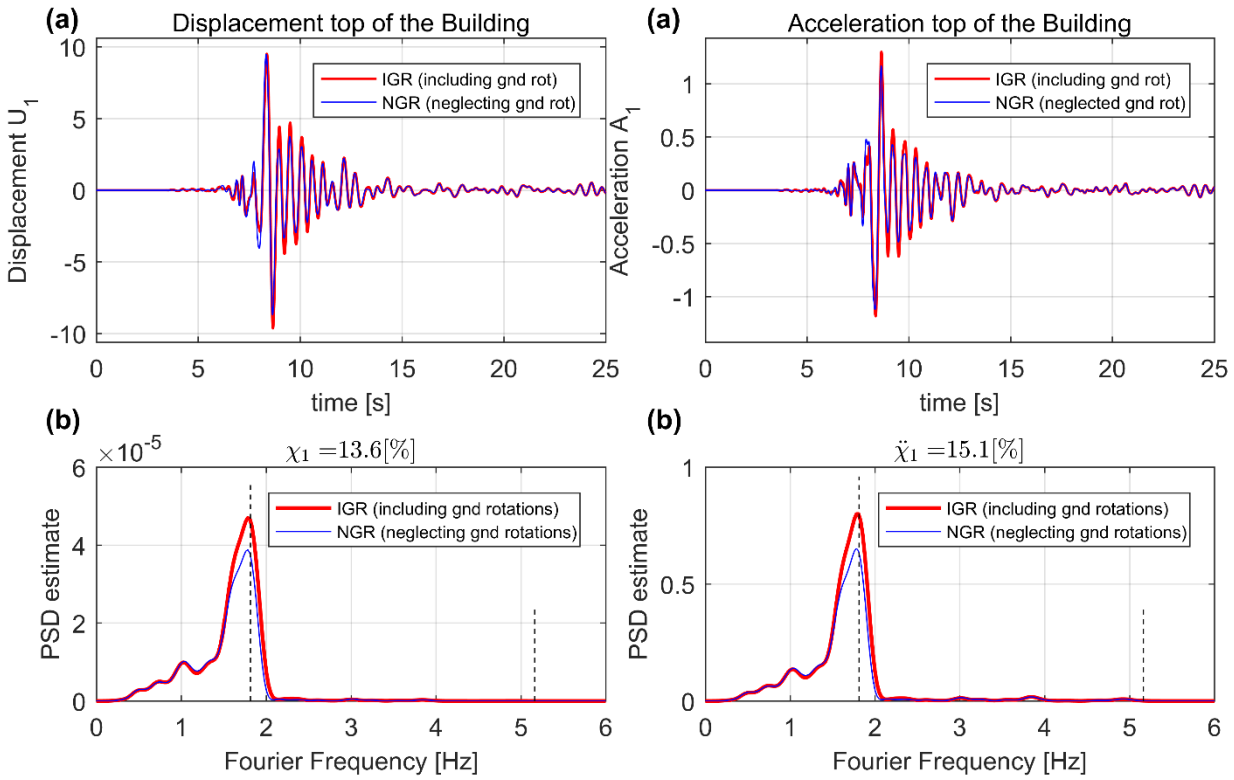

Figure 7.14 (a) Displacement and acceleration responses, (b) Power spectral density of displacement and acceleration – Responses on dense soil for the parameter set (s = h/b = 2.0, T_x = 0.5s, c_1 = 1.16)

7.4.3 Change in power with variation in aspect ratio s and Period on rigid foundation T_x

The variation of change in power (displacement $\chi_1(s, T_x, c_1)$ and acceleration $\ddot{\chi}_1(s, T_x, c_1)$) for a broader range of system parameters are analysed (aspect ratio $s = h/b$ varying between 0.3 and 4, the period of the building on rigid foundation T_x varying between 0.2s and 1.6s, and the response on dense soil, i.e. soil to building density ratio equal to $c_1 = 1.16$). The building is subjected to all earthquake events, for its East-West and North-South components. As mentioned in section 7.3.3, the set of horizontal and rotational ground acceleration was chosen using the maximum *PRGA/PHGA* ratio for each event and directions, depicted by the red zone in Figure 7.11. Note that the parameter range chosen in this chapter could produce a large footprint of the structure. Nevertheless, the spatial variation of rotational and horizontal ground motion across the footprint of the structure is not considered (i.e. the foundation behaves like a stiff body, where the seismic input it is modelled as a point-like input according to Figure 7.1).

Contour plots in Figure 7.15 display the variation of change in power $\chi_1(s, T_x, 1.16)$ for the displacement U_1 on top of the building, for the East-West component. The critical zones in the figure are in red, i.e. where the building's total response power is amplified by the rotational ground motion. For the event #39 and event #45 the biggest amplification in the response lies around $\chi_1(1{,}0.5{,}1.16) = 25\%$ and

$\chi_1(1.3,1.3,1.16) = 35\%$ respectively. These amplifications are not sensitive to the aspect ratio s of the building, but rather on the period of the building T_x.

Each contour plot presented in this chapter contains the results of over 180,000 different time-histories analyses. The University of Bristol's supercomputer, BlueCrystal is employed for these simulations and required approximately 20 minutes run-time.

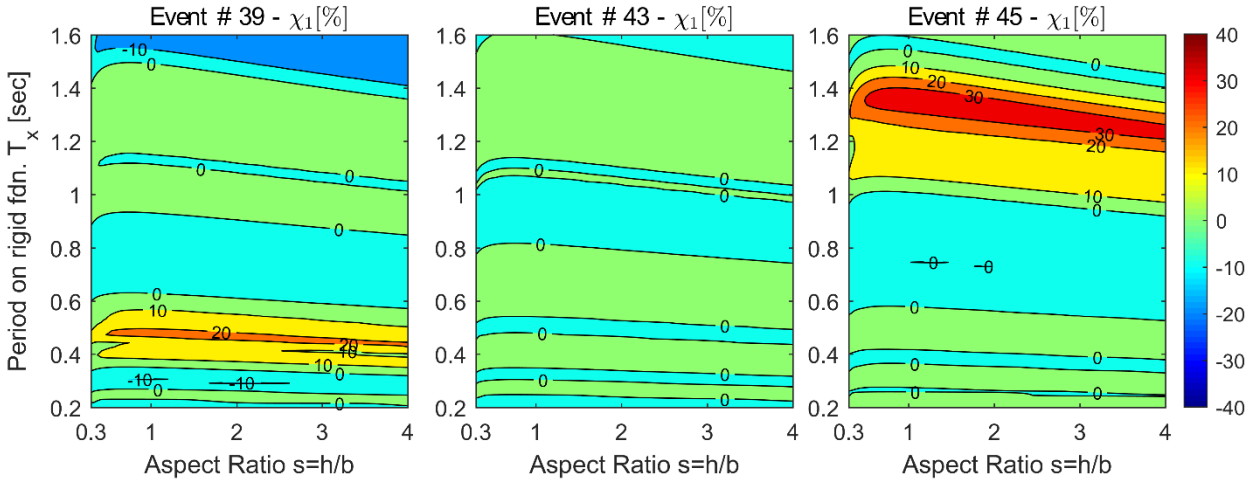

Figure 7.15 Change in displacement power $\chi_1(s,T_x)$ with the variation in aspect ratio s = h/b and the natural period of the building on rigid foundation T_x - Response on dense soil (c_1 = 1.16) for the East-West seismic components

Contour plots in Figure 7.16 show the variation of change in power $\ddot{\chi}_1(s, T_x, 1.16)$ for the acceleration A_1 on top of the building, for the East-West component. For the event #39 and event #45 the biggest amplification in the response lies around $\ddot{\chi}_1(2,0.5,1.16) = 22\%$ and $\ddot{\chi}_1(2,1.3,1.16) = 34\%$ respectively. On the other hand, for the event #43, the effect of rotational ground motion in the structure is negligible for the entire range of parameters. Note that the effects of rotational ground motion do not always increase with the building periods, as one might suppose. For the event #39, the critical height is for a building with a natural period equal to $T_x = 0.5s$. Instead, for the event #45, the critical height varies between buildings with period T_x from 1.2s to 1.4s. This highlights the importance of the frequency content of the earthquake. The explanation of behaviour is discussed in more detail below (see section 7.4.5).

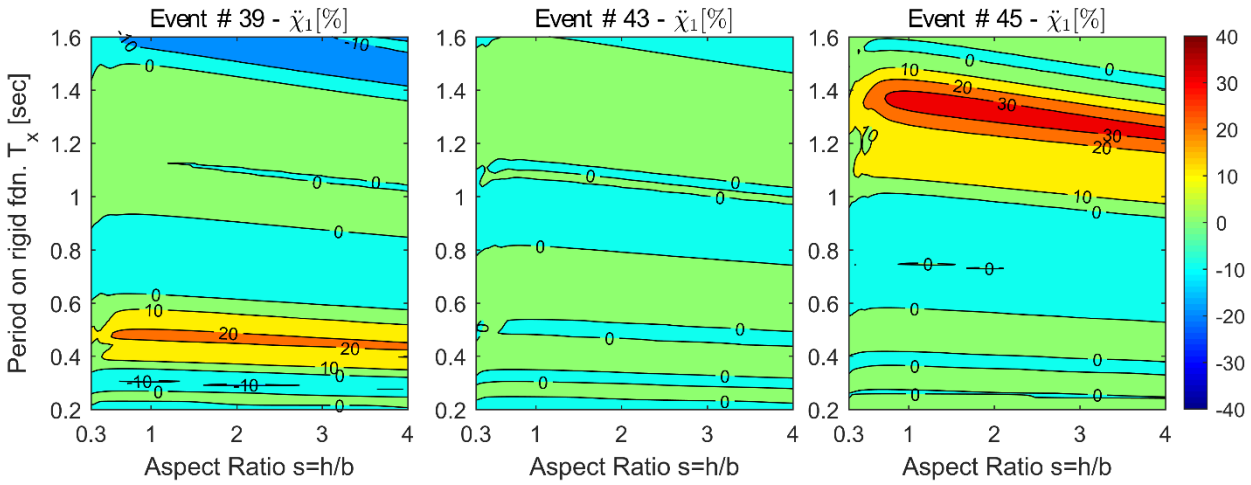

Figure 7.16 Change in acceleration power $\ddot{\chi}_1(s,T_x)$ with the variation in the aspect ratio $s = h/b$ and the natural period of the building on rigid foundation T_x - Response on dense soil ($c_1 = 1.16$) for the East-West seismic components

Figure 7.17 displays the contour plots of change in power for the displacement $\chi_1(s, T_x, 1.16)$, considering the three events for the North-South seismic component. Unlike Figure 7.15 and Figure 7.16, the effect of rotational ground motion in the structure is less important for the three events analysed in this chapter, with a maximum of $\chi_1(2,1.3,1.16) = 23\%$ for the event #45. This is mainly because the relative importance of the rotational to horizontal ground motion is low (as shown in Figure 7.11(b)). Therefore, the responses Including Ground Rotation (*IGR)* are very similar to the response Neglecting Ground Rotation (*NGR*).

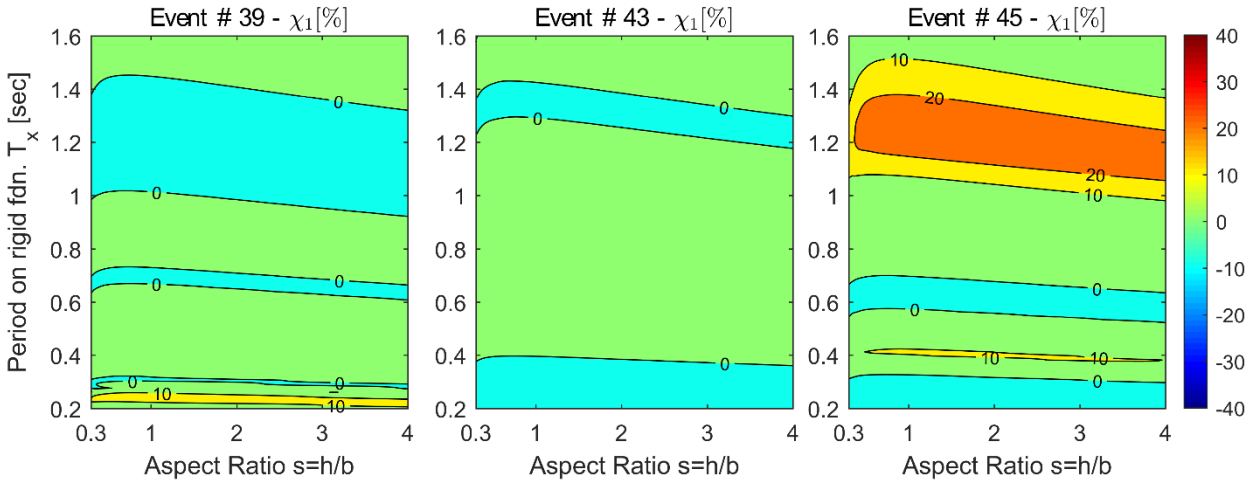

Figure 7.17 Change in displacement power $\chi_1(s,T_x)$ with the variation in aspect ratio $s = h/b$ and the natural period of the building on rigid foundation T_x - Response on dense soil ($c_1 = 1.16$) for the North-South seismic components

Figure 7.18 shows the contour plots of change in power for the acceleration $\ddot{\chi}_1(s, T, 1.16)$, considering the three events for the North-South seismic component. As with the displacements, the effect of rotational ground motion in the structure is small for the three events, with a maximum of $\ddot{\chi}_1(2,1.3,1.16) = 21\%$ for the event #45.

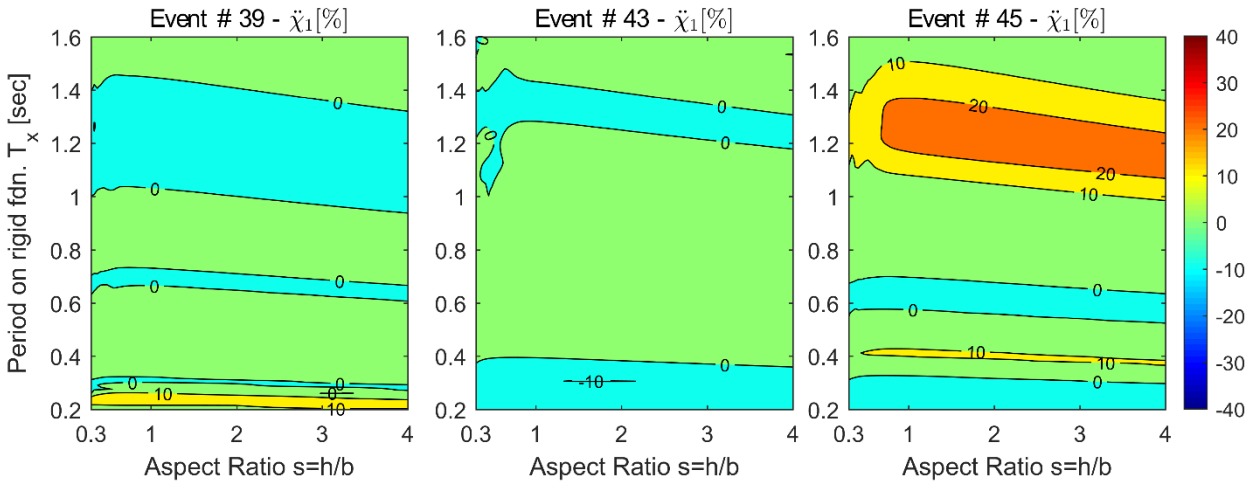

Figure 7.18 Change in acceleration power $\ddot{x}_1(s,T_x)$ with the variation in aspect ratio $s = h/b$ and the natural period of the building on rigid foundation T_x - Response on dense soil ($c_1 = 1.16$) for the North-South seismic components

7.4.4 Change in power with variation in density ratio c_1 and period on rigid foundation T_x

Figure 7.19 displays the contour plots of the change in power $\chi_1(2,T,c_1)$ for the displacement U_1, with density ratio c_1 varying between 0.9 and 1.79 and period of the building T_x varying between 0.2s and 1.6s. The soil to building density ratio c_1, equation (7-10), varies with the soil and building density. So, the change in the density ratio in Figure 7.19 can be viewed as a change in soil and/or building densities. In this chapter, the variation in density ratio comes from a linear change in the soil density, which also produces a change of the other soil characteristics (shear velocity V_s, shear modulus G_s and Poisson´s ratio μ_s). The aspect ratio was set equal to $s = 2.0$. As shown in the Figure 7.15, the biggest amplification in the response lies around $\chi_1(2,0.5,1.6) = 21\%$ and $\chi_1(2,1.3,1.4) = 33\%$ for the event #39 and event #45 respectively. Henceforth the change in displacement and acceleration power just for East-West seismic components are shown because they are the components that generate the most important amplification in the structure.

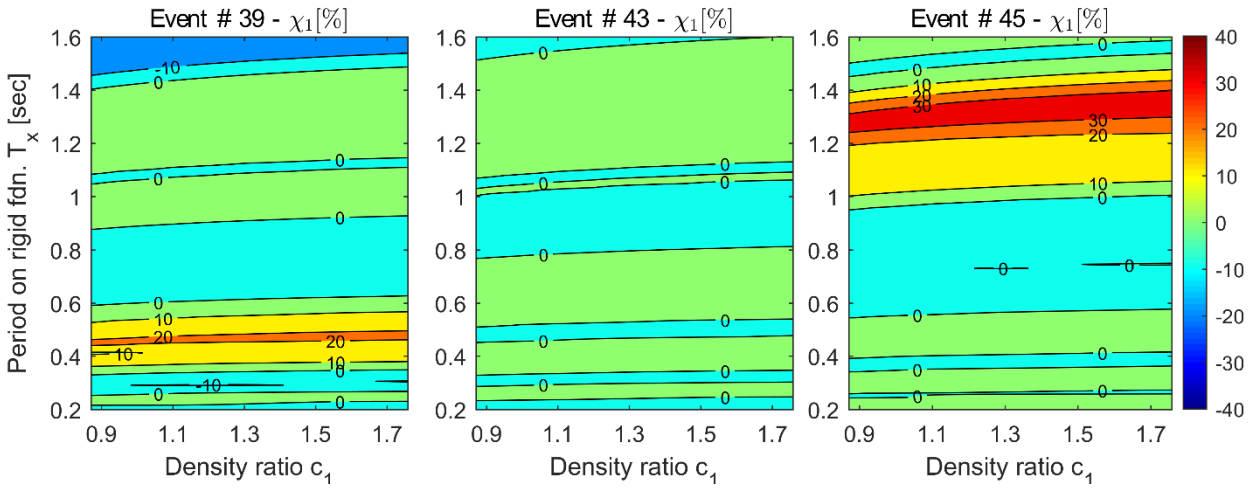

Figure 7.19 Change in displacement power $\chi_1(s,T_x,c_1)$ with the variation in density ratio c_1 and the natural period of the building on rigid foundation T_x - Response on dense soil and aspect ratio s = 2.0 for the East-West seismic components

Figure 7.20 displays the contour plots of the change in power $\ddot{\chi}_1(2,T,c_1)$ for the acceleration A_1, with density ratio c_1 and period of the building T_x. The aspect ratio was set equal to $s = 2.0$. The biggest amplification in the response lies around $\ddot{\chi}_1(2{,}0.5{,}1.0) = 25\%$ and $\ddot{\chi}_1(2{,}1.3{,}1.4) = 36\%$ for the event #39 and event #45 respectively. In general, the effect of rotational ground motion in the building's response does not depend on the soil to building density ratio c_1.

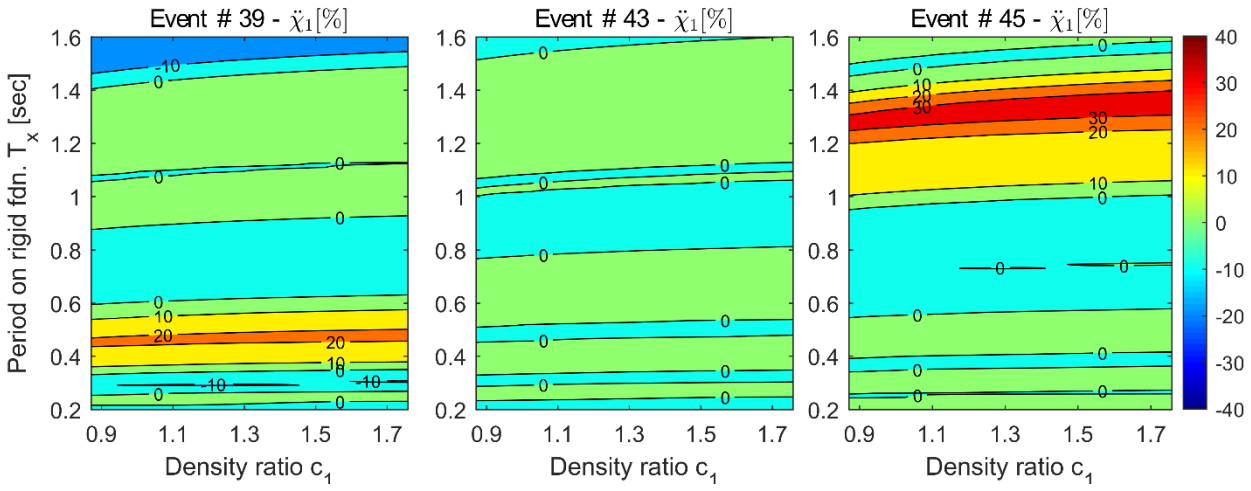

Figure 7.20 Change in acceleration power $\ddot{\chi}_1(s,T_x,c_1)$ with the variation in density ratio c_1 and the natural period of the building on rigid foundation T_x - Response on dense soil and aspect ratio s = 2.0 for the East-West seismic components

Figure 7.21 displays the contour plot of change in power for the displacements $\chi_1(s,T,1.23)$, for very dense soil (soil to building density ratio equal to $c_1 = 1.23$). The aspect ratio $s = h/b$ varying between 0.3 and 4, and the period of the building on rigid foundation T_x varying between 0.2s and 1.6s. The biggest amplification in the response lies around $\chi_1(2{,}0.5) = 20\%$ and $\chi_1(2{,}1.3) = 35\%$ for the event #39 and event #45 respectively.

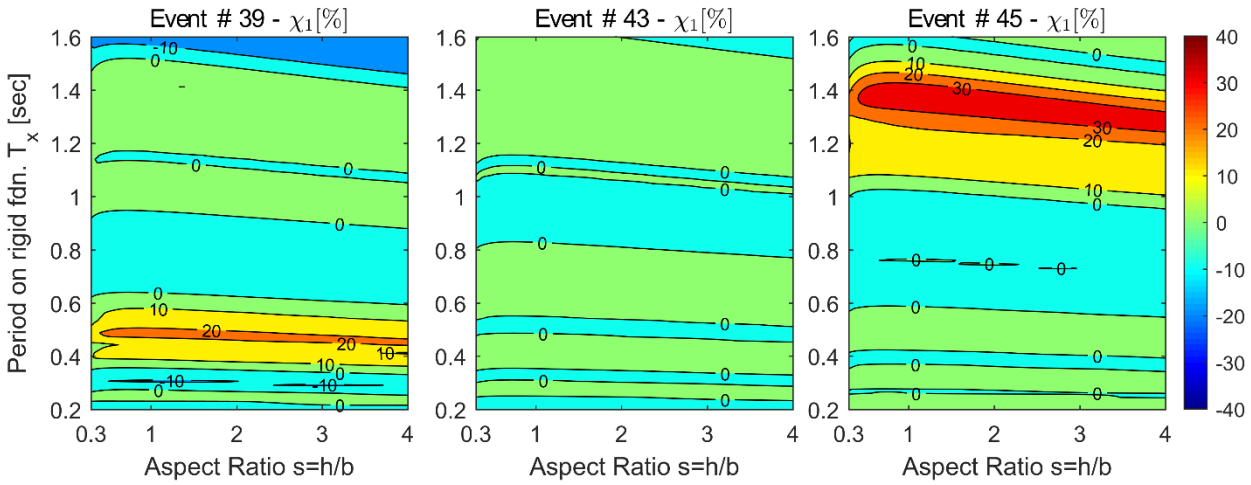

Figure 7.21 Change in displacement power $\chi_1(s,T_x)$ with the variation in aspect ratio s = h/b and the natural period of the building on rigid foundation T_x - Response on very dense soil (c_1 = 1.23) for the East-West seismic components

Figure 7.22 shows the contour plot of change in power for the acceleration $\ddot{\chi}_1(s,T,1.23)$, for very dense soil (soil to building density ratio equal to $c_1 = 1.23$). In general, there are no changes in the building's response for the different range of soil types considered in this study (medium, dense and very dense sand, Table 7-1).

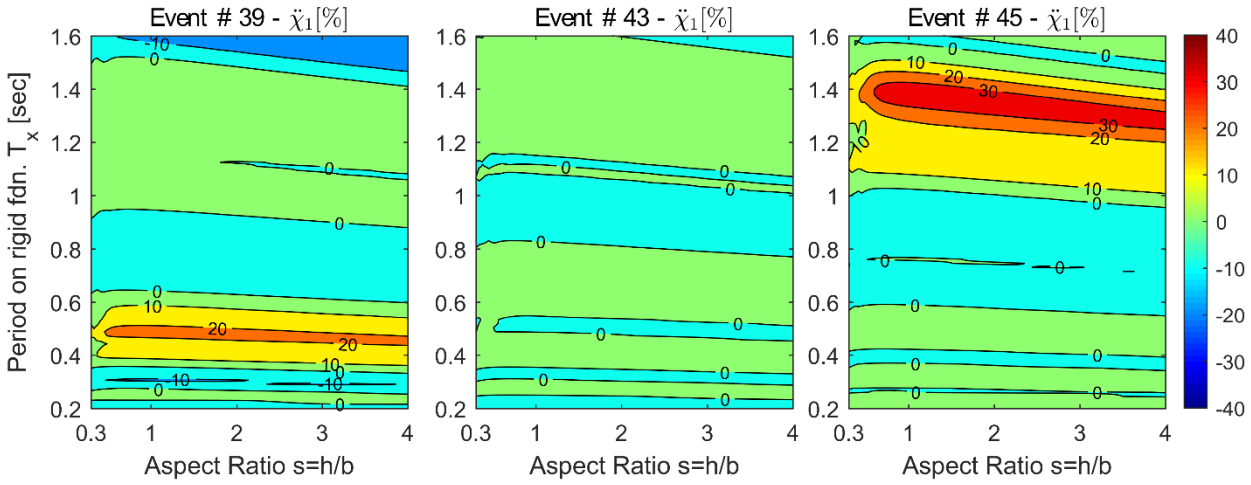

Figure 7.22 Change in acceleration power $\ddot{\chi}_1(s,T_x)$ with the variation in aspect ratio s = h/b and the natural period of the building on rigid foundation T_x - Response on very dense soil (c_1 = 1.23) for the East-West seismic components

As seen in the previous figures, the effects of the rotational ground motion do not always increase with the period of the building, as indicated in previous works (Kalkan and Graizer, 2007; Trifunac, 2009; Falamarz-Sheikhabadi, 2014). This suggests that the effect of soil rotation is not necessarily more damaging for tall structures than for smaller structures. Therefore, a more forensic exploration of the system is required.

7.4.5 Comparison of the structures' response in the frequency domain

In frequency domain system analysis, it is possible to determine the property of the system through the frequency dependent matrix $\mathbf{H}(\omega)$. By taking a Fourier transform of equation (7-13), the set of differential equations with a set of algebraic equations is re-expressed, thus,

$$\mathbf{u}(\omega) = \mathbf{H}(\omega)\mathbf{p_1}\ddot{u}_g(\omega) + \mathbf{H}(\omega)\mathbf{p_2}\ddot{\Theta}_g(\omega), \qquad \mathbf{H}(\omega) = -(\mathbf{K} + i\omega\mathbf{C} - \omega^2\mathbf{M})^{-1} \tag{7-38}$$

where vector $\mathbf{u}(\omega)$ is the Fourier transform of vector $\mathbf{u}(t)$, $\ddot{u}_g(\omega)$ is the Fourier transform of the ground acceleration $\ddot{u}_g(t)$, $\ddot{\Theta}_g(\omega)$ is the Fourier transform of the rotational ground motion $\ddot{\theta}_g(t)$ and ω is the Fourier frequency.

Figure 7.23 displays, as a heuristic case, the response of three structures with different periods (for the event #39) in the frequency domain. It is used the equation (7-38). The structural system's response is given by the sum of two components (i) the responses induced by rotational ground motion $\mathbf{H}(\omega)\mathbf{p_2}\ddot{\Theta}_g(\omega)$ and (ii) the responses induced by the horizontal ground motion $\mathbf{H}(\omega)\mathbf{p_1}\ddot{U}_g(\omega)$. The error in neglecting the effects of rotational ground motion is dependent on the ratio of these two terms.

These two terms contain a vector of frequency dependent DOF responses. In the previous section, the second element in the DOF's vector (i.e. the top of the building) is selected and obtained a measure of the magnitude of this DOF's responses by a norm across all frequencies in equation (7-36). In contrast, for this section, a norm across all DOFs is performed to obtain a measure of the magnitude of the entire system's responses at a particular frequency. Thus, the norm condensation employed in this section is obtained with respect to DOFs rather than with respect to frequency.

Thus, the ratio of rotational ground motion to maximum horizontal ground motion induced responses $\boldsymbol{\lambda}(\omega)$ is defined as follows,

$$\boldsymbol{\lambda}(\omega) = \frac{\left\|\mathbf{H}(\omega)\mathbf{p_2}\ddot{\Theta}_g(\omega)\right\|_\mathbf{2}}{\max_{\omega}\left(\left\|\mathbf{H}(\omega)\mathbf{p_1}\ddot{U}_g(\omega)\right\|_\mathbf{2}\right)} \tag{7-39}$$

where the numerator in the equation (7-39) is the norm of the rotational ground motion induced responses of the structure. The denominator in the equation (7-39) is the maximum (with respect to ω) of the norm of the horizontal ground motion induced responses of the structure.

Figure 7.23(a) shows the norm of transfer functions $\|\mathbf{H}(\omega)\|_\mathbf{2}$ for the three building cases. Figure 7.23(b) displays the ratio $\boldsymbol{\lambda}(\omega)$ for the three buildings. The rotational ground excitation produces an important amplification in the response for the building with a period on a rigid foundation of $T_x = 0.5s$. This is due

to the large ratio $\boldsymbol{\lambda}(\omega)$. In contrast, the effect of the rotational ground motions, for buildings with period $T_x = 0.2s$ and $T_x = 1.0s$, is much smaller. This demonstrates that the influence of rotational ground motion does not necessarily increase as the period of the building increases. Thus, a large ratio of rotational to horizontal ground motion frequency components at/or around the fundamental natural structural frequency is needed, to induce a large error in the analyses by neglecting the rotational ground motion.

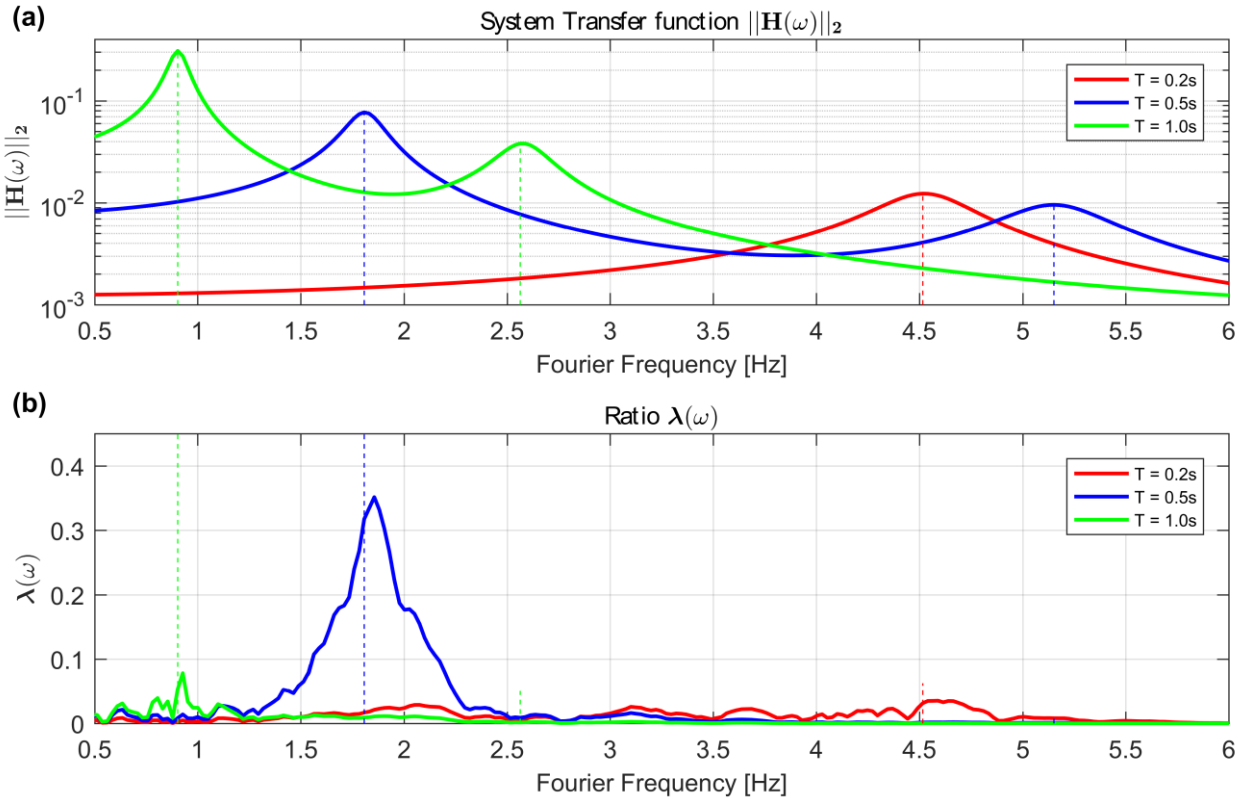

Figure 7.23 Response on dense soil for the parameter set (s = 2.0, T_x = [0.2s, 0.5s, 1.0s], c_1 = 1.16) (a) Transfer function of the building (b) Ratio λ(ω)

7.5 Summary

In this chapter, a theoretical formulation (a reduced-order model) is presented to evaluate the effects of the rotational ground motion upon structures. A multi-station interpolation procedure has been employed to estimate the rotational ground motion. Accelerogram data from the SMART-1 dense accelerometer array in Taiwan were used (Abrahamson et al., 1987). The accuracy of the spatial interpolation scheme for the SMART-1 decreases for frequencies above 5Hz, so it is zero-phase filtered (high-cut) all the vertical acceleration above 5Hz. Therefore, in this work, the seismic response for structures in the range of natural frequencies of 0.6Hz to 5Hz (small frequencies) are calculated and constant rotational spring stiffness (frequency independent) is considered. The analyses have been undertaken for different parameters of the buildings, soil types and seismic events.

The research presented in this chapter has led to the following principal findings:

- It is possible for the rotational ground motion to significantly affect the response of structures. For example, there is an increase in the total acceleration structural response of up to $\ddot{\chi}_1 = 36\%$, for event #45. The displacement responses have a similar trend, reaching a maximum amplification of $\chi_1 = 35\%$, also for event #45. These amplifications neglect any additional effect caused by the nonlinear response of the soil, buildings, and the permanent residual tilting of the buildings.

- Additionally, it should be noted that this event #45 had a magnitude of only M_L=7.0 and the centre of the SMART-1 array was located at a distance of 79km from the epicentre. Therefore, the array was not in the near-field zone of this earthquake. So, it is expected that for more significant near-field earthquakes, the effect of the rotational ground motion in the structural responses should increase.

- Results also indicated that these amplifications do not depend greatly on (i) the aspect ratio $s = h/b$ of the buildings or on (ii) the soil type (medium, dense and very dense sand, Table 7-1) considered in this study.

- In this study, a set of rotational-horizontal ground accelerograms that produced the largest amplification in the structure was required. So, it was found that the relevance of the rotational ground motion in the structure's response depends principally on the relative importance of the rotational to the horizontal ground motion amplitude. That is, the ratio of Peak Ground Rotational Acceleration (*PRGA*) to Peak Horizontal Ground Acceleration (*PHGA*), or ratio *PRGA/PHGA*. The limitations of employing this ratio is that it is necessary to estimate the rotational ground motion first and this is not straightforward. Evidence from the SMART-1 array suggests that the correlation between *PVGA/PHGA* (peak vertical to horizontal ground motion ratio) and *PRGA/PHGA* is not strong. Hence, it is not recommend employing *PVGA/PHGA* as a proxy for *PRGA/PHGA*.

- Counterintuitively, it was found that the effects of the rotational ground motion in the structure's response do not always increase when the period of the structure is increased. For the event #39, the critical height that produces the biggest amplifications in the building's response is for a period equal to 0.5s. Instead, for the event #45, the critical period varies between 1.2s and 1.4s. This highlights the complexity of the problem and the importance of the frequency/phase content of the rotational and horizontal ground accelerations.

- All the results found in this study highlight the importance of the rotational component that accompanies the translational ground motion and that they should be recorded during future

earthquakes. Given that this study is based on a single site and only a few events, the potential 35% error bound in structural responses, when neglecting rotational ground motions, should be viewed as a non-conservative estimate.

7.6 Nomenclature

The units correspond to those defined by the International System of Units, where the abbreviations represent [M] mass, [T] time, [L] length and [rad] radians.

α	Ratio of soil/foundation to building mass of the building []
η	Height to the radius of gyration ratio for the building []
$\varepsilon_{zi}, \varepsilon_{\theta i}$	Mean relative error in vertical acceleration and in slope, respectively []
θ_s	Rotational degrees of freedom at the base of the building []
θ_g	Rotational ground time series []
$\ddot{\theta}_g$	Rotational ground acceleration time series [T^{-2}]
$\ddot{\theta}_{gx}$	Rotational ground acceleration – North-South direction [T^{-2}]
$\ddot{\theta}_{gy}$	Rotational ground acceleration – East-West direction [T^{-2}]
$\hat{\theta}_i$	Estimated (interpolated) rotational acceleration [LT^{-2}]
λ	Predominant Rayleigh wavelength of the SMART-1 site []
$\boldsymbol{\lambda}(\omega)$	Ratio of rotational ground motion to maximum horizontal ground motion induced responses []
μ_s	Poison's ratio of the soil []
ξ_n	Ratio of critical damping of the system []
ρ_b, ρ_s	Average densities of the building and the soil respectively [ML^{-3}]
$\boldsymbol{\phi}_n$	Modal eigenvector of the linear system []
χ_1	Change in disp. power between Including Ground Rotation and Neglecting Ground Rotation [%]
$\ddot{\chi}_1$	Change in accel. power between Including Ground Rotation and Neglecting Ground Rotation [%]
ω_b	Circular frequency parameter for the building [$radT^{-1}$]
ω_{rb}	Modal circular frequency (on a rigid base) for the building [$radT^{-1}$]
ω_s	Circular frequency of soil/foundation (horizontal mode) for the building [$radT^{-1}$]
ω_θ	Circular frequency of soil/foundation (rocking mode) for the building [$radT^{-1}$]
ω	Fourier frequency [$radT^{-1}$]
ω_n	Natural frequencies of the linear system [$radT^{-1}$]
Ω_s	Ratio of horizontal soil/foundation frequency to building frequency parameter []
Ω_θ	Ratio of rocking soil/foundation frequency to building frequency parameter []
A_1	Total acceleration on top of the building []
A_{z1}	Amplitude of vertical ground acceleration [LT^{-2}]
$\hat{A}_{zi}$	Estimated amplitude of vertical ground acceleration [LT^{-2}]
$A_{\theta 1}$	Amplitude of rotational ground acceleration (slope) [LT^{-2}]
$\hat{A}_{\theta i}$	Estimated amplitude of rotational ground acceleration (slope) [LT^{-2}]

a_0	Non-dimensional frequency parameter []
b	Foundation' width [L]
$\boldsymbol{C}$	Damping matrix of the linear system []
c_1	Density ratio (soil/building) parametric constant []
E_s	Total power spectral density []
f	Excitation frequency [Hz]
G_s	Shear modulus of the soil [M $L^{-1}T^{-2}$]
h	Total height of the building [L]
$\mathbf{H}(\omega)$	Frequency dependent matrix []
$\mathbf{K}$	Non-dimensional stiffness matrix of the system []
$\widehat{\mathbf{K}}$	Dimensional stiffness matrix of the system [MT^{-2}]
k_b	Lateral horizontal stiffness of the building [MT^{-2}]
k_s	Lateral horizontal stiffness of the soil/foundation [MT^{-2}]
k_θ	Rotational stiffness of the soil/foundation [ML^2T^{-2}]
$\mathbf{M}$	Non-dimensional mass matrix of the system []
$\widehat{\mathbf{M}}$	Dimensional mass matrix of the system [M]
M_L	Local magnitude of the earthquake
m_b	Total mass of the building [M]
m_s	Soil/foundation mass underneath the building [M]
n_s	Number of storeys of the building []
$\mathbf{p_1}$	Non-dimensional horizontal force vector of the system []
$\widehat{\mathbf{p}}_\mathbf{1}$	Dimensional horizontal force vector of the system [M]
$\mathbf{p_2}$	Non-dimensional rotational force vector of the system []
$\widehat{\mathbf{p}}_\mathbf{2}$	Dimensional rotational force vector of the system [ML]
PGA	Peak ground acceleration [LT^{-2}]
$PRGA$	Peak rotational ground acceleration [T^{-2}]
$PRGA_x$	Peak rotational ground acceleration – North-South direction [T^{-2}]
$PRGA_y$	Peak rotational ground acceleration – East-West direction [T^{-2}]
$PVGA$	Peak vertical ground acceleration [LT^{-2}]
$PHGA_x$	Peak horizontal ground acceleration– East-West direction [LT^{-2}]
$PRGA_y$	Peak horizontal ground acceleration – North-South direction [LT^{-2}]
r	Soil/foundation mass radius of gyration for the building [L]
s	Aspect ratio. Height to width ratio of the building []
T_E	System kinematic energy [ML^2T^{-2}]
T_x	Period of the structure on a rigid foundation [T]

t	Time [T]
U_1	Displacement on top of the building []
U_E	System potential energy [ML^2T^{-2}]
u_1, u_2	Non-dimensional horizontal displacement of the building relative to the ground []
u_s	Non-dimensional horizontal displacement for the foundation mass []
u_g	Non-dimensional horizontal ground displacement time series []
$\ddot{u}_g$	Non-dimensional acceleration ground motion []
$\mathbf{u}$	Non-dimensional degrees of freedom (vector) of the system []
v_f	Site average surface Rayleigh wave velocity [LT^{-1}]
V_s	Shear wave velocity of the soil [LT^{-1}]
x_1, x_2	Horizontal displacements (degrees of freedom) of the building relative to the ground [L]
$\mathbf{x}$	Non-dimensional degrees of freedom (vector) of the system [L]
x_s	Horizontal degree of freedom for the foundation mass [L]
x_g	Horizontal ground displacement time series [L]
$\ddot{x}_g$	Horizontal acceleration ground motion – East-West component [LT^{-2}]
$\ddot{y}_g$	Horizontal acceleration ground motion – North-South component [LT^{-2}]
$\hat{z}_i$	Estimated (interpolated) vertical acceleration [LT^{-2}]
$\ddot{z}_g$	Vertical acceleration ground motion [LT^{-2}]

Chapter 8

Conclusions and future research

8.1 Overview

Conventionally, buildings in urban areas have been seismically designed through conceptualising the response of structures as being stand-alone, i.e. independent from its neighbours. Nevertheless, population growth and the limited available urban space in large cities inevitably result in closer spatial proximity of buildings. Therefore, the high density of structures entails the possibility of seismic interaction of adjacent buildings through the underlying soil. This phenomenon is widely known as Structure-Soil-Structure Interaction (SSSI) and is one of the foremost challenges structural engineers are facing.

This dissertation focussed on expanding the knowledge of the SSSI by performing time-history seismic simulations using different linear and nonlinear reduced-order models. The influence of different parameters of the structures, inter-building spacing and soil type on the seismic response was evaluated. The advantages of these low-order models are that they define the problem in terms of a small number of degrees of freedom and system parameters, so they are computationally efficient for an extensive parametric exploration of this complex problem. The large scope of these analysis made use of the High-Performance Computing (HPC) machine BlueCrystal, belonging to the Advanced Computing Research Centre at the University of Bristol.

Chapter 3 discussed the SSSI between a low-rise building adjacent to a neighbouring much taller building using a 2D linear reduced-order model. Three types of ground motion were considered (Far-Field, Near-Field Without Pulse and Near-Field Pulse-Like record sets). Three million system/ground motion cases were analysed.

Chapter 4 explored the SSSI between a pair of buildings by employing a 2D linear reduced-order model, where one of the buildings is unsymmetrical in plan and hence subject to seismically induced coupled torsion/sway motions. Four million system/ground motion cases were analysed.

In Chapter 5, the problem of soil nonlinearity has been integrated to the 2D reduced-order model by employing the phenomenological Bouc-Wen model approach for the soil directly underneath the foundations. The soil between buildings is modelled as a perfectly elastoplastic material, i.e. linear rotational interaction springs between the buildings are assumed. The ground motion time series used is compatible with the Eurocode 8 elastic spectra. Thirty thousand different nonlinear systems are explored.

Chapter 6 presented a theoretical formulation for the evaluation of SSSI between several buildings in a three-dimensional arrangement that is coupled through the soil. The buildings can have different sizes, properties, and inter-building spacing. This conceptual model reduces the number of DOFs from hundreds of millions in a conventional full 3D FEA to 4*n* (where *n* is the number of buildings). Thus, city-site and city block seismic time-history analyses are far more tractable. In addition, a novel approach is introduced for estimating the auto-rotational and inter-rotational soil/foundations spring stiffnesses that makes use of least-square inverse system identification based on an FEA calibrated empirical relationship between applied surficial moments and rotations.

Lastly, Chapter 7 presented a reduced-order model to evaluate the effects of the rotational ground motions upon structures. A multi-station interpolation procedure has been employed to estimate the rotational ground motion. Accelerogram data from the SMART-1 dense accelerometer array in Taiwan were used. There are of the order of 1.6 million of different full time-histories analyses in this research, with a set of more than 5000 different horizontal-rotational ground motion time-histories employed.

8.2 Conclusions

The research presented in this dissertation leads us to the following key findings and conclusions,

- As a general trend, the linear SSSI models presented in this thesis showed that the interaction effects for building 1 are (i) unfavourable when building 2 is taller, and (ii) beneficial when building 2 is shorter. This behaviour happens regardless of the type of earthquake event (Far-Field, Near-Field Without Pulse and Near-Field Pulse-Like records sets). Also, both adverse and beneficial interaction effects diminish as (i) building spacing increases, and as (ii) the soil stiffness increases (i.e. from loose to dense soil).

- The extended linear model presented in Chapter 3 showed that when there is a large difference in height between the adjacent buildings ($\varepsilon = h_2/h_1 > 2.0$), the taller building imposes a low-frequency ‘rigid body rocking mode’ on the smaller building producing an important increase in

the displacement response (reaching values up to $\chi_1 = 400\%$). Also, this model captures the interaction between the second sway mode of a much taller building with the first sway mode of a shorter building. This produces additional coupled effects, where these interactions are less relevant for higher modes. For the acceleration responses, the greatest amplifications are observed for height ratio approximately of $\varepsilon = 1.1$, with a value of $\ddot{\chi}_1 = 120\%$.

- Chapter 4 highlighted that the significance of the SSSI effects on unsymmetrical buildings was captured for a broad range of frequency ratios Ω_b varying between 0.6 and 2.0, i.e. the power of the earthquake could be passed from the shorter structure to the taller torsionally irregular structure. This amplification in building 1's response corresponds to the interaction between the first torsional/sway mode of building 1 with the first sway mode of building 2. Furthermore, the SSSI does not depend greatly on the torsional frequency ratio Ω_θ.

- The nonlinear analysis showed that the SSSI could generate more significant beneficial and adverse seismic effects when it is compared with a pure linear SSSI analysis. Therefore, this emphasizes the importance of including the nonlinear soil model in the SSSI analysis. Furthermore, just as in linear analysis, (i) the SSSI effects are negligible for well-spaced buildings (i.e. around two times the building base width) and (ii) their influence diminishes as the soil stiffness increases.

- The nonlinear analysis revealed that there is mainly an increase in the seismic response for building 1 when it is flanked by a taller building 2. The amplifications reach values up to $\chi_1 = 450\%$ and $\ddot{\chi}_1 = 110\%$ change in response power for the displacement and acceleration, respectively. Also, there is evidence that after the earthquake ends, significant residual rotations of building 1 considering the SSSI effects are observed. This effect cannot be quantified with traditional linear elastic models.

- The method presented in Chapter 6 to calculate the auto-rotational and inter-rotational soil spring stiffness coefficients showed excellent agreement with previous FEA 2D and experimental data in the literature. Also, the reduced-order model proposed has only $4n$ DOFs (where n is the number of buildings) rather than perhaps hundreds of millions of DOFs for a full 3D FE analysis of simple buildings and their underlying elastic half-space. Therefore, using this procedure does not require any full 3D FE analysis (unless inelastic effects are important), which substantially reduces the computational cost and run time.

- The analysis presented in Chapter 7 indicated that the rotational ground motion can significantly affect the response of structures, reaching an increase on the displacement and acceleration response of up to 35%, for the events recorded in the SMART-1 array. These amplifications do not depend greatly on (i) the aspect ratio $s = h/b$ of the buildings or on (ii) the soil type. The

importance of the rotational ground motion in the structure's response depends principally on the relative importance of the rotational to the horizontal ground motion amplitude. That is, the ratio of Peak Ground Rotational Acceleration (*PRGA*) to Peak Horizontal Ground Acceleration (*PHGA*). Here it is not possible to recommend employing the peak vertical to horizontal ground motion ratio *PVGA/PHGA* as a proxy for the ratio *PRGA/PHGA*.

8.3 Recommendations for Future Research

The accomplishments made in this research open a variety of topics that have yet to be explored fully. Some of the most relevant ones are highlighted as follows,

- Limited work has been performed on investigating the seismic response of multiple structures considering the nonlinear behaviour on both the soil profile and the buildings. Besides, it is important to compare how it differs with the linear analysis. Therefore, it is necessary to develop efficient reduced-order mathematical formulations to perform an extensive parametric exploration of this problem.

- To extend the 3D reduced-order model presented in Chapter 6 in order to include the wave passage effects, time delay and spatially heterogeneous ground displacement. These effects could be relevant when a large group of structures are considered, i.e. site-city interaction or city effects. Furthermore, it is necessary to evaluate the effects in the direction of the alignment between the structures and quantify the interaction considering the off-plane modes.

- More work is needed to understand the dynamic interaction between multiple buildings using reduced-order models, including not only the inter-rotational soil spring stiffness coefficients but also the inter-rotational mass matrix. Note that the distributed (generalised) mass matrix for the soil with off-diagonal terms has yet to be conceptualised.

- To evaluate the kinematic effects on the SSSI, which are important for deep foundations and pile foundations. Also, to develop new models to analyse these effects in 3D.

- To perform physical experiment tests, both shake table and centrifuge tests, to calibrate the 3D reduced-order models. These experimental tests are essential as validation points. Additionally, further work in the experimental field would generate valuable insight into the limitation of the reduced-order models as a research tool for complex structures.

- To produce a set of recommendations, from a structural seismic design point of view, that would allow to include the considerations of the SSSI in a practical way into the design.

References and Bibliography

Abrahamson, N.A., Bolt, B.A., Darragh, R.B., Penzien, J., and Tsai, Y.B. (1987). The SMART I accelerograph Array (1980–1987): a review. *Earthquake Spectra,* 3(2), 263-287.

Alamo, G., Padron, L.A., Aznares, J.J., and Maeso, O. (2015). Structure-soil-structure interaction effects on the dynamic response of piled structures under obliquely incident seismic shear waves. *Soil Dynamics and Earthquake Engineering,* 78, 142-153.

Aldaikh, H., Alexander, NA., Ibraim, E., and Oddbjornsson, O. (2015). Two dimensional numerical and experimental models for the study of structure-soil-structure interaction involving three buildings. *Computers & Structures,* 150, 79-91.

Aldaikh, H., Alexander, N.A., Ibraim, E., and Knappett, J. (2016). Shake table testing of the dynamic interaction between two and three adjacent buildings (SSSI). *Soil Dynamics and Earthquake Engineering,* 89, 219-232.

Aldaikh, H., Alexander, NA., Ibraim, E., and Knappett, J. (2018). Evaluation of rocking and coupling rotational stiffness coefficient of adjacent foundations. *International Journal of Geomechanics,* 18(1), 04017131.

Alexander, N.A. (2008). Multi-support excitation of single span bridges, using real seismic ground motion recorded at the smart-1 array. *Computers & Structures,* 86, 88-103.

Alexander, NA., Ibraim, E., and Aldaikh, H. (2013). A simple discrete model for interaction of adjacent buildings during earthquakes. *Computers & Structures,* 124, 1-10.

Alexander, NA., Chanerley, AA., Crewe, AJ., and Bhattacharya, S. (2014). Obtaining spectrum matching time series using a reweighted volterra series algorithm (RVSA). *Bulletin of the Seismological Society of America,* 104(4), 1663-1673.

Anand, V., and Kumar, S.R. (2018). Seismic Soil-structure Interaction: A State-of-the-Art Review. *Structures,* 16, 317-326.

ASCE/SEI 7. (2005). Minimum Design Loads for Buildings and Other Structures. American Society of Civil Engineers.

ATC-3, Applied Technoogy Council. (1984). Tentative Provisions for the Development of Seismic Regulations for Builsings. National Science Foundation and National Bureau of Standards, Washington, DC. 2nd edition.

Austrell, P.E., Dahlblom, O., Lindemann, J., Olsson, A., Olsson, K.G., Persson, K., Petersson, H., Ristinmaa, M., Sandberg, G., and Wernberg, P.A. (2004). CALFEM. A finite element toolbox to MATLAB (Version 3.4). Lund University, Division of Structural Mechanics and Division of Solid Mechanic.

Aydinoglu, M.N., and Cakiroglu, A. (1977). Dynamic interaction between soil and a group of buildings. *In: Presented at the 6th World Conference on Earthquake Engineering*. New Dehli, India.

Baber, T.T., and Noori, M.N. (1986). Modelling general hysteresis behaviour and random vibration application. *ASME Journal of Vibration, Acoustics, Stress, and Reliability in Design,* 108, 411-420.

Baber, TT., and Wen, YK. (1981). Random vibration of hysteretic degrading systems. *Journal of the Engineering Mechanics,* 107, 1069-1087.

Baker, J.W. (2015). Quantitative classification of near-fault ground motions using wavelet analysis. *Bulletin of the Seismological Society of America,* 31, 1486-1501.

Basu, D., Whittaker, A.S., and Constantinou, M.C. (2012). Estimating rotational components of ground motion using data recorded at a single station. *Journal of the Engineering Mechanics,* 138(9), 1141-1156.

Basu, D., Whittaker, AS., and Constantinou, MC. (2013). Extracting rotational components of earthquake ground motion using data recorded at multiple stations. *Earthquake Engineering and Structural Dynamics,* 42(3), 451-468.

Basu, D., Whittaker, AS., and Constantinou, MC. (2015). Characterizing rotational components of earthquake ground motion using a surface distribution method and response of sample structures. *Engineering Structures,* 99, 685-707.

Behnamfar, F., and Sugimura, Y. (1999). Dynamic response of adjacent structures under spatially variable seismic waves. *Probabilistic Engineering Mechanics,* 14, 33-44.

Betti, R. (1997). Effects of the dynamic cross-interaction in the seismic analysis of multiple embedded foundations. *Earthquake Engineering and Structural Dynamics,* 26, 1005-1019.

Botisetti, C., and Whittaker, A. (2015). Structure-Soil-Structure interaction. *Transaction, SMiRT-23*. Manchester, UK.

Bouc, R. (1967). Forced Vibration of Mechanical Systems With Hysteresis. *In: Presented at the 4th Conference on Nonlinear Oscillations*. Prague, Czechoslovakia.

Boutin, C., and Roussillon, P. (2004). Assessment of the Urbanization Effect on Seismic Response. *Bulletin of the Seismological Society of America,* 94(1), 251-268.

Boutin, C., Hans, S., Ibraim, E., and Rousillon, P. (2005). In situ experiments and seismic analysis of existing buildings. Part II: Seismic integrity threshold. *Earthquake Engineering and Structural Dynamics,* 34(12), 1531-1546.

Bowles, J.E. (1997). *Foundation analysis and design.* (5th ed.). The McGraw-Hill Companies, Inc. New York, USA.

Brigham, E.O. (1988). *The Fast Fourier Transform* (1st ed.). Englewood Cliffs, N.J. USA.: Prentice-Hall, Inc.

Cacciola, P., Espinosa, M.G., and Tombari, A. (2015). Vibration control of piled-structures through structure-soil-structure-interaction. *Soil Dynamics and Earthquake Engineering,* 77, 47-57.

Castellani, A., and Boffi, G. (1996). Rotational components of the surface ground motion during and earthquake. *Earthquake Engineering and Structural Dynamics,* 14, 751-767.

Castellani, A., Stupazzini, M., and Guidotti, R. (2012). Free-field rotations during earthquakes: relevance on buildings. *Earthquake Engineering and Structural Dynamics,* 41, 875-891.

Castellani, A. (2017). Array-derived rotational seismic motions: revisited. *Bulletin of Earthquake Engineering,* 15, 813-825.

Celebi, M. (1993a). Seismic responses of two adjacent buildings. I: Data and analysis. *Journal of Structural Engineering,* 119, 2461-2476.

Celebi, M. (1993b). Seismic responses of two adjacent buildings. II: interaction. *Journal of Structural Engineering*, 119, 2477-2492.

Channerly, A.A., and Alexander, N.A. (2007). Correcting data from an unknown accelerometer using recursive least squares and wavelet de-noising. *Computers & Structures*, 85, 1679-1692.

Chatfield, C. (2003). *The analysis of time Series: an introduction* (6ed ed.). London, UK.: Chapman and Hall/CRC.

Chavez-Garcia, F., and Cardenas-Soto, M. (2002). The contribution of the built environment to the "free-field" ground motion in Mexico City. *Soil Dynamics and Earthquake Engineering*, 22, 773-780.

Chayamghamian, M.R., and Nouri, G.R. (2007). On the characteristics of ground motion rotational components using Chiba dense array data. *Earthquake Engineering and Structural Dynamics*, 36, 1407-1429.

Chopra, A.K. (2000). *Dynamics of structures: Theory and applications to earthquake engineering* (2nd ed.). Englewood Cliffs, N.J. USA.: Prentice-Hall, Inc

Clough, R.W., and Penzien, J. (1993). *Dynamics of structures* (2nd ed.). New York, USA McGrawHill.

Clouteau, D., and Aubry, D. (2001). Modifications of the ground motion in dense urban areas. *Journal of Computational Acoustics*, 9(4), 1659-1675.

Clouteau, D., Broc, D., Devesa, G., Guyonvarh, V., and Massin, P. . (2012). Calculation methods of structure–soil–structure interaction (3SI) for embedded buildings application to NUPEC tests. *Soil Dynamics and Earthquake Engineering*, 32, 129-142.

Cremer, C., Pecker, A., and Davenne, L. (2001). Cyclic macro-element for soil-structure interaction: material and geometrical nonlinearities. *International Journal for Numerical and Analytical Methods in Geomechanics*, 25(13), 1257-1284.

Cremer, C., Pecker, A., and Davenne, L. (2002). Modelling of nonlinear dynamic behaviour of a shallow strip foundation with macroelement. *Journal of Earthquake Engineering*, 6(2), 175-211.

Crowley, H., and Pinho, R. (2010). Revisiting eurocode 8 formulae for periods of vibration and their employment in linear seismic analysis. *Earthquake Engineering and Structural Dynamics*, 39, 223-235.

Cucci, L., and Tertulliani, A. (2011). Clues for a relation between rotational effects induced by the 2009 Mw 6.3 L′Aquila (Central Italy) earthquake and site and source effects. *Bulletin of the Seismological Society of America*, 101, 1109-1120.

Cucci, L., and Tertulliani, A. (2013). The earthquake-rotated objects induced by the 2012 Emilia (Northern Italy) seismic sequence: relation with seismological and geomorphological factors. *Seismological Research Letters*, 84, 973-981.

De la Llera, J.C., and Chopra, A.K. (1995a). A simplified model for analysis and design of asymmetric-plan buildings. *Earthquake Engineering and Structural Dynamics*, 24, 573-594.

De la Llera, J.C., and Chopra, A.K. (1995b). Estimation of accidental torsion effects for seismic design of buildings. *Journal of Structural Engineering*, 121(1), 102-114.

De Stefano, M., and Pintucchi, B. (2002). A review of research on seismic behaviour of irregular building structure since 2002. *Bulletin of Earthquake Engineering*, 6(2), 285-308.

Drosos, V., Gerolymos, N., and Gazetas, G. (2012). Constitutive model for soil amplification of ground shaking: parameter calibration, comparisons, validation. *Soil Dynamics and Earthquake Engineering,* 42, 255-274.

Elnashai, A.S., Gencturk, B., Kwon, O.S., Al-Qadi, I.L., Hashash, Y., Roesler, J.R., Kim, S.J., Jeong, S.H., Dukes, J., and Valdivia, A. (2010). The Maule (Chile) Earthquake of February 27, 2010: Consequence Assessment and Case Studies. University of Illinois at Urbana-Champaign.

EUR 23563 EN-2008. (2008). European commission EUR 23563 EN-2008. A review of the seismic hazard zonation in national building codes in the context of Eurocode 8. European Committee for Standardization.

Eurocode 8 EN-1998. (2004). Design of structures for earthquake resistance - Part 1: General rules, seismic actions and rules for buildings. European Committee for Standardization.

Eurocode 8 EN-1998. (2005). Design of structures for earthquake resistance - Part 6: Towers, mast and chimneys European Committee for Standardization.

Falamarz-Sheikhabadi, M. (2014). Simplified relations for the application of rotational components to seismic design codes. *Engineering Structures,* 59, 141-152.

FEMA P695. (2009). Quantification of Building Seismic Performance Factors. Federal Emergency Management Agency.

Gajan, S., Thomas, J.M., and Kutter, B.L. (2005). Physical and analytical modelling of cyclic load deformation behaviour of shallow foundations. *In: Presented at the 57th annual meeting of earthquake engineering research institute*. Ixtapa, Mexico.

Gazetas, G. (1983). Analysis of machine foundation vibrations: state of the art. *Soil Dynamics and Earthquake Engineering,* 2(1), 2-42.

Ge, Q., Xiong, F., Xie, L., Chen, J., and Yu, M. (2019a). Dynamic interaction of soil – Structure cluster. *Soil Dynamics and Earthquake Engineering,* 123, 16-30.

Ge, Q., Xiong, F., Xie, L., Chen, J., and Yu, M. (2019b). Effects of soil–structure cluster interactions on ground motions. *The Structural Design of Tall and Special Buildings,* 1, e1675.

Gerolymos, N., and Gazetas, G. (2005). Constitutive model 1-D cyclic soil behaviour applied to analysis of layered deposit. *Soils and Foundations,* 45(3), 147-159.

Gerolymos, N., and Gazetas, G. (2007). A model for grain-crushing-induced landslides – application to Nikawa, Kobe 1995. *Soil Dynamics and Earthquake Engineering,* 27, 803-817.

Ghandil, M., Behnamfar, F., and Vafaeian, M. (2016). Dynamic responses of structure-soil-structure systems with an extension of the equivalent linear soil modeling. *Soil Dynamics and Earthquake Engineering,* 80, 149-162.

Ghergu, M., and Ionescu, I.R. (2009). Structure-soil-structure coupling in seismic excitation and "city effect" *International Journal of Engineering Science,* 47, 342-354.

Gueguen, P., Bard, P-Y., and Oliveira, C. (2000). Experimental and Numerical Analysis of Soil Motions Caused by Free Vibrations of a Building Model. *Bulletin of the Seismological Society of America,* 90(6), 1464-1479.

Gueguen, P., Bard, P-Y., and Chavez-Garcia, F.J. (2002). Site-City Seismic Interaction in Mexico City-Like Environments: An Analytical Study. *Bulletin of the Seismological Society of America,* 92(2), 794-811.

Gueguen, P., and Colombi, A. (2016). Experimental and Numerical evidence of the clustering effect of structures on their response during an earthquake: A case study of three identical towers in the city of Grenoble, France. *Bulletin of the Seismological Society of America,* 106(6), 2855-2864.

Gupta, D., and Trifunac, M.D. (1988). A note on computing the contribution of rocking excitation to earthquake response of simple buildings. *Bulletin of the Indian Society of Earthquake Technology,* 25, 73-89.

Gupta, D., and Trifunac, M.D. (1990). Response of multistoried buildings to ground translation and rocking during earthquakes. *Probabilistic Engineering Mechanics,* 5(3), 138-145.

Gupta, D., and Trifunac, M.D. (1991). Effects of ground rocking on dynamic response of multistoried buildings during earthquakes. *Structural Engineering Japan Society of Civil Engineering,* 8(2), 87-94.

Han, B., Chen, S., and Liang, J. (2020). 2D dynamic structure-soil-structure interaction: A case study of Millikan Library Building. *Engineering Analysis with Boundary Elements,* 113, 346-358.

Hans, S., Boutin, C., Ibraim, E., and Rousillon, P. (2005). In situ experiments and seismic analysis of existing buildings. Part I: Experimental investigations. *Earthquake Engineering and Structural Dynamics,* 34(12), 1513-1529.

Hardin, B., and Drnevich, V. . (1972). Shear modulus and damping in soils. Design equations and curves. *Journal of Journal of Soil Mechanics & Foundations Div, Proceedings of ASCE,* 98, 667-692.

Hejal, R., and Chopra, A.K. (1989). Earthquake response of torsionally-coupled frame buildings. *Journal of Structural Engineering,* 115, 834-851.

Hirotani, T., Yoshida, K., Tamosi, S., Yosida, N., and Suzuki, A. (2001). Model test on dynamic cross interaction of adjacent buildings in nuclear power plants - Laboratory test. *In: Transactions of the SMiRT-16*. Washington DC, USA.

Huang, B.S. (2003). Ground rotational motions of the 1999 Chi-Chi, Taiwan earthquake as inferred from dense array observations. *Geophysical Research Letters,* 30(6), 1307-1310.

Imamura, A., Watanabe, T., Ishizaki, M., and M., Motosaka. (1992). Seismic response characteristics of embedded structures considering cross interaction. *In: Presented at the 10th World Conference on Earthquake Engineering*. Madrid, Spain.

Isbiliroglu, Y., Taborda, R., and Bielak, J. (2015). Coupled Soil-Structure Interaction effects of buildings clusters during earthquakes. *Earthquake Spectra,* 31(1), 463-500.

Ishibashi, I., and Zhang, X. (1993). Unified dynamic shear moduli and damping ratio of sand and clay. *Soils and Foundations,* 33, 182-191.

Ismail, M., Ikhouane, F., and Rodellar, J. (2009). The hysteresis Bouc-Wen model, a survey. *Archives of Computational Methods in Engineering,* 16, 161-188.

Jabary, R.N., and Madabhushi, S.P.G. (2017). Structure-soil-structure interaction effects on structures retrofitted with tuned mass dampers. *Soil Dynamics and Earthquake Engineering,* 100, 301-315.

Jalali, R.S., and Trifunac, M.D. (2009). Response spectra for near-source, differential, and rotational strong motion. *Bulletin of the Seismological Society of America,* 99(2B), 1404-1415.

Jalali, R.S., and Trifunac, M.D. (2011). A note on the wave-passage effects in out-of-plane response of long structures to strong earthquake pulses *Soil Dynamics and Earthquake Engineering,* 31, 640-647.

Jalali, R.S., Azgomi, M.N., and Trifunac, M.D. (2013). In-plane response of two-story structures to near-fault ground motion. *Soil Dynamics and Earthquake Engineering,* 55, 263-274.

Kalkan, E., and Graizer, V. (2007). Coupled tilt and translational ground motion response spectra. *Journal of Structural Engineering,* 133, 609-619.

Kausel, E. (2010). Early history of soil–structure interaction. *Soil Dynamics and Earthquake Engineering,* 30, 822-832.

Kham, M., Semblat, J.F., Bard, P-Y., and Dangla, P. (2006). Seismic Site-City Interaction: Main Governing Phenomena through Simplified Numerical Models. *Bulletin of the Seismological Society of America,* 96(5), 1934-1951.

Kirkwood, P., and Dashti, S. (2018). A Centrifuge Study of Seismic Structure-Soil-Structure Interaction on Liquefiable Ground and Implications for Design in Dense Urban Areas. *Earthquake Spectra,* 34(3), 1113-1134.

Kitada, Y., Hirotani, T., and Iguch, M. (1999). Models test on dynamic structure–structure interaction of nuclear power plant buildings. *Nuclear Engineering and Design,* 192, 205-216.

Kitada, Y., Iguchi, M., Fukuwa, N., Kusakabe, K., Nishikawa, T., and Shinozaki, Y. (2001). Model test on dynamic cross interaction of adjacent buildings in nuclear power plants - Overview and outline of earthquake observation in the field test. *In: Transactions of the SMiRT-16*. Washington DC, USA.

Knappett, J., Massen, P., and Caucis, K. (2015). Seismic structure-soil-structure interaction between pairs of adjacent building structures. *Geotechnique,* 65(5), 429-441.

Kobori, T., Minai, R., and Kusakabe, K. (1973). Dynamical characteristics of soil-structure cross-interaction system. *Bulletin of the Disaster Prevention Research Institute,* 22.

Kobori, T., Minai, R., and Kusakabe, K. (1977). Dynamical cross-interaction between two foundations. *In: Presented at the 6th World Conference on Earthquake Engineering*. New Delhi, India.

Kobori, T., and Kusakabe, K. (1980). Cross-interaction between two embedded structures in earthquakes. *In: Presented at the 7th World conference on Earthquake Engineering*. Istanbul, Turkey.

Kozak, J.T. (2009). Tutorial on earthquake rotational effects: historical examples. *Bulletin of the Seismological Society of America,* 99, 998-1010.

Kramer, S.L. (1996). *Geotechnical Earthquake Engineering* (1st ed.). Englewood Cliffs, N.J. USA.: Prentice-Hall Civil Engineering & Engineering Mechanics Series.

Kuzama, K., Kitada, Y., Iguchi, M., Fukuwa, N., and Nishikawa, T. (2003). Model test on dynamic cross interaction of adjacent buildings in nuclear power plants - Overview and outcomes of the project. *In: Transactions of the SMiRT-17*. Prage, Czech Republic.

Laurenzano, G., Priolo, E., Gallipoli, M.R., Mucciarelli, M., and Ponzo, F.C. (2010). Effect of Vibrating Buildings on Free-Field Motion and on Adjacent Structures: The Bonefro (Italy) Case History. *Bulletin of the Seismological Society of America,* 100, 802-818.

Lee, T.H., and Wesley, D.A. (1973). Soil-structure interaction of nuclear reactor structures considering through-soil coupling between adjacent structures. *Nuclear Engineering and Design,* 24(3), 374-387.

Lee, V.W., and Trifunac, M.D. (1987). Rocking strong earthquake accelerations. *Soil Dynamics and Earthquake Engineering,* 6, 75-89.

Lee, V.W., and Trifunac, M.D. (2009). Empirical scaling of rotational spectra of strong earthquake ground motion. *Bulletin of the Seismological Society of America,* 99(2B), 1378-1390.

Lehmann, L., and Antes, H. (2001). Dynamic structure–soil–structure interaction applying the Symmetric Galerkin Boundary Element Method (SGBEM). *Mechanics Research Communications,* 28, 297-304.

Li, H.N., Sun, L.Y., and Wang, S.Y. (2004). Improved approach for obtaining rotational components of seismic motion. *Nuclear Engineering and Design,* 232, 131-137.

Li, P., Liu, S., Lu, Z., and Yang, J. (2017). Numerical analysis of a shaking table test on dynamic structure-soil-structure interaction under earthquake excitation. *The Structural Design of Tall and Special Buildings,* 26, 1-13.

Li, P.Z., Hou, X.Y., Liu, Y.M., and Lu, X.L. (2012). Shaking table model tests on dynamic structure-soil-structure interaction during various excitations. *In: Presented at the 15th World Conference on Earthquake Engineering*. Lisbon, Portugal.

Li, Y., Zhao, M., Xu, Ch.S., Du, X.L., and Li, Z. (2018). Earthquake input for finite element analysis of soil-structure interaction on rigid bedrock. *Tunnelling and Uncerground Space Technology*, 79, 250-262.

Liang, J., Han, B., Todorovska, M.I., and Trifunac, M.D. (2017). 2D dynamic structure-soil-structure interaction for twin buildings in layered half-space I: Incident SH-waves. *Soil Dynamics and Earthquake Engineering,* 102, 172-194.

Liang, J., Han, B., Todorovska, M.I., and Trifunac, M.D. (2018). 2D dynamic structure-soil-structure interaction for twin buildings in layered half-space II: Incident SV-waves. *Soil Dynamics and Earthquake Engineering,* 113, 356-390.

Lin, H.T., Roesset, J.M., and J.L., Tassoulas. (1987). Dynamic interaction between adjacent foundations. *Earthquake Engineering and Structural Dynamics,* 15, 323-343.

Liu, C., Huang, B., and Lee, W.H.K. (2009). Observing rotational and translational ground motions at the HGSD station in Taiwan from 2007 to 2008. *Bulletin of the Seismological Society of America,* 99, 1228-1236.

Loh, C.H. (1985). Analysis of the spatial variation of seismic waves and ground movements from SMART-1 array data. *Earthquake Engineering and Structural Dynamics,* 13, 561-581.

Lu, X., Tian, Y., Wang, G., and Huang, D. (2018). A numerical coupling scheme for nonlinear time history analysis of buildings on a regional scale considering site-city interaction effects. *Earthquake Engineering and Structural Dynamics,* 47, 2708-2725.

Lu, Y., Li, B., Xiong, F., Ge, Q., Zhao, P., and Liu, Y. (2020). Simple discrete models for dynamic structure-soil-structure interaction analysis. *Engineering Structures,* 206(110188).

Luco, J.E., and Westmann, RA. (1972). Dynamic Response of a rigid footing bonded to an elastic half space. *Journal of Applied Mechanics,* 39(2), 527-534.

Luco, J.E., and Contesse, L. (1973). Dynamic structure-soil-structure interaction. *Bulletin of the Seismological Society of America,* 63, 1289-1303.

Ma, F., Zhang, H., Bockstedte, A., Foliente, G.C., and Paevere, P. (2004). Parameter analysis of the differential model of hysteresis. *Journal of Applied Mechanics,* 71, 342-349.

Maccalden, P.B., and Matthiesen, R.B. (1974). Coupled response of two foundations. *In: Presented at the 5th World Conference on Earthquake Engineering*. Rome, Italy.

Masing, G. (1926). Eignespannungen und Verfestigung beim Messing. *In: Presented at the 2nd International Congress on Applied Mechanics*. Zurich, Switzerland.

Mason, H.B., Trombetta, N.W., Chen, Z., Bray, J.D., Hutchinson, T.C., and Kutter, B.L. (2013). Seismic soil–foundation–structure interaction observed in geotechnical centrifuge experiments. *Soil Dynamics and Earthquake Engineering,* 48, 162-174.

MATLAB. (2016). The Mathworks, Inc., version R2016a

Matthees, W., and Magiera, G. (1982). A Sensitivity Study of Seismic Structure-Soil-Structure Interaction Problems for Nuclear Power Plants. *Nuclear Engineering and Design,* 73, 343-363.

Menglin, L., Huaifeng, W., Xi, C., and Yongmei, Z. (2011). Structure–soil–structure interaction: Literature review. *Soil Dynamics and Earthquake Engineering,* 31, 1724-1731.

MidasGen+. (2019). Integrated Solution System for Building and General Structures. MIDAS Information Technology Co, Ltd.

Miranda, E., and Bertero, V. (1994). Evaluation of strength reduction factors of earthquake-resistant design. *Earthquake Spectra,* 10(2), 357-379.

Mizuno, H. (1980). Effects of structure–soil–structure interaction during various excitations. *In: Presented at the 7th World Conference on Earthquake Engineering*. Istanbul, Turkey.

Mulliken, J.S., and Karabalis, D.L. (1998). Discrete model for dynamic through-the-soil coupling of 3D foundations and structures. *Soil Dynamics and Earthquake Engineering,* 27, 678-710.

Mykoniou, K., Butenweg, C., Holtschoppen, B., and Klinkel, S. (2016). Seismic response analysis of adjacent liquid-storage tanks. *Earthquake Engineering and Structural Dynamics,* 45, 1779-1796.

Mylonakis, G., and Gazetas, G. (2000). Seismic Soil-Structure Interaction: beneficial or detrimental? *Journal of Earthquake Engineering,* 4(3), 277-301.

Naito, Y., Yano, T., Suzuki, A., Kurita, S., and Kazama, M. (2001). Model test on dynamic cross interaction of adjacent buildings in nuclear power plants - Field Test. *In: Transactions of the SMiRT-16*. Washington DC, USA.

Naserkhaki, S., and Pourmohammad, H. (2012). SSI and SSSI effects in seismic analysis of twin buildings: Discrete model concept. *Journal of Civil Engineering and Management,* 18(6), 890-898.

NCh 433. (2009). Earthquake Resistant Design of Buildings. National standardization institute.

NEHRP-NIST. (2012). Soil-Structure Interaction for Building Structures. National Institute of Standards and Technology GCR 12-917-21.

Newmark, N.M., and Rosenblueth, E. (1971). *Fundamentals of earthquake engineering* (2nd ed.). Englewood Cliffs, N.J. USA.: Prentice-Hall.

Ngo, V.L., Kim, J.M., Chang, S.H., and Lee, C. (2019). Effects of height and mass ratio on Structure-soil-structure interaction of two structures using centrifugal experiment. *Applied Sciences,* 9, 526.

Niazi, M. (1986). Inferred displacements, velocities and rotations of a long rigid foundation located at El Centro differential array site during the 1979 Imperial Valley, California, earthquake. *Earthquake Engineering and Structural Dynamics,* 14, 531-542.

Nigbor, R.L. (1994). Six-degree-of-freedom ground-motion measurement. *Bulletin of the Seismological Society of America,* 84, 1665-1669.

Oliveira, C., and Bolt, B. (1989). Rotational components of the surface strong ground motion. *Earthquake Engineering and Structural Dynamics,* 18, 517-526.

Padron, L.A., Aznarez, J.J., and Maeso, O. (2009). Dynamic structure–soil–structure interaction between nearby piled buildings under seismic excitation by BEM–FEM model. *Soil Dynamics and Earthquake Engineering,* 29, 1084-1096.

Pais, A., and Kausel, E. (1988). Approximate formulas for dynamic stiffnesses of rigid foundations. *Soil Dynamics and Earthquake Engineering,* 7(4), 213-227.

Paolucci, R., and Smerzini, C. (2008). Earthquake-induced transient ground strain from dense seismic networks. *Earthquake Spectra,* 24(2), 453-470.

Pedretti, S. (1998). *Nonlinear seismic soil-structure interaction: analysis and modelling method.* Politecnico di Milano, Milano, Italy.

PEER. (2014). *Strong Motion Database. The pacific Earthquake Engineering Center and the University of California*. Retrieved from: http://ngawest2.berkeley.edu/

Penzien, J., and Watabe, M. (1975). Characteristics of 3-dimensional earthquake ground motion. *Earthquake Engineering and Structural Dynamics,* 3, 365-373.

Petersen, K.B., and Pedersen, M.S. (2007). *The Matrix Cookbook* (1st ed.): Technical University of Denmark

Priestley, M.J.N., and Park, R. (1987). Strength and ductility of concrete bridges columns under seismic loading. *ACI Structural Journal,* 84(1), 61-76.

Qi, S., and Knappett, J. (2020). Influence of foundation type on seismic response of low-rise structures in liquefiable soil. *Soil Dynamics and Earthquake Engineering,* 128, 105786.

Qian, J., and Beskos, D.E. (1995). Dynamic interaction between 3-D rigid surface foundations and comparison with the ATC-3 provisions. *Earthquake Engineering and Structural Dynamics,* 24, 419-437.

Qian, J., and Beskos, D.E. (1996). Harmonic wave response of two 3-D rigid surface foundations. *Soil Dynamics and Earthquake Engineering,* 15, 95-110.

Qian, J., Tham, L.G., and Cheung, Y.K. (1996). Dynamic cross-interaction between flexible surface footings by combined BEM & FEM. *Earthquake Engineering and Structural Dynamics,* 25, 509-526.

Ramberg, W., and Osgood, W.R. (1943). Description of Stress-Strain-Curves by Three Parameters. NACA.

Roy, C., Bolourchi, S., and Eggers, D. (2015). Significance of structure–soil–structure interaction for closely spaced structures. *Nuclear Engineering and Design,* 295, 680-687.

Rutenberg, A., and Heidebrecht, A. (1985). Response spectra for torsion, rocking and rigid foundations. *Earthquake Engineering and Structural Dynamics,* 13, 543-557.

Sandwell, D.T. (1987). Biharmonic spline interpolation of GEOS-3 and SEASAT altimeter data. *Geophysical Research Letters,* 14(2), 139-142.

Sargeant, S.L., and Musson, R.M. (2009). Short note: rotational earthquake effects in the United Kingdom. *Bulletin of the Seismological Society of America,* 99, 1475-1479.

Schwan, L., Boutin, C., Padron, L.A., Dietz, M.S., Bard, P-Y., and Taylor, C. (2016). Site-City interaction: theoretical, numerical and experimental crossed-analysis. *Geophysical Journal International,* 205, 1006-1031.

SEAOC Bluebook. (1976). *Bluebook: Recommended Lateral Force Requirements and Commentary*: SEAOC.

Semblat, F., Gueguen, P., Kham, M., Bard, P-Y., and Duval, A.M. (2002). Site-city interaction at local and global scales. *In: Presented at the 12th European Conference on Earthquake Engineering*. London, UK.

Semblat, F., Kham, M., Bard, P-Y., and Gueguen, P. (2004). Could "site-city interaction" modify site effects in urban areas? *In: Presented at the 13th World Conference on Earthquake Engineering*. Vancouver, British Columbia, Canada.

Semblat, J.F., Kham, M., and Bard, P-Y. (2008). Seismic-Wave Propagation in Alluvial Basins and Influence of Site-City Interaction. *Bulletin of the Seismological Society of America,* 98(6), 2665-2678.

SMART-1, IES. (1991). Institute of Earth sciences (IES), Academia Sinica. SMART-1 Array data repository, Taiwan; 1980–1991. Retrieved from http://www.earth.sinica.edu.tw/~smdmc/

Smerzini, C., Paolucci, R., and Stupazzini, M. (2009). Experimental and numerical results on earthquake-induced rotational ground motion. *Journal of Earthquake Engineering,* 13, 66-82.

Solari, D., Stura, D., and Vardanega, C. (1980). On the accuracy of numerical models in 3-D soil–structure interaction. *In: Presented at the 7th World Conference on Earthquake Engineering*. Istanbul, Turkey.

Spudich, P., Steck, L., Hellweg, M., Fletcher, J., and Lawrence, M. (1995). Transient stress at Parkfield, California, produced by the M7.4 Landers earthquake of June 28, 1992: observations from the UPSAR dense seismograph array. *Journal of Geophysical Research,* 100, 975-990.

Stathopoulos, K.G., and Anagnostopoulos, S.A. (2010). Accidental design eccentricity: is it important for the inelastic response of buildings to strong earthquakes? *Soil Dynamics and Earthquake Engineering,* 30, 782-797.

Stewart, J.P., Fenves, G.L, and Seed, R.B. (1999). Seismic Soil-Structure Interaction in Buildings. I: Analytical Methods. *Journal of Geotechnical and Geoenvironmental Engineering,* 125(1), 26-37.

Syamal, P. (1985). Dynamic response of bilinear asymmetric structures. *Earthquake Engineering and Structural Dynamics,* 13, 527-541.

Taborda, R., and Bielak, J. (2011a). Full 3D integration of site-city effects in regional scale earthquake simulations. *In: Presented at the 8th International Conference on Structural Dynamics, EURODYN 2011*. Leuven, Belgium.

Taborda, R., and Bielak, J. (2011b). Large-scale earthquake simulation - Computational seismology and complex engineering systems. *Computing in Science & Engineering,* 13, 14-26.

Takeda, T., Sozen, M.A., and Neilsen, N.N. (1970). Reinforced concrete response to simulated earthquakes. *ASCE Journal of the Structural Division,* 96, 2557-2573.

Takeo, M. (1998). Ground rotational motions recorded in near-source region of earthquakes. *Geophysical Research Letters,* 25, 789-792.

Tatsuoka, F., Siddiquee, M., Park, Ch., Sakamoto, M., and Abe, F. (1993). Modelling stress-strain relations of sand. *Soils and Foundations,* 33, 60-81.

Tham, L.G., Qian, J., and Cheung, Y.K. (1998). Dynamic response of a group of flexible foundations to incident seismic waves. *Soil Dynamics and Earthquake Engineering,* 17, 127-137.

Tombari, A., Espinosa, M.G., Alexander, N.A., and Cacciola, P. (2018). Vibration control of a cluster of buildings through the Vibrating Barrier. *Mechanical Systems and Signal Processing,* 101, 2019-2036.

Triantafyllidis, T., and Prange, B. (1987). Dynamic subsoil-coupling between rigid rectangular foundations. *Soil Dynamics and Earthquake Engineering,* 6(3), 164-179.

Triantafyllidis, T., and Neidhart, T.H. (1989). Diffraction effects between foundations due to incident rayleigh waves. *Earthquake Engineering and Structural Dynamics,* 18, 815-835.

Triantafyllidis, T., and Prange, B. (1989). Dynamic subsoil-coupling between rigid, circular foundations on the half-space. *Soil Dynamics and Earthquake Engineering,* 8(1), 9-21.

Trifunac, M.D. (1982). A note on rotational components of earthquake motions for incident body waves. *Soil Dynamics and Earthquake Engineering,* 1, 11-19.

Trifunac, M.D. (2009). The role of strong motion rotations in the response of structures near earthquake faults. *Soil Dynamics and Earthquake Engineering,* 29, 382-393.

Trombetta, N.W., Hutchinson, T.C., Mason, H.B., Zupan, J.D., Bray, J.D., and Bolisetti, C. (2012). Centrifuge modeling of structure–soil–structure interaction: seismic performance of inelastic building models *In: Presented at the 15th World Conference on Earthquake Engineering*. Lisbon, Portugal.

Trombetta, N.W., Mason, H.B., Chen, Z., Hutchinson, T.C., Bray, J.D., and Kutter, B.L. (2013). Nonlinear dynamic foundation and frame structure response observed in geotechnical centrifuge experiments. *Soil Dynamics and Earthquake Engineering,* 50, 117-133.

Trombetta, N.W., Mason, H.B., Hutchinson, T.C., Zupan, J., Bray, J.D., and Kutter, B.L. (2014). Nonlinear soil-foundation-structure and structure-soil-structure interaction: Centrifuge test observations. *Journal of Geotechnical and Geoenvironmental Engineering,* 140(5), 04013057.

Trombetta, N.W., Mason, H.B., Hutchinson, T.C., Zupan, J., Bray, J.D., and Kutter, B.L. (2015). Nonlinear soil-foundation-structure and structure-soil-structure interaction: engineering demands. *Journal of Structural Engineering,* 141(7).

Tsinidis, G., Pitilakis, K., Trikalioti, A.D. (2014). Numerical simulation of round robin numerical test on tunnels using a simplified kinematic hardening model. *Acta Geotechnica* 9 (4), 641–659.

Tsogka, C., and Wirgin, A. (2003). Simulation of seismic response in an idealized city. *Soil Dynamics and Earthquake Engineering,* 23, 391-402.

United Nations – DESA Department of Economic and Social Affairs. (2018). World Urbanization Prospect. The 2018 Revision.

United Nations. (2018). Department of Economic and Social Affairs. Retrieved from https://www.un.org/development/desa/en/

Veletsos, A.S., and Meek, J.W. (1974). Dynamic behavior of building-foundation systems. *Earthquake Engineering and Structural Dynamics,* 3, 121-138.

Veletsos, AS., and Nair, VV. (1975). Seismic interaction of structures on hysteretic foundations. *Journal of Structural Engineering,* 101, 109-129.

Vicencio, F., and Alexander, N.A. (2017). Discrete model for dynamic SSSI through nonlinear soil. *In: Presented at the SEISMICON 2017. First international conference on seismic design of structures and foundations*. London, (UK).

Vicencio, F., and Alexander, N.A. (2018a). Dynamic interaction between adjacent buildings through nonlinear soil during earthquakes. *Soil Dynamics and Earthquake Engineering,* 108, 130-141.

Vicencio, F., and Alexander, N.A. (2018b). Higher mode seismic Structure-Soil-Structure Interaction between adjacent buildings during earthquakes. *Engineering Structures,* 174, 322-337.

Vicencio, F., and Alexander, N.A. (2018c). Discrete model for dynamic SSSI between critical structures under strong ground motion. *In: Presented at the 16th European Conference on Earthquake Engineering.* Thessaloniki, Greece.

Vicencio, F., and Alexander, N.A. (2019a). A parametric study on the effect of rotational ground motions on building structural responses. *Soil Dynamics and Earthquake Engineering*, 118, 191-206.

Vicencio, F., and Alexander, N.A. (2019b). Dynamic Structure-Soil-Structure Interaction in unsymmetrical plan buildings due to seismic excitation. *Soil Dynamics and Earthquake Engineering*, 127, 105817.

Vicencio, F., and Alexander, N.A. (2019c). Numerical analysis of Structure-Soil-Structure Interaction for two different buildings during earthquakes. *In: Presented at the COMPDYN 2019. 7th International Conference on Computational Methods in Structural Dynamics and Earthquake Engineering.* Crete, Greece.

Vicencio, F., and Alexander, N.A. (2021). Method to evaluate the dynamic Structure-Soil-Structure Interaction of 3-D buildings arrangement due to seismic excitation. *Soil Dynamics and Earthquake Engineering*, 141, 106494.

Wang, H.F., Lou, M.L., Chen, X., and Zhai, Y. (2013). Structure-soil-structure interaction between underground structure and ground structure. *Soil Dynamics and Earthquake Engineering*, 54, 31-38.

Wang, HF., Lou, ML., and Zhang, RL. (2017). Influence of presence of adjacent surface structure on seismic response of underground structure. *Soil Dynamics and Earthquake Engineering*, 100, 131-143.

Wang, S., and Schmid, G. (1992). Dynamic structure–soil–structure interaction by FEM and BEM. *Computational Mechanics*, 9, 347-357.

Warburton, G.B., Richardson, J.D., and Webster, J.J. (1971). Forced vibration of two masses on an elastic half space. *Journal of Applied Mechanics*, 38(1), 148-156.

Wen, Y.K. (1976). Method for random vibration of hysteretic systems. *Journal of the Engineering Mechanics*, 102, 249-263.

Wirgin, A., and Bard, P-Y. (1996). Effects of buildings on the duration and amplitude of ground motion in Mexico city. *Bulletin of the Seismological Society of America*, 86, 914-920.

Wong, H.L., and Luco, J.E. (1986). Dynamic interaction between rigid foundations in a layered half-space. *Soil Dynamics and Earthquake Engineering*, 5, 149-158.

Wong, HL., and Trifunac, MD. (1975). Two-dimensional, antiplane, building–soil–building interaction for two or more buildings and for incident planet SH waves. *Bulletin of the Seismological Society of America*, 65, 1863-1885.

Woodgate, K.G. (1998). Efficient stiffness matrix estimation for elastic structures. *Computers & Structures*, 69, 79-84.

Yahyai, M., Mirtaheri, M., Mahoutian, M., and Daryan, A.S. (2008). Soil structure interaction between two adjacent buildings under earthquake load. *American Journal of Engineering and Applied Sciences*, 1, 121-125.

Yano, T., Kitada, Y., Iguchi, M., Hirotani, T., and Yoshida, K. (2000). Model test on dynamic cross interaction of adjacent buildings in nuclear power plants. *In: Presented at the 12th World Conference on Earthquake Engineering.* Auckland, New Zealand.

Yano, T., Naito, Y., Iwamoto, K., Kitada, Y., and Iguchi, M. (2003). Model test on dynamic cross interaction od adjacent buildings in nuclear power plants - Overall evaluation on field test *In: Transactions of the SMiRT-17*. Prague, Czech Republic.

Yin, J., Nigbor, R.L., Chen, Q., and Steidl, J. (2016). Engineering analysis of measured rotational ground motions at GVDA. *Soil Dynamics and Earthquake Engineering,* 87, 125-137.

Zembaty, Z., and Boffi, G. (1994). Effect of rotational seismic ground motion on dynamic response of slender towers. *Eur Earthquake Engineering,* 8, 3-11.

Zembaty, Z. (2009). Tutorial on surface rotation from wave passage effects: stochastic spectral approach. *Bulletin of the Seismological Society of America,* 99(2B), 1040-1049.

Zienkiewicz, O.C., Bianic, N., Shen, F.Q. (1988). Earthquake input definition and the transmitting boundary condition. *In: St. Doltnis, I. (Ed.), Conf: Advances in Computational Non-Linear Mechanics*, 109–138.